AATD System Technical Characteristics, Design Concepts and Trauma Assessment Criteria

Technical Report Documentation Page

1. Report No.	2. Government Accession No.	3. Recipient's Catalog No.

4. Title and Subtitle	5. Report Date
AATD SYSTEM TECHNICAL CHARACTERISTICS, DESIGN CONCEPTS, AND TRAUMA ASSESSMENT CRITERIA	September 1985
	6. Performing Organization Code
	8. Performing Organization Report No.
7. Author(s) J.W. Melvin, A.I. King,* and N.M. Alem	
9. Performing Organization Name and Address The University of Michigan Department of Mechanical Engineering and Applied Mechanics Ann Arbor, Michigan 48109	10. Work Unit No. (TRAIS)
	11. Contract or Grant No. DTNH22-83-C-07005
12. Sponsoring Agency Name and Address U.S. Department of Transportation National Highway Traffic Safety Administration Washington, DC 20590	13. Type of Report and Period Covered TASK E-F FINAL REPORT 8/83 - 9/85
	14. Sponsoring Agency Code

15. Supplementary Notes

NHTSA Contract Technical Manager:
Mark P. Haffner, Office of Crashworthiness Research

16. Abstract

This report establishes the technical characteristics and design concepts for the AATD system, including all body regions and the data processing and certification systems. The development of the biomechanical data base used to produce human impact response and injury information is described, and current recommendations for Trauma Assessment Criteria (TAC) are made. Further analyses aimed at improving future TAC for the head and thorax are also presented.

*Work performed under subcontract to UMTRI by Wayne State University, Detroit, Michigan.

17. Key Words	18. Distribution Statement
Anthropomorphic Test Devices Design Specifications Biomechanical Response Injury Criteria	This document is available to the public through the National Technical Information Service, Springfield, VA 22161

19. Security Classif. (of this report)	20. Security Classif. (of this page)	21. No. of Pages	22. Price
None	None	155	

Form DOT F 1700.7 (8-72) Reproduction of completed page authorized

ACKNOWLEDGMENTS

As Project Director of the AATD program, I would like to acknowledge in this last of five final reports the contributions of Kathleen Weber to the success of Phase 1. Ms. Weber has given unsparingly of her time and effort to see that this program was a success in every way. Virtually every task of the program has benefitted from her work. She has played a critical role in the planning and scheduling of the program tasks, helped establish and maintain high standards of technical quality and fiscal integrity, and assured the quality of the task reports through her skills at writing, synthesizing, and editing diverse technical material. Conducting this program has been complex and, at times, difficult. Ms. Weber's efforts throughout Phase 1 have served to keep the program on course and moving ahead toward the successful completion of its goals.

J.W.M.

The authors of this report would like to acknowledge the contributions of the following individuals in making this report possible. R. Jeff Lehman of UMTRI and Said Nakla and Remi Pluche of WSU provided technical assistance in data analysis and mathematical modeling. Kathleen Richards of UMTRI provided efficient, high-quality graphics support for the text. Leda Ricci of UMTRI provided exceptional word processing expertise and diligent effort in preparing and revising the text of the report.

CONTENTS

LIST OF TABLES

LIST OF FIGURES

INTRODUCTION

This report brings together the results of our various reviews and analyses of accident data, biomechanical response and injury data, anthropometric data, and current ATD design, instrumentation, data processing, and certification procedures in order to establish technical characteristics for the AATD system, develop design concepts, and propose injury criteria that will achieve program goals. In addition to the activities described in previous Task reports, an important additional activity was in progress that provided necessary data for the current Tasks. This was the development of a biomechanical data base, which is described in the first section of this report.

BIOMECHANICAL DATA BASE

DEVELOPMENT OF THE DATA BASE

The biomechanical data base for the AATD program was developed in order to provide a large, consistently formatted data base, whose signals could be analyzed and compared in a uniform manner. Both previously published data and those published data that warranted reanalysis were identified, consolidated, categorized, and recoded or given additional coding as appropriate. The data base was used in producing response corridors for AATD technical characteristics and in analyses to improve injury assessment criteria.

A total of 1,190 tests were initially identified by test number and source as candidates for inclusion in the data base. However, we were able to obtain and include adequate data for only 221 tests, consisting of the following:

107 from UMTRI
55 from Heidelberg University
41 from ONSER
12 from WSU
4 from APR
2 from Calspan

These included the following test configurations:

110 pendulum impacts
52 three-point-harness tests
45 lateral sled tests
14 airbag tests

To augment these data, high-speed movies from 13 UMTRI thoracic pendulum tests were analyzed, and film readings were reformatted as "displacement" signals and incorporated with their corresponding sensor data. Finally, ten of the Heidelberg tests containing nine accelerometer signals were converted to the standard anatomical reference frame.

The resulting collection of tests was reviewed, and each test type was categorized and grouped in prepration for processing. A total of 4,108 signals from 221 tests are contained in the data base. However, many of them are redundant recordings of the same signal or are event timers or time-base signals. The most common signals are accelerations (87%), load cells (10%), and pressure transducers (3%).

One major problem in developing the data base was the fact that, on the one hand, errors were encountered in previously coded data while, on the other, there was a lack of coding of such important test parameters as the injury or instrumentation information. This information was necessary for grouping the signals into meaningful categories and allowing comparison of response from compatible signals. Thus, many special handling procedures had to be developed to recode these parameters and to convert signals into standard anatomical reference frames.

The test parameters that were used as the basis for grouping were: (1) restraint type or impact surface, (2) severity of impact, described by impact velocity, (3) injury level, described by an AIS number, and (4) the subject size and condition. The signals were further subdivided by body area, which included the head, thorax, spine, shoulder, and lower extremities.

Once these groups were established, the first step in the uniform processing of the grouped signals was to determine the frequency spectra of the signals in each group by spectral analysis. In the thorax, for example, the rib, sternum, and spinal accelerations may all have different spectra under the same impact. Also, different impacts, such as belt loadings, steering wheel impacts, airbag loads, and rigid- or padded-wall impacts, may produce different response frequencies at the same location, such as at the sternum. It was therefore important to determine the range of frequencies that were contained in the signals. This information was then used in defining the significant frequency range and subsequent filtering characteristics for analyzing the dynamic response of each particular combination of body region, restraint load type, transducer, and transducer location. The frequency response of a group of data signals was defined in terms of a corner frequency and a roll-off slope. This was done by the following procedure:

1. Determine the power spectra of all pertinent signals in a group.
2. Integrate the power spectra to obtain the cumulative power as a function of frequency.
3. Locate the frequencies on the cumulative power curve at which 50, 75, 90, 95, and 99% of the power has accumulated. These are respectively the -3, -6, -10, -13, and -20 dB points of the filter that is characteristic of the system that produced those signals.
4. Find the mean and standard deviations of these five points.
5. Shift the dB points upward to their corresponding points on the asymptote of the frequency response.
6. Fit the shifted points to the best straight line. This line is then the best estimate of an asymptote to the desired filter.
7. Determine the filter's -3 dB corner as an intersection of the asymptote with the 0 dB line and the filter's order (degree) from the slope of the asymptote, given that -6 dB/decade is added to the slope for every degree of the filter.
8. Overplot the results for various signals and determine the most suitable filter to be used on all data from a given body region. This will also dictate the minimum sampling rate that can be used in digitizing the signals.

The data signals in which skeletal fractures occurred at the transducer site (such as a rib-mounted accelerometer) were excluded from the groups. This analysis was performed on head impact data and thoracic impact data. The resulting filter characteristics for these regions are shown in Figures 1, 2(a), and 2(b). For the head, a low-pass Butterworth filter is defined with a roll-off frequency (i.e., -3dB frequency) of 550 Hertz and a roll-off slope of -26 dB/decade. For the chest, two filters were defined: one for data acquisition and one for data analysis. The data acquisition filter has a roll-off frequency of 500 Hertz and a roll-off slope of -27 dB/decade. The data analysis filter has a roll-off frequency of 180 Hertz and a roll-off slope of -15 dB/decade.

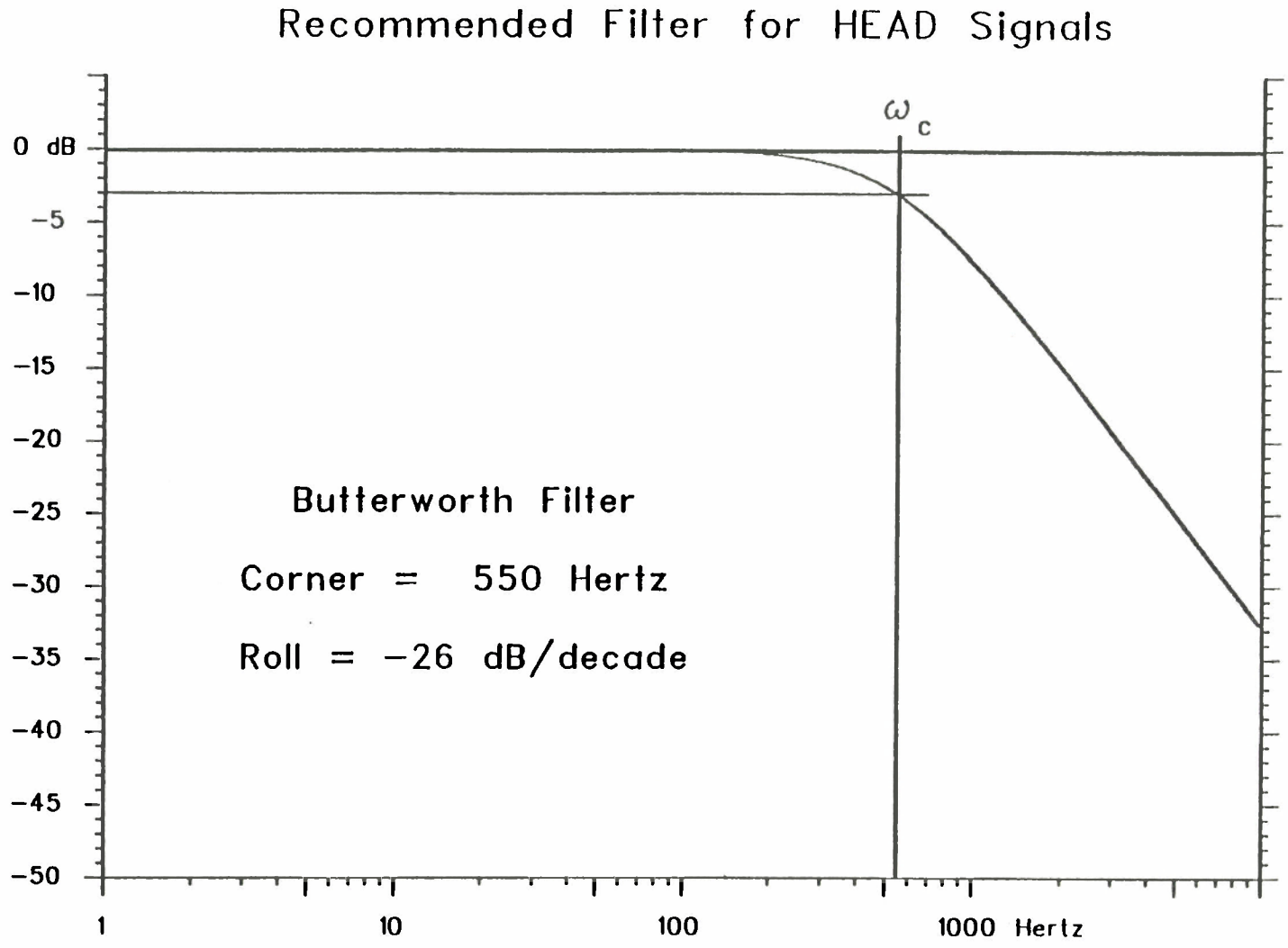

FIGURE 1. Recommended filter for HEAD signals.

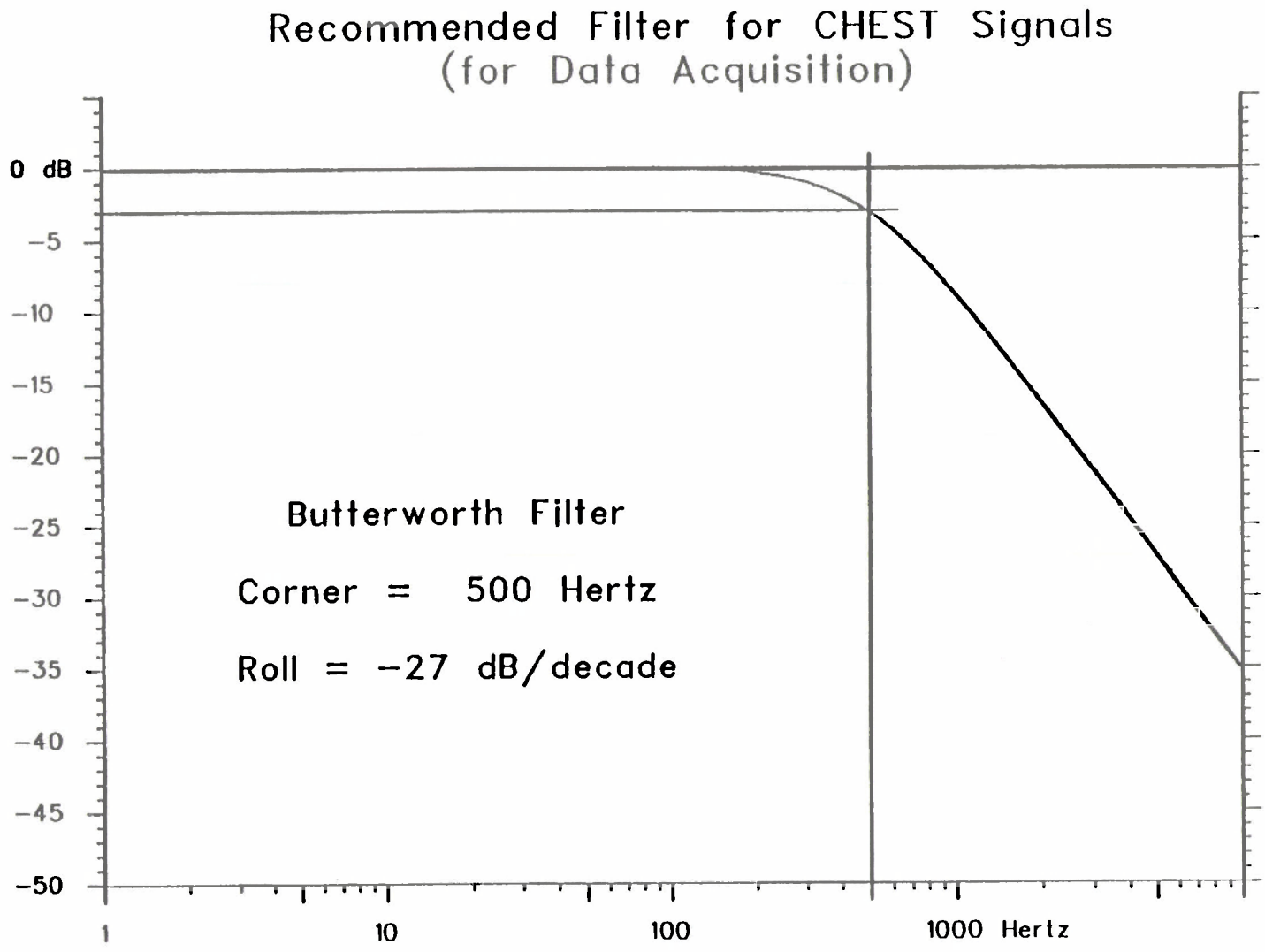

FIGURE 2(a). Recommended data acquisition filter for CHEST signals.

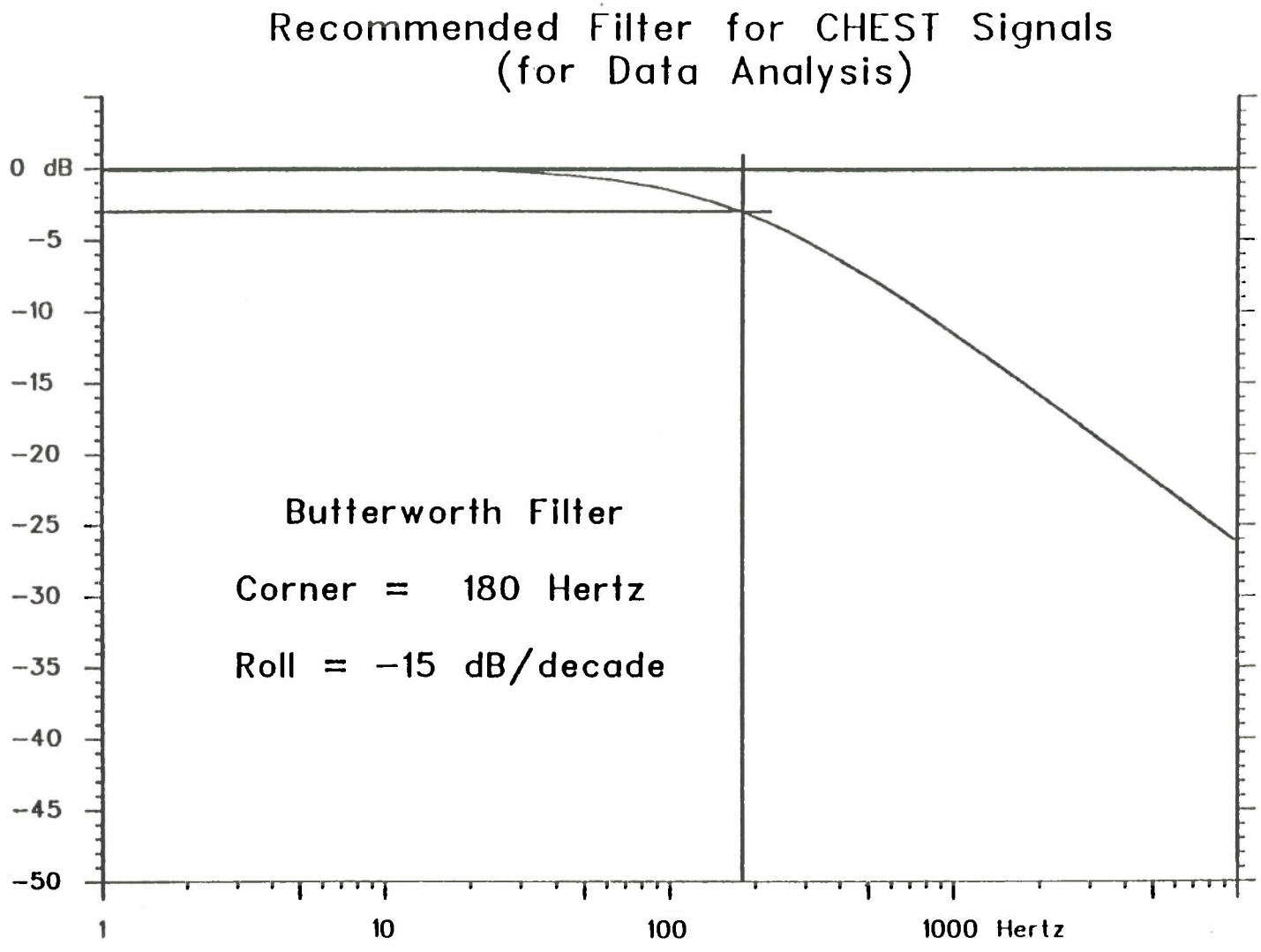

FIGURE 2(b). Recommended data analysis filter for CHEST signals.

After establishing the filter specifications, the next step in the uniform processing of the grouped signals was to normalize or scale the individual signals according to the methods discussed in the next section of this report. It was then possible to begin the task of overplotting the grouped, filtered, and scaled signals. Individual signals within one group of similar impact tests, however, cannot be overplotted readily. Two operations that must be applied are:

1. Bias removal, which will force the signal to be zero prior to the impact and will affect both time and frequency plots; and

2. Alignment, which will shift the signals from different tests (recorded and digitized at different times), so that the beginning of impact begins at the same point in the signal, a shift that will affect time domain overplots but not frequency domain plots.

The thoracic impact group was the largest grouping of the AATD biomechanical data base and will be used here as an example of the above processing steps. The tests in this group were categorized into the following loading types:

ABG	Frontal airbag
3PT	Frontal three-point harness
LAP	Frontal lap belt
PFT	Pendulum frontal
PST	Pendulum side
RIG	Sled rigid wall
MCI	Sled padded wall
DOR	Volvo door, lateral

There was also partitioning by velocity within each test type. This produced a total of fourteen sets of thoracic signals, with as many as twenty-four different tests in one group. Within each group, up to nine transducer/axis combinations were defined as "near," "mid-range," and "far" transducers, depending on their proximity to the impacting surface. There were 1,286 thoracic accelerometer signals available in the data base.

In about 90% of the signals, an automatic alignment was satisfactory. In the remaining cases, alignment was done graphically and interactively. In many cases, polarities of the signals were obviously "wrong" and had to be reversed. Finally, the DC bias was removed from all signals. The processed signals were overplotted, a summary printout of the involved signals was made, and the processed signals were saved on disc file for further processing. A total of 96 overplots (along with +1 S.D., mean, -1 S.D.) were generated.

Following the implementation of all the above data processing steps, the signals in the data base were in a form suitable for the generation of AATD response specification and injury criteria activities. The analysis of thoracic load-deflection responses for rigid moving-mass impact tests is described in the thoracic response section.

USING BIOMECHANICAL IMPACT RESPONSE DATA

The use of cadavers to determine the impact response of the human body relies on many assumptions regarding the realism of the cadaver as a surrogate of the human and our ability to normalize data from different size test subjects given that they are realistic.

It is assumed that the skeletal structures of cadavers are essentially unchanged after death and that the condition of the bone material is representative of the subject's bone condition prior to death. Given the relatively inert nature of the load-carrying microstructure of bone, this assumption is reasonable.

Regarding muscle factors, the cadaver lacks the postural muscle tone of the living, but the ability of active muscle response to affect overall impact response depends on the body region being loaded and the type of loading being applied. Although voluntary pretensing of muscles prior to impact may influence the initial conditions and initial response to some extent, for large direct loads to the body, these effects will be overwhelmed by the high rate of loading and the short duration of the load application. The living neuro-muscular system is not able to respond in a short-duration dynamic loading situation.

An example of such a situation might be a direct impact to the thorax. Although pretensioning of the diaphragm and chest muscles may significantly increase the stiffness of the thorax and thus alter its static load-deflection response, such pretensioning will have relatively little influence on the dynamic response. This is because the dynamic response of the thorax to impact loading appears to be dominated by the inertial and viscous (passive) responses of the structure. Thus, in both frontal and lateral chest impacts, it is the thoracic mass, including muscle tissue, ribs, and viscera, as well as the viscous nature of the latter, that resists the local motion (depression) of the chest wall. Because there are no muscle structures in the thorax that can directly resist such motion, this effect is lacking even among living humans.

On the other hand, musculo-skeletal structures such as those of the spine, in which there is a complex arrangement of muscles for posture and motion control, may have an influence on dynamic response, particularly with indirect impacts or inertial loading associated with restraint system kinematics. Because relatively large motions can be produced in such situations, and these motions can be directly resisted by muscular action, pretensing may have a significant influence on the resulting dynamic response in terms of the phasing of the motions and the peak values of the dynamic parameters. These effects may decrease as impact severity levels increase, but this has not been demonstrated due to obvious limitations on human volunteer testing.

The other major problem with using cadaver-based impact response data is dealing with the differences in size among the test subjects. Some data sources use only male cadavers in a narrow size and weight range approximating the average male (174.7 cm and 77.5 kg), but most data sources have subjects that are quite different in size from the average male, resulting in differences in impact response. In order to reduce the variability of these responses, the techniques of dimensional analysis can be applied to normalize the data to that of the mid-sized male.

The assumptions that the mass densities of the test subjects and the moduli of elasticity of their skeletal material are all approximately the same lead to scaling laws referred to as equal stress and equal velocity scaling. Both Eppinger et al. (1984) and Mertz (1984) have proposed data scaling techniques based on these assumptions. It can be shown that both techniques produce the same scaling laws. These laws are as follows:

Define three basic scaling variables as

$$\lambda_m = \frac{m_s}{m_i}$$

$$\lambda_\rho = \frac{\rho_s}{\rho_i}$$

$$\lambda_E = \frac{E_s}{E_i}$$

where: λ = scaling constant
m = mass
ρ = mass density
E = modulus of elasticity
s = scaled or model data
i = ith subject or prototype data

The assumptions of equal mass density and modulus of elasticity between subjects and the scaled or standard model yields

$$\lambda_\rho = 1 \quad \text{and} \quad \lambda_E = 1$$

The effect of these assumptions yields the following relationships between all other physical parameters (Eppinger et al. 1984).

LENGTH: $\lambda_l = \frac{l_s}{l_i}$, basic definition

MASS: $\lambda_m = \frac{m_s}{m_i} = \lambda_l^3$ due to $\lambda_\rho = 1$

TIME: $\lambda_t = \frac{t_s}{t_i} = \lambda_l = \lambda_m^{1/3}$

VELOCITY: $\lambda_v = \frac{v_s}{v_i} = 1$

ACCELERATION: $\lambda_a = \frac{a_s}{a_i} = \lambda_l^{-1} = \lambda_m^{-1/3}$

FORCE: $\lambda_F = \frac{F_s}{F_i} = \lambda_l^2 = \lambda_m^{2/3}$

The problem with applying these scaling methods is that cadavers cannot practically be selected such that their dimensions and weights exactly fit the above relationships. If the overall height of the subject is used to calculate λ_l, and the total weight is used to calculate λ_m, λ_m will not equal λ_l^3 if the cadaver is not a scaled prototype of the mid-sized AATD. Therefore, since biomechanical data scaling is usually concerned with the adjustment of data related to impact with only one particular body segment (e.g., head, chest, pelvis), and overall height may not always be directly related to other body

dimensions, a mass-based dimensional scaling may be more representative, as indicated below. When additional body regional dimensions, particularly radial dimensions, are available, they may be used to obtain more appropriate scaling.

The anthropometric data from the vehicle occupant anthropometry study of Schneider et al. (1983) were used to investigate scaling by using the small female and large male data as prototypes relative to the mid-sized male as the model. Table 1 lists the basic scaling factor values for the three size ranges. For both the small female and the large male, the scaling factor $\lambda_1 = \sqrt[3]{\lambda_m}$ is closer to the actual torso scaling factor $(\lambda_1)_{TV} = \sqrt[3]{\lambda_{TV}}$, where λ_{TV} is the scaling factor based on torso volume, than the scaling factors given by either the total height or the sitting height. The small female value is within 3.7% and the large male is within 1.6%, while the corresponding height scale factors are within 13.8% and 4.5%, respectively. Thus, scaling of impact data for the torso is best done using the mass ratio as the scale factor for obtaining length scaling when more appropriate measures are lacking. The method used for scaling data for each body region is indicated with the individual discussions of the regional data.

TABLE 1

SCALING FACTOR ANALYSIS

Characteristic	Small Female	Mid-Sized Male	Large Male
Weight (kg)	$\lambda_m = \frac{77.5}{47.3} = 1.638$ $\sqrt[3]{\lambda_m} = 1.179$	$\lambda_m = \frac{77.5}{77.5} = 1$ $\sqrt[3]{\lambda_m} = 1$	$\lambda_m = \frac{77.5}{101.8} = 0.761$ $\sqrt[3]{\lambda_m} = 0.913$
Height (cm)	$(\lambda_1)_H = \frac{174.7}{162.7} = 1.074$	$(\lambda_1)_H = \frac{174.7}{174.7} = 1$	$(\lambda_1)_H = \frac{174.7}{186.1} = 0.939$
Sitting Height (cm)	$(\lambda_1)_{SH} = \frac{91.9}{81.8} = 1.124$	$(\lambda_1)_{SH} = \frac{91.9}{91.9} = 1$	$(\lambda_1)_{SH} = \frac{91.9}{96.9} = 0.948$
Chest Circumference at Nipple (cm)	$(\lambda_1)_{CC} = \frac{101}{83.3} = 1.212$	$(\lambda_1)_{CC} = \frac{101}{101} = 1$	$(\lambda_1)_{CC} = \frac{101}{115.9} = 0.871$
Chest Depth at Nipple (cm)	$(\lambda_1)_{CD} = \frac{23.5}{19} = 1.236$	$(\lambda_1)_{CD} = 1$	$(\lambda_1)_{CD} = \frac{23.5}{26.8} = 0.877$
Chest Breadth at Nipple (cm)	$(\lambda_1)_{CB} = \frac{34.9}{27.6} = 1.264$	$(\lambda_1)_{CB} = 1$	$(\lambda_1)_{CB} = \frac{34.9}{38.4} = 0.909$

TABLE 1 (Continued)

Characteristic	Small Female	Mid-Sized Male	Large Male
Torso Height (cm)	$(\lambda_1)_{TH}=\frac{58}{51.2}=1.133$	$(\lambda_1)_{TH}=1$	$(\lambda_1)_{TH}=\frac{58}{63.5}=0.913$
Torso Volume (cm^3)	$(\lambda_1^3)_{TV}=\frac{39352}{21569}=1.825$ $\sqrt[3]{(\lambda_1^3)_{TV}}=1.222$	$(\lambda_1^3)_{TV}=1$ $\sqrt[3]{(\lambda_1^3)_{TV}}=1$	$(\lambda_1^3)_{TV}=\frac{39352}{54168}=0.727$ $\sqrt[3]{(\lambda_1^3)_{TV}}=0.899$
Whole Body Volume (cm^3)	$(\lambda_1^3)_{WB}=\frac{80254}{48215}=1.665$ $\sqrt[3]{(\lambda_1^3)_{WB}}=1.185$	$(\lambda_1^3)_{WB}=1$ $\sqrt[3]{(\lambda_1^3)_{WB}}=1$	$(\lambda_1^3)_{WB}=\frac{80254}{107964}=0.743$ $\sqrt[3]{(\lambda_1^3)_{WB}}=0.906$

TECHNICAL CHARACTERISTICS AND DESIGN CONCEPTS

The AATD will be designed to provide omnidirectional response in the range of $\pm 90°$ from the front in the horizontal plane. This accounts for virtually all the horizontal collision Injury Priority Rating (IPR) and 82% of all IPR with known principal direction of force (PDOF) (Carsten and O'Day 1984). The exposure severity levels associated with cumulative values of 85% of the IPR are delta Vs of 50 mph for frontal impacts and 30 mph for lateral impacts. It is expected that the AATD would be used unrestrained in such severe environments only if the vehicle structures and interiors to be tested incorporated advanced crashworthiness technology. Thus these delta V levels are taken to be upper limit exposure levels for the velocity of interaction with protective interior systems. The AATD will also be designed for upper body vertical (superior–inferior) impact associated with non–horizontal collisions. Such collisions account for 18% of all IPR with known PDOF.

Measurements to be made by the AATD are based on an analysis of ideal versus feasible measures as listed in Table 2. This analysis identified measures that would be desirable for injury assessment, given that an ideal test device could be developed that could reproduce all the anatomy and biomechanical responses of the human body. These were tempered by the state of the art of measurement technology, and measurements were determined that would be consistent with the AATD design concepts for each body region.

Following a brief discussion of the overall anthropometric specifications for the AATD, specifications for both anthropometry and biomechanical response are presented for each body region, and design concepts, illustrated in Figure 3, are described. Finally, specifications and design concepts are given for the AATD data processing and certification systems.

ANTHROPOMETRY OVERVIEW

The anthropometric specifications for the AATD are based on the detailed external dimensions for the mid–sized male as reported by Schneider et al. (1983). The details of the dimensions, coordinate system definitions, location of body segment centers of gravity, joint center locations, and other general specifications are incorporated into the specifications for the AATD by reference. Figure 4 illustrates the general configuration of these dimensions.

The mass and inertial characteristics for the AATD body segments, however, are different than those reported by Robbins (1983), because the latter assumed the specific gravity of all segments to be 1.000, whereas variations do exist. Table 3 lists the volumes determined by Robbins for each body segment of the mid–sized male, the associated specific gravity for that body region, and the resulting mass of the segment. The total mass of 77.47 kg (170.4 lbs) compares favorably with that of the 1974 Health and Nutrition Examination Survey (HANES) data (Abraham et al. 1979) indicating a 50th percentile male mass of 77.3 kg (170.1 lbs). Table 4 lists the associated segment inertial properties adjusted from Robbins (1983) to account for different specific gravities of the segments, as given in Table 3. These mass and inertial properties are used for the AATD.

TABLE 2

IDEAL AND FEASIBLE MEASURES

Ideal Measures	Feasible Measures
HEAD	
Skull • Global structural deformations. • Local contact forces. • Rigid body motion. Brain • Global pressure distributions. • Global tissue deformations and motions. Face • Bone structural loading • Soft tissue and nerve laceration	Skull • Continuous monitoring of skull deformation at selected sites. • Local contact force at selected sites, but not for the general case of any impact site. • Rigid body three-dimensional motion. Brain: • Continuous monitoring of pressure distributions or of tissue motions and deformations at selected sites. Face: • Facial bone load • Soft tissue lacerations and facial bone fractures, simulated with lacerable and frangible materials
SPINE	
• Motion and/or dislocation of vertebral elements • Local loads between vertebral elements • Input loads to spinal segments • Local deformations of the spinal cord • Muscle, blood vessel, and nerve deformations and lacerations	• Three-dimensional motions of vertebral elements • Local load measurement between vertebral elements at selected sites • Input loads to spinal segments from surrounding body • Continuous measurements of spinal cord, blood vessel, muscle, and nerve deformations at selected sites • Soft tissue, blood vessel, and nerve lacerations, simulated with lacerable materials
THORAX	
• Pressures in the heart, aorta, and lungs • Motions and deformations of the heart, aorta, and lungs • Rib cage motions, deformations, and loads	• Continuous monitoring of the pressure distributions in the heart, aorta, and lungs at selected sites • Continuous monitoring of motions, and deformations of the heart, aorta, lungs, and rib cage at selected sites
ABDOMEN	
• Pressures in the internal abdominal organs • Motions and deformations of the internal abdominal organs	• Continuous monitoring of the pressure distributions in the internal abdominal organs at selected sites • Continuous monitoring of the motions and deformations of the internal abdominal organs at selected sites
LOWER EXTREMITIES	
• Loads in the pelvis, upper leg, knee, and lower leg • Motions and dislocations of joints • Soft tissue and nerve lacerations	• Load measurements in the pelvis, femur, knee, and tibia • Measurement of motions and dislocations of joints • Soft tissue and nerve lacerations, simulated with lacerable materials

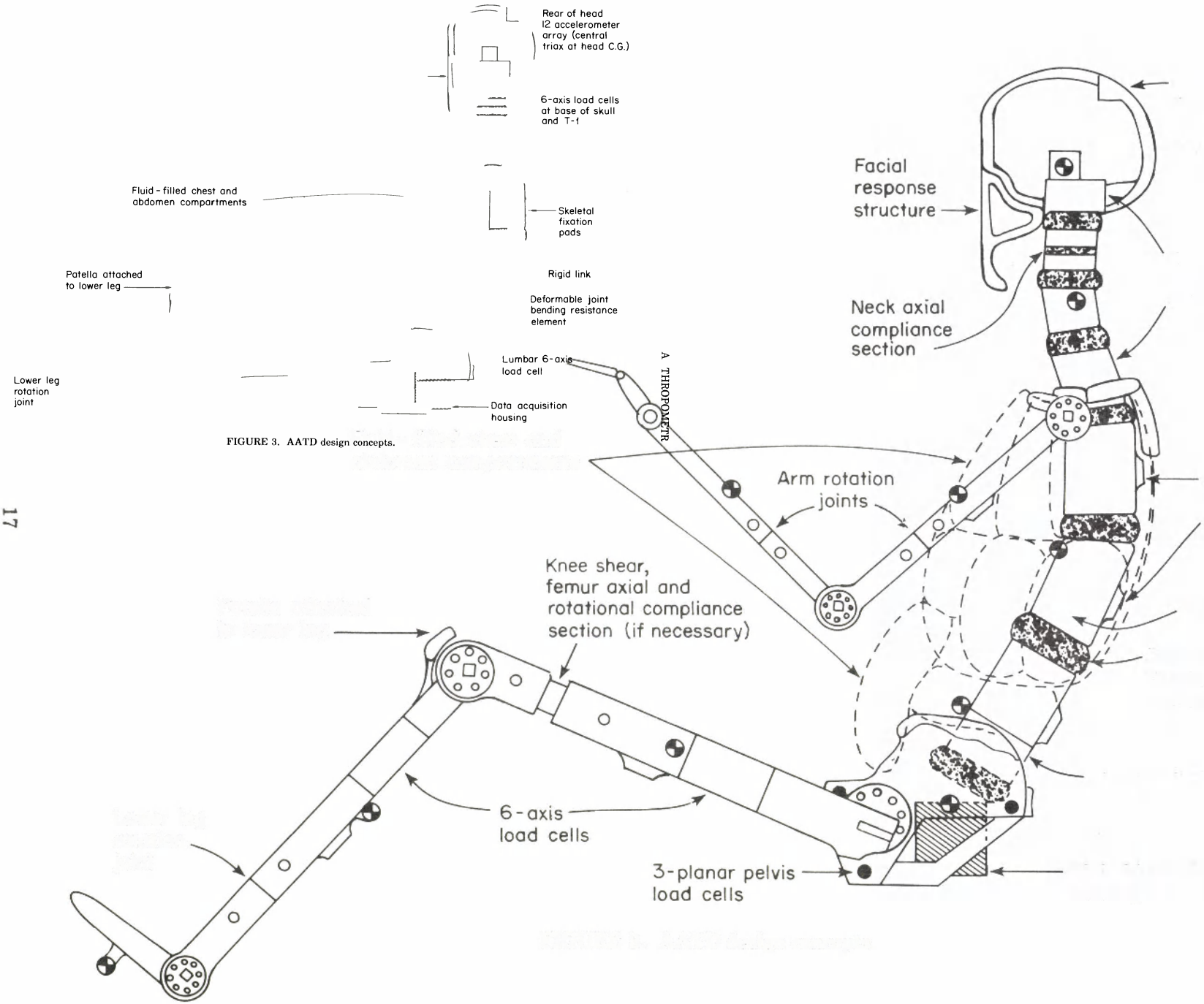

FIGURE 3. AATD design concepts.

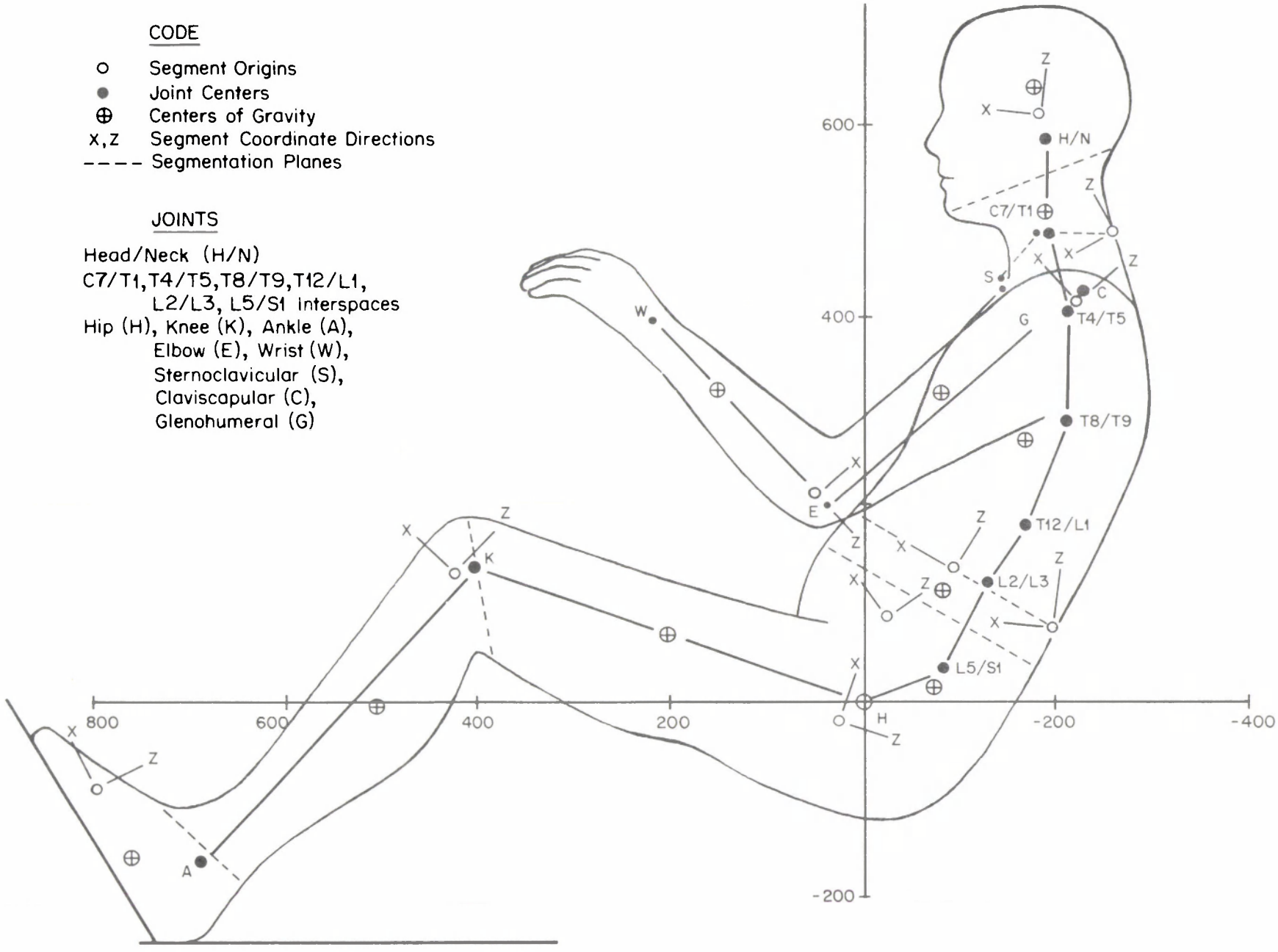

FIGURE 4. Anthropometric specifications for mid-sized male dummy.

TABLE 3

BODY SEGMENT VOLUME AND MASS

Segment	Volume* (cm^3)	Specific Gravity	Mass (kg)
Head	4137	1.097**	4.54
Neck	965	1.097**	1.06
Thorax	23763	0.920†	21.86
Abdomen	2365	1.010†	2.39
Pelvis	11414	1.010†	11.53
Upper Arms (both)	3538	1.058‡	3.74
Lower Arms & Hands (both)	4044	1.099‡	4.44
Upper Legs (both)	17228	1.045‡	18.00
Lower Legs (both)	7174	1.085‡	7.78
Feet (both)	1962	1.085‡	2.13
Whole Body	76562		77.47

* Robbins (1983).
** Mean of Walker et al. (1973), Dempster (1955), and Clauser et al. (1969).
† Dempster (1955), eight subjects.
‡ Clauser et al. (1969), thirteen subjects.

TABLE 4

AATD SEGMENT INERTIAL PROPERTIES

Segment	I_{xx} ($kg \cdot m^2$)	I_{yy} ($kg \cdot m^2$)	I_{zz} ($kg \cdot m^2$)
Head	21.97×10^{-3}	24.30×10^{-3}	15.86×10^{-3}
Neck	1.62×10^{-3}	2.03×10^{-3}	2.51×10^{-3}
Thorax	420.11×10^{-3}	296.48×10^{-3}	277.46×10^{-3}
Abdomen	16.93×10^{-3}	10.76×10^{-3}	25.74×10^{-3}
Pelvis	102.59×10^{-3}	95.18×10^{-3}	119.65×10^{-3}
Upper Arm	11.90×10^{-3}	12.96×10^{-3}	2.45×10^{-3}
Lower Arm with Hand	34.15×10^{-3}	33.99×10^{-3}	2.21×10^{-3}
Upper Leg	128.63×10^{-3}	136.01×10^{-3}	38.36×10^{-3}
Lower Leg	0.95×10^{-3}	4.66×10^{-3}	4.79×10^{-3}

HEAD

The general geometric specifications for the AATD head include the following dimensions:

Head breadth	15.9 cm
Head length	19.7 cm
Head height	23.1 cm
Head circumference	57.1 cm

The coordinates and orientation of the head anatomical coordinate system, the coordinates of the head center of gravity, and the head/neck joint center location (all depicted in Figure 4), as well as the orientation of the principal axes of inertia with respect to the anatomical axes are given in Robbins (1983). The mass and mass moments of inertia for the head are given in Tables 3 and 4.

Information about the biomechanical response of the head is related to three types of loading conditions. These are direct rigid impacts, padded direct impacts, and indirect impact loads due to head motion. Rigid impact response emphasizes the structural, mass, and contact features of the head. Padded impact response emphasizes the local geometry and mass of the head and, to a lesser extent, the structural response of the head. Indirect impact kinematic response emphasizes the mass and overall geometry (mass moments of inertia) of the head, which are given above.

The direct rigid impact represents the most severe test of the ability of a dummy head to respond realistically, because it requires consideration of the combination of head mass, skull structure, scalp characteristics, and local head geometry. The flat rigid impact is also considered to be the most reproducible test condition, because the response depends solely on the mechanical characteristics of the subject and not the striking surface. Padded impacts are less reproducible because of their dependence upon the mechanical properties of the padding, which cannot necessarily be duplicated when desired.

The primary parameter used to describe direct head impact response is impact force. This quantity is chosen because it is the one experimental measurement common to all cadaver head impact response studies, and because measurement techniques were more reliable for dynamic force than for acceleration at the time the data were collected (early 1970s). For dummy testing, however, impact force is not usually measured directly. Rather, it is usually only indicated from measurements of head acceleration at the center of gravity. Thus, the relationship between head CG acceleration responses and impact loading are important for interpreting test results using the AATD head.

In the following sections, specifications are given for response of the AATD head under direct-impact conditions, and acceleration responses under low and high impact velocities are discussed. Finally, the special problem of facial deformation, which affects head acceleration response, is addressed.

Direct-Impact Force Response. Data on the nonfracture rigid impact force response of the head have been produced by two groups. Wayne State University has conducted a free-fall head impact study using seven embalmed cadavers that were tested intact and then tested decapitated (Hodgson and Thomas 1975). The study also included seven tests with unembalmed cadavers where a 4.54-kg (10-lb) impact mass was dropped onto the frontal region of the cadaver heads. Impact force and head accelerations were measured in all tests. The transducer data were filtered at approximately SAE channel class 1000 since they were recorded with a Visicorder 1650 galvanometer. The other source of rigid, nonfracture head impacts is a series of tests conducted by Stalnaker and described by Prasad et al. (1985, pp. 12-14). Here, six unembalmed cadavers were tested without apparent fracture at much higher impact velocities than in the WSU studies.

The WSU data have been analyzed by the SAE-HBSS activity (SAE J1460 1985; Prasad et al. 1985, pp. 9-12), and summary plots of both peak force and peak acceleration versus drop height have been developed. As explained in the HBSS analysis, an adjustment in the actual impact velocities had to be made for the WSU tests. Recently, Mertz (1985) has published a new calibration curve for the WSU intact-cadaver/pallet-drop-test method. This curve has been used to adjust the original WSU velocity values. The new adjusted values are included in Table 5 along with the associated peak force values for intact cadaver head impacts on both rigid surfaces and on 90-durometer rubber surfaces. The 90-durometer rubber-surface impacts were included in the table because they generally gave peak-force values that were similar to the rigid impact-surface values at the same impact velocity. In some cases, the rubber-surface peak-force values can aid in adjusting an outlier value (cadaver 3083, rigid impact to the top of the head) or can be used in place of a low velocity rigid impact (cadaver 3116, rigid impact to the front of the head). For the purposes of this analysis, if the 90-durometer peak-force value was greater than the corresponding rigid-surface value at the same velocity, or if the rigid test was conducted at a velocity lower than its companion tests, then the rubber-surface value was used. The case of cadaver 3083 appears to be an outlier, and the rubber-surface force value was used.

The data in Table 5 indicate that for a given impact site (frontal, side, top, or rear) the variations between cadavers are large. However, for any one cadaver the results for different impact sites are remarkably similar (within 20% of the mean value).

The decapitated head mass values are given for each cadaver in Table 6 along with scaled force values obtained from the force values taken from Table 5. The force values were scaled by the factor $(m_s/m_i)^{2/3}$, where m_s is the head mass of the standard subject (4.54 kg) and m_i is the cadaver head mass. The result of this scaling is a mean peak force response of 5.16 kN $\pm$1.15 S.D. for all tests. Cadavers 2864 and 3184 both have mean peak force values that are greater than one standard deviation from the mean, one being high and one being low. Exclusion of the data from these two subjects significantly reduces the standard deviation of the data but does not significantly change the overall mean value. Similarly, for each impact site, the mean values are only slightly changed (less than 8%) by exclusion of the data from those two subjects. The mean data for each impact location varies less than 10% from the overall mean value of 5.16 kN. The associated mean time durations (measured at the base of the force-time curve) for the impacts to each region are frontal 5.4 ms, side 5.6 ms, rear 6.6 ms, and top 7.9 ms. The variations between front, side, and rear time durations are probably due to skull/impact-surface interaction differences which produce differences in waveform shape, while the much longer top impact duration is likely due to the increased effective mass of the head interaction with the torso through the neck.

TABLE 5

INTACT CADAVER PEAK NONFRACTURE HEAD
IMPACT FORCES (UNSCALED)
(Hodgson and Thomas 1975)

Cadaver No.	Impact Surface	Front Force		Side Force		Top Force		Rear Force	
		Force (kN)	Vel. (m/s)	Force (kN)	Vel. (m/s)	Force (kN)	Vel. (m/s)	Force (kN)	Vel. (m/s)
2864	Rigid	3.78	1.92	6.67	1.92	5.78	1.92	6.67	1.92
	90 Durometer	4.67	1.92	4.23	1.92	4.45	1.92	4.89	1.92
2953	Rigid	4.89	1.74	4.00	1.44	3.34	1.74	5.34	1.74
	90 Durometer	4.45	1.74	4.89	1.21	3.56	1.74	4.89	1.74
3030	Rigid	5.56	1.92	4.89	1.92	4.89	1.92	4.67	1.92
	90 Durometer	5.34	1.92	3.78	1.92	4.23	1.92	4.45	1.92
3042	Rigid	4.45	1.92	4.89	1.92	4.45	1.92	4.45	1.92
	90 Durometer	4.67	1.92	4.23	1.92	4.45	1.92	4.23	1.92
3083	Rigid	4.89	1.92	4.23	1.92	8.23	1.92	4.23	1.92
	90 Durometer	4.89	1.92	3.56	1.92	4.00	1.92	4.23	1.92
3116	Rigid	3.34	1.26	3.78	1.59	3.34	1.74	4.23	1.92
	90 Durometer	4.00	1.92	3.78	1.59	3.11	1.74	4.00	1.92
3184	Rigid	2.89	1.74	2.89	1.74	2.45	1.74	3.34	1.74
	90 Durometer	2.67	1.44	3.34	1.74	2.67	1.74	3.56	1.74

TABLE 6

SCALED PEAK NONFRACTURE HEAD IMPACT FORCE

Cadaver No.	Head Mass (kg)	Front (kN)	Side (kN)	Top (kN)	Rear (kN)	Row Mean
2864	3.77	5.29*	7.75	6.54	7.55	6.78
2953	3.77	5.64	5.54*	4.03*	6.05	5.29
3030	3.86	6.19	5.45	5.45	5.20	5.57
3042	3.55	5.51*	5.77	5.25	5.25	5.45
3083	3.41	5.92	5.12	4.84*	5.12	5.25
3116	3.64	4.64*	4.39	3.87	4.91	4.45
3184	3.86	3.22	3.22	2.97*	3.97*	3.45
Column Mean	3.69	5.19	5.32	4.71	5.44	5.18
Column Mean without cadavers 2864 and 3184	3.6	5.56	5.25	4.69	5.31	5.20

*90-durometer surface values.

The use of a moving mass impactor for conducting certification tests of head impact response is being advocated for the AATD. The impactor velocity for such a test must be higher than the equivalent head-drop test velocity in order to obtain the same stored energy in the head. In terms of the impactor mass, m_I, the head mass, m_H, and the equivalent drop test velocity, V_D, the initial velocity of the impact mass, V_{IO}, is given by

$$V_{IO} = \sqrt{\frac{m_I + m_H}{m_I}}\, V_D \tag{1}$$

The momentum change of the head at maximum head deflection (where the impact mass and the head mass have the same velocity V_C) is given by

$$m_H(V_{HO}-V_C) = m_I(V_{IO}-V_C) \tag{2}$$

where V_{HO} equals the initial velocity of the head. For a moving mass impactor test $V_{HO}=0$, while for a head-drop test $V_{IO}=V_C=0$ and $V_{HO}=V_D$. Conservation of linear momentum yields

$$m_I V_{IO} = (m_I+m_H)V_C \tag{3}$$

and the combination of (3) and (1) yields

$$V_C = \sqrt{\frac{m_I}{m_I+m_H}}\, V_D \tag{4}$$

The momentum change in a moving mass impactor test, where the initial impactor velocity is given by Equation (1), will be less by a factor $\sqrt{m_I/(m_I+m_H)}$ than that of the equivalent (in terms of energy stored) drop test.

Since the intent of such adjustments is to obtain a similar response of the head in terms of peak force (assuming little or no rate-of-loading effects), the reduced momentum change of the impactor test will result in a correspondingly reduced time duration for the force-time waveform if it has a similar shape. For a 23.4-kg (51.5-lb) impactor mass and the 4.55-kg (10-lb) AATD head, the resulting reduction factor would be 91.5%. Thus the corresponding time durations associated with a 5162-N (1160-lb) peak force would be

Frontal	4.9 ms
Side	5.1 ms
Rear	6.0 ms

The mean for the three regions would be 5.5 ms.

The WSU unembalmed cadaver, 4.55-kg (10-lb) drop-weight impacts to the frontal region produced the results shown in Table 7. The effect of the relatively low-mass impactor (approximately equal to a typical head mass) on pulse duration is demonstrated in Test 3305. Here the drop-weight velocity of 2.72 m/s (8.9 ft/s) is equivalent to a head-drop velocity of 1.83 m/s (6.3 ft/s), which is near the velocity at which many of the embalmed head-drop tests were conducted. The peak force in that test was much higher than in the comparable embalmed tests, most likely because of differences in the mechanical properties of the scalps, which would tend to shorten the pulse duration for the unembalmed head. The force-level differences alone, however, cannot account for the 1.9-ms duration for that test. Adjustment for the higher force level, the slightly different velocity, and the impactor mass predicts that a frontal impact producing a waveform with 4890-N peak force and 5-ms duration in an embalmed cadaver (No. 3083) would become a 2.1-ms duration impact with the drop weight impactor.

TABLE 7

SCALED WSU/VRI UNEMBALMED CADAVER
4.55 kg DROP WEIGHT IMPACT TESTS

Test No.	Impact Site	Head Mass* (kg)	Impactor Velocity (m/s)	Eqv Drop Velocity (m/s)	Peak Force (kN)	Scaled Pk Force (kN)	Time Duration (ms)	Scaled Time Duration
3305	Front	5.5	2.72	1.83	7.8	6.9	1.9	1.8
3308	Front	3.2	2.23	1.71	5.6	7.0	2.0	2.2
3310	Front	3.3	2.23	1.70	4.9	6.1	2.0	2.2
3316	Front	4.8	2.23	1.56	5.8	5.6	2.3	2.3
3324	Front	3.0	2.23	1.73	5.8	7.6	1.8	2.1
3327	Front	4.0	2.23	1.63	6.5	7.0	1.1	1.2
3328	Front	4.4	2.23	1.59	4.7	4.8	2.5	2.5

*Estimated from impulse and momentum exchange.

Table 7 also lists the scaled peak force values based on the estimated head masses. The latter were obtained by comparison of the impactor force and head acceleration waveforms where possible and by head dimensions in those cases where the acceleration data were deficient. The mean scaled peak force for the seven tests is 6418 N (1443 lb) with a standard deviation of ±996 N (224 lb). This is some 24% higher than the embalmed cadaver values. The living human values are most likely somewhere between those of the embalmed cadaver with its toughened tissues and the unembalmed, unperfused cadaver with its flaccid tissues. The mean scaled-time duration for the tests is 2.1 ms.

Combining the results of the embalmed and unembalmed frontal-bone impact tests yields a mean combined peak force of 5800 N (1304 lb) and a mean time duration of 3.9 ms for a 23.4-kg (51.5-lb) moving-mass-impactor test at 2.0 m/s (6.6 ft/s). Since the embalmed data show little difference in peak forces as a function of the region of impact, the peak force value of 5800 N (1304 lb) should hold for the side, rear, and top as well as for the front of the head. The time durations would be proportionally reduced to 4 ms for the side and 4.8 ms for the rear.

The UMTRI unembalmed cadaver nonfracture head impacts were conducted with a 10-kg (22-lb) moving mass rigid impactor at velocities ranging from 5.7 m/s to 7.4 m/s (18.7 to 24.3 ft/s). Table 8 shows the scaled peak-force and time-duration values for the six tests. The mean scaled peak-force value for the five tests with the lowest impact velocities is 15 kN (3370 lb). The mean scaled time durations for the four tests with consistent values is 4.2 ms. (The two tests with much longer durations may have actually produced minimal fractures to have such a result.) The equivalent test velocity for a 23.4-kg (51.5-lb) impactor would be 5.5 m/s (18 ft/s). The associated time duration would be 4.6 ms.

TABLE 8

SCALED UMTRI UNEMBALMED CADAVER HEAD IMPACT TEST RESULTS

Test No.	Impact Site	Head Mass (kg)	Eqv Drop Velocity (m/s)	Peak Force (kN)	Scaled Pk Force (kN)	Time Duration (ms)	Scaled Time Duration (ms)
C-2	Side	4.41	4.7	13.8	14.1	4.8	4.85
C-3	Side	4.68	4.9	17.8	17.5	3.8	3.76
C-4	Side	5.05	6.0	18.0	16.8	4.2	4.06
C-5	Side	4.05	4.9	13.4	14.4	6.0	6.24
C-6	Front	4.68	5.0	14.2	14.0	6.4	6.34
76A144	Front	4.27*	5.5	14.6	15.2	3.8	3.88

*Estimated.

In summary, the AATD head response to impacts with a rigid 23.4-kg (51.5-lb) moving-mass impactor can be defined at two impact velocities, 2.0 m/s (6.6 ft/s) and 5.5 m/s (18 ft/s). As shown in Figure 5, the low velocity specification would have a mean peak-force response of 5800±580 N (1300±130 lb) and a mean duration of 4.2±0.6 ms. The high velocity specification would have a mean peak force of 15.0±1.5 kN

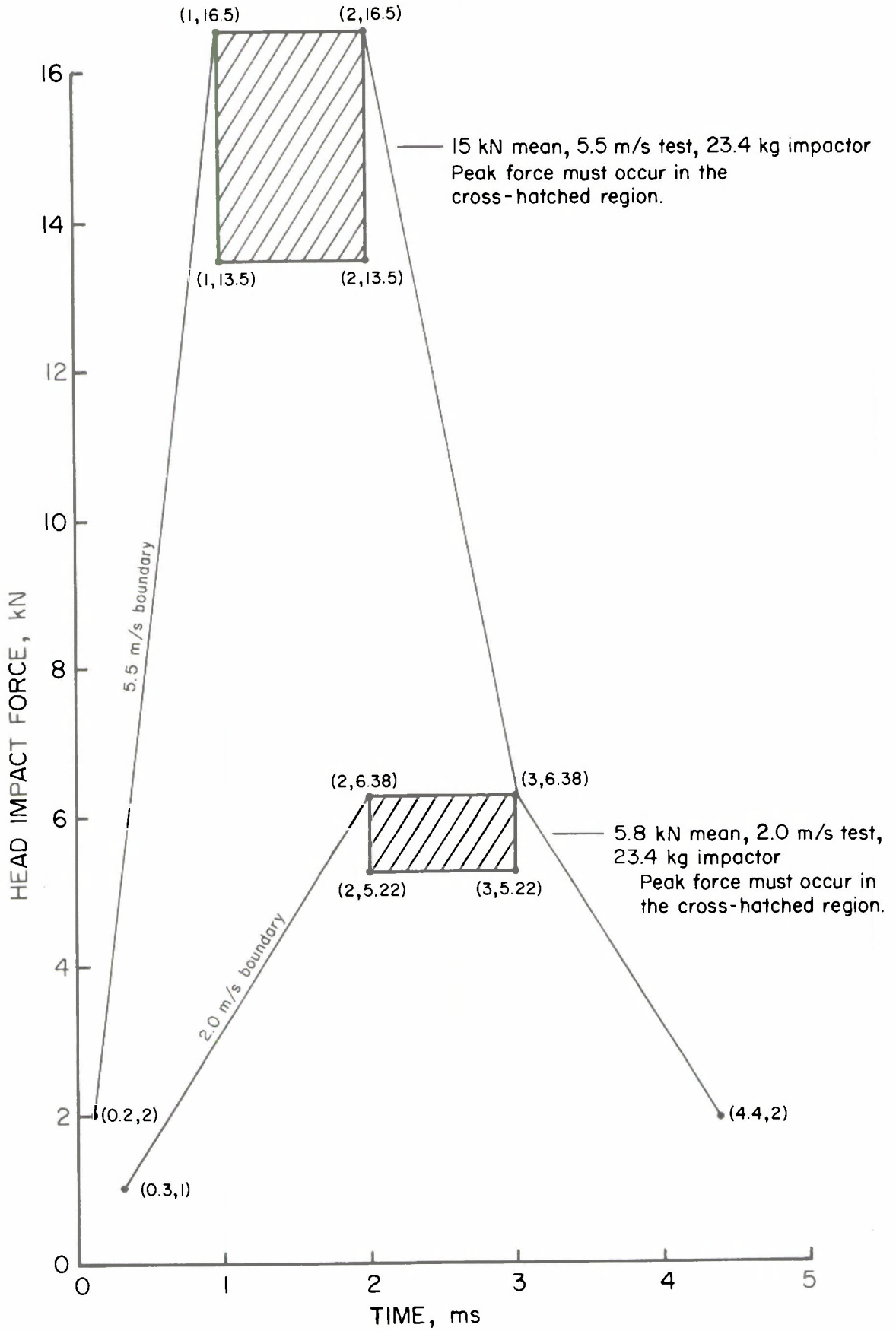

FIGURE 5. Rigid impact response specifications for the AATD head.

(3370±370 lb) and a mean duration of 4.6±0.7 ms. These values would be applicable to frontal, lateral, and rear head impacts. Top-of-the-head impacts would have the same force values, but the duration would be increased by 50%. The filtering for these specifications should be SAE channel class 1000, since they are based on data from tests that are not available for reprocessing to other specifications.

Direct-Impact Acceleration Response. The human head consists of three major structures that determine its response to a direct impact. These are the scalp, the skull, and the brain. In all cadaver testing, the accelerations of the head are measured at points on the skull. The center of mass of the head lies in the brain tissue, but the accelerations at that point have never been measured experimentally in an unembalmed cadaver. Instead, assumptions are made that the skull reacts as a rigid structure and that the brain mass is completely coupled within the skull. These assumptions allow the transformation or, in some cases, the simple substitution of acceleration data measured on the skull to the equivalent acceleration at the head center of gravity.

Under simple, well-defined, low-velocity loading conditions, such as those in the 2.0-m/s WSU tests (Hodgson and Thomas 1975), it appears to be possible to directly use the response of an accelerometer mounted in the direction of impact, but on the opposite side of the head, as an estimation of the acceleration at the center of gravity. The embalmed cadaver data give the following mean far-side peak accelerations: front 105 G, side 112 G, and rear 113 G. The average of these three responses is 110 G, which, when scaled to the AATD head mass, yields a value of 103 G. Similarly, the WSU unembalmed cadaver test data give a mean frontal-impact peak acceleration of 174 G (using only tests 3305, 3310, 3316, and 3324, the other three tests appearing to have poor accelerometer coupling). This value scales to 169 G for the AATD head mass. The mean head acceleration for the pooled data is 136 G, which corresponds closely to a rigid body acceleration of 130 G, based on an impact force of 5800 N and a head mass of 4.55 kg.

At the higher impact severity condition of 5.5 m/s, however, the structural deformations of the skull make both the simple substitution of a far-side acceleration or the more complex transformation of point-wise acceleration measurements questionable. The one UMTRI test in which reliable skull acceleration measurements were made (76A144) used an array of three triaxial accelerometers each mounted separately to the skull. The 14.6-kN peak force achieved in the test was close to the 15.0-kN level of the AATD specification, but the transformed head center-of-gravity acceleration peak was 515 G, which is much greater than the equivalent 336-G rigid-body acceleration for a 15-kN force and a 4.55-kg head mass. Clearly, the biomechanical response of the human head at high impact velocities and loads near the fracture level cannot be assumed to be a rigid-body response.

Although acceleration specifications cannot be made at this time, the 5.5-m/s force response requirement will ensure that the AATD head will have the essential response characteristics of the human head under high severity loading. If a head design using a deformable scalp in combination with a rigid skull achieves the required responses at the 2.0-m/s and the 5.5-m/s levels, it should also result in a more accurate representation of head CG accelerations than present dummy heads. The GM-ATD-502 head (the precursor of the present GM Hybrid III head) was shown by Hubbard and McLeod (1974) to give appropriate biomechanical response (250 G) at a 2.7-m/s drop velocity, and yet, at a drop velocity of 4.2 m/s, it produced an excessive acceleration peak of nearly 500 G. This response would be equivalent to a rigid-body force of 22.3 kN, significantly greater than the AATD requirement at an even higher impact velocity. Thus, the high velocity response requirement of the AATD will ensure a head design that has sufficiently accurate response over the range of biomechanically significant impacts.

Facial Impact Response. The influence of the deformation characteristics of the face upon the resulting head accelerations during facial impacts has been shown by Tarriére et al. (1981). Unfortunately, the test data available to characterize facial impact response is very limited. Essentially three of the four tests reported in that work are suitable for defining the force–time response of the face impacting a fiat rigid surface. The data also list the force at fracture, the head acceleration at fracture, and the average deformation of the face during contact.

The data traces from test numbers 91, 92, and 105 were used to prepare an envelope of force–time response shown in Figure 6. Also shown are the mean fracture–force level 7.5 kN (1686 lb) and mean peak–force level 10.5 kN (2360 lb). The bimodal example curve (shown as a dashed line) is typical of the actual data and results from the fracture and collapse of the facial skeleton. The head deceleration peaks associated with the force–time response of Figure 6 are 168 G for the first peak and 235 G for the second peak.

The average crushing of the facial skeleton was 0.73 cm (0.29 in) at a drop height of 2.5 m (8.2 ft). The corresponding moving mass impactor velocity for such a head impact would be 7.65 m/s (25 ft/s). The traditional 15.2–cm (6–in) diameter rigid impactor could be used instead of the load plate used by Tarriére et al., since the facial area is about 40% of that of the 15.2–cm–diameter impactor.

The main purpose of simulating the facial structural response is to produce more realistic head accelerations during facial impacts. For this purpose, it may be possible to produce a force–time response that lies within the corridors of Figure 6 using a soft deformable material that can recover after impact. For the purpose of indicating facial injury, however, a frangible or crushable material that deforms permanently could be used.

Head Design Concepts (Refer to Figure 3, p. 15). The head will be designed to have biofidelity of response for front, side, top, and possibly rear rigid impacts as well as facial impact response biofidelity. The response specifications are given for two test velocities. The low (2.0 m/s) velocity requirements can be met with a rigid–skull/deformable–scalp design approach. The high (5.5 m/s) velocity response might also be met with a rigid–skull/deformable–scalp design, but the large skull deformations that occur in the human under such severe loading conditions may require a deformable (less stiff) skull structure in the critical front, side, and top regions.

The initial method of choice is the rigid–skull/deformable–scalp design approach. The rear and lower skull structure will be made rigid, in any event, to allow the integration of a twelve–accelerometer array, in the form of four triaxial sets, for complete head motion analysis. One of the triaxial accelerometer sets will be located at the head center–of–gravity to allow direct measurement of the translational accelerations at that point. The remaining three sets will form the conventional array for three–dimensional motion measurement of such parameters as angular acceleration and angular velocity. The use of three triaxial arrays instead of biaxial arrays will allow measurements to be made even if transducer malfunctions cause some data channels to be missing.

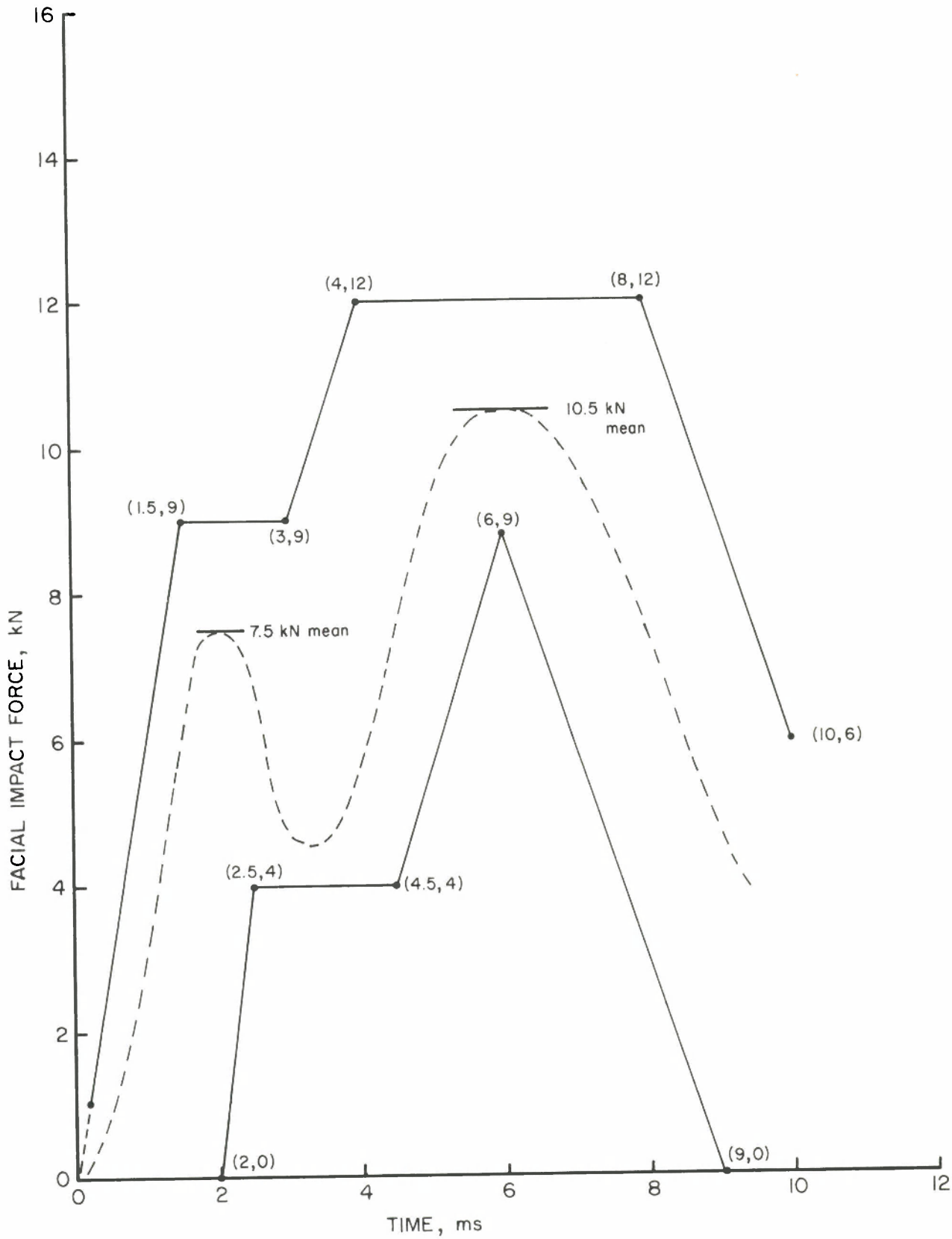

FIGURE 6. AATD facial impact response (7.65 m/s, rigid disc impactor, 15.2-cm diameter, and 23.4-kg mass).

The rigid rear/base skull structure would be separate from the front/side/top structure. It would also serve as the mounting for the neck structure and its load cell. Cast aluminum will be used for the rigid skull. If flexible regions are needed, aluminum castings may be suitable, but composite materials or other cast metals may be necessary to achieve the desired flexibility. Durability and reproducibility problems may be more significant with composite materials, however.

The scalp material will be the primary factor in controlling the head impact response, and the repeatability and reproducibility of the materials used in the scalp design will be of central concern. Present ATD scalps are thermoplastic polymeric materials that require heated molds for preparation. Thermosetting polymeric materials, which can be cast at low pressures and low temperatures, may offer a suitable alternative to the thermoplastic materials.

The face will be featureless to aid in producing repeatable impact response. The facial structure will be supported by the rigid rear/base skull structure and will be designed to meet the facial impact response specifications. The facial structure will have two design options. One design will consist of a durable polymeric material, much like the scalp material, which will allow proper facial impact response but will not indicate trauma. This durable face will be replaceable with an optional frangible or crushable structure for use when an indication of facial bone fracture is needed. The skin covering the face will be separate from the facial response structure and will be fabricated in a durable form as well as a lacerable form for facial injury assessment.

SPINE

The basic geometric specifications for the AATD spine are given by Robbins (1983) in terms of the locations of the following joint centers: head/neck, C7/T1, T4/T5, T8/T9, T12/L1, L2/L3, L5/S1. The corresponding chord lengths between these centers are as follows:

Head/Neck to C7/T1	11.9 cm
C7/T1 to T4/T5	7.7 cm
T4/T5 to T8/T9	11.0 cm
T8/T9 to T12/L1	12.8 cm
T12/L1 to L2/L3	6.1 cm
L2/L3 to L5/S1	9.3 cm

The major portion of the spine is contained within the torso of the body, and the overall mass and inertial characteristics of those torso regions incorporate the mass and inertial characteristics of the spine. The neck body segment, however, does not completely incorporate the cervical spine, and its general dimensions are listed by Robbins (1983) as follows:

Neck circumference	38.8 cm
Neck breadth	11.8 cm
Neck length	8.5 cm

The neck length is determined by the definition of the segmentation planes and is significantly shorter than the cervical spine length of 11.9 cm.

The coordinates and orientation of the neck, the thoracic and abdominal coordinate systems, the coordinates of the associated centers of gravity (all depicted in Figure 4) and the orientation of the principal axes of inertia with respect to the anatomical axes for each region are given in Robbins (1983). The mass and mass moments of inertia for the neck are given in Tables 3 and 4.

Cervical Spine Response. The work of Wismans and Spenny (1983, 1984) represents a comprehensive effort to define the response of the head/neck system in terms suitable for design specifications. This work in combination with the modeling work of Bowman et al. (1984) and the classic experimental work of Mertz et al. (1973) and Patrick and Chou (1976) provide a basis for defining the static and dynamic response of the cervical spine to moderately severe acceleration environments using human volunteer data (see Nyquist and King 1985, pp. 52-63). Such levels of crash environments are most likely the conditions under which neuromuscular control mechanisms can play a significant role in head motion control, these effects being overwhelmed by the magnitude of dynamic forces and the rapidity of their application in severe crash environments.

The basic linkage geometry for the cervical spine as proposed by Wismans and Spenny consists of a rigid link with an upper and lower pivot. The upper pivot represents the head/neck junction, and the lower pivot was found to lie near the C7/T1 joint. The length between the pivots was found to be 12.5 cm based on head-trajectory matching of some volunteer tests for both frontal and lateral flexion. This length is very close to the chord length of 11.9 cm between the head/neck and C7/T1 joints as defined for the mid-sized male by Robbins (1983). In fact, Wismans and Spenny used the trajectory of the head anatomical coordinate system origin as their initial indicator of a lower-neck rotation center and found a value of 15.0 cm for both lateral and frontal tests. The equivalent dimension for the mid-sized male is 14.7 cm, which is even closer than the

cervical spine link match. The same type of two-joint configuration was used by Bowman et al. (1984), but the neck link was extensible rather than rigid.

The Wismans and Spenny and the Bowman et al. studies have produced joint mechanical characteristics that can be used to define the resistance to rotational motion for AATD cervical spine design purposes. Wismans and Spenny have defined these responses as spring-like and for the loading phase only. They could thus be considered static moment-angle responses, since their analysis does not include a damping term. Bowman et al. did consider the entire load-unload response and included damping parameters as well as elastic resistance parameters.

The characterizations of the lower (C7/T1) pivot responses for both studies were similar. Wismans and Spenny allowed for an initial position of 20° of neck rotation before prescribing a linear response between joint moment and neck/torso angle for frontal motion. In the AATD, the upright seated position would produce approximately a zero initial angle as defined by Wismans and Spenny, and therefore the initial offset of 20° should be removed from their characterization, leaving a linear frontal flexion response with a slope of 1.25 N·m/deg. The equivalent response from the Bowman et al. analysis yielded a bending stiffness of 2.4 N·m/deg for frontal flexion, with corresponding damping values of 0.0034 N·m·s/deg for loading and unloading and an energy restitution coefficient of 0.11. These values are different than those presented in the Bowman et al. (1984) paper and represent subsequent work by Bowman to improve the model using additional test data. The only other parameter that was revised was the axial neck compression stiffness, which was changed to 400 N/cm. All other parameters given by Bowman et al. (1984) remain as stated in the paper.

The higher stiffness given by Bowman et al. for frontal flexion is understandable when the upper (head/neck) pivot characteristics are compared. The authors found a bending stiffness value of 2.5 N·m/deg with a damping coefficient of 0.026 N·m·s/deg for loading and unloading and an energy restitution coefficient of 0.5. Wismans and Spenny chose to use a locking concept in which the head is free to rotate some 25° relative to the neck without resistance and then is locked up with essentially infinite bending stiffness at that angle. This combination of a less stiff lower pivot and, eventually, a very stiff upper pivot produces an overall bending moment response relative to the total head/torso angle, which may be similar to the Bowman et al. response at the larger head/torso angles. It should be noted that none of the data used to produce these results approached the torque/angle limits associated with the Mertz and Patrick corridors and thus did not require the implementation of joint-stop characteristics.

Wismans and Spenny characterized the lateral responses of the cervical spine joints in a manner similar to those for frontal motion but with greater stiffness and less free motion. For the lower pivot they chose a bilinear moment/angle relation with an initial stiffness of 0.67 N·m/deg up to the point (10 N·m, 15 deg), followed by a stiffness of 2.6 N·m/deg. The upper pivot allowed 10° of free motion (head relative to neck) before locking up with an infinite stiffness. Two other features were presented by the authors. One was that the lower pivot should be located 20 mm off the midsagittal plane away from the motion of the head. The other was the inclusion of torsional motion of the head about the longitudinal axis of the spine. This torsional motion was of the same magnitude as the corresponding head lateral flexion motion. The resistance to the torsional motion was found to be about 0.4 N·m/deg. Bowman et al. found a similar value of rotational stiffness of 0.339 N·m/deg with an associated damping coefficient of 0.0054 N·m·s/deg for both loading and unloading and an energy restitution coefficient of 0.2.

The lower pivot parameters found by the Bowman et al. analysis were a lateral bending stiffness of 2.71 N·m/deg with zero damping coefficients for loading and unloading and an energy restitution coefficient of 0.4. The upper pivot characteristics were a lateral bending stiffness of 3.74 N·m/deg with zero damping coefficients and an energy restitution coefficient of 0.7.

Bowman et al. also estimated parameters for axial loading due to head inertia and for bending in extension. For neck axial loading, the elongation stiffness was 1644 N/cm and the compression stiffness was 400 N/cm. The damping coefficients for both loading and unloading were 15 N·s/cm and the energy restitution coefficients were 0.99 for both elongation and compression. The extension bending stiffness for the lower pivot was 0.84 N·m/deg with zero damping coefficients and an energy restitution coefficient of 0.10. The upper pivot extension bending stiffness was 0.714 N·m/deg with a zero damping coefficient in loading and a 0.026 N·m·s/deg coefficient in unloading. The energy restitution coefficient was 0.95.

The parameters given above have been shown by both studies to simulate the actual human volunteer test data. Spenny has subsequently shown that the dynamic torque data at the head/neck joint, when plotted versus the angle between the head and the torso, fall within the Mertz and Patrick corridor for frontal flexion and the Patrick and Chou corridor for lateral flexion. The joint parameters and linkage specifications in combination with the overall dynamic response requirements for the torso/cervical-spine/head system, shown in Figures 7, 8, and 9, provide the necessary description of the response specifications for the performance of the AATD cervical spine.

In the case of the individual joint characteristics, there are two possibilities for defining the joint stiffnesses. The Wismans and Spenny concept of free motion of the upper spinal joint, even if it is limited to a few degrees, is questionable for the design of an ATD spine, because of the potential for artifactual responses under higher severity impacts and an attendant lack of control over the position of the head during testing. Thus, the joint characteristics determined by Bowman et al. appear to be more suitable for defining the AATD cervical-spine joint responses. These characteristics are related to medium severity exposures, and their linear nature must be modified by joint-stop provisions to ensure meeting the response corridors at higher severities. The ranges of motion needed to meet the requirements are

Frontal flexion	75°
Extension	90°
Lateral flexion	50°
Rotation	65°

The test procedures needed to evaluate the dynamic performance of the AATD cervical-spine design concepts may involve mini-sled head/neck tests as described by Wismans and Spenny (1984) for initial screening. The more complete development, however, will require the use of whole-body systems tests simulating the human volunteer test conditions, in order to account for influences from the thoracic spine design in the AATD.

The response of the head/spine system to impacts to the top of the head has been studied by Alem et al. (1984). Five male cadavers were impacted on the top of the head by a 10-kg (22-lb) impactor, with a 15.2-cm (6-in) diameter face covered with 5.1 cm (2 in) of Ensolite® AL energy-absorbing foam. An impactor velocity of 8 m/s (26.2 ft/s) was used in all five tests. The combination of impactor velocity and padding was chosen to avoid injuries and provide response information only. The acceleration of the head was

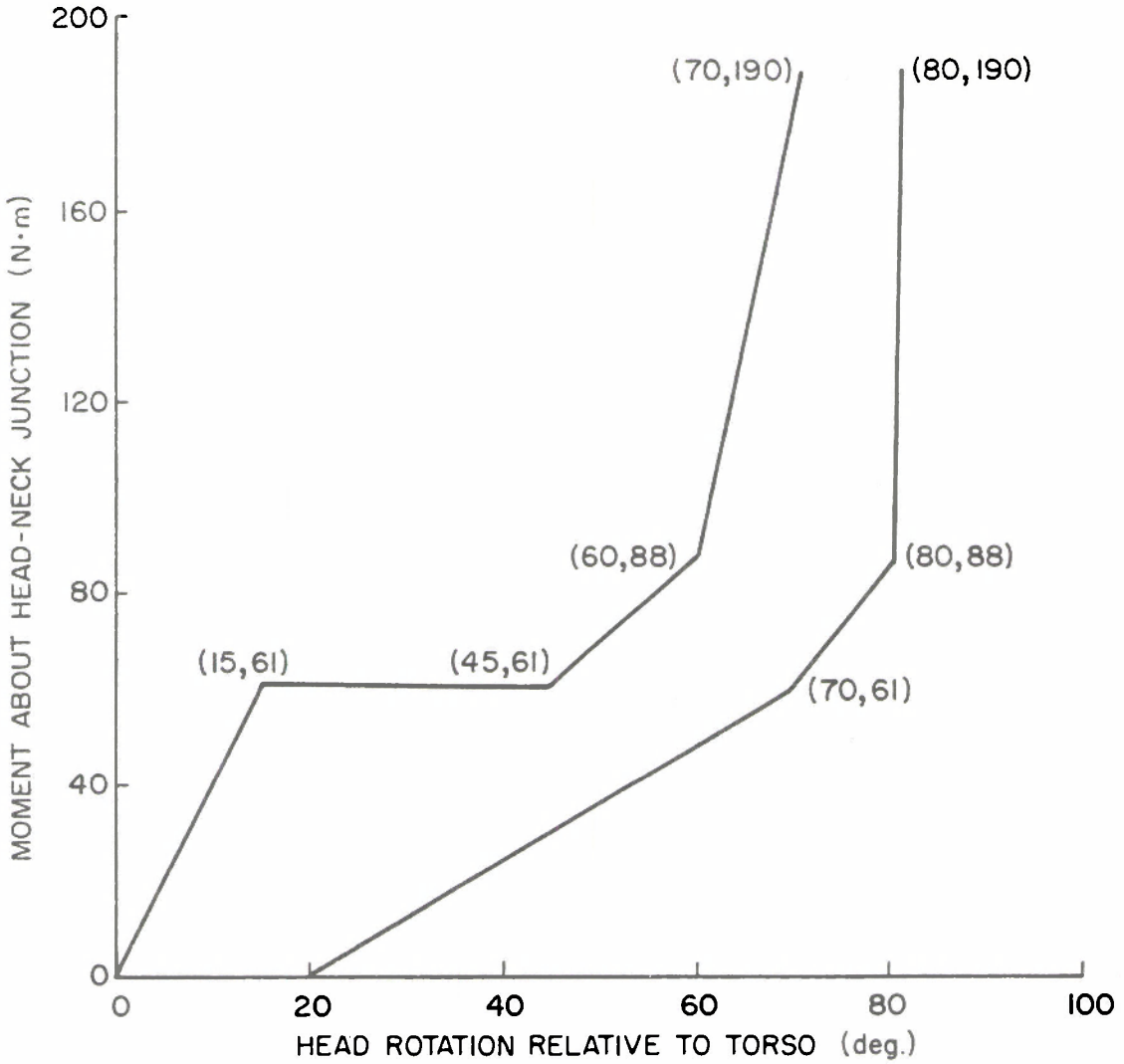

FIGURE 7. Loading corridor for neck flexion (forward bending) based on Mertz et al. (1973).

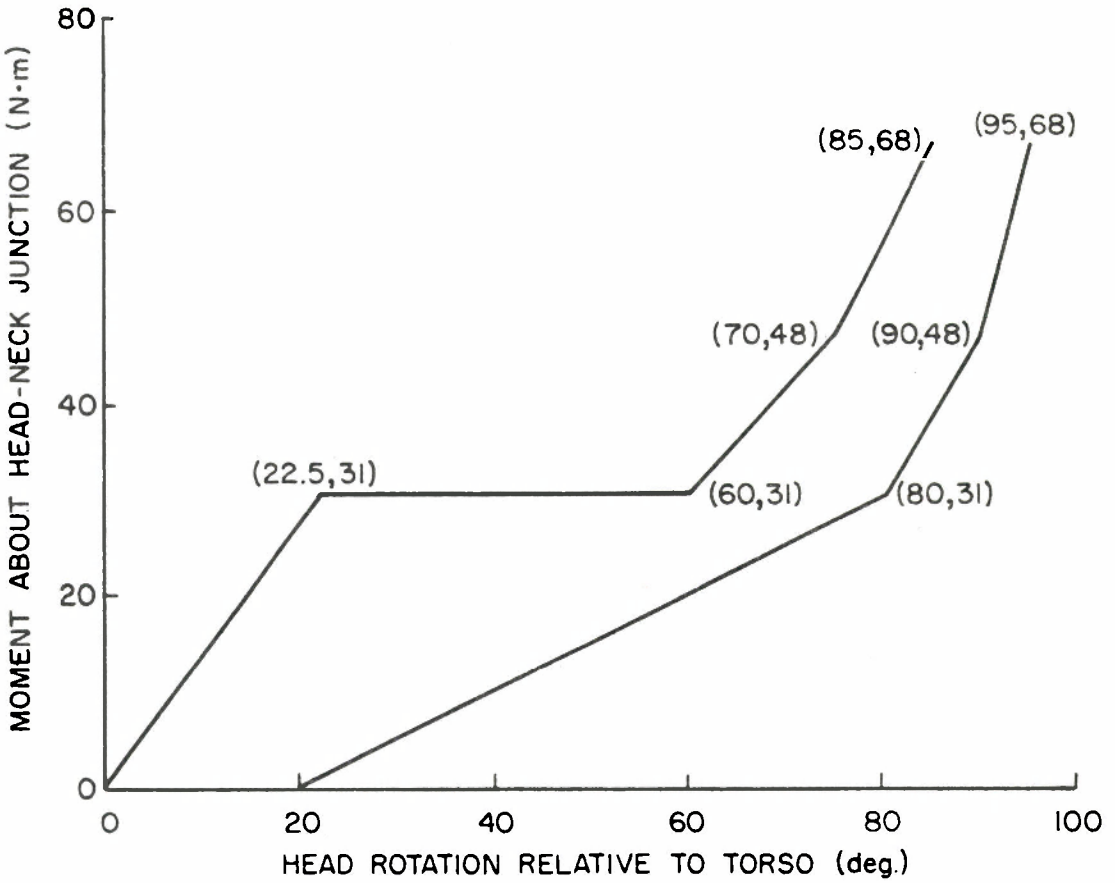

FIGURE 8. Loading corridor for neck extension (rearward bending) based on Mertz et al. (1973).

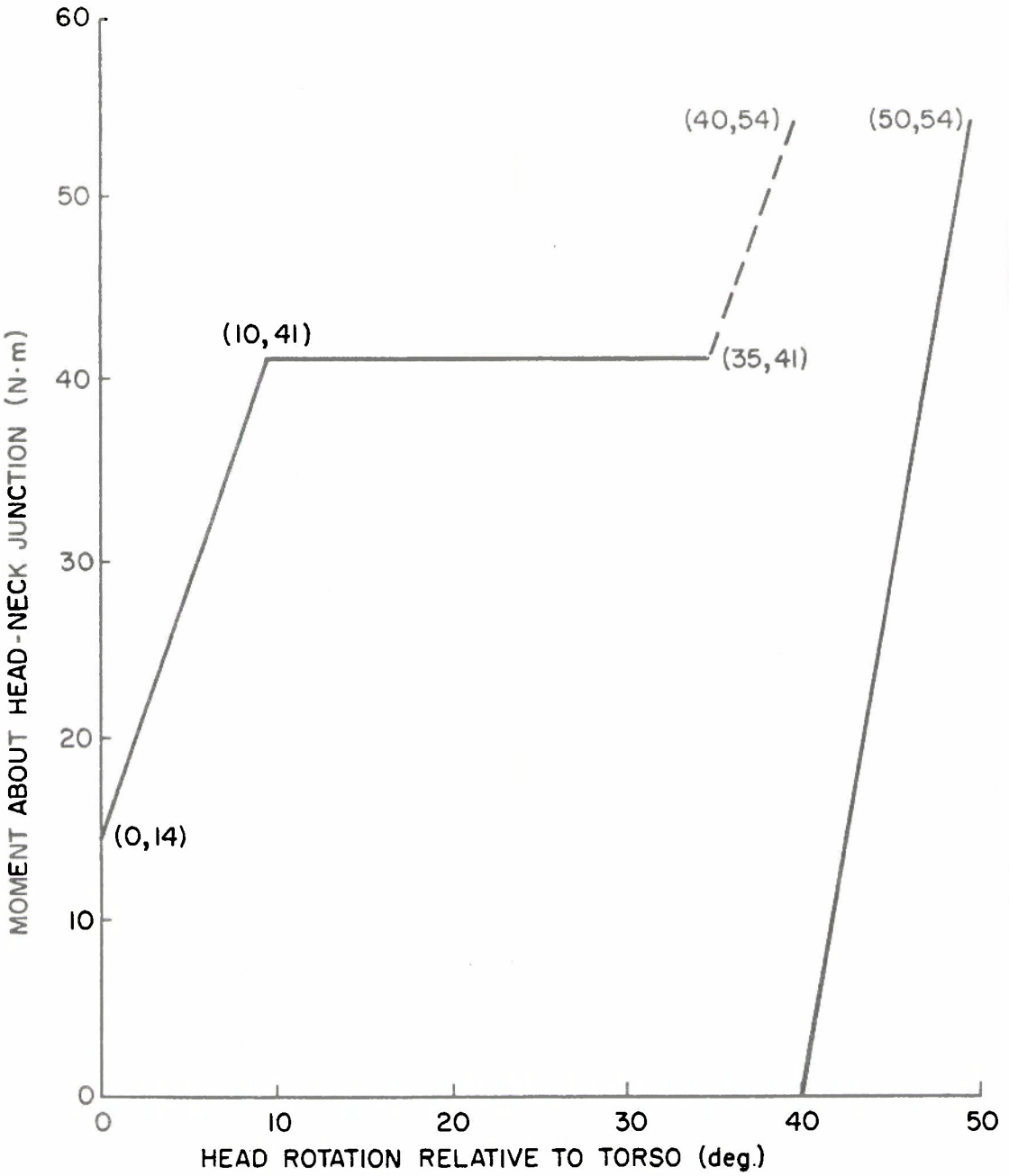

FIGURE 9. Lateral flexion response envelope established by Patrick and Chou (1976).

measured with a nine-accelerometer plate, and triaxial accelerometer clusters were mounted on the T1 and T12 vertebrae. The mean impactor force-time history with a ± 1 standard deviation band is shown in Figure 10. The corresponding T1 Z-direction mean acceleration-time history with a one-standard-deviation band is shown in Figure 11. The same filter was used to process impact force, head, and spinal acceleration signals. This was a digital Butterworth filter with corner at 150 Hz, and a roll-off slope of 24db/octave. This filter was chosen after careful examination of the spinal acceleration signals resulting from head crown impacts, and was applied to all signals because impedance curves were being generated, requiring uniform filtering process. The time shift between the force peak and the spinal acceleration peak is 5.1 ms. When tested under the same conditions, the AATD should produce a force-time history that falls within the data band of Figure 10 and exhibit an acceleration-time history at the T1 level that falls within the data band of Figure 11.

Thoracolumbar Spine Response. Data for defining the static and dynamic response of the thoracolumbar spine are available from the studies conducted at Wayne State University and summarized in Nyquist and King (1985, pp. 63-75). The studies defined a moment of applied torso force about the pelvic left-right axis (H-point axis, defined by the two hip-joint centers), which was plotted as a function of the thorax-to-pelvis angle.

One study, referred to as the GM study (Nyquist and Murton 1975), used a thoracic target at the T8 level to define spinal motion relative to the pelvis. The initial value of such an angle (T8 relative to pelvis) for the seated anthropometry of the AATD (Schneider et al. 1983, Drawing No. MM-104) is 148°. The GM study produced corridors defining static bending response of the thoracolumbar spine for the loading conditions of the experiment. Neither this study nor the other WSU study (referred to as the NHTSA study) actually produced static deformations of the thoracic spine. It would appear that only the spine below T12 was involved in the tests as conducted.

The response corridors developed from the GM study have been adjusted to account for the seated AATD anthropometry and to provide for a continuous envelope of response through the initial conditions of the seated AATD. The resulting corridors for static flexion and extension bending response are shown in Figure 12. The range-of-motion limits were left unchanged, but some of the corridor boundaries were shifted to accommodate the continuous response through the initial position of 148°. The original boundaries are shown as dotted lines in the figure. The static flexion and extension response of the AATD must lie within these corridors and exhibit the joint motion limits of 77° flexion and 209° extension. A linear bending response obtained by connecting the initial condition point (148,0) with the limit endpoints of (77,418) for flexion and (209, −158) for extension yields bending stiffnesses of 8.9 and 2.6 N·m/deg, respectively. These requirements can also be met with nonlinear moment/angle responses.

The dynamic thoracolumbar spine response tests of the NHTSA study (King and Cheng 1984; Mallikarjunarao et al. 1977; Mital et al. 1978a, 1978b; Cheng et al. 1979) provide some information on the relative flexibilities of both the thoracic and lumbar spines. The total angular motions were similar under the test conditions used, but, because of the fewer number of spinal elements in the lumbar spine, the individual mobilities of the lumbar spinal elements were found to be greater than those of the thoracic spinal elements by 66% for the tensed males. Thus, the overall static bending stiffness of the thoracic spine can be estimated to be similar to that of the lumbar spine, due to its greater length, even though the individual elements may be somewhat stiffer.

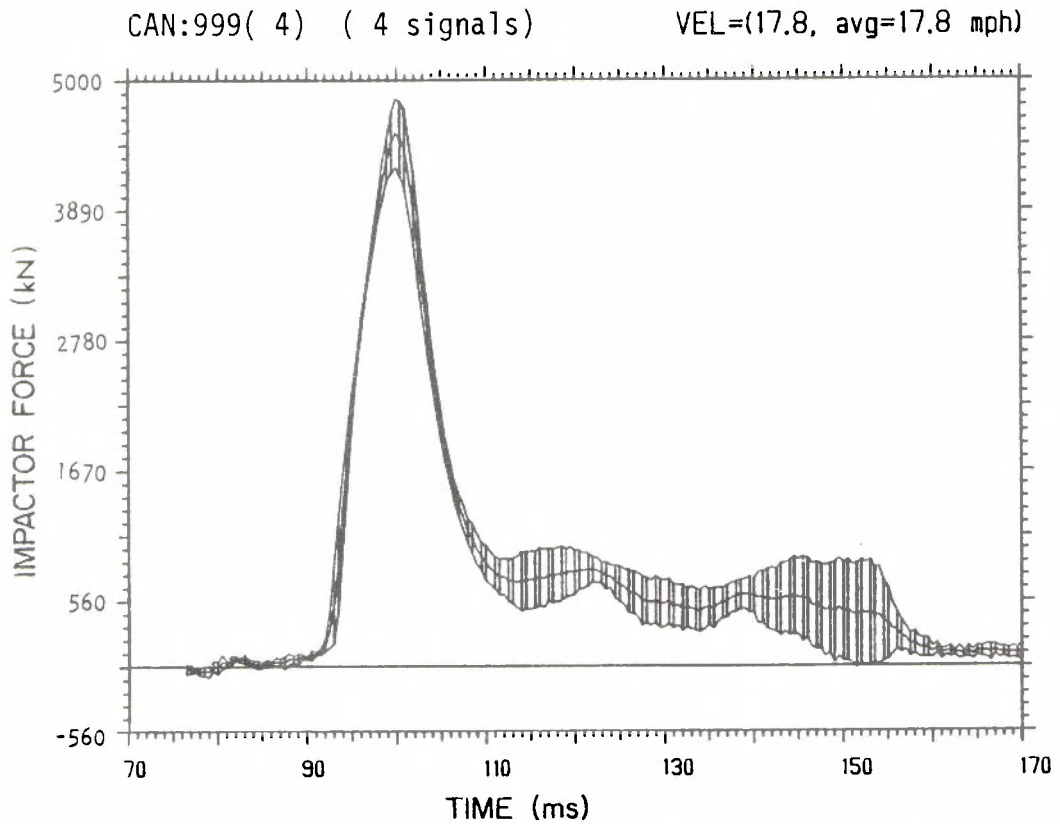

FIGURE 10. Impactor force-time histories for 8 m/s top-of-head impacts.

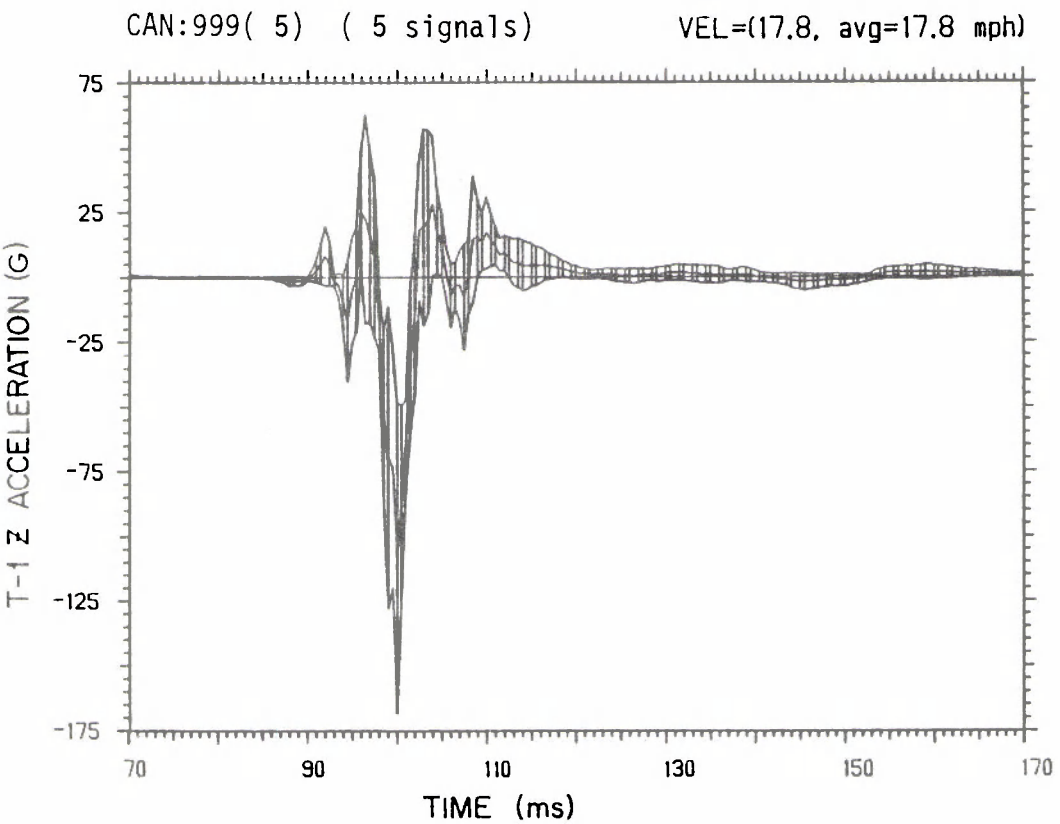

FIGURE 11. T-1 Z-direction acceleration-time response for 8 m/s top-of-head impacts.

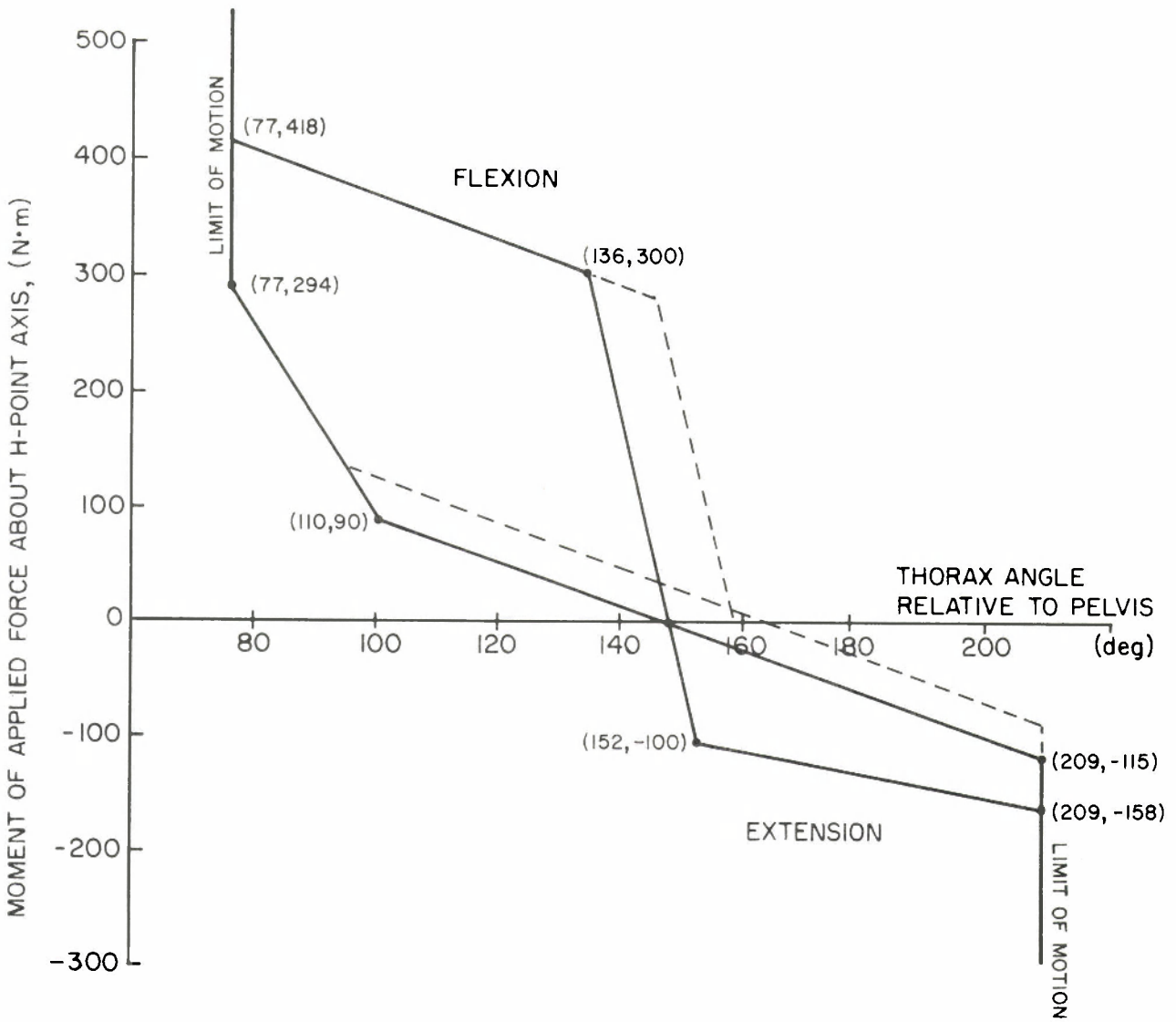

FIGURE 12. Static bending response corridors for the AATD thoracolumbar spine.

Spinal Design Concepts (Refer to Figure 3, p.15). The spine will be designed as a total system from the base of the head to the top of the pelvis. Spinal flexibility will be achieved through the use of discrete joint structures located at appropriate intervals along the spine. The spinal structure will consist of a series of rigid links connecting the joint structures, and the joints will have omnidirectional motion capability.

In the cervical spine region, three joints will be needed to achieve the range-of-motion requirements (75° flexion, 90° extension), even though theoretically two joints would suffice. This is due to the fact that omnidirectional joints with integral joint resistance provisions are restricted to about 35° of motion per joint. The three joints will be located at the head/neck junction, the middle of the cervical spine (C4/C5), and the base of the neck (C7/T1). The joint C4/C5 will be designed to provide for neck torsional stiffness and axial stiffness control.

The remainder of the spine will have joints located at the upper thorax (T4/T5), middle thorax (T8/T9), lower thorax (T12/L1), and the base of the spine (L5/S1). These joints will provide for omnidirectional bending motion control. Provision will be made for torsional stiffness control at the lower thorax (T12/L1) joint.

The joint designs throughout the spine will be of the same basic character, with only detail changes in size and stiffness to accommodate the specific needs of the response specifications at each joint. The basic design concept is a well-defined, fixed joint-center (either a ball-joint or a universal joint) surrounded by a joint motion-resistance element. The fixed joint-center will provide a well-defined linkage configuration, while the joint motion-resistance element will be circular in shape to provide a continuous resistance to motion as a function of motion direction. The mechanical properties of the resistance element depend on the response specification. Solid rubber discs have been used commonly for this purpose, but other concepts, such as pneumatic or fluid-filled toroidal bladders, could also be designed to achieve the proper system response. The isolation of the linkage configuration from the resistance control (unlike a monolithic rubber beam design) will allow rapid and easy identification of deficient components in certification testing. Examples of these concepts for joint design are given in Culver et al. (1972) and Melvin et al. (1972).

The provision for torsional motion control can best be accomplished with a torsion-bar element incorporated in the joint-center attachment to the rigid spine links. Axial compliance, if needed, can be provided by elastic support for the torsion-bar anchor internal to the rigid link. Provisions will also be made at each joint to allow adjustment of the initial configuration of the spine in the sagittal plane through the use of interchangeable wedge-shaped rigid blocks of different sizes that can be inserted and fastened in place.

The rigid spine segment between T1 and T4 will provide the structural attachment for the shoulders, the thoracic structure will be attached to the T5-T8 and T9-T12 segments, and the abdominal structure will be attached to the L2-L5 segment. All of these spinal segments will have provisions for locating and rigidly anchoring the associated body segments so that their spatial positions can be fixed in the certification testing fixture.

It is obvious that the response of many of the spinal joints will be influenced by surrounding structures in the AATD. This is particularly true in the case of the thoracic joints. Thus, the interactions with surrounding structures must be evaluated before the final design of the pertinent joints is determined. The effect of thoracic spinal mobility on the cervical spine response will also have to be assessed during the whole-body testing before the cervical-spine joint designs can be finalized.

The spinal instrumentation will consist of six-axis load cells mounted at the base of the head, the base of the neck, and the base of the spine. Measurements at these locations will augment the measurements being made in adjacent structures, such as the head, chest, and abdomen, and aid in interpretation of body loading from diverse restraint configurations.

THORAX

The general geometric specifications for the AATD thorax include the following dimensions.

Chest breadth at axilla	30.4 cm
Chest circumference at axilla	103.9 cm
Chest breadth at nipple	34.9 cm
Chest circumference at nipple	100.7 cm
Chest circumference at 10th rib	90.6 cm
Chest depth at substernale	23.0 cm
Chest depth at nipple	23.3 cm

The coordinates and orientation of the thoracic anatomical coordinate system, the coordinates of the thoracic center-of-gravity, and the orientation of the principal axes of inertia with respect to the anatomical axes are given in Robbins (1983). The mass and mass moments of inertia for the thorax are given in Tables 3 and 4.

The biomechanical response of the thorax to impact can be characterized by a wide variety of direct loading situations and response measures. The loading conditions include that from (1) moving-mass impactors with rigid 15.2-cm (6-inch) diameter surfaces in both frontal and lateral impacts, (2) rigid and padded flat walls in lateral impacts, and (3) shoulder belts and air bags in frontal impacts. The response measures include applied impact load, chest wall and spine accelerations, and chest deflections. The data have been obtained primarily from cadavers, but some limited data are available from human volunteers. The following section describes the method used to analyze available rigid moving-mass impact data to develop response parameters.

Analysis of Load-Deflection Response Data. The purpose of this analysis was to identify the mechanical parameters related to rigid moving-mass impacts to the front of the thorax. A procedure was developed to analyze the force-time history and the chest-deflection time-history for a particular test in terms of an elastic (spring-like), viscous (damper-like), and inertial (mass-like) response. The procedure assumed that, at any instant in time, the measured impact force F(t) is equal to the sum of spring force FK(t), damping force FC(t), and inertial force FI(t), i.e.,

$$F(t) = FK(t) + FC(t) + FI(t)$$

By postulating particular functions for each of the forces, such as the spring force being a linear function of chest deflection, $FK(t)=K \cdot D(t)$, the damping force being a linear function of the deflection rate, $FC(t)=C \cdot V(t)$, and the inertial force being a linear function of the acceleration of the chest wall, $FI(t)=m \cdot A(t)$, and, substituting these functions in the above equation, the result is an equation that can be used to identify the postulated functions. In the case cited above, K would be the spring rate, C would be the damping constant, and m would be the effective mass being accelerated by the impactor. The resulting equation would be

$$F(t) = K \cdot D(t) + C \cdot V(t) + m \cdot A(t)$$

where D, V, A, and F are all measured, known quantities, and K, C, and m are unknown. Thus only three sets of (F,D,V,A,) at three different instants of time are sufficient to determine the three unknowns, K, C, and m. Clearly, there are more than just two time instants for which (F,D,V,A) are known. This fact was used to compute the least square solution to a set of linear, simultaneous, overdetermined algebraic equations:

$$\begin{bmatrix} D_1 & V_1 & A_1 \\ D_2 & V_2 & A_2 \\ \cdot & \cdot & \cdot \\ \cdot & \cdot & \cdot \\ \cdot & \cdot & \cdot \\ D_n & V_n & A_n \end{bmatrix} \begin{bmatrix} K \\ C \\ m \end{bmatrix} = \begin{bmatrix} F_1 \\ F_2 \\ \cdot \\ \cdot \\ \cdot \\ F_n \end{bmatrix}$$

The solution vector [K,C,m] is the best estimate from the data of the spring, damping, and mass constants that were postulated as models.

A more complex model for the spring or damper function may be postulated to include nonlinear functions with more than a single constant defining these functions. The equations remain linear as long as the model constants can be factored out of the function.

A number of different simple models, five in all, were studied in conjunction with the UMTRI thoracic impact data. These models included functions representing linear, quadratic stiffening, quadratic softening, bidirectional, and bilinear behavior for either the spring or the damping function. The method for obtaining load-defiection information from ten frontal UMTRI thoracic tests involved combining the electronic force-time histories with the deflection measurements obtained from analysis of the high-speed movies of the tests. The details of these methods are described in Alem and Nakla (1986). In addition, the extensive published tests of Kroell et al. (1971, 1974), in the form of load and displacement time histories, were digitized for determining the load-deflection response of the thorax.

Comparison of the test procedures used in the UMTRI tests with those of the Kroell et al. tests led to the conclusion that the configuration of the thorax relative to the impact surface in the Kroell et al. series was the more suitable for determining impact response because the impactor surface was parallel to the chest surface. Consideration of the linear velocity sensitivity of the dynamic responses of the thorax (Melvin et al. 1985, Figures 3-2 and 3-3) and the general progressive stiffening behavior of soft tissues in compression led to the choice of an equation in which the impact force was given by

$$F(t) = K \cdot D^2(t) + C \cdot V(t) + m \cdot A(t)$$

A total of twenty-eight tests were analyzed with this equation. There were four low velocity (4.2 to 5.2 m/s or 9.4 to 11.7 mph), nineteen medium velocity (6.3 to 8.2 m/s or 14.1 to 18.4 mph), and five high velocity (9.7 to 10.2 m/s or 21.6 to 22.8 mph) tests. The individual best-to-fit constants for each test, their mass-scaled values, and the means and standard deviations for the scaled values in each velocity grouping and for the overall scaled data are given in Table 9 along with the individual impactor velocities, V_I, and impactor masses, m_I. Examples of the test data and the fitted curves are given for each velocity grouping in Figures 13, 14, and 15.

Static Load Deflection Response. Static loading data on the thoracic response of human volunteers and cadavers exist for frontal loading with both rigid discs and shoulder belts (Melvin et al. 1985, pp. 98-106). The static load-deflection curve of the chest under loading by a fiat 15.2-cm (6-inch) diameter disc at mid-sternum should approximate a linear stiffness of 263 ± 40 N/cm (150 ± 23 lb/in) for deflections up to 4 cm (1.6 in). At deflections above 7.6 cm (3.0 in) the slope of the load-deflection curve should approximate

TABLE 9: CHEST RESPONSE SCALING

Run	Subj	Wt (lb)	V_I (mph)	m_I (lb)	m (ib)	C (lb·s/in)	K* (lb/in^2)	m_s^*	C_s^*
MEDIUM VELOCITY									
60	11FF	130	14.1	43.0	0.531	1.91	55.3	0.696	2.29
61	12FF	138	16.2	50.4	0.767	1.96	88.4	0.948	2.26
65	13FM	168	16.6	50.4	0.685	1.98	48.4	0.695	2.00
66	14FF	127	16.4	50.4	0.625	1.98	65.8	0.839	2.41
69	15FM	117	15.4	52.0	0.560	2.00	102.0	0.816	2.57
76	18FM	145	15.0	52.0	0.434	3.09	60.8	0.510	3.44
77	19FM	145	15.0	52.0	0.940	2.55	109.0	1.105	2.84
79	20FM	125	15.0	52.0	0.964	3.26	72.6	1.315	4.01
83	22FM	165	15.0	52.0	0.699	2.79	58.7	0.722	2.85
85	23FF	135	17.3	43.0	0.063	1.64	74.5	0.080	1.92
96	34FM	130	18.4	41.8	0.463	2.62	49.6	0.607	3.14
99	36FM	165	16.1	41.8	0.686	3.10	100.0	0.709	3.17
178	46FM	209	16.4	42.5	0.969	2.44	39.5	0.791	2.13
182	48FM	142	15.8	23.0	0.334	2.05	39.8	0.401	2.32
190	54FF	82	15.0	43.1	0.614	1.70	40.2	1.277	2.77
196	58FM	152	15.1	23.0	0.504	2.41	35.1	0.565	2.60
202	62FM	111	15.5	22.0	0.239	1.36	22.2	0.367	1.81
203	63FM	194	15.5	50.7	0.377	1.71	80.3	0.331	1.57
204	64FM	139	15.5	50.7	0.333	1.90	64.0	0.408	2.18
AVG							**63.5**	**0.694**	**2.54**
SD							**23.7**	**0.312**	**0.59**
LOW VELOCITY									
171	42FM	120	10.9	50.4	0.570	2.22	83.1	0.810	2.81
177	45FM	141	11.3	50.7	0.613	2.34	55.0	0.741	2.66
189	53FM	170	11.7	50.6	1.130	3.45	86.0	1.133	3.46
200	60FM	175	9.4	50.6	0.862	3.15	76.0	0.840	3.10
AVG							**75.0**	**0.881**	**3.00**
SD							**23.7**	**0.312**	**0.59**
HIGH VELOCITY									
86	24FM	180	21.6	50.4	0.390	3.44	70.3	0.369	3.32
93	31FM	165	22.8	50.8	0.329	3.40	69.8	0.340	3.48
94	32FM	120	22.2	50.4	0.180	2.60	61.7	0.256	3.29
104	37FM	163	22.0	50.4	0.268	4.30	150.0	0.280	4.43
191	55FM	179	22.2	43.1	0.784	2.79	78.4	0.747	2.70
AVG							**86.0**	**0.398**	**3.44**
SD							**32.4**	**0.179**	**0.56**
TOTAL									
AVG							**69.2**	**0.668**	**2.77**
SD							**25.9**	**0.308**	**0.66**

* Scaling factors are $\lambda_K = 1$ (because it is a deflection-squared spring), $\lambda_m = \lambda_m$, $\lambda_C = (\lambda_m)^{2/3}$.

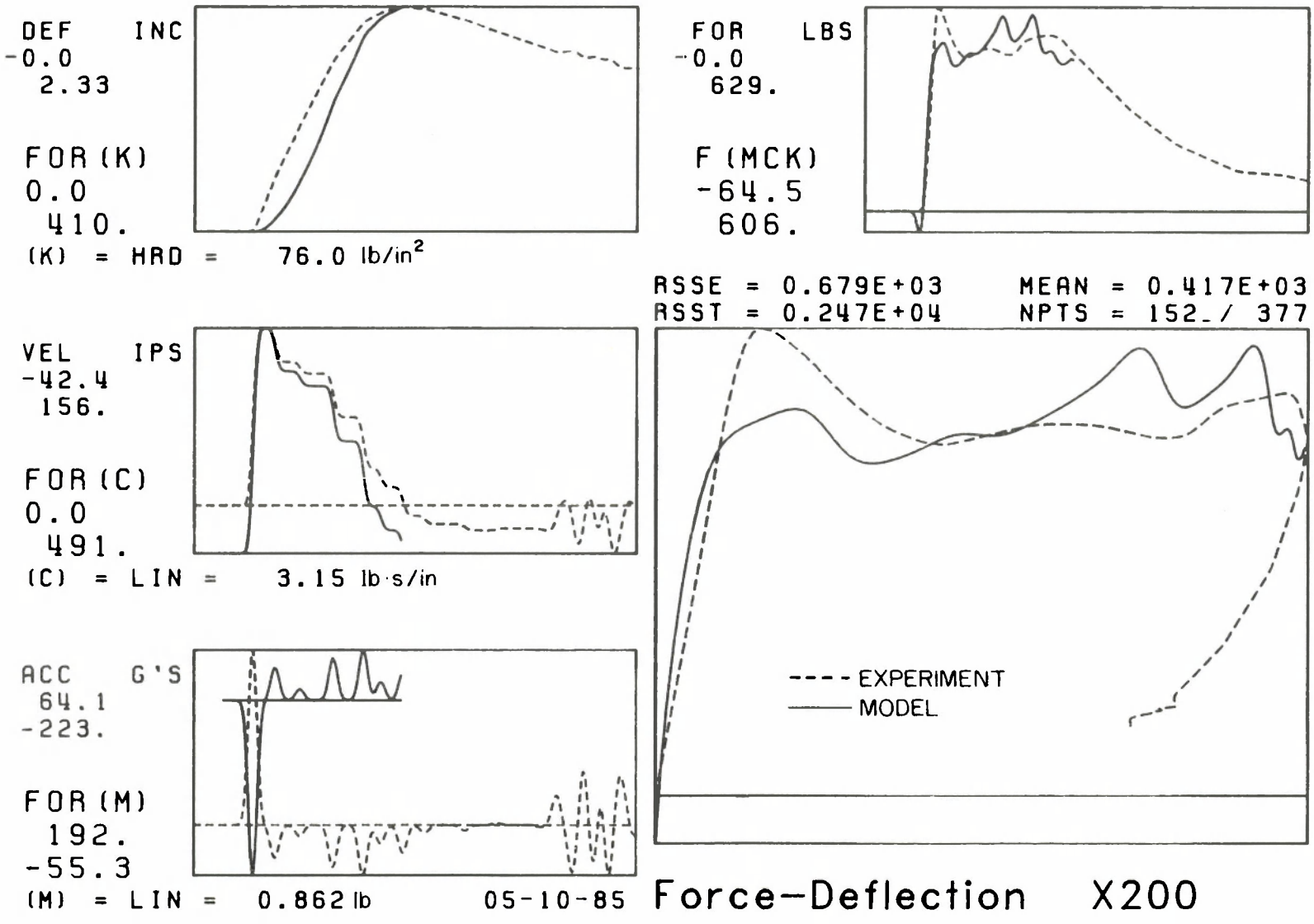

FIGURE 13. Kroell et al. thoracic impact force–deflection response (test no. 200, 4.2 m/s).

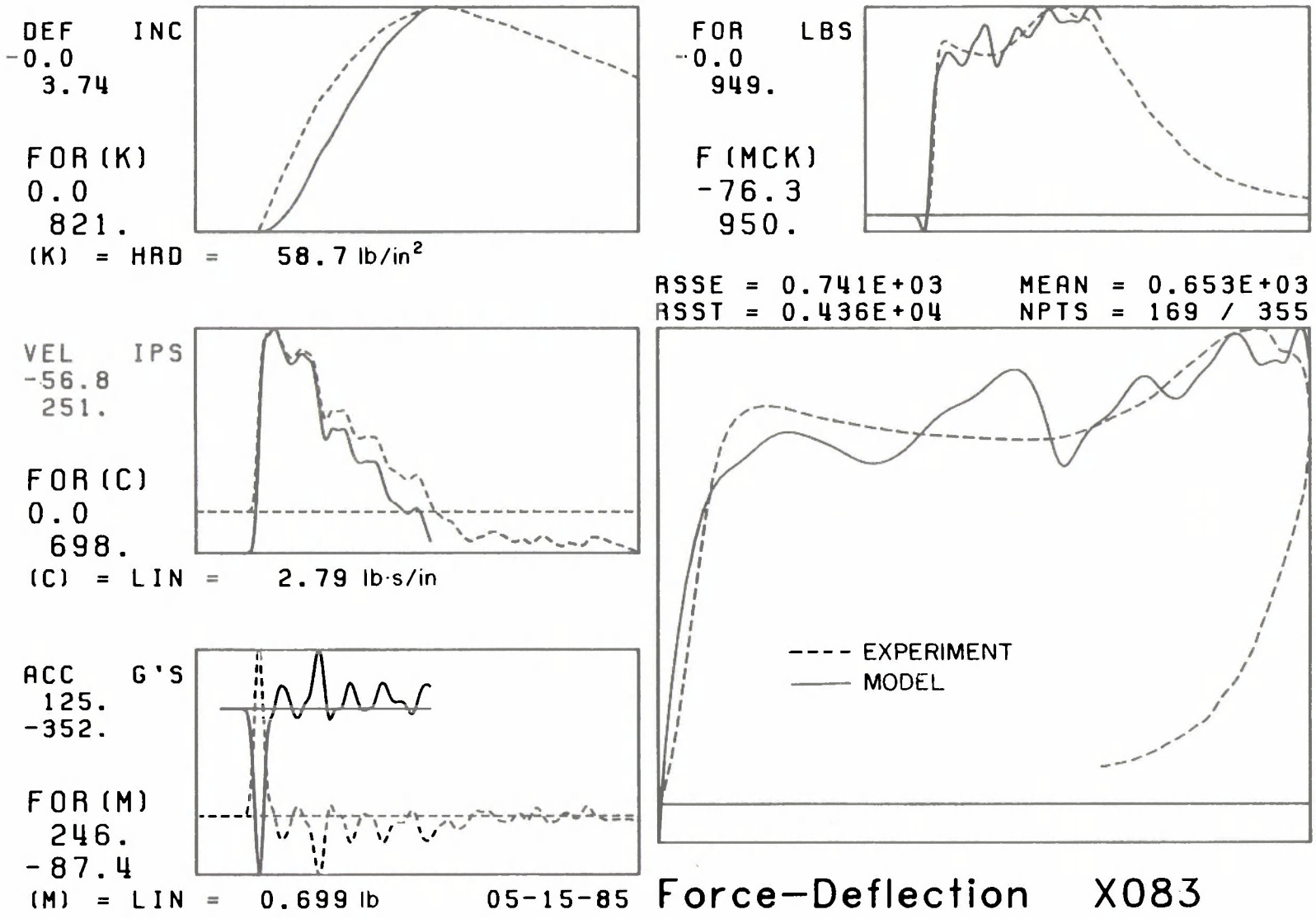

FIGURE 14. Kroell et al. thoracic impact force–deflection response (test no. 83, 6.7 m/s).

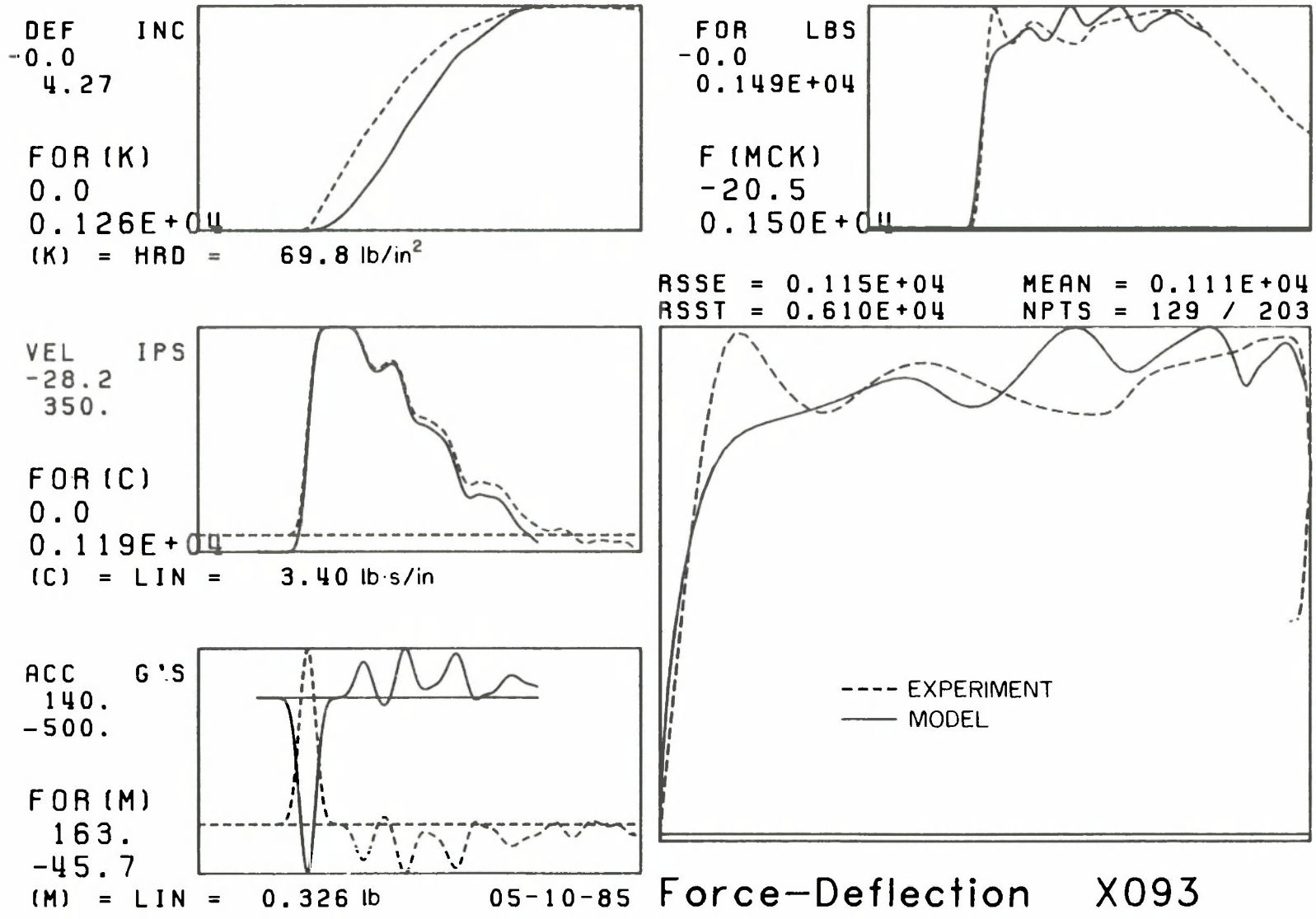

FIGURE 15. Kroell et al. thoracic impact force–deflection response (test no. 93, 10.2 m/s).

1200±180 N/cm (685±103 lb/in). This nonlinear overall load-deflection response can also be represented in a continuous manner by a load-deflection relationship given by

$$F_F = (48 \pm 7 \text{ N/cm}^2)d_F^2 \quad \text{or} \quad (69 \pm 10 \text{ lb/in}^2)d_F^2$$

where F_F=frontal load, and d_F=frontal deflection. This is based on the mean nonlinear (deflection squared) spring from the curve-fitting of the Kroell response data (see Table 9).

The static normal belt-load/chest-deflection response at mid-sternum should approximate a linear stiffness of 676±101 N/cm (386±58 lb/in) for deflection up to 2.54 cm (1 in). The corresponding stiffness value for the upper lateral regions of the front of the chest, with clavicular structures in place, should be 948±142 N/cm (541±81 lb/in), while the lower lateral regions of the front of the chest should exhibit a stiffness in the range of 400±60 N/cm (228±34 lb/in). The tests to determine these static responses to shoulder-belt loading should duplicate the techniques of L'Abbé et al. (1982).

The static lateral force-deflection characteristics of the chest have not been studied. If the chest were a linear elastic structure, theoretical calculations for a ring-like structure with the dimensions of the AATD chest predict a slightly higher stiffness (on the order of 1.24 times) for the lateral direction than the frontal, due to the more curved nature of the lateral aspects of the chest. Thus, the static lateral force-deflection response of the chest for loading by a 15.2-cm (6-in) diameter rigid disc should be similar to that for frontal loading but with 19% lower deflection for a given load. This would give an overall static load deflection relationship of the form

$$F_L = (74 \pm 11)d_L^2$$

where F_L=lateral load (N), and D_L=lateral deflection (cm).

Dynamic Load-Deflection Response. The dynamic response of the chest to flat rigid-disc frontal impacts has been discussed extensively by Melvin et al. (1985). The summary response curves for apparent initial stiffness and plateau forces as functions of impactor velocity (Figures 3-2 and 3-3 of Task B report) can be represented by the following equations:

$$S_{AI} = 0.263 + 0.603(V\text{-}1.3) \qquad (V > 1.3 \text{ m/s})$$

and

$$F_P = 1 + 0.750(V\text{-}3.73) \qquad (V > 3.73 \text{ ms})$$

where: S_{AI} = apparent initial stiffness, kN/cm
F_P = plateau force, kN
V = impactor velocity, m/s

The variations of the test subject mass from that of the AATD specifications must be accounted for through scaling of the data using the factor $\lambda_1 = \sqrt[3]{\lambda_m}$. For the stiffness data $(S_{AI})_{scaled} = \lambda_1(S_{AI})_m$, whereas for the force plateau data $(F_P)_S = \lambda_1^2(F_P)_m$. This scaling does not change the form of the above relationships, only the parameter values. The scaled relationships are

$$S_{AIS} = 0.255+0.603(V - 1.1) \qquad (V>1.1 \text{ m/s})$$

$$F_P = 1.1+0.750(V - 3.47) \qquad (V>3.47 \text{ m/s})$$

The equations can be combined to define an equivalent deflection d_{PI} at which the plateau would theoretically begin. This idealized response would be characterized by the equation:

$$F_P = S_{AI}d_{PI} \qquad \text{or} \qquad d_{PI} = \frac{F_P}{S_{AI}}$$

The maximum deflection of the chest occurs when the impactor velocity and the chest reach a common velocity. Thus, the force at maximum deflection is primarily a static response. Accordingly, the deflection at the end of the plateau region can be estimated by the combination of the plateau force at a given velocity and the associated static deflection needed to produce a static force level equal to the plateau force. This can be expressed by the equation

$$F_P = S_E d_{PF}^2 \qquad \text{or} \qquad d_{PF} = \sqrt{F_P/S_E}$$

where S_E equals the coefficient of the nonlinear static elastic response of the chest and is equal to (48 ± 7) N/cm^2 for frontal loading. Figure 16 shows the resulting idealized response curves (with $\pm15\%$ ranges) generated from the above equations for three impactor velocities: 4.3, 6.7, and 10 m/s (14, 22, and 32.8 ft/s). The first two velocities are those of the present Part 572 test procedure. The corresponding values for defining the curves are given in Table 10. The impactor mass should be 23.4 kg (51.5 lb).

The results of the curve-fitting analysis of the Kroell data, Table 9, also yield characteristic values for velocity and acceleration coefficients that can be used, along with the nonlinear static spring coefficient, as guides to the nature of the parameters needed for a properly responding thorax design. The mean value of the linear velocity coefficient is 4.85 ± 0.73 N·s/cm (2.77 ± 0.42 lb·s/in), and the mean value of the linear acceleration coefficient is 0.30 ± 0.045 kg (0.67 ± 0.1 lb).

There are limited data on the lateral impact response of the chest under loading conditions similar to those used in frontal testing. Stalnaker et al. (1973) reported on cadaver tests using the same test techniques. The test methods were quite different from those employing a moving-mass impactor of the type used in present ATD certification procedures. Consequently, Neathery (1974) concluded that the data were not strictly comparable to the traditional Kroell data. The Stalnaker data can, however, be used to indicate general similarities and differences between frontal and lateral loading. In particular, Stalnaker found that, under identical input conditions, the apparent initial lateral stiffness $(S_{AI})_L$ of the chest was approximately 63% of the apparent initial frontal stiffness $(S_{AI})_F$ and that the plateau force levels were approximately the same. This implies that the linear velocity coefficient would be similar to the frontal coefficient but that the effective initial mass involved in the response may be lower than that for frontal loading due to the geometric differences between the front and the side of the thorax. This information along with the lateral static chest response relation can be applied by the previously described methods for defining the idealized thoracic frontal response to generate analogous lateral response specifications. Figure 17 shows the resulting idealized response curves (with $\pm15\%$ ranges) generated from that analysis for the same three impactor velocities 4.3, 6.7, and 10 m/s (14, 22, and 32.8 ft/s). The corresponding values for defining the curves are given in Table 11.

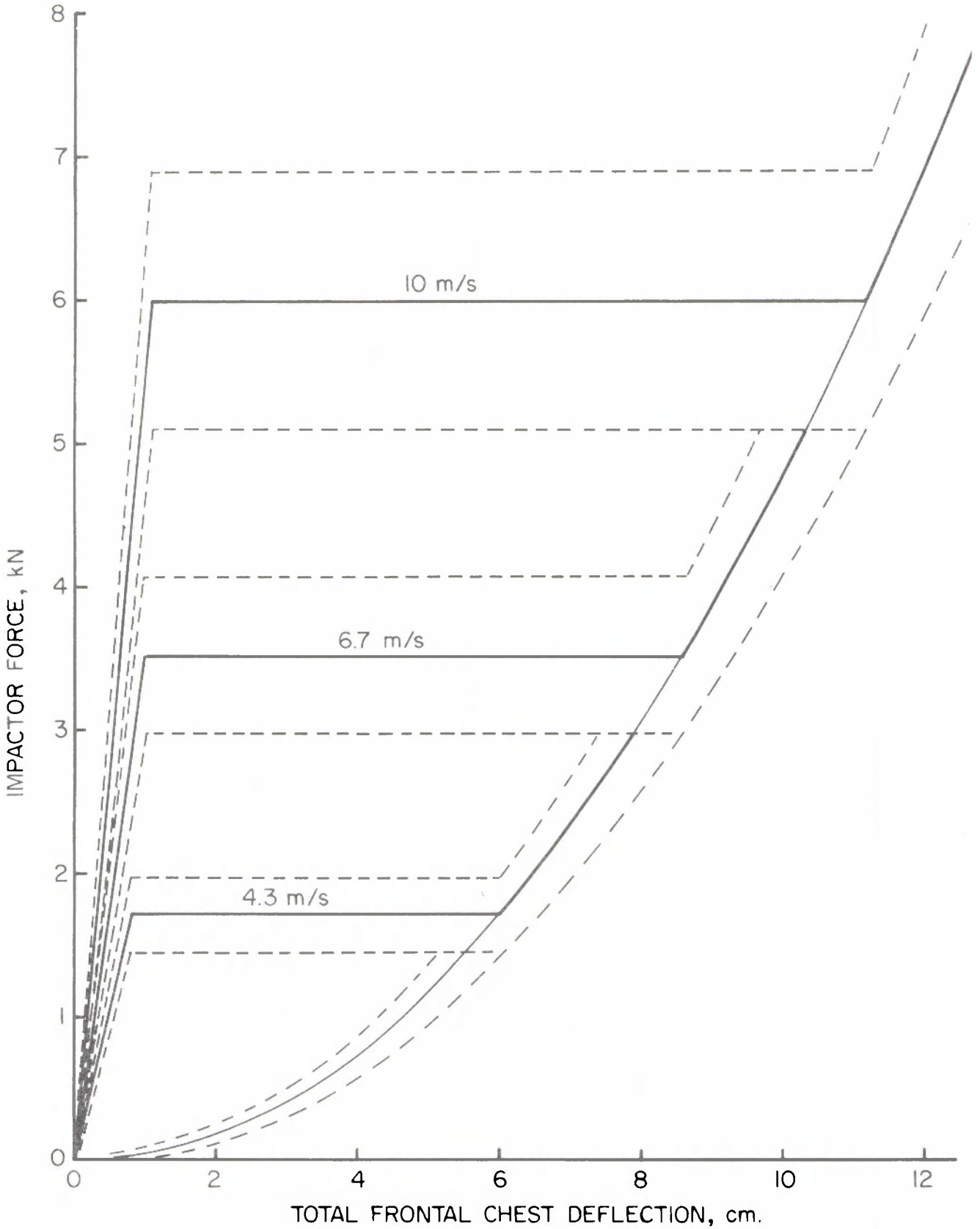

FIGURE 16. AATD frontal thoracic impact response—loading only (15.2-cm rigid disc, 23.4-kg impact mass).

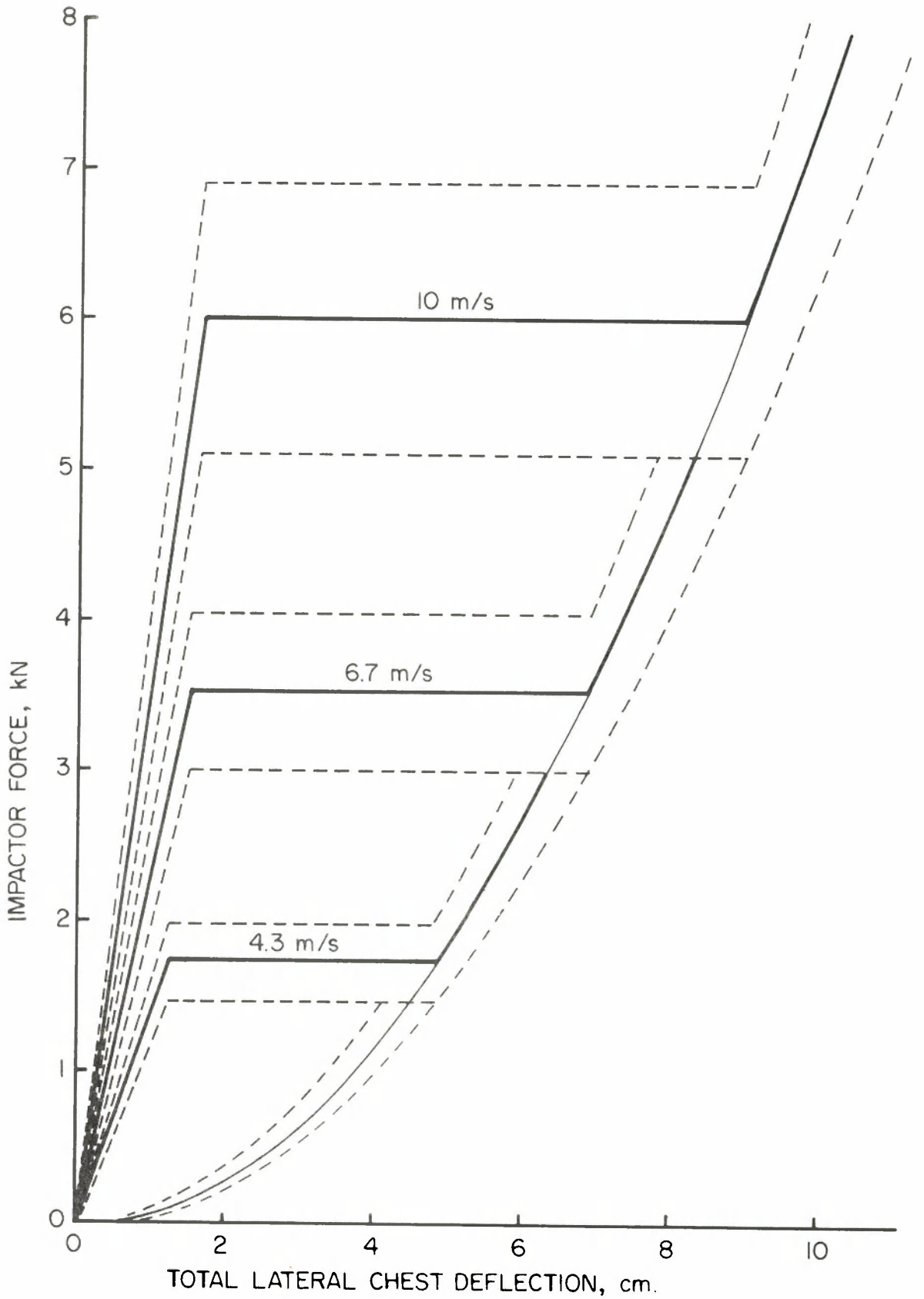

FIGURE 17. AATD lateral thoracic impact response—loading only (15.2-cm rigid disc, 23.4-kg impact mass).

TABLE 10

AATD IDEALIZED FRONTAL THORACIC IMPACT RESPONSE PARAMETERS
(Rigid disc impactor, 15.2-cm diameter and 23.4-kg mass)

Impactor Vel (m/s)	S_{AI} (kN/cm)	F_P (kN)	d_{PI} (cm)	d_{PF} (cm)
4.3	2.18±0.33	1.72±0.26	0.79	6.0
6.7	3.63±0.54	3.52±0.53	0.97	8.6
10.0	5.62±0.84	6.00±0.90	1.07	11.2

TABLE 11

AATD IDEALIZED LATERAL THORACIC IMPACT RESPONSE PARAMETERS
(Rigid disc impactor, 15.2-cm diameter and 23.4-kg mass)

Impactor Vel (m/s)	S_{AI} (kN/cm)	F_P (kN)	d_{PI} (cm)	d_{PF} (cm)
4.3	1.38±0.21	1.72±0.26	1.25	4.8
6.7	2.29±0.34	3.52±0.53	1.54	6.9
10.0	3.55±0.53	6.00±0.90	1.69	9.0

The response of the thorax to frontal and lateral impact loads has been defined above for loading only. The unloading behavior of the thorax has been shown by Kroell et al. to dissipate the energy of deformation. In crash testing, the unloading response is not as critical as the loading response, as long as sufficient energy dissipation occurs. This may be specified in terms of a hysteresis ratio, which is the ratio of the area bounded by the loading and unloading portions of the force-deflection curve to the area under the loading portion of the curve. For sufficient response, this ratio should be more than 75% but less than 85%.

The response of the thorax to oblique impacts that are between the frontal and lateral directions has not been quantified by similar methods. Nusholtz et al. (1983b) reported on low-level (2-m/s) impacts in the frontal, lateral, and 45° oblique directions in terms of point-of-impact impedance. These non-injurious impacts produced similar mechanical impedance values in all three directions in the same test subject. Thus it is likely that the oblique response of the thorax is bounded by the frontal and lateral responses.

Whole-Body Testing Response. The dynamic and static load-deflection responses of the thorax discussed above are the primary specifications for the thorax. There are, however, a number of other loading conditions and response measurements that can be used to aid in the specification of thoracic response. These are associated with thoracic performance in a system or whole-body test. In contrast to test methods that apply a well-defined load only to the thorax, systems tests load other body regions along with the thorax using three-point harnesses, airbags, or lateral walls. In tests of this type, the primary response measurements are accelerations at specific locations on the thorax, but these are accompanied, in some cases, by belt, steering column, or wall loads. Information of this sort, while not as specific for design purposes as load-deflection information, is nevertheless important for verifying the correctness of the overall response of the thorax under more complicated test conditions.

Mertz (1984) analyzed the APR whole-body lateral drop tests and presents normalized average thoracic force-time curves as well as proposed corridors for a 1-m (3.28-ft) drop onto a rigid surface and a 2-m (6.56-ft) drop onto a padded surface. The drop test produces an impact situation similar to a whole-body lateral impact test and is thus a realistic simulation of actual crash conditions. As a response test, however, it is lacking in that it overdrives the system and is ill-defined in terms of loaded area and loading interactions with other body regions. Because the entire torso is brought to a halt during the loading (compression) phase, the momentum of the event is quite different than that of a pendulum impact of equal velocity. If, however, the pendulum velocity is high enough to produce the same energy of deformation in the chest, the rate sensitivity of the chest will produce a load-deflection curve for the pendulum test that is significantly different from the drop test. Because less energy will be absorbed by the chest during the early compression phase of the drop test, that test will still produce higher peak forces than a pendulum test, because there will be greater deflections of the chest at the end of the compression phase.

A similar type of response corridor for whole-body lateral thoracic impact can be obtained from lateral rigid wall sled tests, such as those conducted at the University of Heidelberg and included in the AATD data base. Five tests were run at 32 km/h (20 mph), and load cells were placed on the rigid wall to measure thorax and pelvis loads separately. The sled test method provides a greater degree of control on subject positioning and surface interaction than does the drop test method, and the lateral rigid-wall test-buck configuration is well-defined and in use at a number of test facilities.

The five 32 km/hr (20 mph) test responses have been combined to produce a mean force-time response shown in Figure 18. Signals used for thoracic corridors were all filtered with a 200-Hz Butterworth filter with a slope of 24 dB/octave. This filter was based on initial examination of grouped thoracic signals, and turned out to be very close to the frequency response characteristics of the thorax derived from a more exhaustive investigation of the data base, the results of which are presented in a separate report (Alem and Nakhla 1986). The range shown about the mean curve is plus-and-minus one standard deviation. The corridors drawn about the data represent simple straight-line boundaries for the plus-and-minus one standard deviation curves, except at the peak load value where a variation of $\pm 15\%$ of the peak load is indicated. The coordinates of the boundaries are given in Table 12.

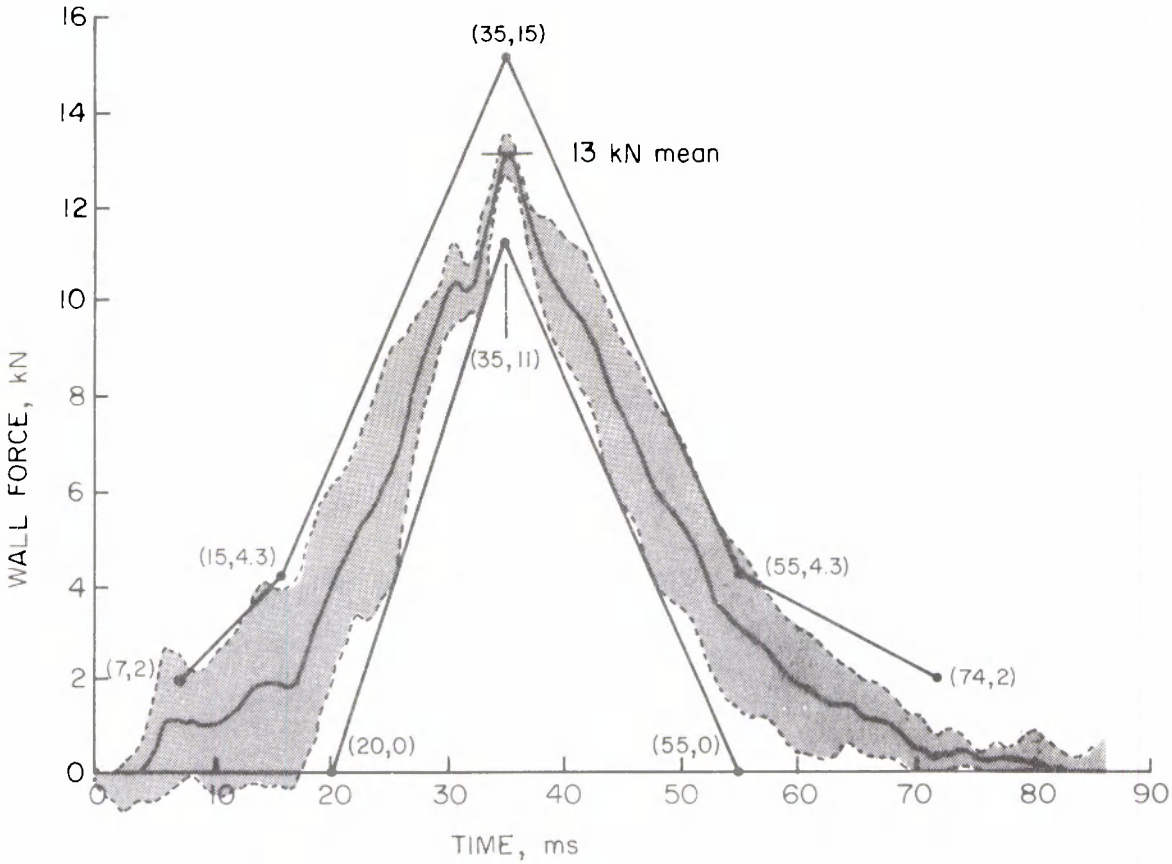

FIGURE 18. Idealized lateral thoracic force-time corridor for a 32 km/h rigid wall sled test.

TABLE 12

LATERAL RIGID WALL THORACIC FORCE-TIME CORRIDORS
32 km/h (20 mph)

Upper Boundary		Lower Boundary	
Force (kN)	Time (ms)	Force (kN)	Time (ms)
0	0	0	20
4.3	15		
15	35	11	35
4.3	55		
2	90	0	55

The use of the twelve-accelerometer array (originally ten, see Robbins et al. 1976) is recommended for measuring thoracic response in whole-body test conditions. This method is superior to a single triaxial accelerometer measurement, or other specialized methods, in that several rib-cage and spinal acceleration measures are routinely made. These give a more global characterization of the structural response of the thorax, and the same measurement system can be used under a variety of loading conditions. While the acceleration-time history of a particular point on the chest under a specific loading condition is not particularly useful for a designer initiating a new mechanical chest concept, it can be very useful for evaluating the efficacy of a prototype design that has been constructed and tested to load-deflection specifications.

Restraint loading and thoracic acceleration data are useful, then, as secondary design specifications and prototype performance specifications under systems testing conditions. The test conditions would duplicate the test set-up of the original cadaver tests, including accelerometer placement, and would be used in addition to the primary thoracic load-deflection response specifications in assessing the success of the design concept. The present AATD data base contains sufficient tests in the categories shown in Table 13 for use as secondary performance specifications for the AATD thorax.

TABLE 13

TWELVE-ACCELEROMETER ARRAY THORACIC RESPONSE DATA SUMMARY

Direction	Type	Velocity (m/s)	Number of Tests
Frontal	Pendulum Impactor	4.5	5
Frontal	Sled Three-Point Belt	13.4	6
Frontal	Sled Airbag	13.4	7
Lateral	Pendulum Impactor	4.3	4
Lateral	Pendulum Impactor	6.3	8
Lateral	Rigid Wall	8.9	12
Lateral	Rigid Wall	11.2	6
Lateral	Padded Wall	6.7	4
Lateral	Padded Wall	8.9	9

The individual accelerometer data from the above tests have been grouped according to comparable location and direction in the following manner:

- Near-Side: Those accelerometers located near the loaded surface of the chest and oriented in the direction of impact.
- Far-Side: Those accelerometers located opposite the loaded surface of the chest and oriented in the direction of impact.
- Intermediate: Those accelerometers located on the surface of the chest at points between the near and far sides.

Table 14 categorizes specific accelerometers for the two loading directions. The near-side grouping is presumed to represent the response of the chest wall to the loading surface. The far-side grouping represents transmitted and whole-body effects of the load. The intermediate grouping represents global structural responses using the response in both the loading direction and that perpendicular to the loading direction.

TABLE 14

THORACIC ACCELEROMETER GROUPINGS

Category	Frontal	Lateral
Near-Side	Upper/Lower Sternum X	Left Upper/Lower Rib Y
Far-Side	Spine (T1,T12) X Spine (T1,T12) Z	Right Upper/Lower Rib Y
Intermediate	Left/Right Lower Rib X Left/Right Upper Rib Y	Spine (T1,T12) Y Spine (T1,T12) X Sternum X

To generate response corridors, filtered data traces for each grouping of accelerometers were aligned according to the principal response peak. Those traces with spurious peaks due to transducer malfunctions were eliminated. Once aligned, the traces were scaled by $(\lambda_m)^{1/3}$, then combined, and a mean response trace was produced along with a band of plus-and-minus one standard deviation about that mean curve. To obtain information on the phasing of the responses between groups, the time between the near-side peak and the corresponding intermediate and far-side peaks was determined for each individual test, and then the mean values for those time intervals were calculated for each test condition.

Figures 19 through 27 display the response histories for each of the test conditions listed in Table 14. These represent secondary specifications for AATD thoracic performance under the specific test conditions given. They are to be used to assess the overall efficacy of a thoracic design concept, since they represent the range of thoracic loading conditions found in the automobile crash environment. Thus, a candidate thorax design should exhibit general agreement with those waveforms in terms of magnitude and phasing in order to be considered an appropriate design. It is quite likely that not all the waveforms can be completely matched, and therefore some compromises will have to be made as the design concept evolves. From the standpoint of structural response and loading surface interaction, however, the near-side and intermediate responses are more important than the far-side responses.

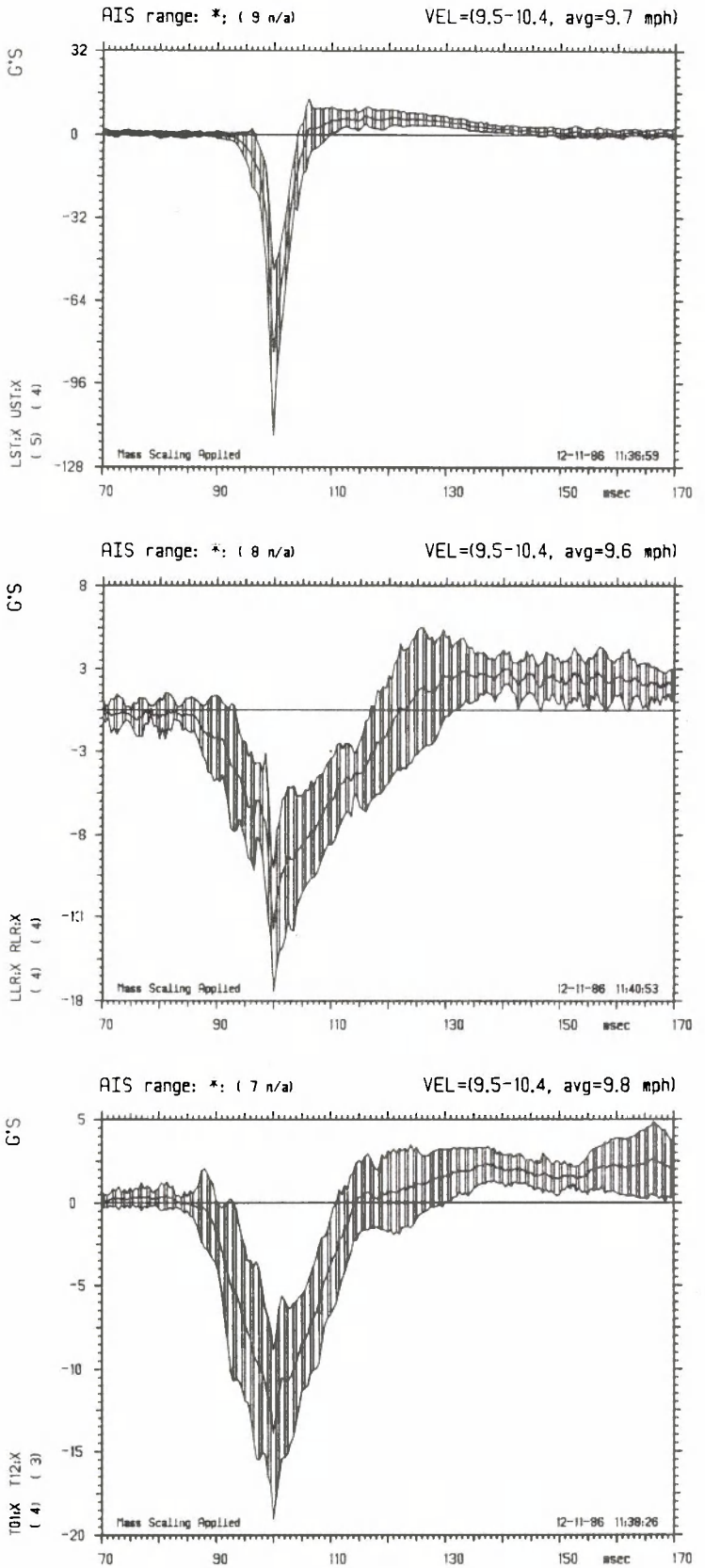

Sternum X
(Near)

	Test ID	Xduc	Test Type
1.	76T050	LST:X	PEN: NON
2.	76T053	LST:X	PEN: NON
3.	76T056	LST:X	PEN: NON
4.	76T059	LST:X	PEN: NON
5.	77T068	LST:X	PEN: NON
6.	76T050	UST:X	PEN: NON
7.	76T056	UST:X	PEN: NON
8.	76T059	UST:X	PEN: NON
9.	77T068	UST:X	PEN: NON

Principle Peak: Mean +1 SD = -52.2
Mean = -84.1
Mean -1 SD = -116.1

Peak Time Shift: 0.0 ms

Left/Right Lower Rib X
(Intermediate)

	Test ID	Xduc	Test Type
1.	76T050	LLR:X	PEN: NON
2.	76T053	LLR:X	PEN: NON
3.	76T056	LLR:X	PEN: NON
4.	76T059	LLR:X	PEN: NON
5.	76T050	RLR:X	PEN: NON
6.	76T053	RLR:X	PEN: NON
7.	76T056	RLR:X	PEN: NON
8.	77T068	RLR:X	PEN: NON

Principle Peak: Mean +1 SD = -9.5
Mean = -13.3
Mean -1 SD = -17.0

Peak Time Shift: 6.6 ms

Spine (T1,T12) X
(Far)

	Test ID	Xduc	Test Type
1.	76T050	T01:X	PEN: NON
2.	76T056	T01:X	PEN: NON
3.	76T059	T01:X	PEN: NON
4.	77T068	T01:X	PEN: NON
5.	76T056	T12:X	PEN: NON
6.	76T059	T12:X	PEN: NON
7.	77T068	T12:X	PEN: NON

Principle Peak: Mean +1 SD = -8.8
Mean = -13.9
Mean -1 SD = -19.0

Peak Time Shift: 6.3 ms

FIGURE 19. Thoracic response in frontal pendulum impactor tests (4.5 m/s).

Sternum X
(Near)

	Test ID	Xduc	Test Type
1.	H79006	LST:X	SLD: 3PT
2.	H79007	LST:X	SLD: 3PT
3.	H79008	LST:X	SLD: 3PT
4.	H79009	LST:X	SLD: 3PT
5.	H79011	LST:X	SLD: 3PT
6.	DOTIIF20	UST:X	SLD: 3PT
7.	H79006	UST:X	SLD: 3PT
8.	H79007	UST:X	SLD: 3PT
9.	H79008	UST:X	SLD: 3PT
10.	H79009	UST:X	SLD: 3PT
11.	H79011	UST:X	SLD: 3PT

Principle Peak: Mean +1 SD = -34.8
Mean = -45.4
Mean -1 SD = -55.9

Peak Time Shift: 0.0 ms

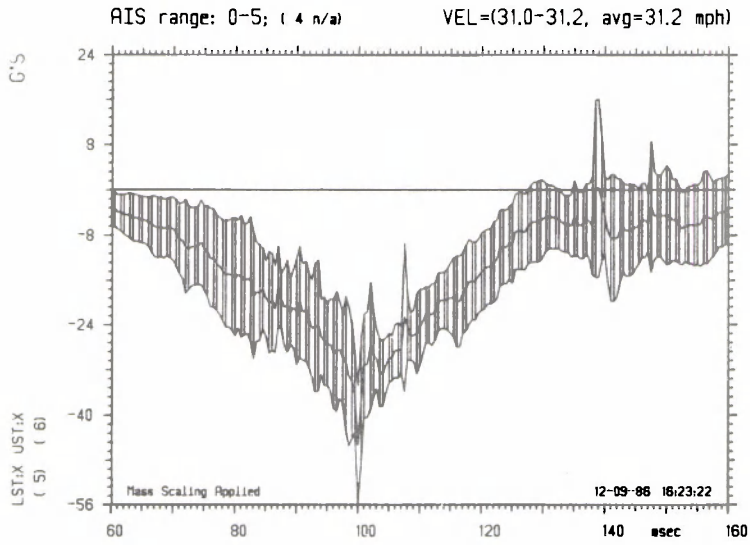

Left/Right Lower Rib X
(Intermediate)

	Test ID	Xduc	Test Type
1.	DOTIIF20	LLR:X	SLD: 3PT
2.	H79007	LLR:X	SLD: 3PT
3.	H79008	LLR:X	SLD: 3PT
4.	H79009	LLR:X	SLD: 3PT
5.	H79011	LLR:X	SLD: 3PT
6.	H79006	RLR:X	SLD: 3PT
7.	H79008	RLR:X	SLD: 3PT
8.	H79009	RLR:X	SLD: 3PT
9.	H79011	RLR:X	SLD: 3PT

Principle Peak: Mean +1 SD = -34.5
Mean = -48.0
Mean -1 SD = -61.4

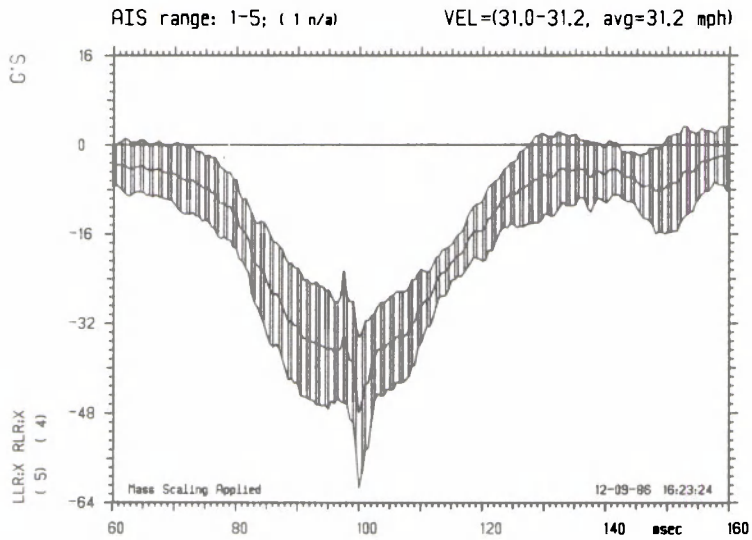

Left/Right Upper Rib Y
(Intermediate)

	Test ID	Xduc	Test Type
1.	DOTIIF20	LUR:Y	SLD: 3PT
2.	H79006	LUR:Y	SLD: 3PT
3.	H79008	LUR:Y	SLD: 3PT
4.	H79009	LUR:Y	SLD: 3PT
5.	H79011	LUR:Y	SLD: 3PT
6.	H79006	RUR:Y	SLD: 3PT
7.	H79007	RUR:Y	SLD: 3PT
8.	H79008	RUR:Y	SLD: 3PT
9.	H79009	RUR:Y	SLD: 3PT
10.	H79011	RUR:Y	SLD: 3PT

Principle Peak: Mean +1 SD = 38.6
Mean = 24.3
Mean -1 SD = 14.8

Peak Time Shift: 2.0 ms

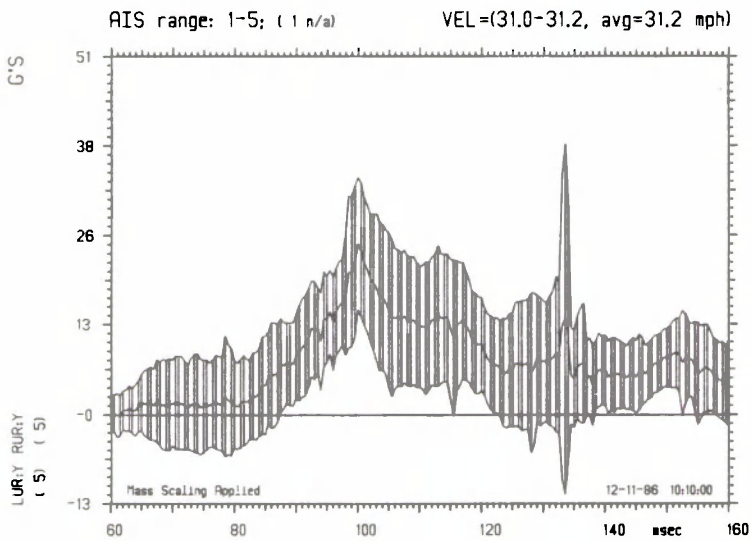

FIGURE 20. Thoracic response in frontal sled three-point-belt tests (13.4 m/s).

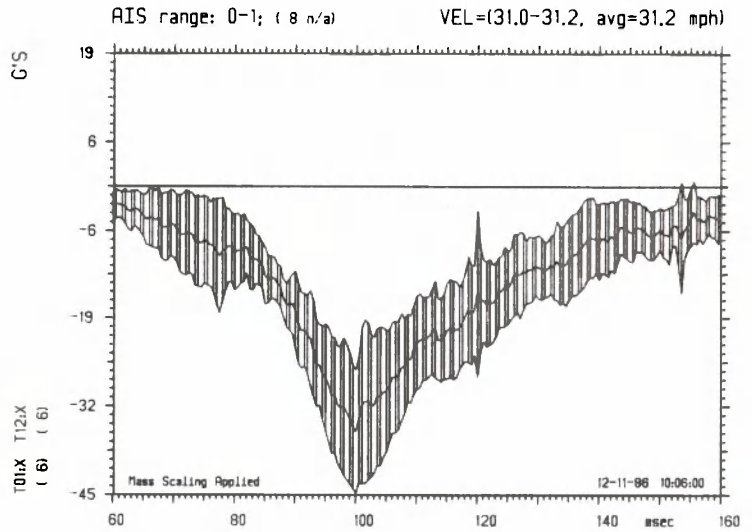

Spine (T1,T12) X
(Far)

	Test ID	Xduc	Test Type
1.	DOTIIF20	T01:X	SLD: 3PT
2.	H79006	T01:X	SLD: 3PT
3.	H79007	T01:X	SLD: 3PT
4.	H79008	T01:X	SLD: 3PT
5.	H79009	T01:X	SLD: 3PT
6.	H79011	T01:X	SLD: 3PT
7.	DOTIIF20	T12:X	SLD: 3PT
8.	H79006	T12:X	SLD: 3PT
9.	H79007	T12:X	SLD: 3PT
10.	H79008	T12:X	SLD: 3PT
11.	H79009	T12:X	SLD: 3PT
12.	H79011	T12:X	SLD: 3PT

Principle Peak: Mean +1 SD = -26.8
Mean = -35.7
Mean -1 SD = -44.6

Peak Time Shift: 2.0 ms

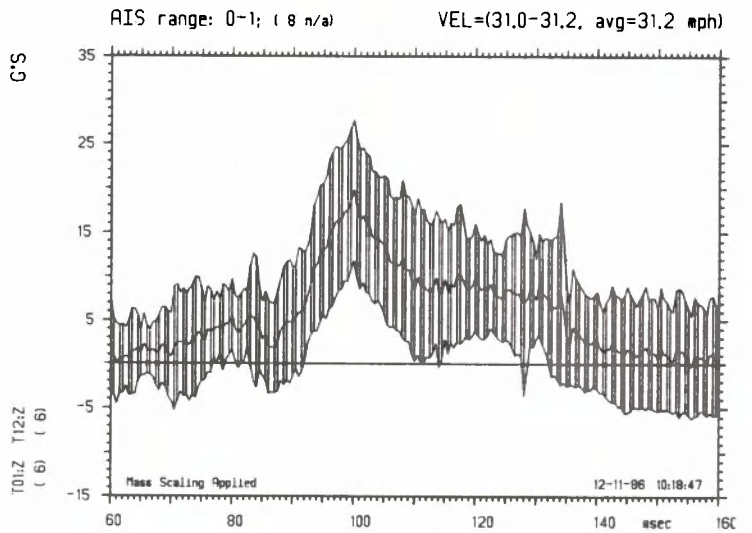

Spine (T1,T12) Z
(Far)

	Test ID	Xduc	Test Type
1.	DOTIIF20	T01:Z	SLD: 3PT
2.	H79006	T01:Z	SLD: 3PT
3.	H79007	T01:Z	SLD: 3PT
4.	H79008	T01:Z	SLD: 3PT
5.	H79009	T01:Z	SLD: 3PT
6.	H79011	T01:Z	SLD: 3PT
7.	DOTIIF20	T12:Z	SLD: 3PT
8.	H79006	T12:Z	SLD: 3PT
9.	H79007	T12:Z	SLD: 3PT
10.	H79008	T12:Z	SLD: 3PT
11.	H79009	T12:Z	SLD: 3PT
12.	H79011	T12:Z	SLD: 3PT

Principle Peak: Mean +1 SD = 27.7
Mean = 19.7
Mean -1 SD = 11.8

Peak Time Shift: 2.0 ms

FIGURE 20. (Continued).

Sternum X
(Near)

	Test ID	Xduc	Test Type
1.	DOT:3022	LST:X	SLD: ABG
2.	DOT:3026	LST:X	SLD: ABG
3.	DOT:3032	LST:X	SLD: ABG
4.	DOT:3035	LST:X	SLD: ABG
5.	DOT:3040	LST:X	SLD: ABG
6.	DOT:3041	LST:X	SLD: ABG
7.	DOT:3038	UST:P	SLD: ABG
8.	DOT:3039	UST:P	SLD: ABG
9.	DOT:3022	UST:X	SLD: ABG
10.	DOT:3026	UST:X	SLD: ABG
11.	DOT:3032	UST:X	SLD: ABG
12.	DOT:3040	UST:X	SLD: ABG
13.	DOT:3041	UST:X	SLD: ABG

Principle Peak: Mean +1 SD = -44.2
Mean = -50.5
Mean -1 SD = -56.8

Peak Time Shift: 0.0 ms

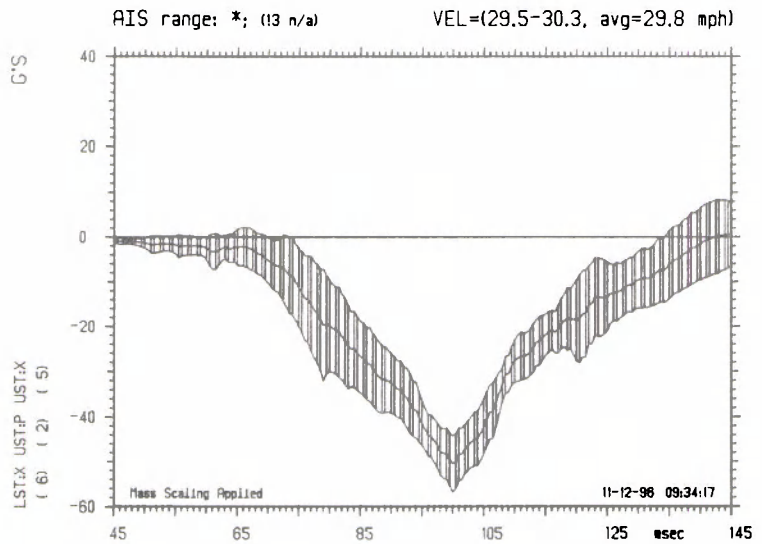

Left/Right Lower Rib X
(Intermediate)

	Test ID	Xduc	Test Type
1.	DOT:3022	LLR:X	SLD: ABG
2.	DOT:3026	LLR:X	SLD: ABG
3.	DOT:3032	LLR:X	SLD: ABG
4.	DOT:3035	LLR:X	SLD: ABG
5.	DOT:3039	RLR:X	SLD: ABG
6.	DOT:3041	LLR:X	SLD: ABG
7.	DOT:3022	RLR:X	SLD: ABG
8.	DOT:3026	RLR:X	SLD: ABG
9.	DOT:3032	RLR:X	SLD: ABG
10.	DOT:3035	RLR:X	SLD: ABG
11.	DOT:3038	RLR:X	SLD: ABG
12.	DOT:3039	LLR:X	SLD: ABG

Principle Peak: Mean +1 SD = -25.4
Mean = -41.7
Mean -1 SD = -64.0

Peak Time Shift: 1.3 ms

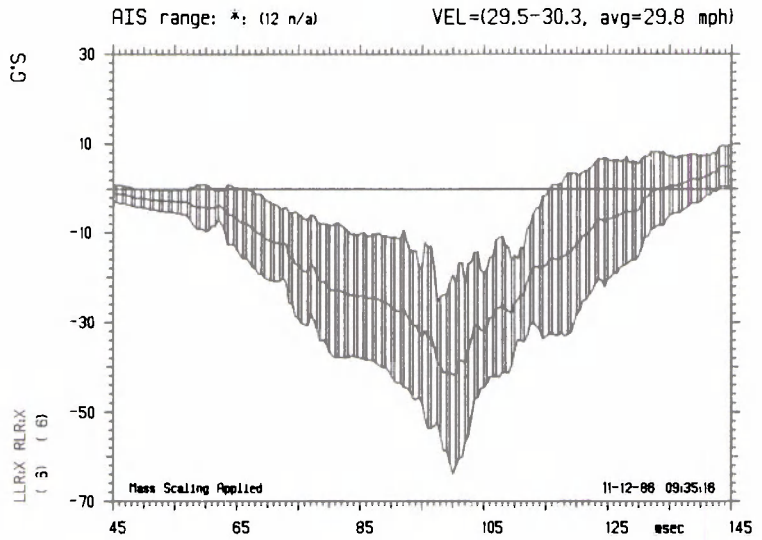

Left/Right Upper Rib Y
(Intermediate)

	Test ID	Xduc	Test Type
1.	DOT:3022	LUR:Y	SLD: ABG
2.	DOT:3026	LUR:Y	SLD: ABG
3.	DOT:3035	LUR:Y	SLD: ABG
4.	DOT:3039	LUR:Y	SLD: ABG
5.	DOT:3040	LUR:Y	SLD: ABG
6.	DOT:3041	LUR:Y	SLD: ABG
7.	DOT:3026	RUR:Y	SLD: ABG
8.	DOT:3039	RUR:Y	SLD: ABG
9.	DOT:3040	RUR:Y	SLD: ABG
10.	DOT:3041	RUR:Y	SLD: ABG

Principle Peak: Mean +1 SD = 45.8
Mean = 35.8
Mean -1 SD = 25.9

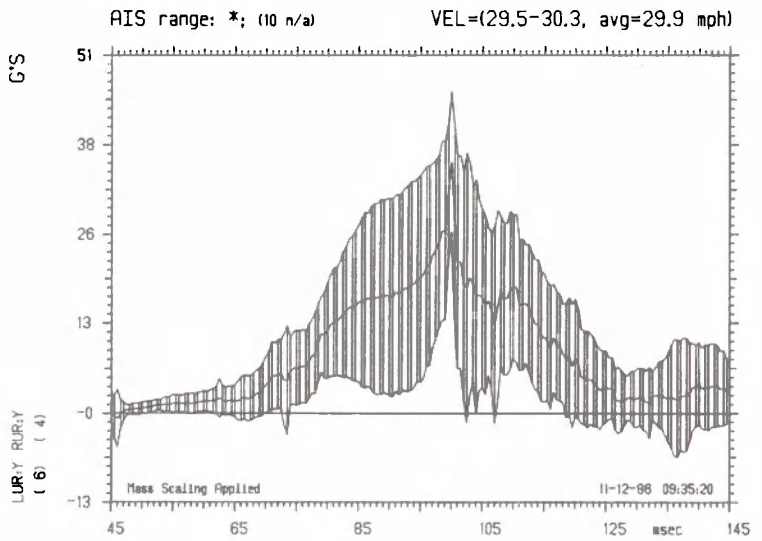

FIGURE 21. Thoracic response in frontal sled airbag tests (13.4 m/s).

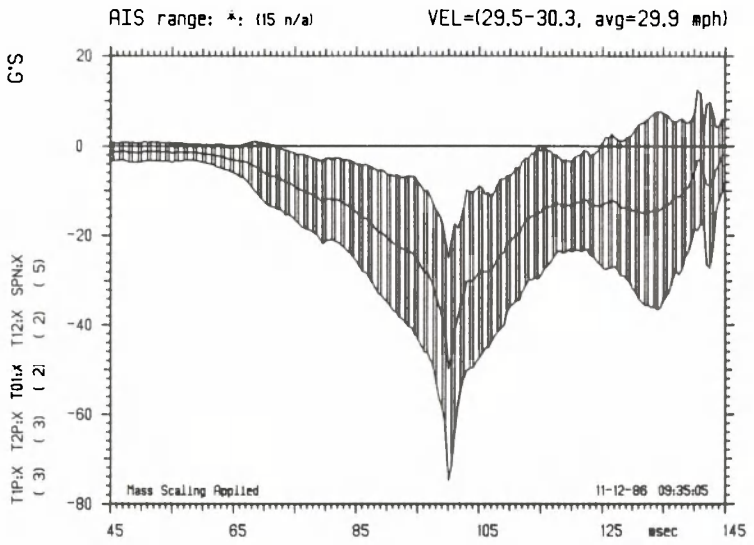

Spine (T1,T12) X
(Far)

	Test ID	Xduc	Test Type
1.	DOT:3022	T1P:X	SLD: ABG
2.	DOT:3032	T1P:X	SLD: ABG
3.	DOT:3035	T1P:X	SLD: ABG
4.	DOT:3022	T2P:X	SLD: ABG
5.	DOT:3032	T2P:X	SLD: ABG
6.	DOT:3035	T2P:X	SLD: ABG
7.	DOT:3040	T01:X	SLD: ABG
8.	DOT:3039	T01:X	SLD: ABG
9.	DOT:3040	T12:X	SLD: ABG
10.	DOT:3041	T12:X	SLD: ABG
11.	DOT:3032	SPN:X	SLD: ABG
12.	DOT:3035	SPN:X	SLD: ABG
13.	DOT:3039	SPN:X	SLD: ABG
14.	DOT:3040	SPN:X	SLD: ABG
15.	DOT:3041	SPN:X	SLD: ABG

Principle Peak: Mean +1 SD = -24.8
Mean = -49.8
Mean -1 SD= -74.8

Peak Time Shift: 6.7 ms

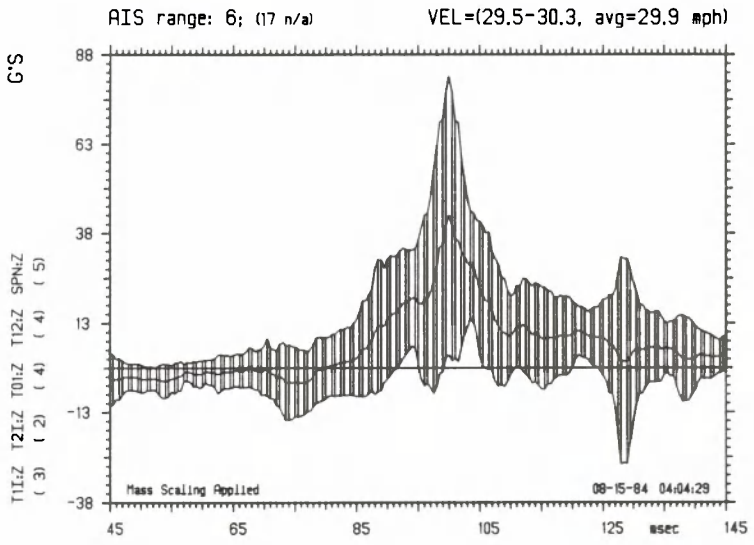

Spine (T1,T12) Z
(Far)

	Test ID	Xduc	Test Type
1.	DOT:3026	T1I:Z	SLD: ABG
2.	DOT:3032	T1I:Z	SLD: ABG
3.	DOT:3035	T1I:Z	SLD: ABG
4.	DOT:3022	T2I:Z	SLD: ABG
5.	DOT:3026	T2I:Z	SLD: ABG
6.	DOT:3038	T01:Z	SLD: ABG
7.	DOT:3039	T01:Z	SLD: ABG
8.	DOT:3040	T01:Z	SLD: ABG
9.	DOT:3041	T01:Z	SLD: ABG
10.	DOT:3038	T12:Z	SLD: ABG
11.	DOT:3039	T12:Z	SLD: ABG
12.	DOT:3040	T12:Z	SLD: ABG
13.	DOT:3041	T12:Z	SLD: ABG
14.	DOT:3026	SPN:Z	SLD: ABG
15.	DOT:3035	SPN:Z	SLD: ABG
16.	DOT:3040	SPN:Z	SLD: ABG
17.	DOT:3041	SPN:Z	SLD: ABG
18.	DOT:3026	SPN:Z	SLD: ABG

Principle Peak: Mean +1 SD = 81.4
Mean = 42.4
Mean -1 SD = 13.6

FIGURE 21. (Continued).

Left Upper Rib Y
(Near)

	Test ID	Xduc	Test Type
1.	76T062	LUR:Y	PEN: NON
2.	76T065	LUR:Y	PEN: NON
3.	77T074	LUR:Y	PEN: NON
4.	77T071	LUR:Y	PEN: NON

Principle Peak: Mean +1 SD = -32.9
Mean = -65.1
Mean -1 SD = -101.6

Peak Time Shift: 0.0 ms

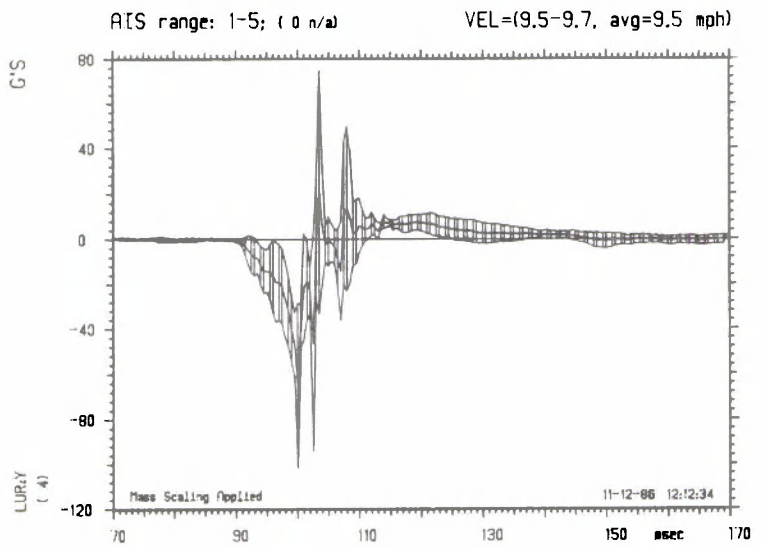

Spine (T1,T12) Y
(Intermediate)

	Test ID	Xduc	Test Type
1	76T062	T01:Y	PEN: NON
2	76T065	T01:Y	PEN: NON
3	77T074	T01:Y	PEN: NON
4	77T071	T01:Y	PEN: NON
5	76T062	T12:Y	PEN: NON
6	76T065	T12:Y	PEN: NON
7	77T074	T12:Y	PEN: NON
8	77T071	T12:Y	PEN: NON

Principle Peak: Mean +1 SD = -8.3
Mean = -14.9
Mean -1 SD = -21.5

Peak Time Shift: 4.4 ms

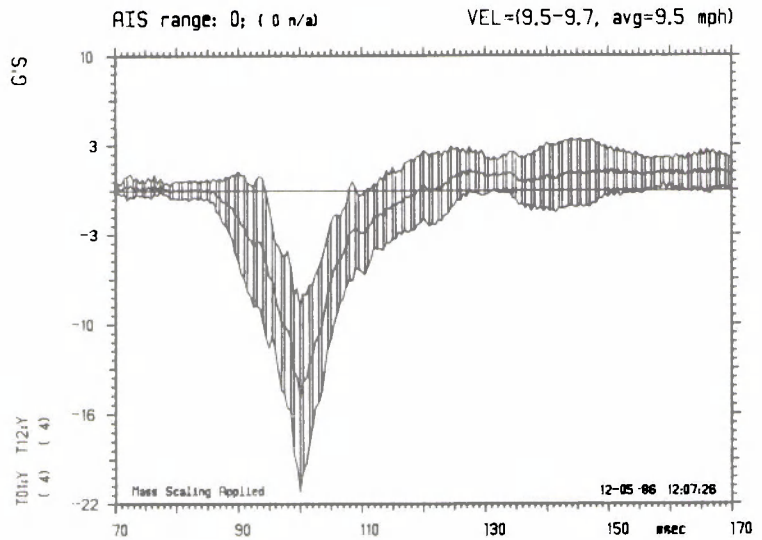

Spine (T1,T12) X
(Intermediate)

	Test ID	Xduc	Test Type
1.	76T062	T01:X	PEN: NON
2.	76T065	T01:X	PEN: NON
3.	77T074	T01:X	PEN: NON
4.	77T071	T01:X	PEN: NON
5.	77T071	T12:X	PEN: NON

Principle Peak: Mean +1 SD = 14.7
Mean = 6.0
Mean -1 SD = 0.8

Peak Time Shift: 0.0 ms

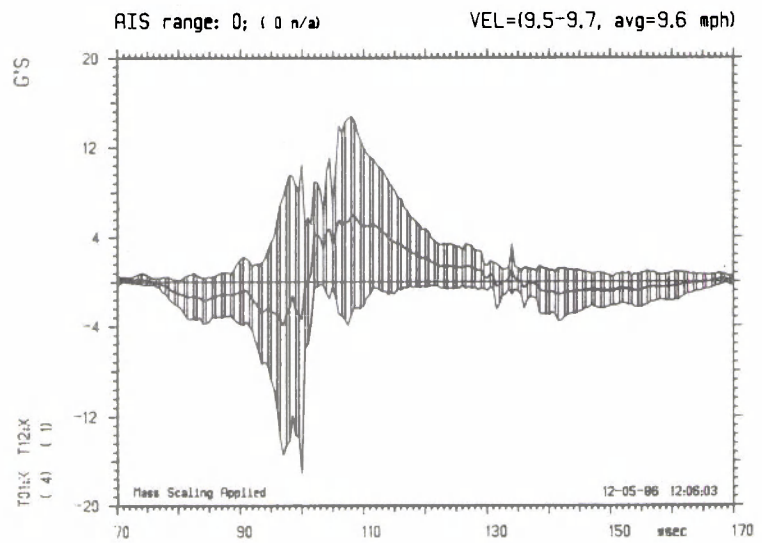

FIGURE 22. Thoracic response in lateral pendulum impactor tests (4.3 m/s).

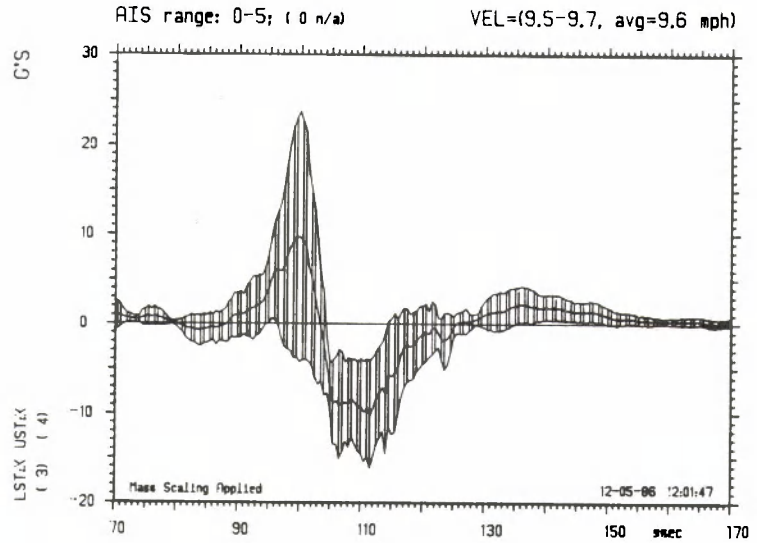

Sternum X
(Intermediate)

	Test ID	Xduc	Test Type
1.	761062	LST:X	PEN: NON
2.	771074	LST:X	PEN: NON
3.	771071	LST:X	PEN: NON
4.	761062	UST:X	PEN: NON
5.	761065	UST:X	PEN: NON
6.	771074	UST:X	PEN: NON
7.	771071	UST:X	PEN: NON

Principle Peak: Mean +1 SD = 23.7
Mean = 9.7
Mean -1 SD = 0.6

Peak Time Shift: 0.0 ms

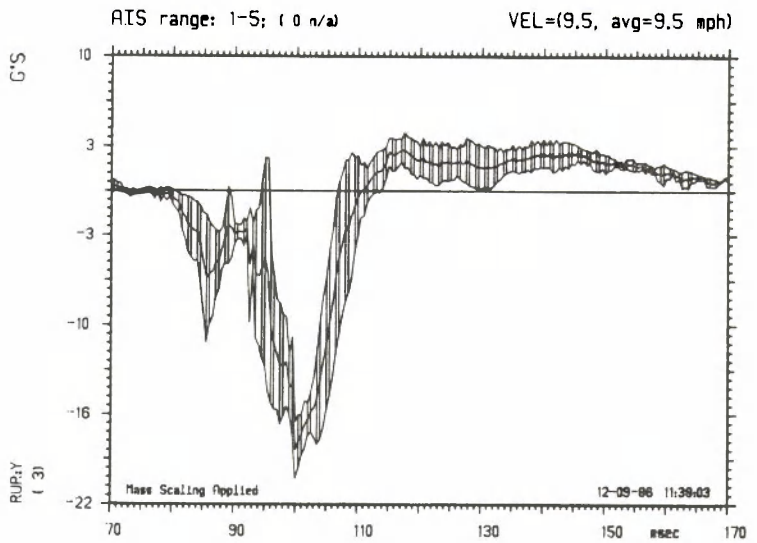

Right Upper Rib Y
(Far)

	Test ID	Xduc	Test Type
1.	761062	RUR:Y	PEN: NON
2.	761065	RUR:Y	PEN: NON
3.	771074	RUR:Y	PEN: NON

Principle Peak: Mean +1 SD = -16.5
Mean = -18.6
Mean -1 SD = -20.6

Peak Time Shift: 4.9 ms

FIGURE 22. (Continued).

Left Upper Rib Y
(Near)

	Test ID	Xduc	Test Type
1.	77T077	LUR:Y	PEN: NON
2.	77T080	LUR:Y	PEN: NON

Principle Peak: Mean +1 SD = -55.5
Mean = -79.0
Mean -1 SD = -171.9

Peak Time Shift: 0.0 ms

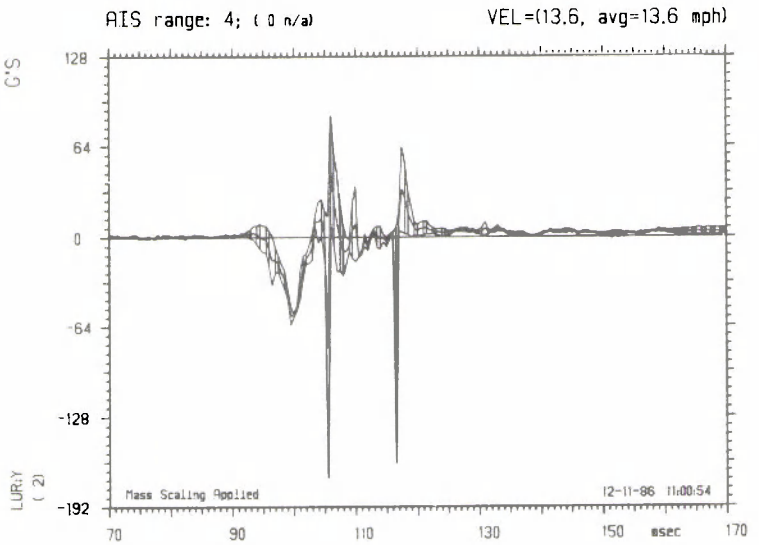

Spine (T1,T6,T12) Y
(Intermediate)

	Test ID	Xduc	Test Type
1.	77T077	T01:Y	PEN: NON
2.	77T080	T01:Y	PEN: NON
3.	80L112	T06:Y	PEN: NON
4.	80L100	T06:Y	PEN: NON
5.	80L132	T06:Y	PEN: NON
6.	80L122	T06:Y	PEN: NON
7.	77T080	T12:Y	PEN: NON

Principle Peak: Mean +1 SD = -4.9
Mean = -12.5
Mean -1 SD = -20.2

Peak Time Shift: 1.1 ms

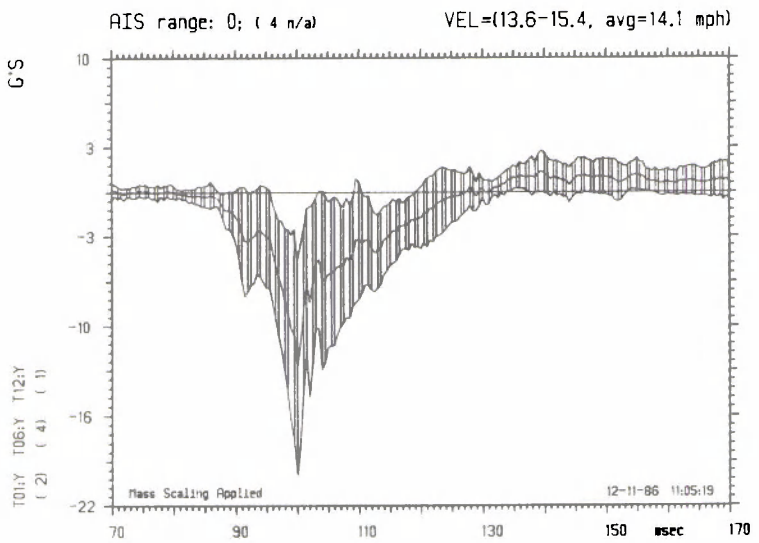

Spine (T1,T6,T12) X
(Intermediate)

	Test ID	Xduc	Test Type
1.	77T077	T01:X	PEN: NON
2.	77T080	T01:X	PEN: NON
3.	80L112	T06:X	PEN: NON
4.	80L100	T06:X	PEN: NON
5.	80L127	T06:X	PEN: NON
6.	77T080	T12:X	PEN: NON

Principle Peak: Mean +1 SD = -1.9
Mean = -8.3
Mean -1 SD = -14.9

Peak Time Shift: 0.0 ms

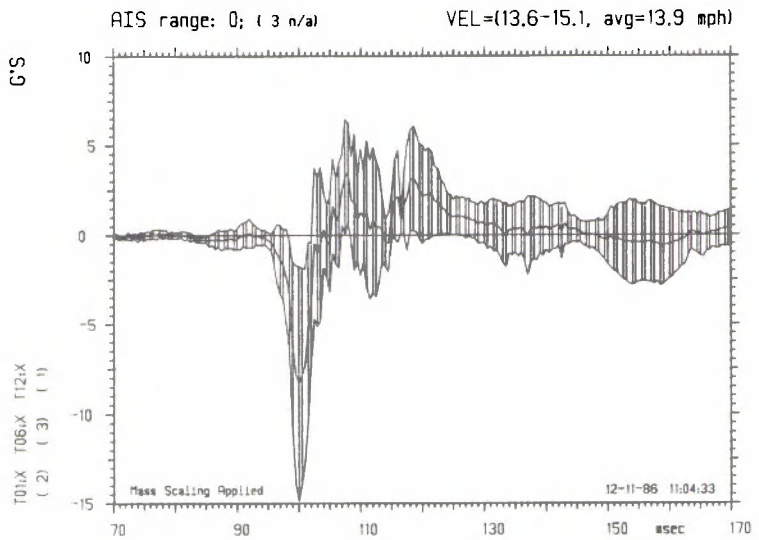

FIGURE 23. Thoracic response in lateral pendulum impactor tests (6.3 m/s).

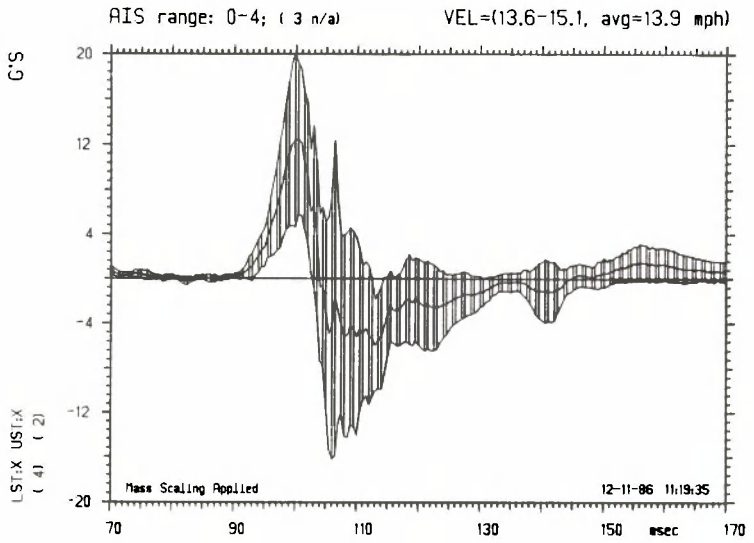

Sternum X
(Intermediate)

	Test ID	Xduc	Test Type
1.	771077	LST:X	PEN: NON
2.	80L112	LST:X	PEN: NON
3.	80L100	LST:X	PEN: NON
4.	80L132	LST:X	PEN: NON
5.	771077	UST:X	PEN: NON
6.	771080	UST:X	PEN: NON

Principle Peak: Mean +1 SD = 20.0
Mean = 12.5
Mean -1 SD = 5.8

Peak Time Shift: 2.1 ms

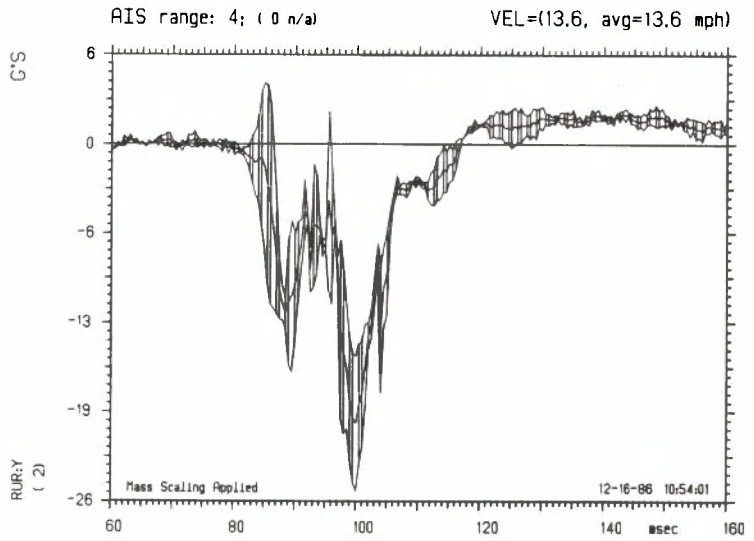

Right Upper Rib Y
(Far)

	Test ID	Xduc	Test Type
1.	771077	RLR:Y	PEN: NON
2.	771080	RLR:Y	PEN: NON

Principle Peak: Mean +1 SD = -15.2
Mean = -20.0
Mean -1 SD = -24.9

Peak Time Shift: 11.5 ms

FIGURE 23. (Continued).

Left Upper/Lower Rib Y (Near)

	Test ID	Xduc	Test Type
1.	H82016	LLR:Y	SLD: RIG
2.	H82020	LLR:Y	SLD: RIG
3.	H82014	LLR:Y	SLD: RIG
4.	H82021	LLR:Y	SLD: RIG
5.	H82022	LLR:Y	SLD: RIG
6.	H82015	LLR:Y	SLD: RIG
7.	H82016	LUR:Y	SLD: RIG
8.	H82020	LUR:Y	SLD: RIG
9.	76T010	LUR:Y	SLD: RIG
10.	H81025	LUR:Y	SLD: RIG
11.	H82002	LUR:Y	SLD: RIG
12.	H82014	LUR:Y	SLD: RIG
13.	H82021	LUR:Y	SLD: RIG
14.	H82022	LUR:Y	SLD: RIG
15.	76T011	LUR:Y	SLD: RIG
16.	77T089	LUR:Y	SLD: RIG
17.	77T092	LUR:Y	SLD: RIG
18.	H82015	LUR:Y	SLD: RIG

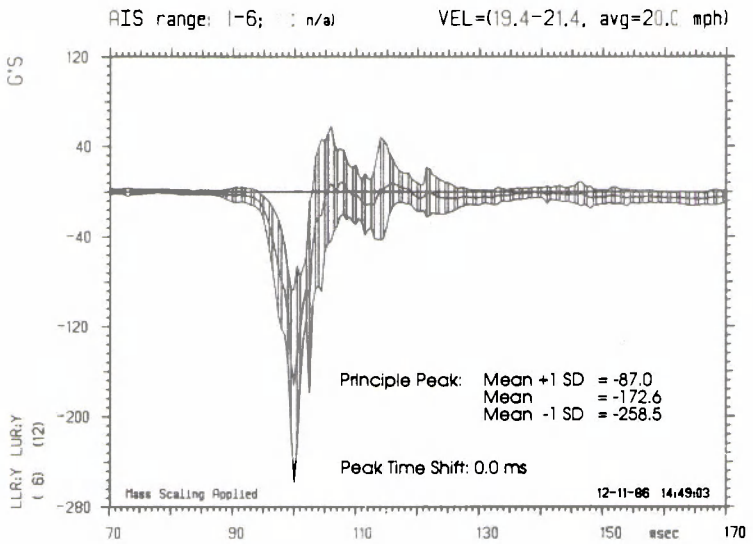

Spine (T1,T12) Y (Intermediate)

	Test ID	Xduc	Test Type
1.	H82016	T01:Y	SLD: RIG
2.	H82020	T01:Y	SLD: RIG
3.	H81025	T01:Y	SLD: RIG
4.	H82002	T01:Y	SLD: RIG
5.	H82014	T01:Y	SLD: RIG
6.	H82021	T01:Y	SLD: RIG
7.	H82022	T01:Y	SLD: RIG
8.	77T089	T01:Y	SLD: RIG
9.	77T092	T01:Y	SLD: RIG
10.	H82015	T01:Y	SLD: RIG
11.	H82016	T12:Y	SLD: RIG
12.	H82020	T12:Y	SLD: RIG
13.	76T010	T12:Y	SLD: RIG
14.	H81025	T12:Y	SLD: RIG
15.	H82002	T12:Y	SLD: RIG
16.	H82014	T12:Y	SLD: RIG
17.	H82021	T12:Y	SLD: RIG
18.	H82022	T12:Y	SLD: RIG
19.	76T011	T12:Y	SLD: RIG
20.	77T089	T12:Y	SLD: RIG
21.	77T092	T12:Y	SLD: RIG
22.	H82015	T12:Y	SLD: RIG

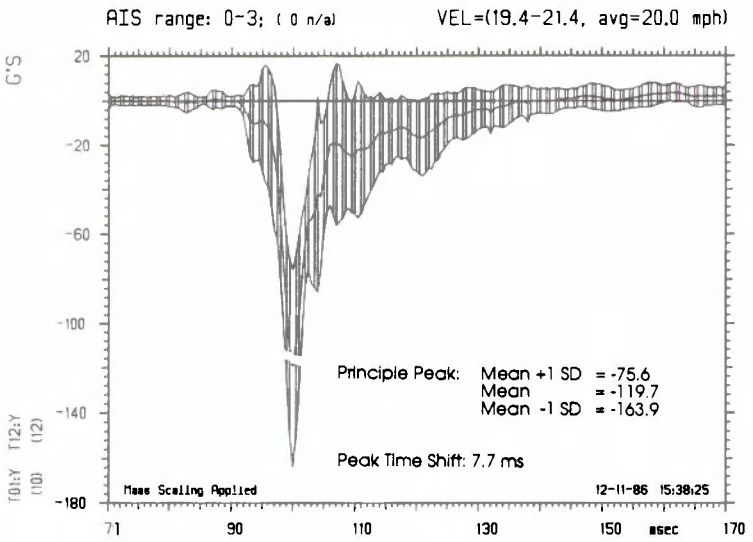

Spine (T1,T12) X (Intermediate)

	Test ID	Xduc	Test Type
1.	H82016	T01:X	SLD: RIG
2.	H82020	T01:X	SLD: RIG
3.	76T010	T01:X	SLD: RIG
4.	H81025	T01:X	SLD: RIG
5.	H82002	T01:X	SLD: RIG
6.	H82014	T01:X	SLD: RIG
7.	H82021	T01:X	SLD: RIG
8.	H82022	T01:X	SLD: RIG
9.	76T011	T01:X	SLD: RIG
10.	77T092	T01:X	SLD: RIG
11.	H82015	T01:X	SLD: RIG
12.	H82016	T12:X	SLD: RIG
13.	H82020	T12:X	SLD: RIG
14.	76T010	T12:X	SLD: RIG
15.	H81025	T12:X	SLD: RIG
16.	H82002	T12:X	SLD: RIG
17.	H82014	T12:X	SLD: RIG
18.	H82021	T12:X	SLD: RIG
19.	H82022	T12:X	SLD: RIG
20.	76T011	T12:X	SLD: RIG
21.	77T092	T12:X	SLD: RIG
22.	H82015	T12:X	SLD: RIG

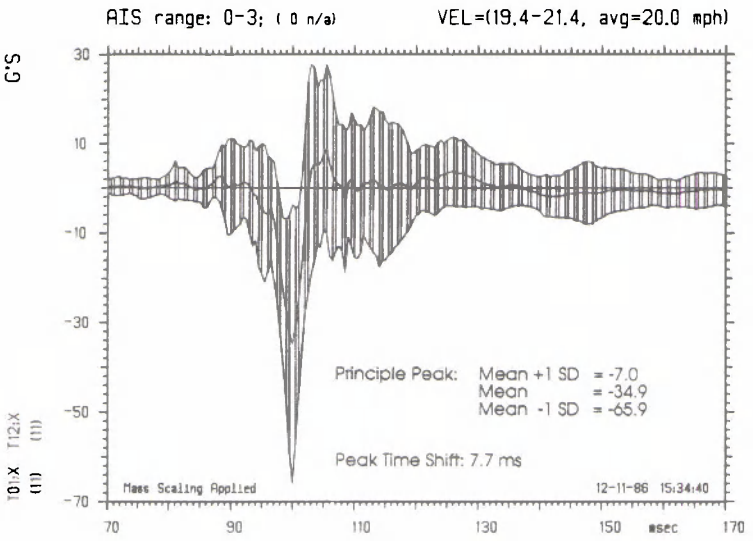

FIGURE 24. Thoracic response in lateral rigid wall tests (8.9 m/s).

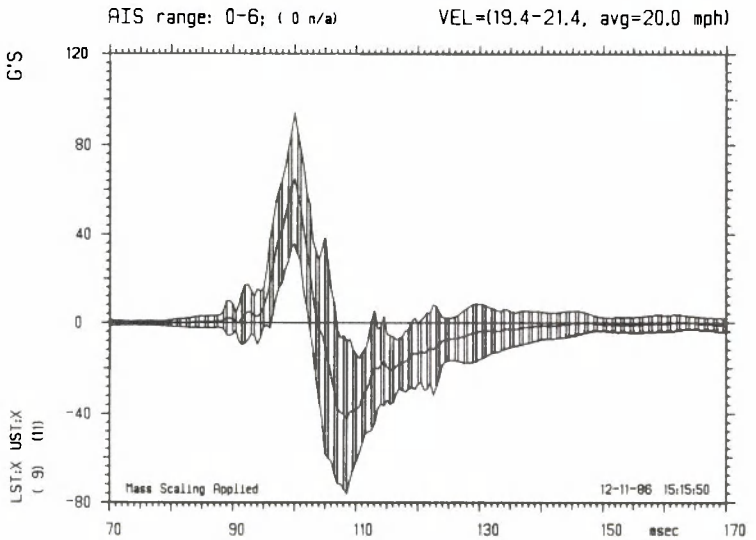

Sternum X
(Intermediate)

	Test ID	Xduc	Test Type
1.	H82020	LST:X	SLD: RIG
2.	76T010	LST:X	SLD: RIG
3.	H81025	LST:X	SLD: RIG
4.	H82002	LST:X	SLD: RIG
5.	H82014	LST:X	SLD: RIG
6.	H82021	LST:X	SLD: RIG
7.	H82022	LST:X	SLD: RIG
8.	76T011	LST:X	SLD: RIG
9.	H82015	LST:X	SLD: RIG
10.	H82016	UST:X	SLD: RIG
11.	H82020	UST:X	SLD: RIG
12.	76T010	UST:X	SLD: RIG
13.	H81025	UST:X	SLD: RIG
14.	H82002	UST:X	SLD: RIG
15.	H82014	UST:X	SLD: RIG
16.	H82021	UST:X	SLD: RIG
17.	H82022	UST:X	SLD: RIG
18.	76T011	UST:X	SLD: RIG
19.	77T092	UST:X	SLD: RIG
20.	H82015	UST:X	SLD: RIG

Principle Peak: Mean +1 SD = 94.1
Mean = 64.9
Mean -1 SD = 35.6

Peak Time Shift: 6.6 ms

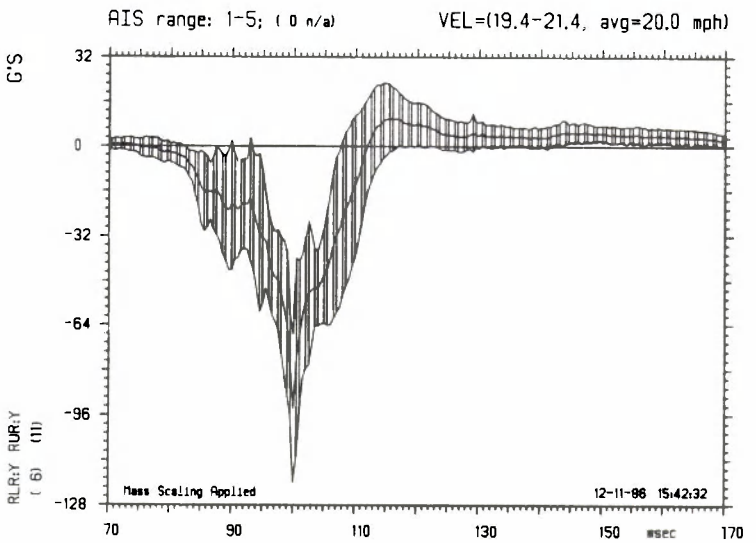

Right Upper/Lower Rib Y
(Far)

	Test ID	Xduc	Test Type
1.	H82016	RLR:Y	SLD: RIG
2.	H82020	RLR:Y	SLD: RIG
3.	H82014	RLR:Y	SLD: RIG
4.	H82021	RLR:Y	SLD: RIG
5.	H82022	RLR:Y	SLD: RIG
6.	H82015	RLR:Y	SLD: RIG
7.	H82016	RUR:Y	SLD: RIG
8.	H82020	RUR:Y	SLD: RIG
9.	76T010	RUR:Y	SLD: RIG
10.	H81025	RUR:Y	SLD: RIG
11.	H82002	RUR:Y	SLD: RIG
12.	H82014	RUR:Y	SLD: RIG
13.	H82021	RUR:Y	SLD: RIG
14.	H82022	RUR:Y	SLD: RIG
15.	77T089	RUR:Y	SLD: RIG
16.	77T092	RUR:Y	SLD: RIG
17.	H82015	RUR:Y	SLD: RIG

Principle Peak: Mean +1 SD = -67.4
Mean = -93.8
Mean -1 SD = -120.1

Peak Time Shift: 15.8 ms

FIGURE 24. (Continued).

Left Upper Rib Y
(Near)

	Test ID	Xduc	Test Type
1.	H81016	LUR:Y	SLD: RIG
2.	H81022	LUR:Y	SLD: RIG
3.	H81027	LUR:Y	SLD: RIG
4.	H82009	LUR:Y	SLD: RIG
5.	H82012	LUR:Y	SLD: RIG
6.	76T009	LUR:Y	SLD: RIG

Principle Peak: Mean +1 SD = -78.8
Mean = -175.9
Mean -1 SD = -317.2

Peak Time Shift: 0.0 ms

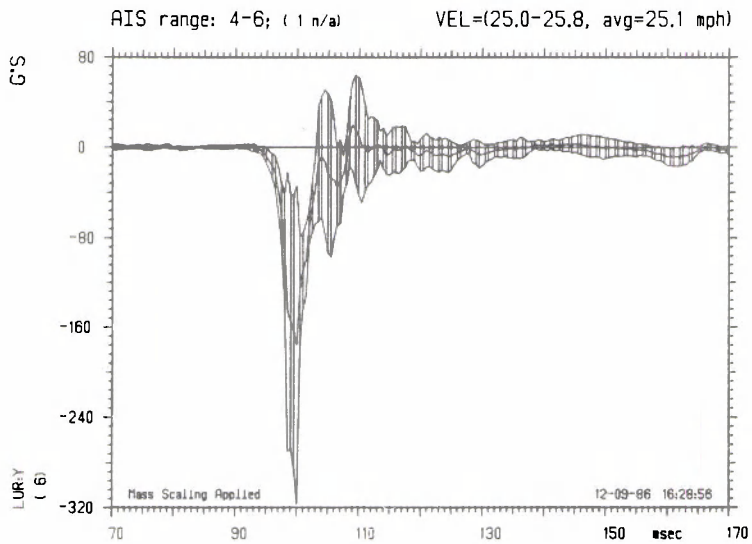

Spine (T1,T12) Y
(Intermediate)

	Test ID	Xduc	Test Type
1.	H81022	T01:Y	SLD: RIG
2.	H81027	T01:Y	SLD: RIG
3.	H82009	T01:Y	SLD: RIG
4.	H82012	T01:Y	SLD: RIG
5.	H81016	T1R:Y	SLD: RIG
6.	H81022	T12:Y	SLD: RIG
7.	H81027	T12:Y	SLD: RIG
8.	H82009	T12:Y	SLD: RIG
9.	H82012	T12:Y	SLD: RIG
10.	76T009	T12:Y	SLD: RIG
11.	H81016	T2R:Y	SLD: RIG

Principle Peak: Mean +1 SD = -98.9
Mean = -132.7
Mean -1 SD = -166.5

Peak Time Shift: 5.3 ms

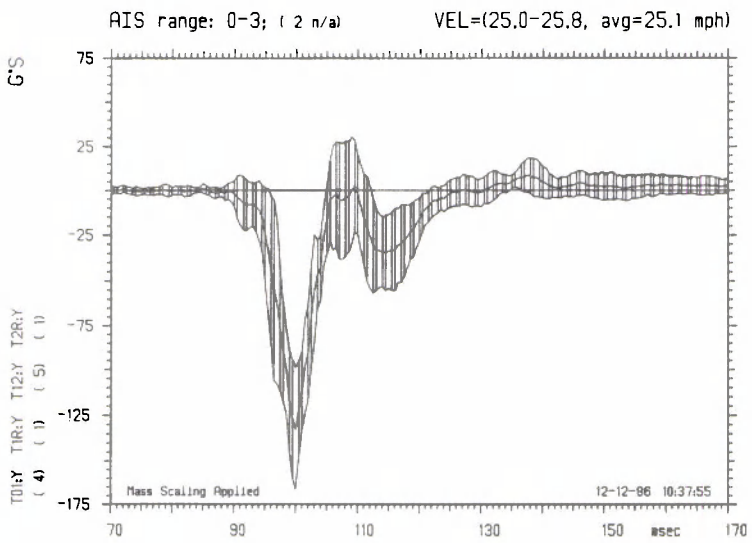

Spine (T1,T12) X
(Intermediate)

	Test ID	Xduc	Test Type
1.	H81022	T01:X	SLD: RIG
2.	H81027	T01:X	SLD: RIG
3.	H82009	T01:X	SLD: RIG
4.	H82012	T01:X	SLD: RIG
5.	76T009	T01:X	SLD: RIG
6.	H81016	T1P:X	SLD: RIG
7.	H81022	T12:X	SLD: RIG
8.	H81027	T12:X	SLD: RIG
9.	H82009	T12:X	SLD: RIG
10.	H82012	T12:X	SLD: RIG
11.	76T009	T12:X	SLD: RIG
12.	H81016	T2P:X	SLD: RIG

Principle Peak: Mean +1 SD = -39.2
Mean = -66.0
Mean -1 SD = -92.8

Peak Time Shift: 5.3 ms

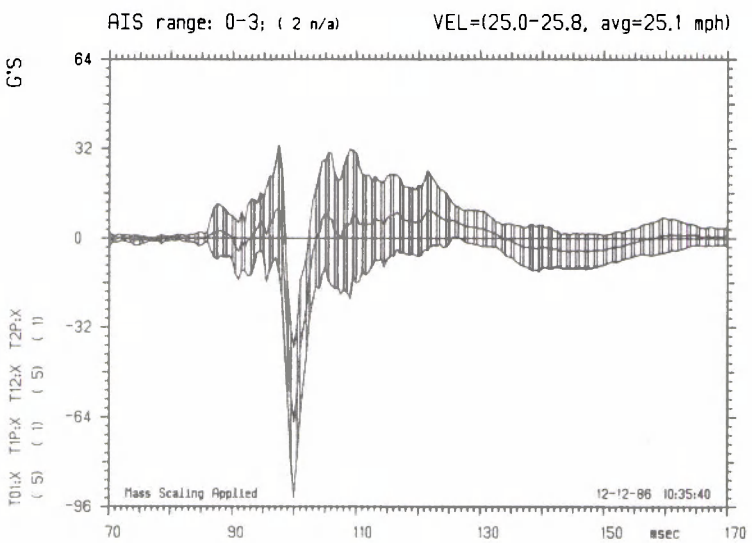

FIGURE 25. Thoracic response in lateral rigid wall tests (11.2 m/s).

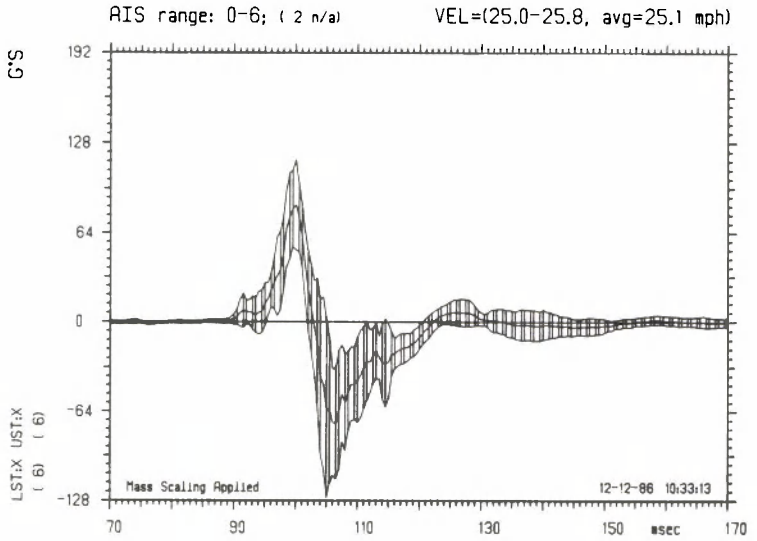

Sternum X
(Intermediate)

	Test ID	Xduc	Test Type
1.	H81016	LST:X	SLD: RIG
2.	H81022	LST:X	SLD: RIG
3.	H81027	LST:X	SLD: RIG
4.	H82009	LST:X	SLD: RIG
5.	H82012	LST:X	SLD: RIG
6.	76T009	LST:X	SLD: RIG
7.	H81016	UST:X	SLD: RIG
8.	H81022	UST:X	SLD: RIG
9.	H81027	UST:X	SLD: RIG
10.	H82009	UST:X	SLD: RIG
11.	H82012	UST:X	SLD: RIG
12.	76T009	UST:X	SLD: RIG

Principle Peak: Mean +1 SD = 116.3
Mean = 84.0
Mean -1 SD = 53.3

Peak Time Shift: 7.3 ms

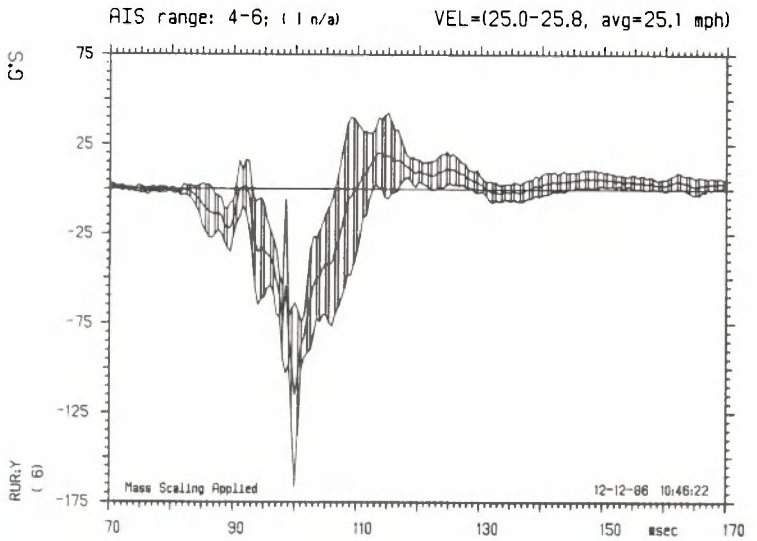

Right Upper Rib Y
(Far)

	Test ID	Xduc	Test Type
1.	H81016	RUR:Y	SLD: RIG
2.	H81022	RUR:Y	SLD: RIG
3.	H81027	RUR:Y	SLD: RIG
4.	H82009	RUR:Y	SLD: RIG
5.	H82012	RUR:Y	SLD: RIG
6.	76T009	RUR:Y	SLD: RIG

Principle Peak: Mean +1 SD = -74.6
Mean = -115.2
Mean -1 SD = -166.5

Peak Time Shift: 11.1 ms

FIGURE 25. (Continued).

Left Upper/Lower Rib Y (Near)

	Test ID	Xduc	Test Type
1.	H-83-010	LLR:Y	SLD: MCI
2.	H81015	LUR:Y	SLD: MCI
3.	H81021	LUR:Y	SLD: MCI
4.	76T029	LUR:Y	SLD: MCI
5.	H-83-010	LUR:Y	SLD: MCI

Principle Peak: Mean +1 SD = -50.3
Mean = -65.1
Mean -1 SD = -79.9

Peak Time Shift: 0.0 ms

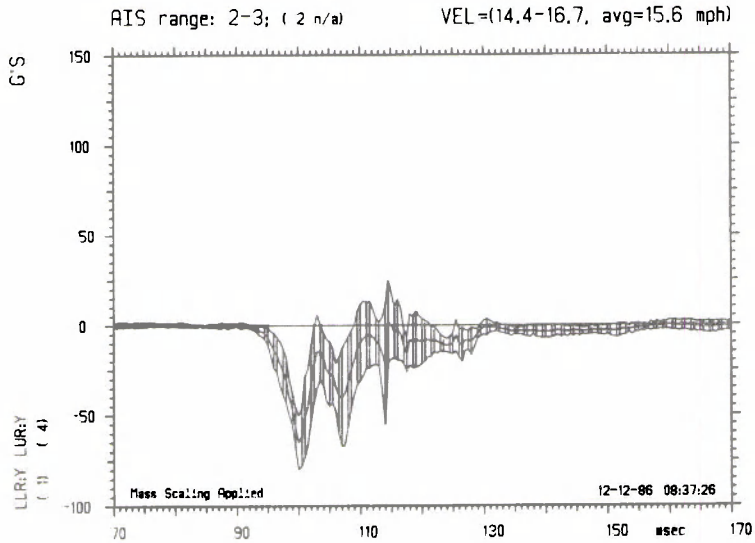

Spine (T1,T12) Y (Intermediate)

	Test ID	Xduc	Test Type
1.	H-83-010	T01:Y	SLD: MCI
2.	H81015	T1R:Y	SLD: MCI
3.	H81021	T1R:Y	SLD: MCI
4.	76T029	T12:Y	SLD: MCI
5.	H-83-010	T12:Y	SLD: MCI
6.	H81015	T2R:Y	SLD: MCI
7.	H81021	T2R:Y	SLD: MCI

Principle Peak: Mean +1 SD = -37.9
Mean = -49.5
Mean -1 SD = -119.3

Peak Time Shift: 6.3 ms

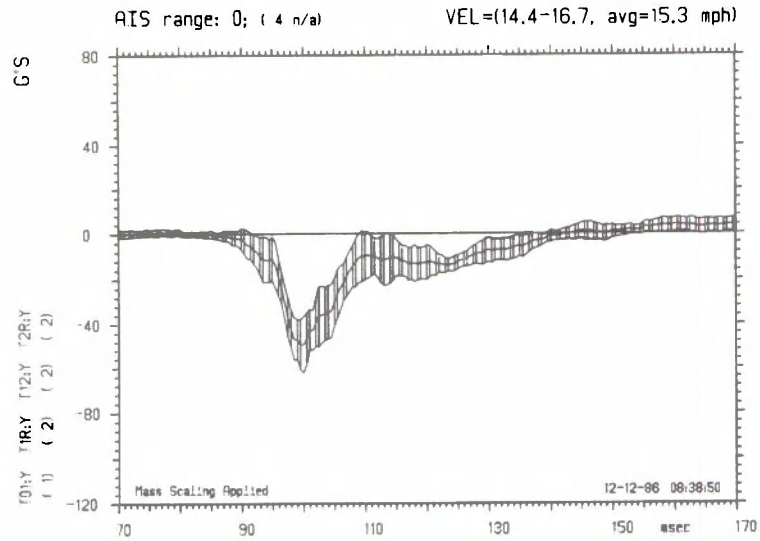

Spine (T1,T12) X (Intermediate)

	Test ID	Xduc	Test Type
1.	76T029	T01:X	SLD: MCI
2.	H81015	T1P:X	SLD: MCI
3.	H81021	T1P:X	SLD: MCI
4.	76T029	T12:X	SLD: MCI
5.	H-83-010	T12:X	SLD: MCI
6.	H81015	T2P:X	SLD: MCI
7.	H81021	T2P:X	SLD: MCI

Principle Peak: Mean +1 SD = -8.9
Mean = -14.6
Mean -1 SD = -20.3

Peak Time Shift: 6.3 ms

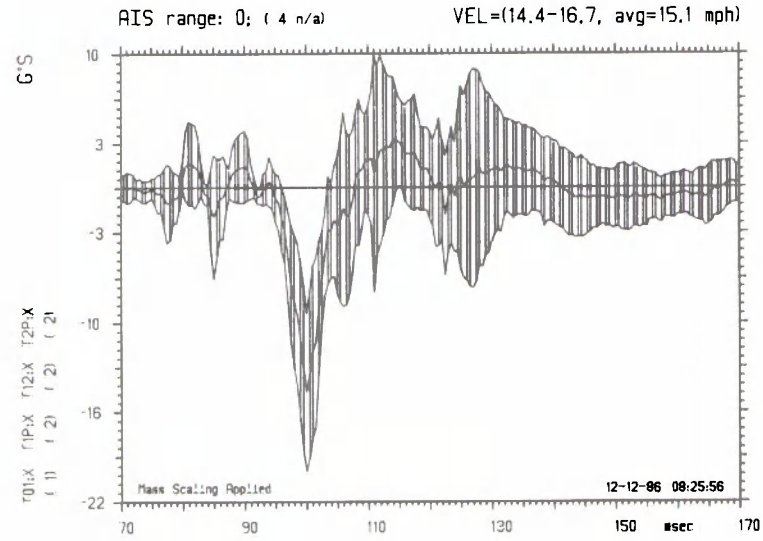

FIGURE 26. Thoracic response in lateral padded wall tests (6.7 m/s).

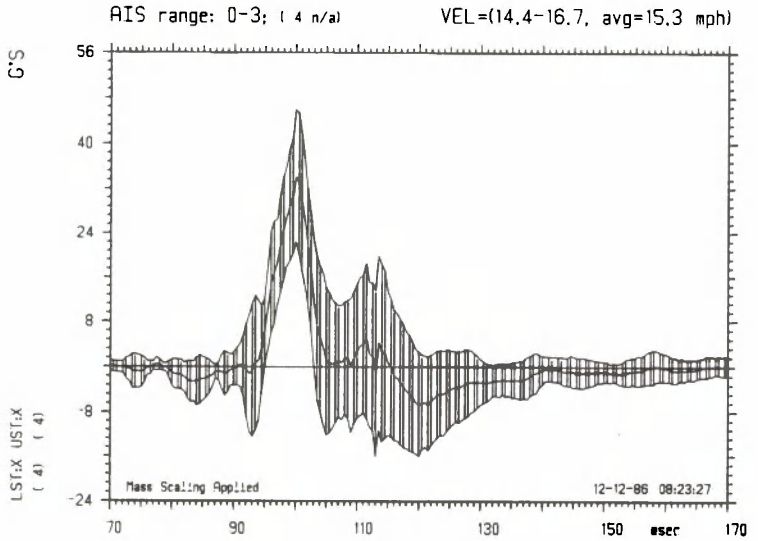

Sternum X
(Intermediate)

	Test ID	Xduc	Test Type
1.	H81015	LST:X	SLD: MCI
2.	H81021	LST:X	SLD: MCI
3.	76T029	LST:X	SLD: MCI
4.	H-83-010	LST:X	SLD: MCI
5.	H81015	UST:X	SLD: MCI
6.	H81021	UST:X	SLD: MCI
7.	76T029	UST:X	SLD: MCI
8.	H-83-010	UST:X	SLD: MCI

Principle Peak: Mean +1 SD = 45.9
Mean = 34.1
Mean -1 SD = 22.3

Peak Time Shift: 4.9 ms

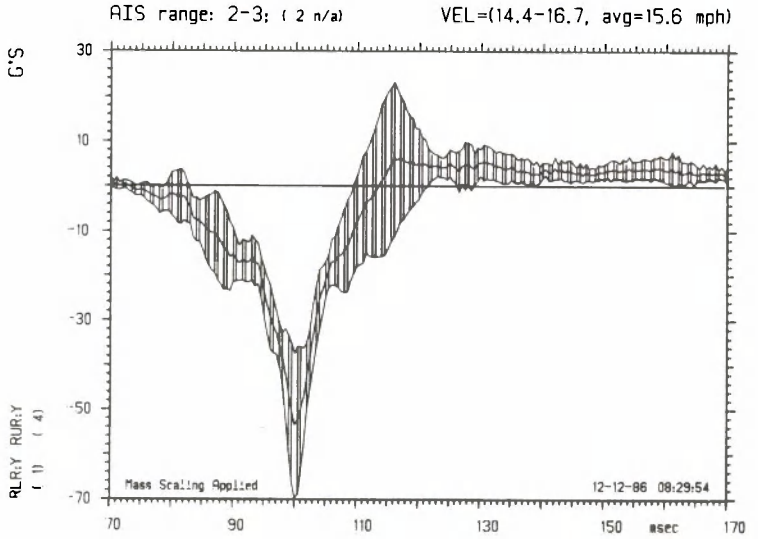

Right Upper/Lower Rib Y
(Far)

	Test ID	Xduc	Test Type
1.	H-83-010	RLR:Y	SLD: MCI
2.	H81015	RUR:Y	SLD: MCI
3.	H81021	RUR:Y	SLD: MCI
4.	76T029	RUR:Y	SLD: MCI
5.	H-83-010	RUR:Y	SLD: MCI

Principle Peak: Mean +1 SD = -37.5
Mean = -53.6
Mean -1 SD = -69.7

Peak Time Shift: 17.9 ms

FIGURE 26. (Continued).

Left Upper/Lower Rib Y (Near)

	Test ID	Xduc	Test Type
1	H-83-012	LLR:Y	SLD: MCI
2	H-83-020	LLR:Y	SLD: MCI
3	76T034	LUR:Y	SLD: MCI
4	H-83-011	LUR:Y	SLD: MCI
5	H-83-012	LUR:Y	SLD: MCI
6	H-83-020	LUR:Y	SLD: MCI
7	H81011	LUR:Y	SLD: MCI
8	H81012	LUR:Y	SLD: MCI
9	77T095	LUR:Y	SLD: MCI
10	77T098	LUR:Y	SLD: MCI

Principle Peak: Mean +1 SD = -49.6
Mean = -83.6
Mean -1 SD = -125.4

Peak Time Shift: 0.0 ms

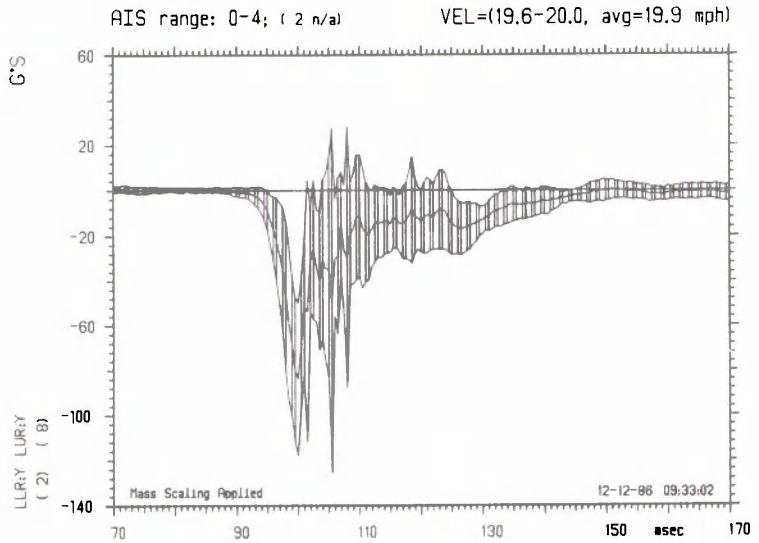

Spine (T1,T12) Y (Intermediate)

	Test ID	Xduc	Test Type
1.	H-83-012	T01:Y	SLD: MCI
2.	H-83-020	T01:Y	SLD: MCI
3.	77T095	T01:Y	SLD: MCI
4.	77T098	T01:Y	SLD: MCI
5.	H81011	T1R:Y	SLD: MCI
6.	H81012	T1R:Y	SLD: MCI
7.	76T034	T12:Y	SLD: MCI
8.	H-83-011	T12:Y	SLD: MCI
9.	H-83-012	T12:Y	SLD: MCI
10.	H-83-020	T12:Y	SLD: MCI
11.	76T039	T12:Y	SLD: MCI
12.	77T095	T12:Y	SLD: MCI
13.	77T098	T12:Y	SLD: MCI
14.	H81011	T2R:Y	SLD: MCI
15.	H81012	T2R:Y	SLD: MCI

Principle Peak: Mean +1 SD = -61.4
Mean = -83.1
Mean -1 SD = -104.8

Peak Time Shift: 7.1 ms

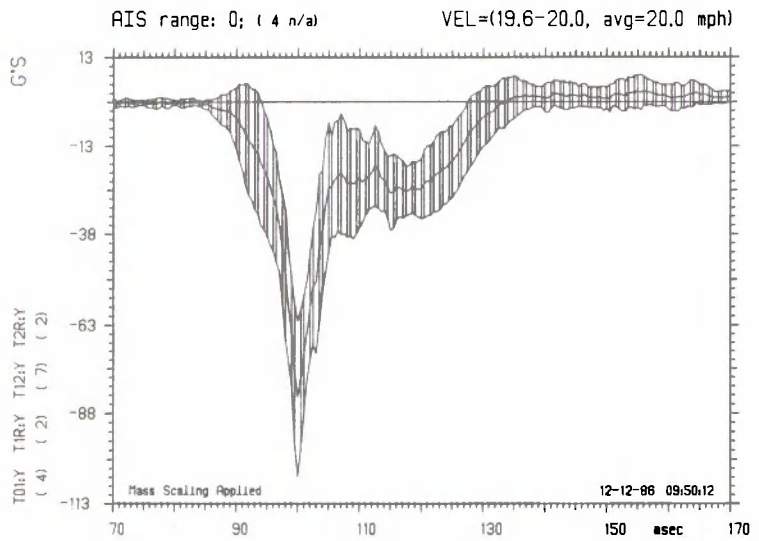

Spine (T1,T12) X (Intermediate)

	Test ID	Xduc	Test Type
1.	H-83-012	T01:X	SLD: MCI
2.	77T095	T01:X	SLD: MCI
3.	H81011	T1P:X	SLD: MCI
4.	H81012	T1P:X	SLD: MCI
5.	76T034	T12:X	SLD: MCI
6.	H-83-011	T12:X	SLD: MCI
7.	H-83-012	T12:X	SLD: MCI
8.	H-83-020	T12:X	SLD: MCI
9.	77T095	T12:X	SLD: MCI
10.	77T098	T12:X	SLD: MCI
11.	H81011	T2P:X	SLD: MCI
12.	H81012	T2P:X	SLD: MCI

Principle Peak: Mean +1 SD = -14.4
Mean = -25.0
Mean -1 SD = -36.4

Peak Time Shift: 7.1 ms

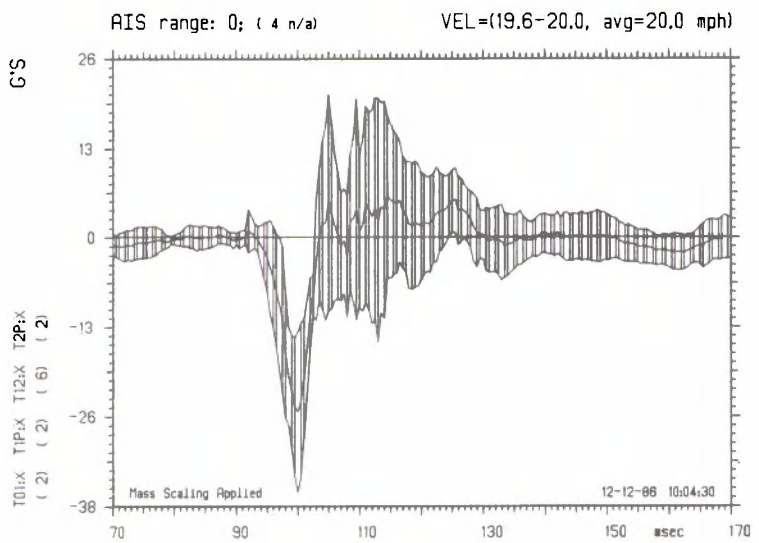

FIGURE 27. Thoracic response in lateral padded wall tests (8.9 m/s).

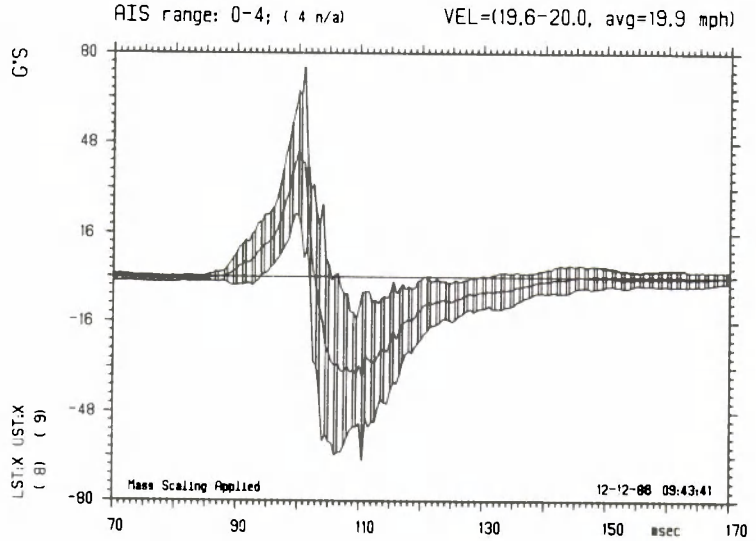

Sternum X
(Intermediate)

	Test ID	Xduc	Test Type
1.	76T034	LST:X	SLD: MCI
2.	H-83-011	LST:X	SLD: MCI
3.	H-83-012	LST:X	SLD: MCI
4.	H-83-020	LST:X	SLD: MCI
5.	H81011	LST:X	SLD: MCI
6.	H81012	LST:X	SLD: MCI
7.	77T095	LST:X	SLD: MCI
8.	77T098	LST:X	SLD: MCI
9.	76T034	UST:X	SLD: MCI
10.	H-83-011	UST:X	SLD: MCI
11.	H-83-012	UST:X	SLD: MCI
12.	H-83-020	UST:X	SLD: MCI
13.	H81011	UST:X	SLD: MCI
14.	H81012	UST:X	SLD: MCI
15.	76T039	UST:X	SLD: MCI
16.	77T095	UST:X	SLD: MCI
17.	77T098	UST:X	SLD: MCI

Principle Peak: Mean +1 SD = 74.8
Mean = 44.4
Mean -1 SD = 22.9

Peak Time Shift: 14.9 ms

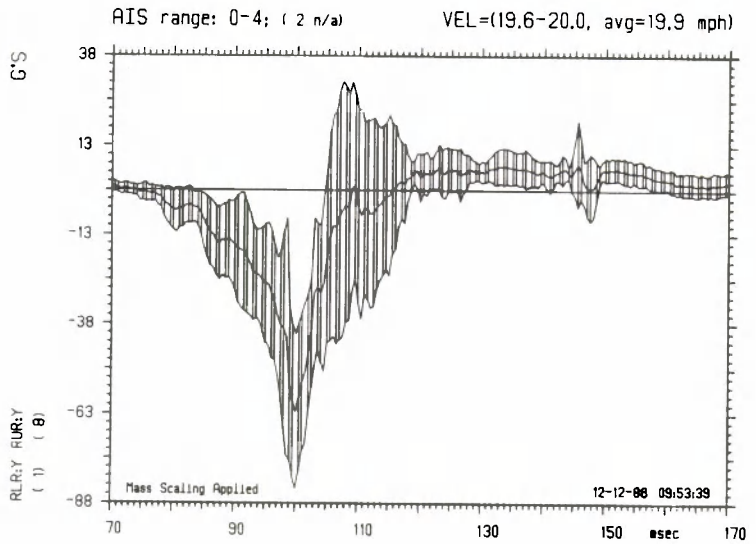

Right Upper/Lower Rib Y
(Far)

	Test ID	Xduc	Test Type
1.	H-83-020	RLR:Y	SLD: MCI
2.	76T034	RUR:Y	SLD: MCI
3.	H-83-011	RUR:Y	SLD: MCI
4.	H-83-012	RUR:Y	SLD: MCI
5.	H-83-020	RUR:Y	SLD: MCI
6.	H81011	RUR:Y	SLD: MCI
7.	H81012	RUR:Y	SLD: MCI
8.	76T039	RUR:Y	SLD: MCI
9.	77T098	RUR:Y	SLD: MCI

Principle Peak: Mean +1 SD = -40.3
Mean = -61.9
Mean -1 SD = -83.6

Peak Time Shift: 19.1 ms

FIGURE 27. (Continued).

Thoracic Design Concepts (Refer to Figure 3, p.15). The thoracic design concept is based on the observations that static response of the human thorax represents the behavior of the rib cage, while the dynamic response is dominated by inertial and viscous behavior of the thoracic soft tissue. The rib cage also serves to distribute load. With these observations in mind, the thorax structure will have a thin, flexible, monolithic shell to define its shape and to provide load distribution. The shell is not intended to resist the applied loads but only serves to distribute the forces over underlying structures. It will therefore not have a significant influence on overall thoracic response.

The response elements in the thorax will be an array of fluid-filled bag compartments within the shell. Each bag will be constructed of cord-reinforced rubber and will represent a flexible, constant-volume reservoir. There will be five compartments on each of two levels, dividing the chest into upper and lower levels with frontal, lateral, and oblique sections. The fluid in each compartment will communicate through an orifice to a common gas-pressure-controlled reservoir (accumulator). The accumulator structure will be part of the rigid spine structures. One-way flow-control valves will be provided in the passages from the individual compartments to the common reservoir to prevent flow from one compartment to another instead of into the accumulator. The bag volumes, the accumulator fluid volume and gas volume, the accumulator initial gas pressure, and the orifice sizes will be adjusted to produce the desired thoracic static (gas pressure-volume characteristic) and dynamic (fluid-flow resistance and inertia) responses. The compartmentalization of the chest structure will allow positional variation of local response in order to better match human response to asymmetric loads, such as those from shoulder belts in frontal crashes or steering wheels in oblique crashes.

Each compartment will have a pressure transducer mounted in it, as will the gas section of the accumulator. The compartment transducers will indicate the region of loading and the loading rate (related to the flow rate) from the resistance to flow. The central accumulator gas pressure will indicate total global deformation of the chest independent of the region or direction of loading. The use of well-defined materials, such as silicone fluids and nitrogen gas, to control response will minimize repeatability, reproducibility, and temperature-sensitivity problems. These materials will also produce a very durable response-control system, since overloading or excess deformation of the system cannot damage its elastic or viscous elements. The expected peak unit pressures in the system are expected to be less than 690 kPa (100 psi), well within the capability of the structures involved.

The fluid-filled chest concept also allows the potential for a new injury assessment technique to be developed. Because the energy of deformation applied to the chest will result in fluid flow and resulting volume changes, the pressure transducers in the chest can be used to directly measure the energy of deformation of the chest. This quality, and particularly its viscous component, have been related to internal organ injury under simple experimental conditions. The fluid-filled chest would allow the application of this criteria to the more complicated general loading conditions found in crash testing. Making the transition from conventional injury assessment measures, such as rib-cage and spinal accelerations, to a totally new concept will require some intermediate steps in order to develop confidence in the new method. This will be accomplished during the development of the thoracic structure. Since the thoracic response specifications are based on test data that were instrumental in formulating conventional injury assessment measures (such as peak rib-cage deflection) as well as the viscous injury criteria and acceleration-based criteria, the development data from the pressure transducers can be correlated with the conventional measures during response development. This is also true of the whole-body acceleration specifications. Thus, the new injury assessment techniques can be compared

and correlated with the present criteria to allow the new measures to be evaluated during the thoracic response development process.

An alternative thoracic design concept would involve a more traditional ATD thoracic design using a rib-cage structure to provide the elastic static response. The main difference from present designs would be that the rib cage would not provide the major dynamic response. This should eliminate the present problems with overstressing such structures. The rib concept may allow spring steel to be used, but if the stresses are too great, fiber-reinforced composite ribs may be necessary.

The dynamic viscous and inertial response would be accomplished by a simple thoracic cage insert consisting of a deformable elastomeric bag filled with a fluid or a viscoelastic soft polymer, such as Sorbothane®. Deformation transduction would not be global, as with the first design concept, but rather at selected sites, possibly through the use of strain gauges on the ribs. A twelve-accelerometer array could also be attached to the ribs for injury assessment. Although possibly simpler in concept, this second design would not offer as complete a solution to the present problems with ATD thoracic designs that the first concept would offer.

ABDOMEN

The general geometric specifications for the AATD abdomen include the following dimensions.

Waist breadth (at umbilicus)	31.5 cm
Waist depth (at umbilicus)	25.2 cm
Waist circumference (at umbilicus)	91.7 cm
Abdominal breadth (maximum)	32.6 cm
Abdominal depth (maximum)	26.0 cm
Abdominal circumference (maximum)	94.7 cm

The coordinates and orientation of the related anatomical coordinate system, the coordinates of the abdominal center of gravity, and the orientation of the principal axes of inertia with respect to the anatomical axes are given in Robbins (1983). The mass and mass moments of inertia for the abdomen are given in Tables 3 and 4.

The biomechanical response of the abdomen to direct impact has received little attention in the literature. Walfisch et al. (1980) conducted lateral whole-body drop tests using a 7-cm (2.76-in) wide simulated rigid armrest. Stalnaker and Ulman (1985) have recently analyzed a series of frontal and lateral abdominal impacts to subhuman primates for the purpose of defining human abdominal impact response through the use of scaling. The Walfisch et al. (1980) test results were used to check the scaled data. Little difference was found between frontal and lateral impact response.

Stalnaker and Ulman found that the typical dynamic abdominal force-deflection characteristics could be described in terms that are very similar to those of thoracic response, namely, an initial rapid rise in force with little deformation, followed by a plateau region where the mean force remains generally constant, and finally, a region of increasing force but at a rate that is lower than the initial rising force region. The subhuman primate data were produced at relatively high impact velocities (on the order of 10 to 15 m/s). The data were adjusted within species using equal-stress/equal-velocity scaling relations. However, the scaling among species as well as the extrapolation to the human were based on linear regression techniques that included a direct proportionality between subject mass and the response parameters (plateau force and final region stiffness). Since the purpose of their regression analysis was to scale the data to fit the anthropometry of man, it would seem that a better method would be to use the equal-stress/equal-velocity scaling to achieve this extrapolation. Table 15 lists the pertinent factors from the Stalnaker and Ulman analysis along with forces and stiffnesses scaled according to dimensional analysis. The forces were scaled by the factor $(\lambda_m)^{2/3}$ and the stiffnesses by the factor $(\lambda_m)^{1/3}$. The mean scaled plateau force of 3709 N (834 lb) and the mean scaled final region stiffness of 813 N/cm (464 lb/in) are both considerably lower than the Stalnaker and Ulman values of 5391 N (1212 lb) and 2047 N/cm (1169 lb/in), respectively.

The Stalnaker and Ulman work used the Part 572 ATD anthropometry to normalize their data. The abdominal dimensions of the AATD are somewhat greater than those of the Part 572 ATD, and thus require adjustment of the deflection limit values. The authors gave limit values for abdominal-penetration associated with spinal contact as 60% body compression for frontal impacts and 45% body compression for lateral impacts. For the AATD, the corresponding limits are 15.6 cm (6.1 in) frontal and 14.7 cm (5.8 in) lateral. The limits for the end of the plateau region were given as 27% body compression for frontal impacts and 23% body compression for lateral impacts. The resulting AATD values are 7.0 cm (2.76 in) for frontal impacts and 7.5 cm (2.95 in) for lateral impacts.

TABLE 15

SCALED ABDOMINAL IMPACT RESPONSE PARAMETERS

Subject	Avg.* Subject Mass (m_s) (kg)	λ_m (77.5/m_s)	Avg.* Plateau Force (N)	Scaled Plateau Force (N)	Avg.* Final Region Stiff. (N/cm)	Scaled Final Region Stiffness (N/cm)	Avg. Velocity (m/s)
Squirrel, Monkey	0.60	129.2	159	4064	197	996	10.15
Vervet Monkey	3.55	21.8	492	3839	210	586	11.57
Rhesus Monkey	5.10	15.2	547	3356	296	733	12.03
Baboon	15.45	5.0	1223	3576	547	935	14.17
Man	77.50	1	—	3709 (mean)	—	813 (mean)	11.98 (mean)

*Data from Stalnaker and Ulman (1985).

Some problems remain with the interpretation of both abdominal impact studies for the purpose of defining the AATD test conditions. Stalnaker and Ulman do not specify a loading surface geometry for their human moving-mass impact corridors. Walfisch et al. used an unusual drop test method in which the interaction of the body and the simulated armrest was limited to the depth of the armrest. This technique restricted the penetration and supported the surrounding body mass in an undefined manner. In addition, the 7-cm (2.76-in) armrest (measured with respect to the anatomical Z-axis) most certainly loaded the lower rib cage as well as the abdomen. The problems associated with interpreting these tests for AATD specifications are similar in some ways to those discussed in relation to the APR whole-body lateral chest-impact drop tests. The test technique may be useful for evaluating a complete ATD but is not as useful for defining basic response characteristics.

The frontal impacts of the Stalnaker and Ulman paper were all conducted with a loading surface that was wider than the abdominal breadth but narrow in height, so that it loaded the abdomen like a misplaced lap belt or a steering wheel rim. If an impactor shape is to be used for both lateral and frontal abdominal impacts, it must be able to clear the rib cage and the pelvis in a lateral impact. This consideration would limit the impactor height to about 4 cm (1.58 in). Abdominal breadth considerations would require at least a length of 35 cm to ensure full contact across the front of the abdomen. A 4- by 35-cm flat rigid impactor surface and a 10.0-kg (22-lb) mass would be consistent with the Stalnaker and Ulman data base.

The Walfisch et al. data demonstrate some rate sensitivity at the two drop velocities. Since the Stalnaker and Ulman analysis indicates the characteristic force-deflection response of a rate sensitive system like the thorax, it is reasonable to assume a linear sensitivity of the plateau force to impact velocity.

Based on the above considerations, the AATD abdominal response corridors for three impact velocities can be defined in the same way that the AATD thoracic force–deflection corridors have been defined, with a single corridor for both lateral and frontal response. Figure 28 shows the resulting corridors for three impactor velocities. They include mean response lines with ±15% ranges. Table 16 lists the values used to define the curves. The resulting static limit force–deflection response is very similar to that of the lateral chest response (Figure 17). Thus, the bilinear static limit response could be replaced by the nonlinear response given above for the lateral chest response. The dynamic abdominal loading characteristics are considerably lower, however, than the lateral chest characteristics. The unloading phase of the abdominal response should produce a hysteresis ratio of more than 75% but less than 85%.

TABLE 16

AATD IDEALIZED ABDOMINAL IMPACT RESPONSE PARAMETERS
(Rigid bar impactor, 4 cm by 35 cm, 10.0 kg)

Impactor Vel (m/s)	S_{AI} (kN/cm)	F_P (kN)	d_{PI} (cm)	d_{PF} (cm)
4.3	0.67±0.10	1.33±0.20	2.0	4.32
6.7	1.04±0.16	2.07±0.31	2.0	5.23
12.0	1.86±0.28	3.71±0.56	2.0	7.25

Abdominal Design Concepts (Refer to Figure 3, p.15). The similarity of the response of the abdomen to that of the thorax leads to the concept of an abdominal structure with features that are similar to those of the thorax. The flexible outer shell material of the thoracic design will not be used, however, just the fluid-filled compartments. Only three compartments are needed: two lateral and one frontal. The same accumulator method will be used, with the accumulator structure housed in the lumbar spine segment. The control pressures and the fluid and gas volumes will be adjusted for the less stiff abdominal dynamic response. The outer covering of the abdomen will be softer than the shell of the thorax, will not provide any load distribution function, and will function only to provide a continuous surface over the individual fluid compartments.

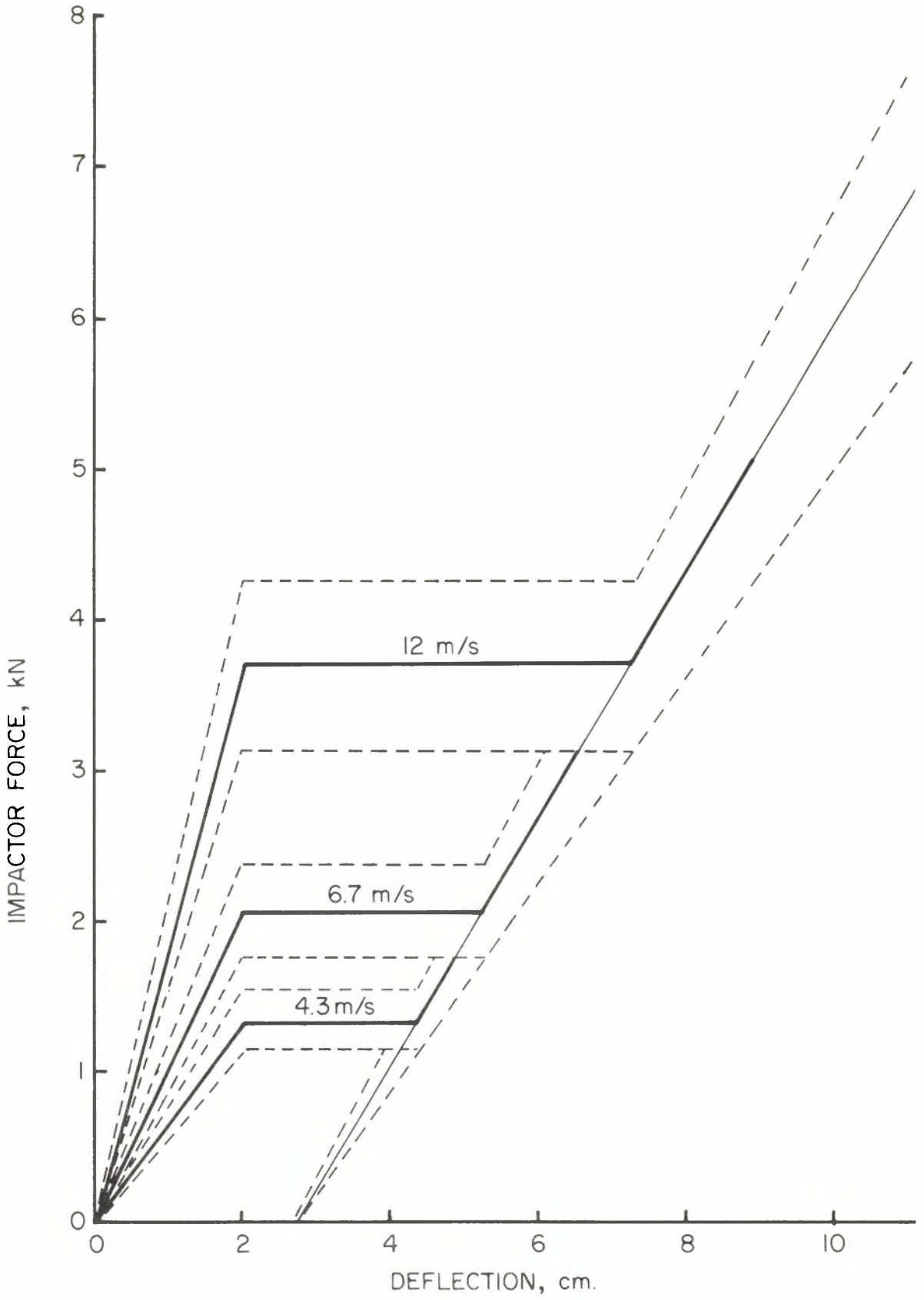

FIGURE 28. AATD abdominal impact response, frontal and lateral (rigid bar impactor 4- by 35-cm and 10-kg mass).

PELVIS

The general geometric specifications for the AATD pelvis include the following dimensions:

Hip breadth	39.4 cm
Hip circumference	94.4 cm
Pelvic length	23.5 cm
Bispinous breadth	22.5 cm

The coordinates and orientation of the pelvic anatomical coordinate system, the coordinates of the pelvic center-of-gravity, as well as the orientation of the principal axes of inertia with respect to the anatomical axes are given in Robbins (1983). The mass and mass moments of inertia for the pelvic region are given in Tables 3 and 4.

The pelvis of the seated vehicle occupant does not usually sustain direct impact loads in a frontal crash. Rather, the pelvis is loaded indirectly through knee-femur impacts or directly loaded by a restraint system such as a lap belt. Lap belt loading produces low loading rates, which in combination with the stiff nature of the adult pelvis, result in a rigid body response of the pelvic structure under such conditions. In lateral impacts, however, the pelvis may be exposed to direct loading. The nature of the forces produced in lateral impacts to the pelvis is determined by the mass and structural characteristics of the pelvic region as well as by the mechanical properties of the striking surface. Nusholtz et al. (1982) found that, for padded lateral impacts to the hip, the pelvic region impact impedance was mass-like up to frequencies of 50 Hz. The scaled effective mass value from the mean of three test subjects was 27 kg (59.4 lb). This value is over twice as great as the pelvic segment mass of 11.53 kg (25.37 lb) from Table 3. In an analysis of whole-body lateral rigid-wall cadaver tests, Marcus et al. (1983) found that 28% of the total body mass acted upon the wall-mounted pelvic loading surface. For the AATD, this would correspond to an effective mass of 21.7 kg (47.7 lb). Thus, the coupling of other body regions, primarily the upper legs and abdomen, adds to the effective mass of the pelvic region during lateral wall impacts.

Haffner (1985) has developed a simple linear dynamic model of the lateral pelvis structural response consisting of two masses connected by a parallel spring and damper combination. The model constants were developed from fitting two of the Heidelberg wall tests, in which both pelvic load and acceleration were measured. The struck-side upper-leg/pelvis mass was found to be 5.2 kg (11.4 lb), and the remaining "pelvic" mass was found to be 9.3 kg (20.4 lb). The spring constant was 5.25 kN/cm (3000 lb/in), and the damping constant was 0.035 kN·s/cm (20 lb·s/in). The total mass of the model, then is 14.5 kg (31.8 lb), which is slightly lower than the effective mass of the Marcus et al. (1983) analysis of the lateral wall impact data. This difference may be due to the different methods used. In Marcus et al., the effective mass is determined by impulse and momentum balance, whereas the Haffner method matches on peak force and acceleration as well as waveform. As Cesari et al. (1984) point out, the mass determined by peak comparison is approximately half that obtained by the impulse and momentum approach, because the peak force and acceleration occur approximately 40% earlier in the time history and, at that time, a smaller part of the body is involved in the impact.

It is important for pelvic response realism that both the effective mass and the stiffness of the pelvic structure be matched to that of the human. Cesari et al. (1984) report on the development of the Eurosid pelvis. Their data show that they were able to produce a pelvis design that gave a relationship between peak force and peak acceleration that was similar to that of the data from cadaver tests under the same test conditions.

This would indicate that the effective mass of the design based on peak force and acceleration values was similar to that of the human. However, their data show that, when peak impact forces or peak pelvic accelerations were plotted as functions of impactor velocities, the Eurosid pelvis consistently produced values that were much higher than the cadaver values. Apparently the pelvic stiffness and the coupling of the other body region masses were not well matched in that design.

The only data available on the lateral compliance of the pelvis are a series of compression tests conducted by Messerer (1880). In those tests the pelvis was loaded by blocks through the hip joints, and in only one case (unnamed) was the deflection measured. A maximum deflection of 27 mm (1.06 in) was achieved at fracture. Messerer noted that the shape of the pelvic ring changed noticeably in all tests. Since there was no indication as to which test the deflection was measured, an estimate of the lateral pelvic stiffness, based on an average fracture load of 2838 N (638 lb) or a maximum fracture load of 4404 N (990 lb), yields values of 1051 N/cm (600 lb/in) and 1631 N/cm (931 lb/in), respectively. These values are considerably lower than the 5254 N/cm (3000 lb/in) stiffness found by Haffner (1985) for dynamic response. Such a difference is common when comparing the static response of a bone structure such as the skull or pelvis with an effective dynamic stiffness determined by modeling. The static stiffness is determined by symmetrically compressing the structure between opposing load surfaces, whereas the dynamic response is related to a load on one side only and results in asymmetric structural deformations and an apparent higher stiffness. As an aid in the initial design of a pelvic structure, a static lateral stiffness of approximately 1750 N/cm (1000 lb/in) is indicated as a starting point.

The specification of the response of the pelvis to dynamic lateral loading can be based on two types of impact tests: (1) direct pelvic impact with a 15.2-cm (6-in) diameter, 23.4-kg (51.5-lb) rigid disc impactor, and (2) whole-body rigid-wall lateral sled impacts. Nusholtz et al. (1982) provide rigid moving-mass impactor data on seven test subjects with the impactor centered on the acetabulum. The impactor was a 15.2-cm rigid disc impactor with a mass of 56 kg (123 lb). The average test velocity was 5.8 m/s (19 ft/s). Five of the tests produced pelvic fractures, but only two of those fractured directly at the impact site. The other three produced remote fractures in the pubic bones. The two nonfracture peak forces and the three remote-fracture peak forces, when scaled to the AATD mass, result in a mean peak-force value of 7941 N (1785 lb). The scaled average time duration is 43 ms. The equivalent test velocity for a 23.4-kg (51.5-lb) impactor mass would be 6.7 m/s (22 ft/s), and the equivalent mean time duration would be 37 ms. The resulting idealized response corridors for this test condition are shown in Figure 29. The mean peak force is given as 8.0 ± 1.2 kN (1800 ± 270 lb). The skewed nature of the time history is based on the general waveforms in pelvic impacts.

The whole-body lateral pelvic impact response corridor can be defined from the five 32-km/hr (20-mph) rigid-wall impact tests used to define the similar thoracic whole-body lateral response (Figure 18). The filter used for pelvic acceleration signals was the same 200-Hz, 24 dB/octave filter used for thorax signals, even though it was expected that the pelvis would have a lower frequency content. However, initial examination of the pelvis signals did not warrant the use of a lower-corner filter, but suggested that most significant frequencies are below the 200-Hz point. The mean force-time response with a range of plus-and-minus one standard deviation was plotted from the AATD data base and is the basis for the corridors shown in Figure 30. The corridors represent simple straight-line boundaries for the plus-and-minus one standard deviation curves, except at the peak load value where a variation of $\pm 15\%$ of the peak load is indicated.

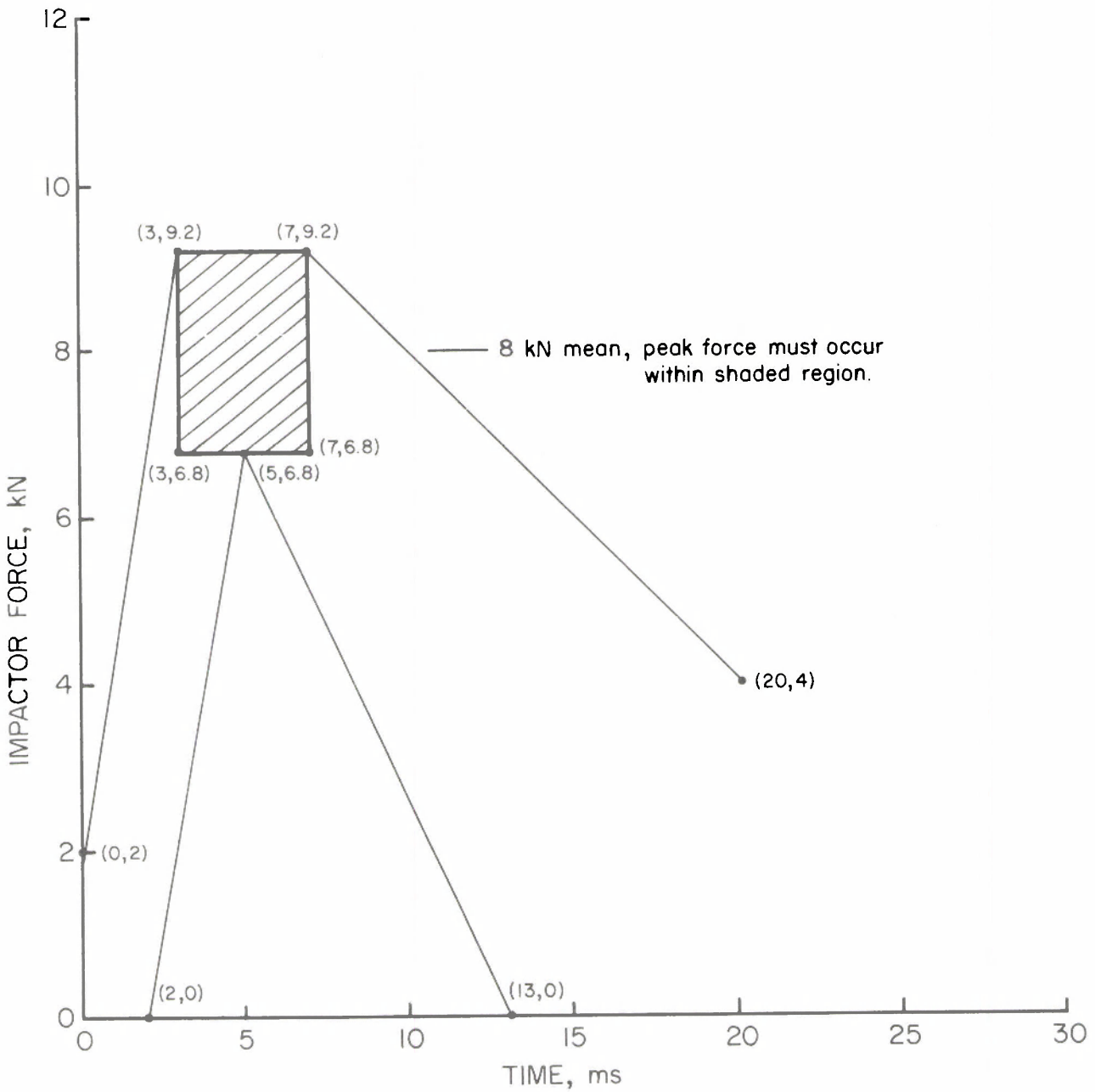

FIGURE 29. Pelvic lateral impact response (15.2-cm diameter, 23.4-kg rigid impactor, 6.7 m/s impact velocity).

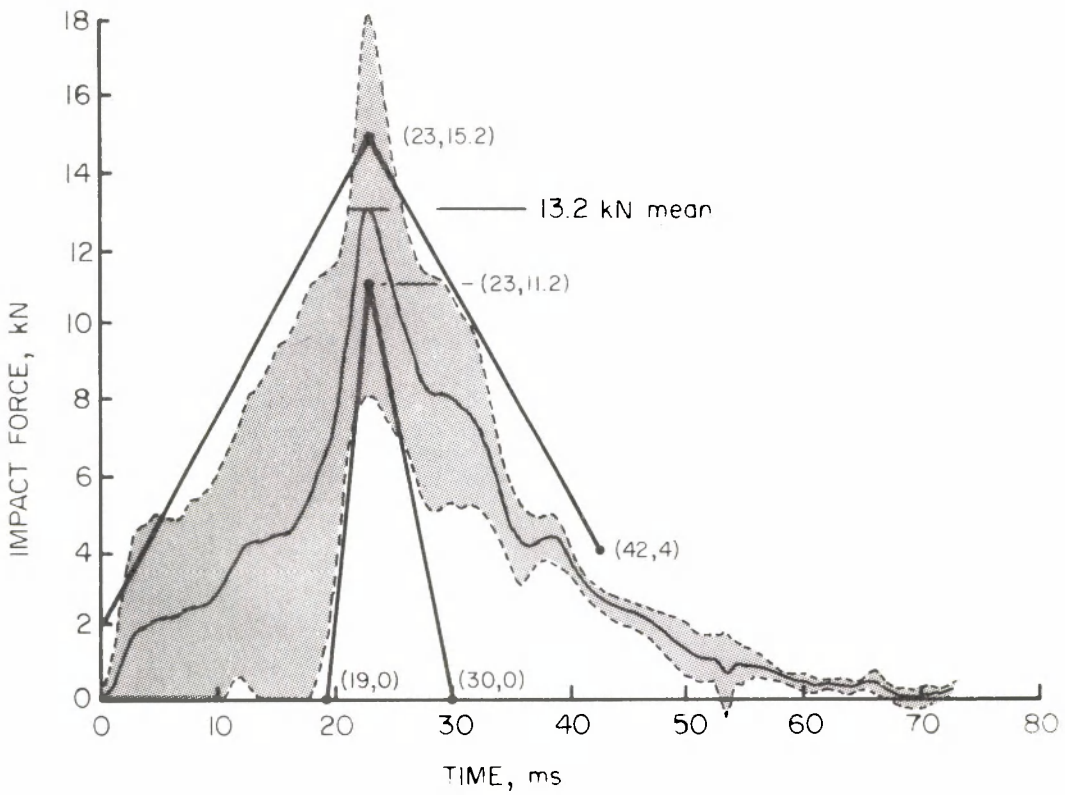

FIGURE 30. Whole-body lateral pelvic impact response (32-km/hr rigid-wall impact).

Pelvic Design Concepts (Refer to Figure 3, p.15). The pelvic design concept features a simple geometric structure fabricated from steel tubular elements. This structure will (1) provide a lightweight, strong unit for tying the extremities and the torso together, (2) allow lateral pelvic and hip-joint load measurement, and (3) provide a protected space for housing a future data acquisition system. The simple geometric nature of the basic pelvic structure will allow for lateral structural compliance to be designed into the system and the mass of the pelvic structure matched to human values.

The anatomical details of critical points for proper restraint system engagement and interaction, such as the iliac bones and ischial tuberosities, will be provided only where needed. Three uniaxial load cells will be used for lateral force measurement and will be located at the pubic bone area, the sacral area, and the hip joint area. It may be possible to sense the pubic and sacral loads with a flexible pelvic ring structure and associated strain gauges at those points. The soft tissue mass and compressive properties will be chosen to provide humanlike response in lateral and frontal impacts in concert with the pelvic structure design.

EXTREMITIES

The basic geometric specifications for the AATD upper and lower extremities are given by Robbins (1983). These specifications include joint-center locations, segment lengths, the coordinates and orientation of their coordinate systems, the coordinates of the associated centers-of-gravity (all depicted in Figure 4), and the orientation of the principal axes of inertia with respect to the anatomical axes for each region. The masses and mass moments of inertia for each extremity segment are given in Tables 3 and 4.

In general, the role of the extremities in ATD dynamic response is to provide proper linkage configuration, inertial characteristics, and joint range-of-motion and resistance. There are two cases in which direct load transmission through the extremities requires the specification of impact response. One situation involves lateral loading to the shoulder complex in side impacts, and the other is lower-extremity loading in frontal crashes.

The dynamic response of the shoulder has been studied in cadavers by Tarriére et al. (1980) using a 23.4-kg (51.5-lb) rigid impactor with a flat 15.2-cm (6-in) diameter face. Four test subjects were used to specify a corridor of response for the force-deflection behavior of the shoulder when impacted at 4.3 m/s (14.1 ft/s). The resulting corridor is shown in Figure 31. (A slightly different corridor was shown by Maltha and Janssen (1984) based on their analysis of the data.)

The frontal impact response of the flexed knee-thigh-hip complex has been studied by Horsch and Patrick (1976), and the results of some of the cadaver tests have been used to specify the knee impact response of the Hybrid III ATD. The test methods used to establish these responses involve impacts with three different masses (0.5, 1.5, and 5.0 kg) all at 2.1 m/s impact velocity. The Hybrid III ATD specification (GM Hybrid III Manual, Drawing No. 79051-65) involves impacting the flexed knee with the leg rigidly mounted to a fixture. This test requirement results in a realistically responding knee structure, but it does not address the inertial and body-region coupling associated with the response of the entire knee-thigh-hip complex. Horsch and Patrick also tested additional cadavers in a whole-body test using the same procedures. The data from these tests can be used to specify the whole-body response of the AATD knee-thigh-hip complex. The responses in terms of peak force with a one-standard-deviation range for both test conditions are given in Tables 17 and 18.

Impact loading to the lower leg can produce knee-joint loading and associated posterior subluxation of the knee joint. Viano et al. (1978a) studied the joint stiffness for static posterior tibia subluxation relative to the femur. The mean value of the stiffness, based on five cadaver knees, was 1490 N/cm (850 lb/in). These data were used in the development of the Hybrid III ATD knee joint, and a specific test method was developed for assessing knee shear load response (GM Hybrid III Manual, Drawing No. 83-5002-001). The test involves striking a knee loading fixture, specific to the knee joint design, with a moving impact mass of 12 kg (26.5 lb) having a flat circular face of 76 mm (3.0 in) diameter. The impact velocity is 2.75 m/s (9.0 ft/s), and the face of the impactor is covered with 1.45 cm (0.57 in) of Ensolite® AL energy-absorbing foam. The force-deflection response is defined by the values given in Table 19.

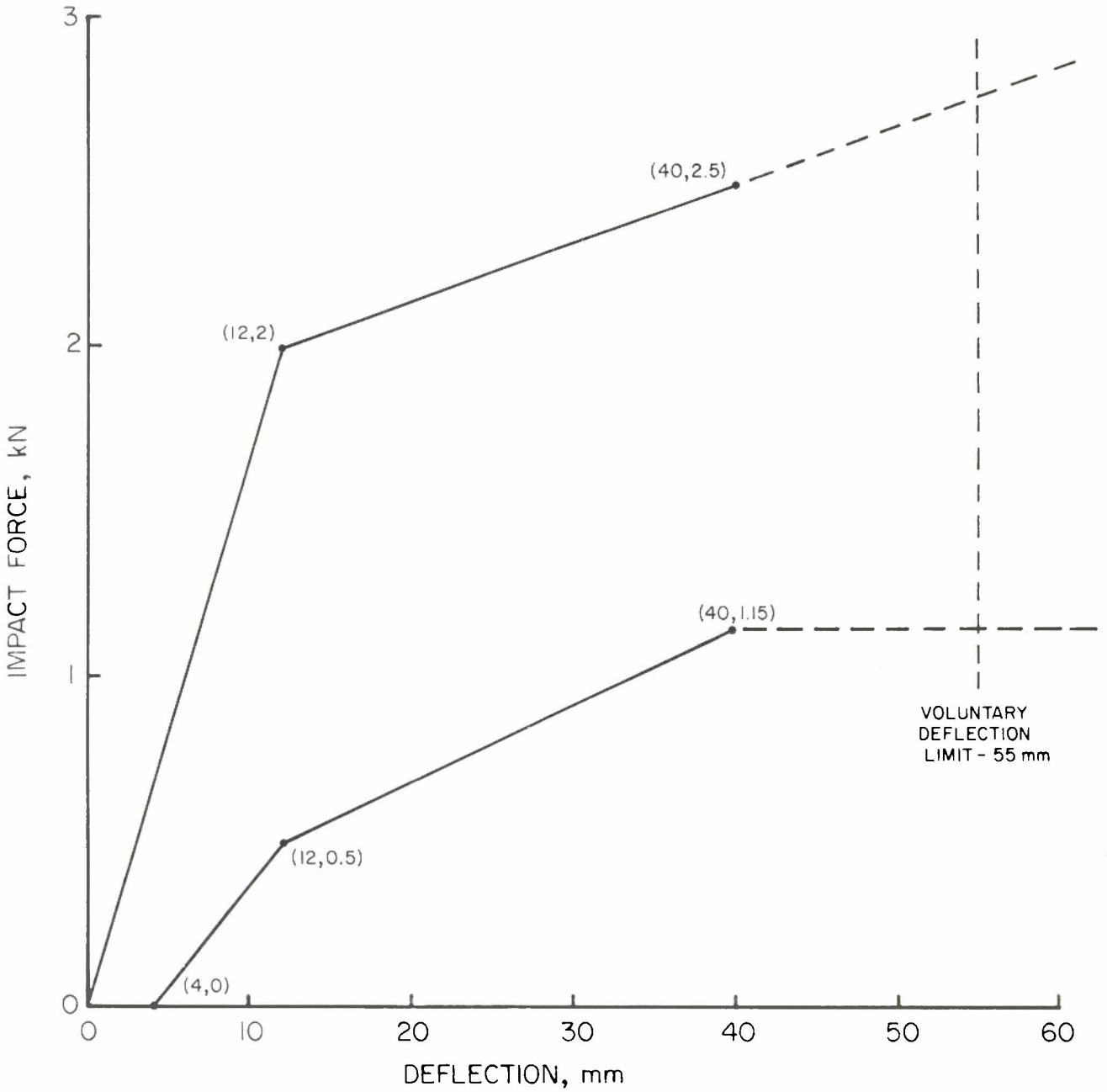

FIGURE 31. Shoulder impact response (4.3 m/s, 15.2-cm diameter, 23.4-kg rigid impactor).

TABLE 17

FIXED-LEG IMPACT RESPONSE

Pendulum Mass (kg)	Pendulum Face Diam. (mm)	Impact Velocity (m/s)	Peak Force (N)
0.5	51	2.1	948±250
1.5	51	2.1	2500±690
5.0	76	2.1	5703±1264

TABLE 18

WHOLE-BODY KNEE IMPACT RESPONSE

Pendulum Mass (kg)	Pendulum Face Diam. (mm)	Impact Velocity (m/s)	Peak Force (N)
0.5	51	2.1	693±176
1.5	51	2.1	1410±343
5.0	76	2.1	2273±474

TABLE 19

KNEE-JOINT SHEAR LOAD RESPONSE

Displacement (mm)	Force (kN)
10.0	1.49±0.23
14.4	2.15±0.33
18.0	2.68±0.41

Extremity Design Concepts (Refer to Figure 3, p.15). The upper-leg design concept will be similar to conventional ATD designs with a strong skeletal structure for durability. The effective mass and axial compliance of the upper legs will be achieved through the use of realistic soft-tissue mass in conjunction with lightweight design of the femoral structure. Steel or aluminum will be used if possible, although fiber-reinforced composites may be necessary to achieve adequate strength and low mass. The shaft of the femur will contain a six-axis load cell and an axial and rotational compliance section (if necessary) to ensure that the whole-body knee impact response is realistic. A knee-joint shear-stiffness control structure, similar to that in the present Hybrid III ATD knee, as well as multi-axial force and moment measurement in the lower leg is planned.

The extremity joints will be single-axis planar joints or combinations of such joints to achieve the appropriate degrees of freedom for a particular joint. This is preferable to ball-type joints for the purpose of joint resistance control. The ranges of motion of the joints will be humanlike, and the resistance characteristics will be adjustable (either frictional or elastic) to achieve resistance ranges from 0 to 2 G. The resistive torque-angle response will be humanlike as will the joint-stop characteristics.

The shoulder design will have a clavicle structure that can carry shoulder-belt and steering-wheel-rim impact loads in the frontal direction while maintaining lateral compliance for side impacts. A number of linkage configurations may be capable of meeting these specifications. One design that shows promise is the shoulder cam arrangement being developed for the Eurosid ATD (Neilson et al. 1985). The design uses the clavicle as a cam for lateral impacts. This allows the shoulder to rotate forward as it moves laterally, so that the arm can clear the chest. The linkage should reach its lateral deflection limit slightly after the chest reaches it lateral deflection limit.

DATA PROCESSING

The primary specifications for the data processing system to be integrated with the AATD are described in detail in Arendt et al. (1984). Basic to these recommendations is the concept of an on-dummy microprocessor-based system to perform analysis and control functions as well as to allow transfer of measured data to an external test set. This test set would also be microcomputer-based and would provide rapid turnaround for calibration, signal analysis, and pass/fail indications. Instrumentation requirements, using ISO 6487 (1980) as a guide, are given in Table 20, and environmental specifications, using test methods from MIL-STD 810D (1983) are given in Table 21. Electronic instrumentation should be verified prior to each test, and sensors should be calibrated at regular intervals, not to exceed six months, according to the procedures outlined in MIL-C-45662A (1962).

TABLE 20

ADVANCED DUMMY INSTRUMENTATION REQUIREMENTS

Amplitude Linearity	2.5%
Amplitude Resolution	12 bits (0.02%)
Time Linearity	1%
Time Synchronization	0.1 ms
Time Zero Offset	0.1 ms
Sample Rate	8000 Hz
Record Time (per channel)	500 ms

TABLE 21

ENVIRONMENTAL SPECIFICATIONS

Parameter	Design Limits
High Temperature	180°F.
Low Temperature	−10°F.
Temperature Shock	170°F.
Humidity	85%
Acceleration (linear)	10 G
Vibration	1 G RMS Random
Shock	500 G, 0.5 ms
EMI/RFI	Standard Industrial

The present report[1] revises and upgrades certain specifications to reflect AATD needs and requirements that have changed since the initial report. These changes, discussed in more detail below, are as follows:

[1]Based on a progress report by R.H. Arendt, MGA Research Corporation, Akron, N.Y., October 1984.

1. The data system, including circuits cards, will be housed within the pelvis in a space 12 cm (4.72 in) wide, 6.5 cm (2.56 in) high, and 6.5 cm deep. This is a total volume of 503 cm^3 (30.93 in^3).
2. The channel capacity will be 72 with expansion capability to 100.
3. All areas will be shock hardened to withstand 500 G for 0.5 ms.
4. Record times per channel will be extendable to 5 seconds for special test purposes, at the expense, however, of the number of channels available.
5. The channel class for head impact data may be less than 1000, depending on sampling rate, memory size, and record times desired.

The on-dummy data acquisition system will be developed on a circuit-card level. The printed circuit cards will mount into a card cage that is an integral part of the dummy design. Consequently, it will not be necessary to provide space within the dummy for a removable enclosure that contains the system printed circuit cards. Rather, only the individual circuit cards will be removable from the dummy. An illustration of this concept is presented in the diagram shown in Figure 32. The space available is indicated above.

The channel capacity for the on-dummy data system was initially designed to accommodate 40 data channels. More recently, the desired channel capacity was increased to 72 to 100 data channels. The data system design was reviewed and revised to increase the number of input channels as shown in Figure 33.

The modified system design presented in Figure 33 is based on the use of a 16-bit microprocessor to regulate data acquisition and data storage in dynamic RAM memory. The design illustrated in Figure 33 is based on a 24-channel module concept. That is, twenty-four data channels are processed on one analog card that contains provisions for channel gain, multiplexing, sample/hold, and analog-to-digital conversions. The overall size of the analog input circuit card with provisions for 24 data channels is currently estimated to be 12 cm by 6.5 cm.

The analog input card is regulated by the system CPU card under program control. The size of the CPU card with provisions for a minimum of 72 data channels is also estimated to be the same as the analog input card. Test data generated by the analog input card is transferred to the data memory card, also 12 cm by 6.5 cm. Preliminary component layouts for the 24-channel analog input card, the 72-channel CPU card, and the 512K memory card are presented in Figures 34, 35, and 36, respectively.

For class 1000 data, a rate of 8000 samples per second is required to properly convert analog data into a digital form. If the data channel class is reduced to class 600, a sample rate of about 3000 samples per second would be appropriate. The reduced sample rate allows a larger number of data channels or longer record time to be used for a given memory size. Alternatively, a smaller memory size is required for a fixed number of data channels and fixed record length.

The memory circuit card illustrated in Figure 36 provides 512K of 12-bit memory. This is adequate for 72 data channels recording for a duration of two seconds at a digitizing rate of 3000 samples per second per channel. The card is based on the use of a 256K-bit memory chip manufactured by Texas Instruments.

FIGURE 32. Instrumentation mounting.

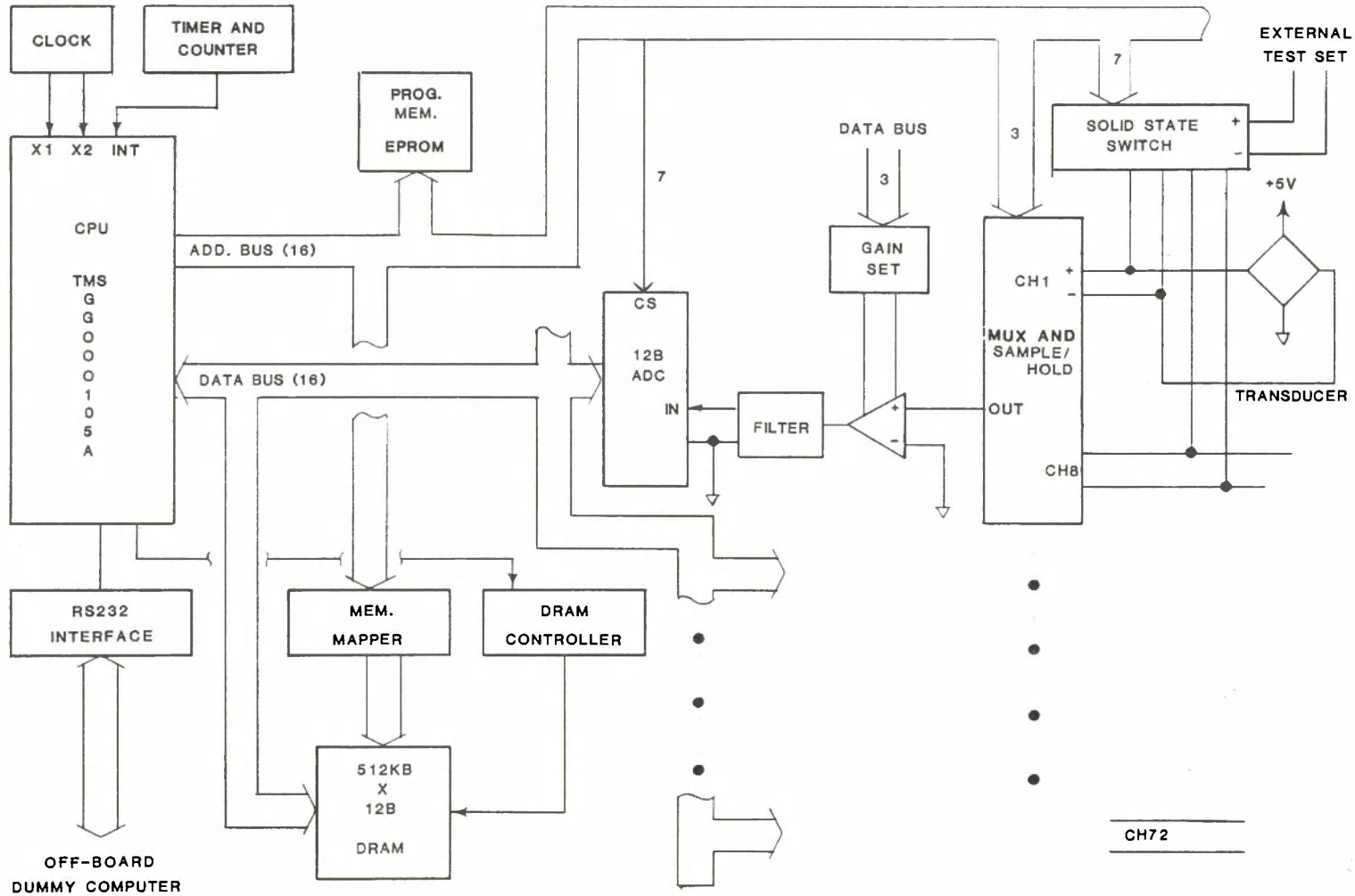

FIGURE 33. Overall system block diagram.

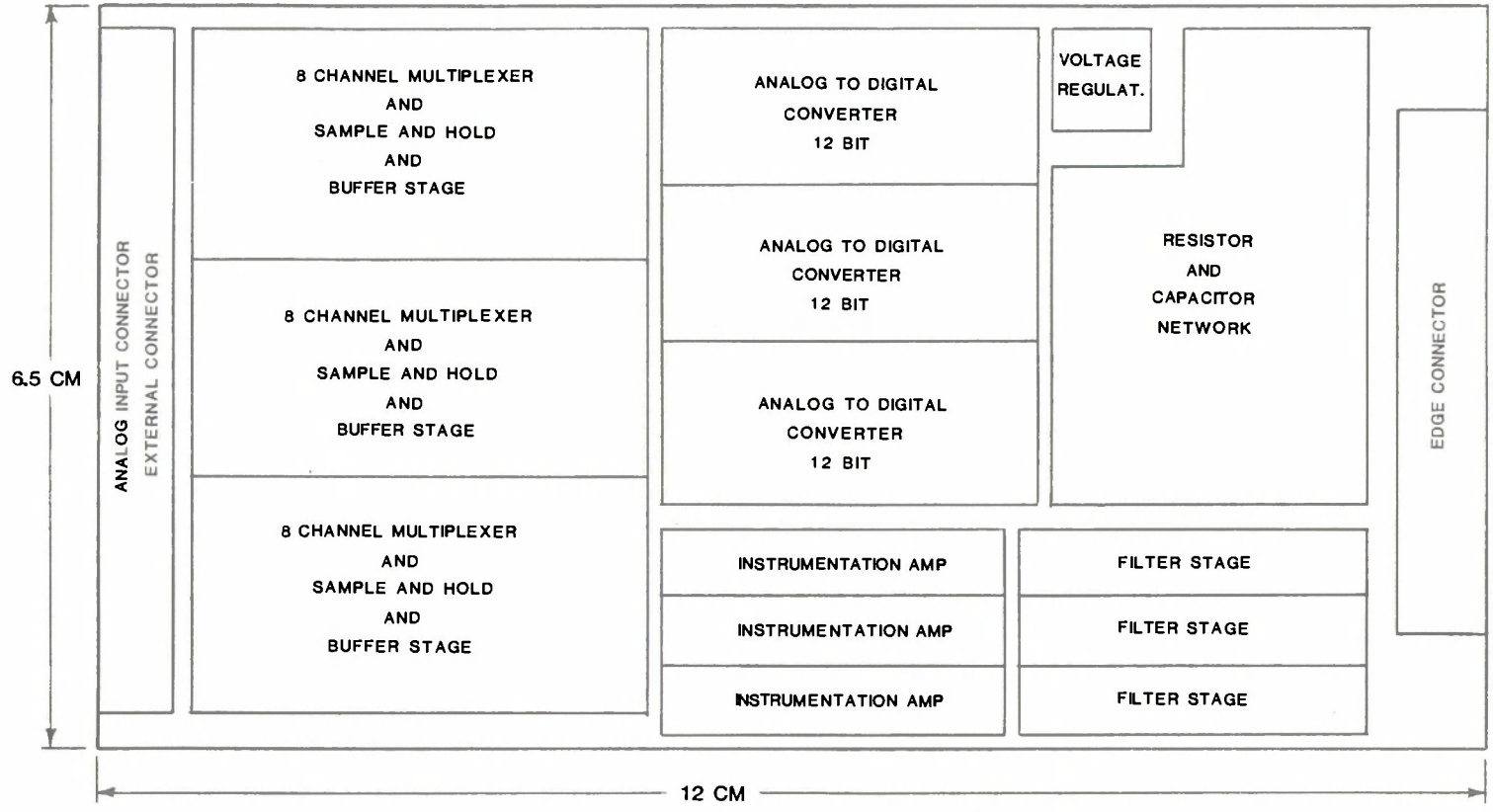

FIGURE 34. Analog input card.

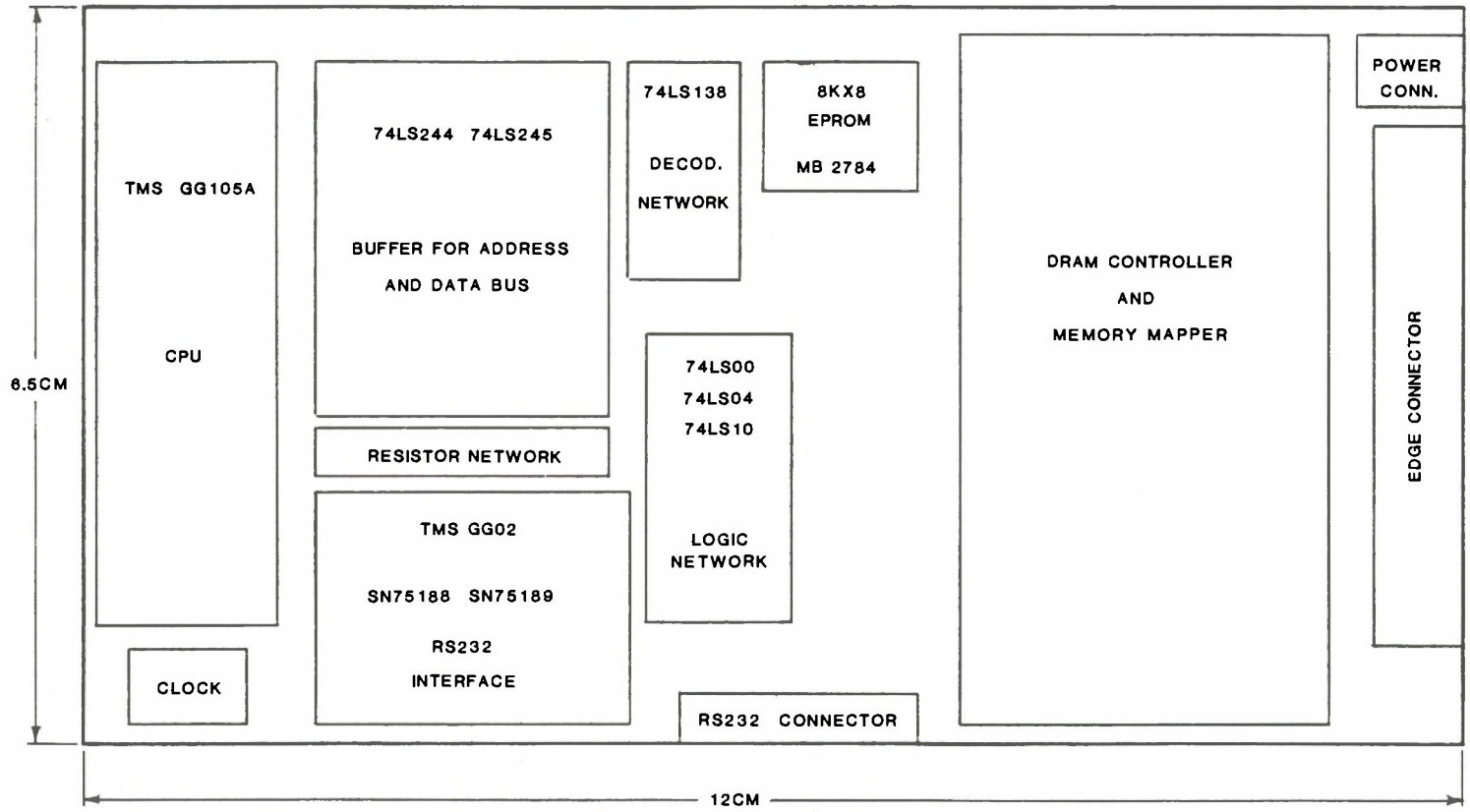

FIGURE 35. CPU control card.

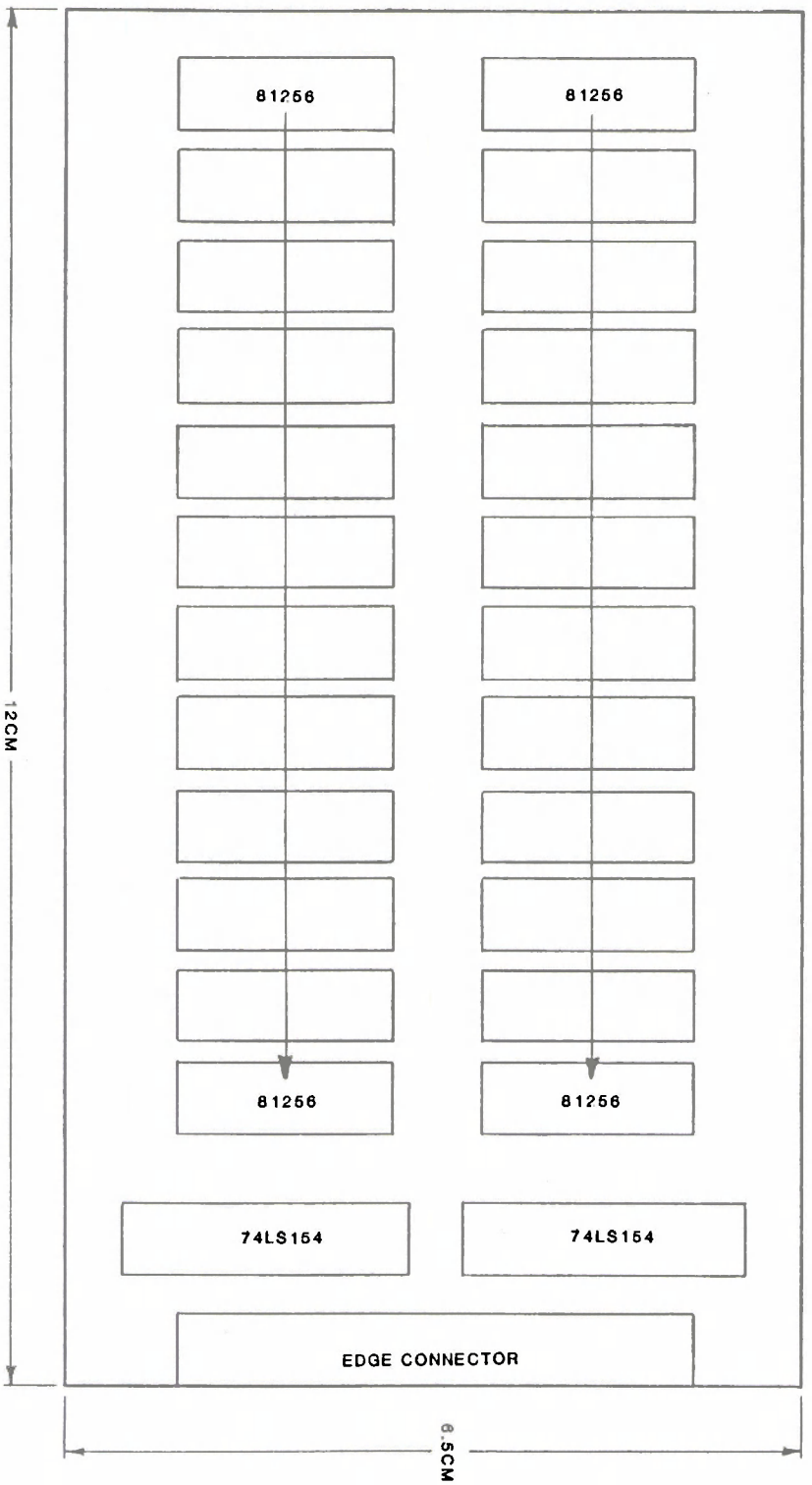

FIGURE 36. Memory card.

CERTIFICATION SYSTEM

The AATD certification approach, as described in Arendt et al. (1984) includes different types of testing corresponding to different test goals. These are briefly summarized as follows:

1. Manufacturers' certification, to ensure that components meet design specifications;
2. Regularly scheduled inspection, maintenance, and calibration, involving complete disassembly of the AATD;
3. Biomechanical response certification, performed with a completely assembled dummy and including response and injury-related criteria; and
4. Component testing, to be used only when failure or misadjustment is indicated from the above.

A key factor in this approach is the use of an on-dummy data acquisition and processing system for certification purposes at a minimum or as part of the complete AATD data processing system.

In this report,[2] the means of handling the AATD to achieve repeatable whole-body testing as well as the mechanism for performing this testing are described.

In order to certify AATD components within an assembled dummy, a fixturing device is needed to hold certain parts in place while allowing others to freely move. The system illustrated in Figure 37 would restrain the dummy at selected locations through the use of rods that would be attached at built-in points on both the dummy and the fixturing device. The device itself would have removable sections for different test conditions and would swivel about a vertical axis for impacts from various directions. Although the figure illustrates constraining rods in only the longitudinal direction, lateral fixturing mechanisms would also be available.

Surrounding the dummy and fixturing device would be a structural frame with a movable carriage on which an impactor is mounted (Figure 38). The carriage could be moved vertically and longitudinally, while the impactor could be rotated in both horizontal and vertical planes. This flexibility along with dummy rotation would accommodate all possible impact orientations.

The impactor itself would be a pneumatically-powered piston device to which various impact surfaces could be attached. At present, only two surfaces are planned, a 15.2-cm (6-in) disc and a 4- by 35-cm (1.6- by 13.8-in) bar. The piston mass with the disc surface will be 23.4 kg (51.5 lb) and the piston mass with the bar surface will be 10.0 kg (22.0 lb). The velocity range will be between 2 and 12 m/s (6.6 and 39.4 ft/s). This range would be difficult to achieve using a gravity-powered impactor but is easily within the capability of a pneumatic system.

---

[2]Based on a progress report by D.J. Segal, MGA Research Corporation, Akron, N.Y., October 1984.

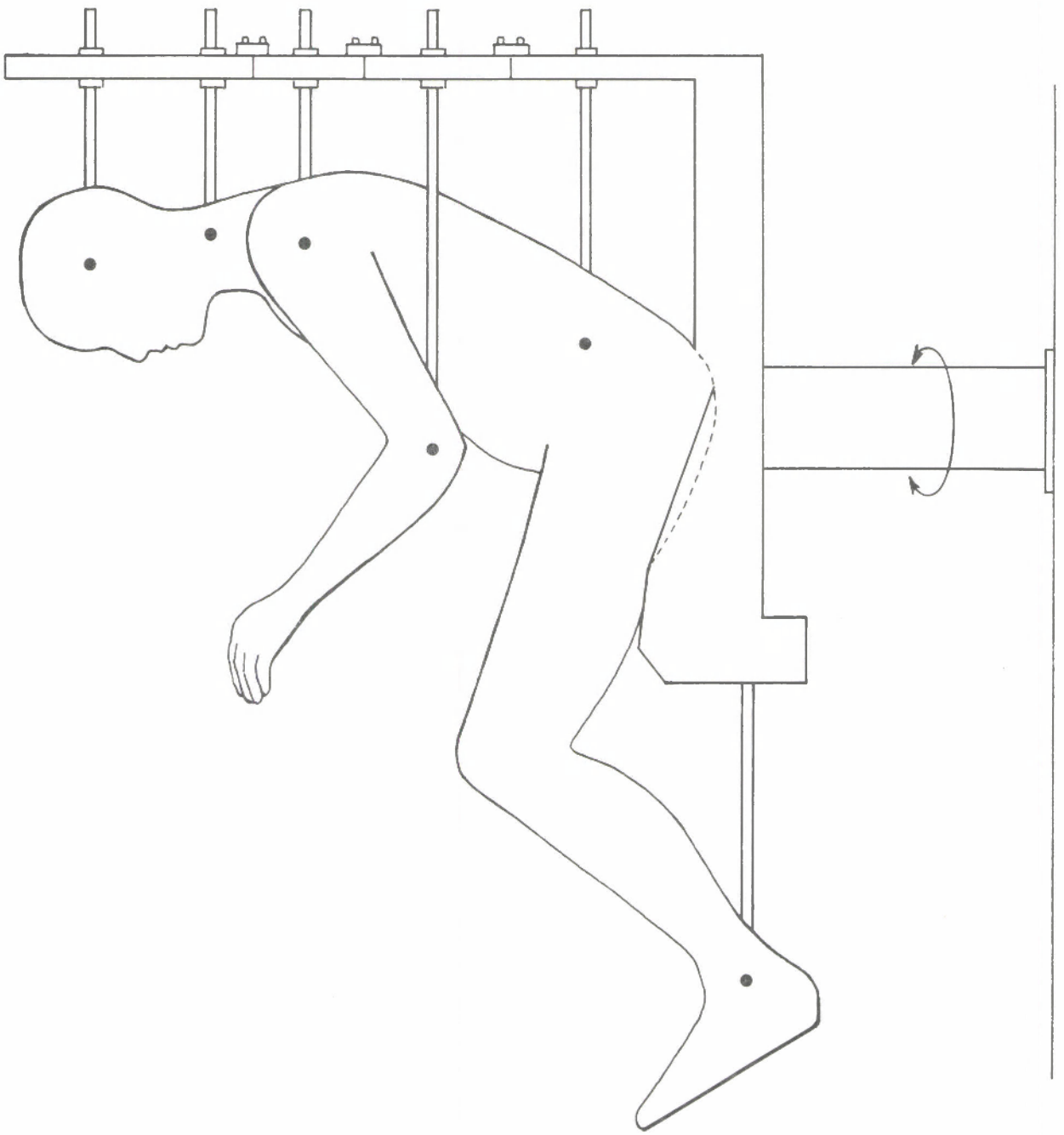

FIGURE 37. Dummy fixturing concept.

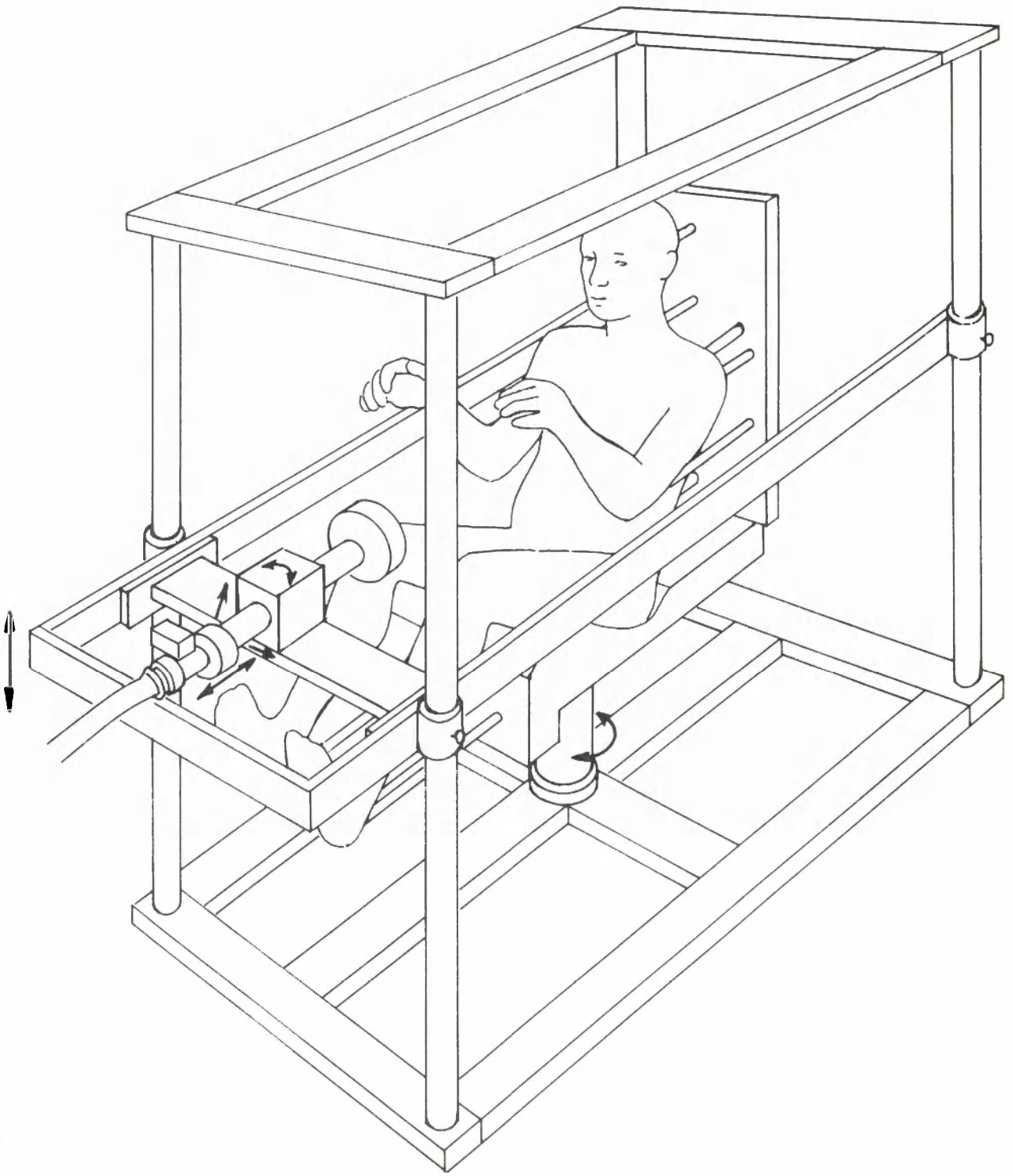

FIGURE 38. Adjustable impact device concept.

TRAUMA ASSESSMENT CRITERIA

In order to ensure that meaningful measurements related to injury assessment will be made in the AATD, mechanical parameters must first be identified that best predict injury and describe its relative severity. The analyses presented here have been divided into two parts: current recommendations for injury assessment criteria (TAC) and exploratory data analysis to develop improved and possibly entirely new TAC concepts.

CURRENT TRAUMA ASSESSMENT CRITERIA RECOMMENDATIONS

To arrive at these recommendations, existing injury criteria were evaluated, and these were modified or changed to reflect current data and the measurement capabilities made possible by the AATD design concepts. The following sections present the rationale and results of this analysis for each body region.

Head. A variety of mechanisms have been postulated for mechanical damage to the brain from impacts to the head. They include (1) direct brain contusion from skull deformation at the point of contact; (2) indirect brain contusion produced by negative pressure on the opposite side of the impact; (3) brain contusion from movement of the brain against rough and irregular interior skull surfaces; (4) brain deformations as it responds to pressure gradients and motions relative to the skull, resulting in shear stresses in the brain matter; and (5) subdural hematoma from movement of the brain relative to its dural envelope, resulting in tears of connecting blood vessels. The latter three mechanisms have also been postulated for mechanical damage resulting from head motions due to indirect impact.

An ideal test device would simulate all the detailed mechanical and anatomical properties of the human head and allow direct measurement of the mechanical parameters associated with all of these mechanisms, e.g., global skull structural deformations, local head contact forces, and skull rigid-body motions, as well as global brain pressure distributions, tissue deformations, and motions. Consideration of the practicality of some of these measurements reduces the choices of measured parameters to a limited few. If a nondeformable skull structure is used in the AATD and there is no brain tissue simulation, then the only measurable quantities left would be those related to the rigid-body motion of the head, either from direct or indirect impact.

The current method of injury assessment in the head involves the measurement of resultant triaxial translational acceleration at the center of gravity of the head and subsequent analysis to produce a HIC value. The biomechanical basis for the HIC method, however, is related only to direct impacts to the head. The influences of rotational accelerations and velocities on brain injury have been postulated, but threshold values for the human are not well established. In most general automotive head impact motions, the effects of angular acceleration and velocity are implicitly included in the head CG translational accelerometer signals and, thus, the HIC value will reflect the severity of head impact motions regardless of their nature. The difficulty in determining when head contact is taking place in some crash tests has led to the concept of limiting the HIC computation to a maximum interval of 15 ms in any test (Prasad and Mertz 1985).

For indirect impact, a HIC value of 1000 would be equivalent to a constant deceleration of 85 G for 15 ms, resulting in a velocity change of 12.5 m/s (41 ft/s). The asymptotic value for average deceleration at long durations for the Wayne State Tolerance Curve was suggested by Patrick et al. (1965) to be 80 G, because the long-duration portion of the curve was obtained from whole-body exposures that did not involve direct head impact. This corresponds to a HIC interval of 17.5 ms for a HIC value of 1000, assuming a constant deceleration at the 80-G level. The corresponding velocity change is 13.7 m/s (45 ft/s).

Thus, the limitation of the HIC calculation to an interval of 15 ms appears consistent with the Wayne State Tolerance Curve and with the levels of head-velocity change expected in modern automotive crash environments. Concern over the effect of longer-duration head accelerations may more appropriately be directed toward rotational motions of the head and resulting neck loading.

The question of the combined effects of rotational and translational accelerations on head injury have not been addressed in the literature. This topic has been investigated as part of AATD project and is discussed in a later section of this report.

Injury assessment for the face is based on the load-carrying ability of the facial skeleton and is sensitive to load distribution. Facial contact forces can be determined from the head acceleration and neck force measurements. Estimates of loaded area can be made by conventional marking procedures (chalk, paint, etc.) or by presssure-indicating films. Tolerable facial forces for distributed loads and steering-wheel rim-type loads have yet to be determined. Tolerable loads for concentrated loading to various facial bones are summarized in Table 22.

TABLE 22

FACIAL IMPACT INJURY THRESHOLDS FOR CONCENTRATED LOADS
(6.5 cm^2 loaded area)
(Schneider and Nahum 1972)

Bone	Force (kN)
Mandible (A-P)	1.78
Mandible (Lateral)	0.89
Maxilla	0.66
Zygomatic Arch	0.89
Frontal	4.00
Zygomatic Areas	0.89

Spine. The primary mechanisms of injury to the cervical spine involve damage to the bony elements, with subsequent disruption of the spinal cord being the most serious result. The mechanisms involve dislocations of one vertebral body upon another, fracture of vertebral bodies with associated displacement of bone fragments into the spinal canal, and rupture of intervertebral discs with protrusion into the spinal canal. An additional injury mechanism is ligamentous stretching and rupture with attendant stretching of the spinal cord and/or disruption of the cord by associated bony element motions. Although these mechanisms have been identified in a qualitative manner, the actual loads, moments, displacements, and/or motions of the cervical spine that lead to injury are not well documented at this time. A further complication is that rather low load levels have been found experimentally to produce serious damage when the spine is in an asymmetrical configuration (i.e., head rotated and fiexed) at the time of impact (Nusholtz et al. 1983a).

An ideal cervical spine design in an ATD would allow measurement of vertebral element motions, local loads between vertebral elements, input loads into spinal segments, and local deformations of the spinal cord. The AATD cervical spine design will not have such fine detail because of the lack of substantive information about the mechanical responses of the human system, and because of the need to avoid undue complexity in ATD systems. The AATD will, however, provide for the measurement of the input forces and moments at both ends of the cervical spine and will have a linkage system that produces humanlike head motions and joint resistance.

Bending Moment. The work of Mertz and Patrick (1967, 1971), Mertz et al. (1978), and Nyquist et al. (1980) have been used by Mertz (1984) to formulate injury assessment guidelines for interpreting neck loads obtained at the head/neck–junction load cell in the Hybrid III ATD (see also Nyquist and King 1985, p. 80). The reference value for the cervical-spine (C1) bending moment in fiexion is 190 N·m (140 ft·lb), which is taken to imply that significant neck injury is unlikely if this value is not exceeded. The corresponding bending–moment value in extension is 57 N·m (42 ft·lb).

For the base of the cervical spine (C7/T1), Wismans and Spenny (1984) indicate from their analyses of human volunteer tests that the magnitude of the bending moment at that joint is about twice that at the top of the cervical spine. Applying this finding to the Mertz reference values yields 380 N·m (280 ft·lb) for fiexion and 114 N·m (84 ft·lb) for extension at C7/T1.

The structure of the lumbar spine is generally similar to that of the lower cervical spine, but the lumbar spine is much larger. Yamada (1970) gives the effective cross–sectional area of cervical vertebrae as 305 mm^2 and of lumbar vertebrae as 1055 mm^2. These areas would give a relative linear dimension ratio of 1.87 for the lumbar vertebrae with respect to the cervical vertebrae.

Yamada also indicates that the compressive failure stress of the lumbar vertebrae is one half that of the cervical vertebrae. Thus, the bending moment limit, based on compressive bending stresses, for lower lumbar (L5/S1) wedge fracture in fiexion could be estimated by the moment limit for equal stress. This would be 1.87^3 or 6.5 times as great as the C7/T1 limit, multiplied by 0.5 to account for the lower material failure stress of the lumbar vertebrae. The resulting value is 1235 N·m (910 ft·lb) for flexion. Similarly, the value for extension is 370 N·m (273 ft·lb).

The injury threshold values for spinal bending moment are summarized in Table 23.

TABLE 23

SPINAL BENDING MOMENT INJURY THRESHOLDS

Direction	Top (C1)	C7/T1	Base (L5/S1)
Flexion	190 N·m	380 N·m	1235 N·m
Extension	57 N·m	114 N·m	370 N·m
Lateral	Between the above	Between the above	Between the above

Force–Time. The load guidelines given by Mertz (1984) for the top of the cervical spine (C1) can also be applied to the base of the cervical spine (C7/T1), if the effect of the mass of the neck is assumed to be negligible. These limits are shown in the lower portion of Figure 39.

The application of the guidelines to the lumbar spine requires adjustment for size through the use of an area factor 1.87^2 or 3.5 for long–duration loading where injury may be related to gross vertebral motions and dislocations resulting from axial tension, compression, or shear loading. For shorter time durations, the Mertz guidelines must be modified to reflect different failure stress levels in the case of tension and compression, since gross motion modes of failure may not develop.

Yamada indicates that the tensile failure load of the intervertebral discs is slightly lower than that of the vertebral bodies. Taking the average of the ratios of the tensile–failure loads of the bodies and the discs for both the lumbar and the cervical spine yields a multiplication factor of 3.85 for a short–duration loading limit. For short–duration compressive loading, the failure stress of the vertebral bodies is the limiting factor. Thus, the cervical spine limit in compression should be multiplied by the area ratio (3.5) and reduced by one half for the lumbar failure stress reduction, yielding a factor of 1.75 for a short–duration loading limit.

The above analysis has been applied to the Mertz guidelines for the cervical spine, and the resulting curves for lumbar spine loading are shown in the upper portion of Figure 39.

Thorax. Thoracic injury mechanisms include rib–cage skeletal fractures, contusions of the heart and lungs, tearing and rupture of the vascular and pulmonary systems, and disruption of the heart–muscle conducting system. Many of the above injuries are thought to occur due to excessive deformations of the thorax when directly loaded. Severe deformations during frontal impact may result in trapping and crushing of the thoracic organs between the chest wall and the spine. Inertial reactions of the organs to high body forces during chest loading are thought to produce stresses and deformations in the tissues of the organs, resulting in injury. At high velocities, such injuries may occur with very little rib cage deflection.

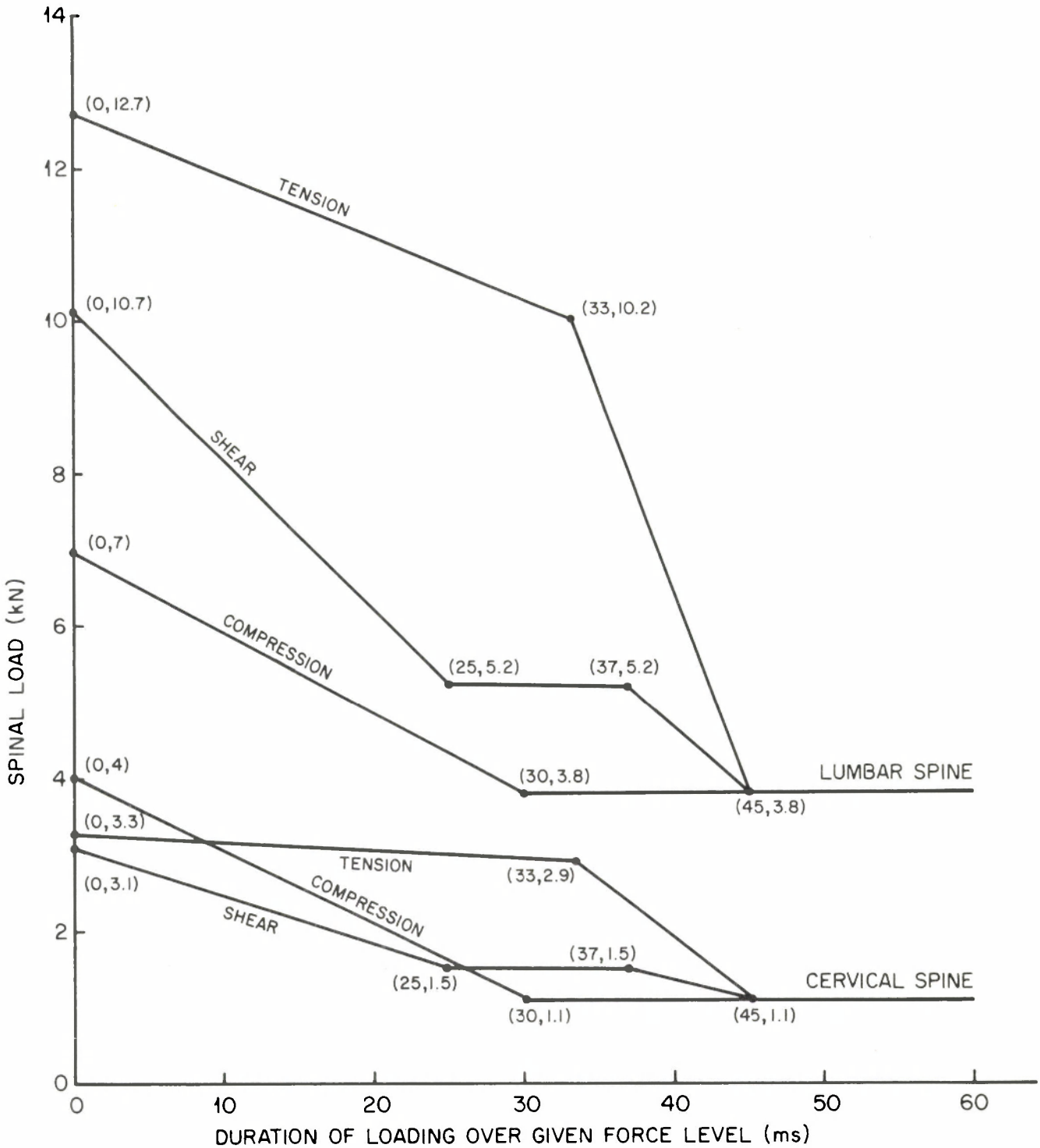

FIGURE 39. Spinal force-time limits for injury assessment.

An ideal thoracic test device would allow measurement of pressures in the heart, aorta, and lungs as well as the motions and deformations in these organs. The test device would also allow the measurement of rib cage motions, deformations, and loads. To the extent that a thoracic test device simulates internal organ structures and rib cage details, it is possible to measure pressures, motions, and deformations at selected sites in the thorax. At the present time, it does not appear feasible to simulate internal organs in detail in a test device. However, since the skeletal structure of the rib cage is not likely to account for the marked rate sensitivity of the chest under dynamic loading conditions (compact bone material would be expected to only double its stiffness as strain rates go from static to impact conditions), it is thought that the source of this effect is the viscous resistance of the fluid-filled internal organs. The use of fluid-filled structures in the AATD thorax design would aid in providing the proper response to impact loads and would allow pressure measurements to be made.

Present ATD criteria for judging injury potential to the thorax involve deflections of the rib cage at a specific location and/or acceleration of the spine or chest wall. All of these measures attempt to relate the impact to the degree and extent of deformation and loading of the chest. Spinal acceleration may be related to the total load on the thorax, but it does not give information on the degree or extent of chest deformation. A single deflection measurement may give information on the degree or depth of deformation in the region of the measurement, but not on the extent or breadth of deformation (i.e., concentrated versus distributed loads). The concept of combining sternal deflection and spinal acceleration limits for frontal loading is an attempt to deal with these problems.

An acceleration-based injury criterion for lateral loading to the thorax has been proposed by Eppinger et al. (1984). The development of the criterion assumed that the acceleration-time histories of the chest wall and spine (twelve-accelerometer method) are sufficient to describe the mechanical input to the thorax during impact. A series of 49 cadaver lateral impact tests using rigid- and padded-wall, pendulum-impactor, and car-door impact conditions was analyzed. A variety of acceleration parameters were evaluated, and a combination of peak T12 lateral acceleration and peak left-upper-rib acceleration, normalized by the cadaver mass and then combined with subject age, was used to form the Thoracic Trauma Index (TTI). The success of the TTI was judged by its ability to compact the data at a given AIS level and provide good separation of data between AIS levels, particularly at the higher levels of injury.

Viano and Lau (1985) have recently reviewed thoracic injury criteria and have suggested a viscous tolerance criterion using the combination of deformation velocity, V, and thoracic compression (C) in the form $VC_{max} = [V(t)*C(t)]_{max}$. The paper analyzes the Kroell thoracic impact data base and concludes that $VC_{max} = 1.3$ m/s (4.3 ft/s) corresponds to a 50% probability of AIS ≥ 3. The 20% probability level corresponds to $VC_{max} = 0.9$ m/s (3.0 ft/s).

The concept of an absorbed-energy criterion for predicting thoracic injury has been further investigated for a variety of loading conditions. The results of this analysis are presented in a later section of this report.

The thoracic design concepts for the AATD lend themselves to measuring global deformation of the chest by means of (1) pressure measurement within the gas chamber of the accumulator structure, and (2) determination of the local rate of deformation through measurement of fluid pressure in the individual fluid-filled compartments. During the thorax development process, however, a twelve-accelerometer array will be used to assess its response performance in whole-body tests such as those used to develop the TTI and other acceleration-based injury criteria. Thus, during the development of the AATD

thorax, it will be possible to compare and relate the information obtained with pressure measurements to those obtained with acceleration measurements as well as to deflection and deflection-rate parameters.

The recommended trauma assessment criterion levels to be used with the AATD for the purpose of developing the equivalent system-pressure criteria are as follows:

Frontal deflection at mid-sternum	7.5 cm	(3.0 in)
Lateral deflection at nipple level	6.0 cm	(2.4 in)
VC_{max}	0.9 m/s	(3.0 ft/s)

Deflection limits at intermediate locations would be appropriately in between these extremes.

The lower lateral deflection limit is based on the fact that the thorax is stiffer in the lateral direction, while the identical VC_{max} value is used because the rate sensitivity of the thorax is the same in frontal and lateral loading.

Abdomen. Injury mechanisms in the abdomen are primarily the result of deformation or penetration of the abdominal contents with associated generation of significant forces or pressures in the deformed organs. In addition, at high impact velocities, solid organs such as the liver may undergo severe damage due to pressure generation alone, with little deformation.

In an ideal test device, the abdomen would contain simulations of the various abdominal organs, with pressure and motion measurements being made in each organ. In the AATD, the abdominal structure will consist of fluid-filled compartments in which local pressures will be measured and global deformation of the compartments indicated by gas pressure measurements in the accumulator section.

Rouhana et al. (1985) report on an extensive series of lateral impacts to the rabbit abdomen. The impact velocity of the rigid disc impactor was varied from 3 to 15 m/s (10 to 49 ft/s), and the forced abdominal compression was varied from 10 to 50%. The study proposed an abdominal injury criterion (AIC) that is a function of the impactor velocity times the compression level (V*C). The authors indicated more work is necessary before the AIC can be applied to human beings.

Stalnaker and Ulman (1985) analyzed a large series of frontal and lateral abdominal impacts using subhuman primates over a wide range of sizes. They analyzed the test data in terms of V*C for injury prediction purposes. They found threshold values for the V*C product at the AIS-3 level that were similar in magnitude to those produced by the Rouhana et al. study. The authors conclude that, since the size range of the test subjects was much greater than the range between the largest subhuman primate and the human, the consistency of the V*C values found throughout the various species in the study permitted the extension of the findings directly to the human. As did Rouhana et al., Stalnaker and Ulman found the right side of the abdomen more susceptible to injury than the left side. They also found the upper abdomen most susceptible to injury in frontal impacts, with a V*C value of 3.02 m/s (9.9 ft/s) for an AIS-3 level injury. This is similar to the average combined V*C value for the left- and right-side impacts at the 50% probability level of AIS-3 in the Rouhana et al. study. The latter display their data in terms of the probability of injury versus V*C. The average of left- and right-side V*C values for a 20% probability of an AIS-3 injury to the abdomen is 1.65 m/s (5.41 ft/s). Based on the Stalnaker and Ulman study, this value should also apply to the human abdomen.

Rouhana et al. present their experimental data in the format of impactor velocity versus forced compression with lines of constant V*C shown for various percentages of experiments with AIS-3 outcomes. These curves indicate a strong velocity sensitivity above 10 m/s (33 ft/s) and a strong compression sensitivity below that velocity. Thus, the V*C abdominal injury criterion would indicate that, in the 12-m/s (39-ft/s) abdominal response test, injury would occur during the force plateau region of the curve rather than during the static response portion of the curve. The pressures generated by the force plateau would be about 265 kPa (38.4 psi) for the 4- by 35-cm (1.6- by 13.8-in) impactor face.

Melvin et al. (1973) and Lau and Viano (1981) have both reported that a dynamic pressure of approximately 300 kPa (43 psi) results in liver injuries when the organ is directly loaded. This pressure, multiplied by the impactor area of 140 cm^2 (22 in^2) for the AATD abdominal impact response test, results in a dynamic load of 4.2 kN (944 lb), a load that corresponds to an abdominal deflection of 7.9 cm (3.1 in) according to the response curves given in Figure 28 for impacts of 12 m/s or less.

Thus it would appear that a deflection-limit criterion, a pressure-limit criterion, and the V*C criterion would give generally equivalent ratings based on the conditions of the abdominal impact response test. The recommended limits for frontal through lateral loading of the abdomen would be:

Deflection	7.5 cm	(3.0 in)
Dynamic pressure	265 kPa	(38.4 psi)
V*C	1.65 m/s	(5.4 ft/s)

Because the deflection level and the rate of deflection of the AATD abdomen will be related to fluid pressure measurement in the fluid-filled compartments and gas pressure measurement in the accumulator section of the structure, test instrumentation designed to relate these measurements to the above criteria will be necessary as part of the development of the AATD abdomen.

Pelvis. Lateral loading to the pelvis and associated hip-joint structures can result in fractures of the bony structure at many sites around the pelvic ring. Injuries to the pelvis, not including the hip joint, can be classified as isolated fractures of the pelvic ring, double or multiple fractures of the pelvic ring, and fractures of the sacrum and coccyx.

An ideal test device would have a pelvis with a humanlike pelvic structure that could be strain-gauged at critical points to indicate impending failure strains. The AATD pelvic structure will not have a humanlike structure, but rather an idealized one with equivalent stiffness and mass. Load cells will be strategically located at three points to allow the determination of load distribution on the hip joint and iliac bone as well as sensing of the total pelvic load.

Haffner (1985) has analyzed the test data from 84 cadaver experiments in which the predominant dynamic measure of pelvic loading was pelvic acceleration. The goal of the work was to develop a function for the prediction of pelvic fracture probability using lateral pelvic acceleration and age data. Two functions were developed, one based on peak acceleration and age and the other based on maximum pelvic strain and age. The maximum pelvic strain was computed from the acceleration-time history using a simple spring-mass-damper model of the pelvis. The data were analyzed statistically using the maximum likelihood approach. It was found that a Weibull distribution representation of the data yielded a higher maximum likelihood value than did a normal distribution

assumption, and the maximum pelvic strain approach gave a higher maximum likelihood value than did the peak acceleration approach.

Data were also presented showing the relationship between pelvic force and peak pelvic deceleration in those tests where both were measured. Using the peak pelvic acceleration and age function, the peak acceleration value for a 20% probability of fracture at an age of 45 years is 138 G. This corresponds to a peak-force level of approximately 15.8 kN (3550 lb) scaled to the AATD anthropometry. This load value is related to a well-distributed load and does not take into account the possibility of local loading, such as at the hip joint. In order to account for local loading in the AATD, where three independent load cells will be used, a total load limit value of 15 kN (3375 lb) is recommended, but with the provision that no single load cell value exceed 5 kN (1125 lb).

Lower Extremities. The mechanisms of injury to the lower extremities due to blunt loading involve either fracture of bony structures or disruption and dislocation of joints by damage to ligamentous structures. The mechanical properties and failure modes of long bones have been studied extensively, while information on joint ligamentous structural response and failure is limited. For the knee/femur/pelvis complex, tolerance data consists primarily of axial loads along the femur. The lateral bending response of the long bones (femur and tibia) can be used to define their lateral loading tolerance in terms of a maximum bending moment. No biomechanical tolerance data are available for the hip joint, but fore-and-aft shear load and displacement limits can be defined for the knee joint.

An ideal lower extremity design would allow measurement of forces and moments in the upper leg, knee, and lower leg as well as motions in the joints. The AATD lower extremity design provides for the measurement of upper leg loading using a six-axis (three forces and three moments) load cell. The lower leg design will also incorporate multi-axial load and moment measurement. The shear loads acting across the knee joint can be determined using the load-cell data from the upper and lower legs, and the effect of the shear load can be determined from the knee shear-motion control element if desired.

The axial loading tolerance of the femur has traditionally been characterized by a compressive load limit, even though the failure of the bone material is due to tensile stresses from femoral shift bending or from wedging and bending of the femoral condyles by the patella. Tolerable load values reflect the possibility of bending failure due to long load durations and other forms of bone failure, such as patellar and condylar fractures at short load durations. If measurements of bending moments are made in addition to axial force measurements, then bending failure can be monitored by the bending moment measurement, and the axial loading failures can be monitored by axial load measurement. This would allow the present axial force limit of 10 kN (2250 lb) for the femur to be retained.

Transverse bending data on the failure of long bones are given by Messerer (1880) and Yamada (1970). Messerer tested specimens from only six male subjects, while Yamada reports on tests with femurs from 35 subjects. Messerer found a mean failure moment in transverse three-point bending of 310 N·m (229 ft·lb), while Yamada gives a mean value of 211 N·m (156 ft·lb). The large difference between the values may be related to the differences in anthropometry of the two groups. Both studies also give the failure stress values obtained by determining the cross-sectional geometry of the bone at the failure site and applying the relation:

$$\sigma = \frac{Mc}{I}$$

where: σ = maximum bending stress
M = maximum bending moment
c = distance from the bending axis to the point of maximum stress
I = area moment of inertia of the cross section

The ratio M/σ is equal to I/c, which is called the section modulus and is determined by the cross-sectional geometry.

Messerer gives an average maximum stress value of 153.5 MPa (22,246 psi), while Yamada gives a value of 189.3 MPa (27,435 psi). Calculating the section modulus for the average values of each data set indicates that the bones in Messerer's study had a section modulus about 1.8 times as large as that reported by Yamada. Since the subjects in Messerer's study were more likely to be similar to the AATD anthropometry, Yamada's maximum moment values should be adjusted by the 1.8 factor. Yamada also gives the standard deviations on the data for each age group, the 40- to 49-year-old group being the most representative for the AATD. The maximum bending moment value associated with the mean failure load of 2466 N (554 lb) minus two standard deviations (49 N) is 203 N·m (150 ft·lb). Thus, the scaled reference limit for the transverse femur bending moment would be 366 N·m (270 ft·lb).

Similarly, the tibial bending moment data from Yamada can be adjusted by the use of the Messerer data. This yields a scaled reference limit for the transverse tibia bending moment of 244 N·m (180 ft·lb).

Viano et al. (1978a) studied shear loading through the knee joint due to proximal tibial impacts. Using a padded moving-mass impactor to produce direct impacts to the proximal tibia at 6 m/s (20 ft/s), fractures of the tibia and fibula or ligament damage were produced at force levels of 3.28 to 6.89 kN (737 to 1549 lb). In the case of male cadavers, none of the failures occurred below 4 kN (900 lb). In a subsequent sled test program, a bolster load of 4 kN per knee produced knee joint failure in an 81-year-old 54-kg (119-lb) male of 161-cm (63-in) stature. This load would scale to 5 kN (1125 lb) for the AATD anthropometry. A 4-kN reference shear load for the tibia in conjunction with the bending moment limit of 244 N·m will serve to limit the allowable knee shear forces to tolerable levels. Additional limits on knee shear loading can be achieved by the use of limits on knee shear-control element displacements. A limit of 15 mm (0.6 in) has been suggested by Mertz (1984) based on the Viano et al. static test results.

DATA ANALYSES TO IMPROVE TRAUMA ASSESSMENT CRITERIA

Head Injury Criteria. Injury criteria for the head are currently based on translational accelerations during direct impact to the head. Rotational accelerations of the head during indirect impact have also been studied to assess their role in producing head injury, but threshold values for angular acceleration and angular velocity are not well established for man. The interactions of translational and rotational motions in the production of brain injury have not yet been addressed in research studies.

In general, the inertial body forces acting on an element of brain tissue are the result of the acceleration of that element. That acceleration is a function of the translational and angular accelerations and the angular velocity of the head coordinate system, as well as the position of the element relative to the head coordinate system. How these quantities interact and combine to produce stresses in the brain tissue depends upon

the mechanical and inertial characteristics of the brain and skull as well as the waveform and phasing of the kinematic parameters that describe a particular head motion.

Newman (1985) has hypothesized that the onset of brain damage will occur when the combined effect of translational and rotational acceleration is to produce a stress that exceeds some critical stress value. Using the analogy of maximum shear stress failure theory, where failure occurs when the square root of the sum of the squares of the tensile stress ratio and the shear stress ratio exceeds a critical value, Newman suggests a similar form for combining translational and angular accelerations. The result could be called an acceleration influence plot, where translational accelerations are plotted versus the corresponding angular acceleration values at each instant in time. A boundary, defined by threshold values of both translational acceleration and rotational acceleration, would be elliptical in form as outlined by the square root of the sum-of-the-squares approach given for combining stress ratios.

In order to investigate empirical approaches to understanding the combined effects of translational and rotational motions on head injury and to develop a better analytical understanding of such effects, studies were undertaken with the following features.

1. As a guide to the analysis of experimental data, a simplified two-dimensional finite element (FE) model of the skull/brain system, capable of demonstrating the effects of rotational and translational motions of the brain within the skull, was developed. The simulation was restricted to midsagittal plane motion.

2. A set of experimental head-impact data from human cadaver experiments was selected for defining translational and rotational acceleration ranges to be used with the model.

3. Experimental cadaver head-motion data from direct impacts and indirect impacts were analyzed in the influence plot manner to aid in developing that method of interpreting head motion data. The results of the modeling were also used to study methods of interpreting experimental data.

Development of a Two-Dimensional Skull/Brain Model. Several FE models of the head have been developed in the last ten years. The trend was to model more accurately the shape of the brain and to include various constituents of the brain. The models were either two- or three-dimensional. For most of the models, their validity was based on their ability to accurately predict stress or strain in the brain or the frequency response of the brain.

The head model developed by Shugar (1977) is an example of a versatile model capable of being adapted to suit a variety of purposes. It was able to simulate direct or indirect impact, and its results were compared with experimental data. The responses of the skull and brain were predicted for a variety of dynamic conditions, totaling 75 runs. The development of the model included the modifications of the isoparametric elements in order to simulate the nearly incompressible properties of the brain tissue. It was a three-dimensional model with an option for scaling, by using a preprocessor for automatic mesh generation. It emphasized wave propagation as one of the mechanisms of injury and showed that the FE program, FEAP (Finite Element Application Program), was an accurate computational code. Several other parameters were computed, including skull principal stresses for different types of impact.

Other FE models were developed by Khalil and Viano (1977), Khalil and Hubbard (1977), and Ward (1982). Discussions of the requirements for a viable FE model were given by Khalil and Viano (1982) and Ward (1981).

The development and implementation of the simplified two-dimensional model for this project is described in detail in an appendix to this report and is only summarized here. First, an attempt was made to determine the most realistic set of material properties for the skull, cerebrospinal fluid (CSF), brain, muscles, and neck. Selection of these values was based on the dimensions of the FE mesh, data given in the literature, and the response of the model compared with experiments. The FE code used was FEAP. The material properties and model geometry were then refined, and production runs were made to produce stress and strain results due to a variety of impact conditions with a pulse duration of 10 ms. In a final activity, longer pulse duration impacts (30 ms) were simulated.

A total of eight preliminary runs were made to study the response of the model. They represented impacts that resulted in linear accelerations between 144 and 560 G and angular accelerations between 6,200 and 40,000 rad/s^2.

Based on the results of this initial model, changes were made to the skull geometry to eliminate high stresses at the corners within the skull, and the base of the skull was enlarged. This resulted in a model with 156 nodes and 137 elements, including 36 skull elements, 34 CSF elements, and 67 brain elements, which could be used to identify regions of high stress and strain in the brain (shear and normal) due to an impact. The material behavior of the head tissues was modeled using ELMTO2, which can represent a nonlinear anistrophic viscoelastic continuum.

The modified model was used to make a total of 35 short time-duration runs. The tentorium was first introduced in Run No. 15 and the bar element neck in Run No. 19. The neck was changed to quadrilateral elements in Run No. 30. The linear acceleration range was 100 to 325 G and that for angular acceleration was 4,000 to 30,000 rad/s^2. These acceleration values were computed for the crown (top of the head), so that they could be compared with experimental data taken from the same area.

In the final activity of this study, a series of eight runs were made with an impact duration of 30 ms. Six were made with the neck represented by two-bar elements and muscles, and two were run with seven quadrilateral elements without muscles. The typical force pulse was a half-sine wave of the same magnitude as that used in the shorter duration runs. The duration of the runs were 40 ms to ensure that all peak responses had occurred before the run was terminated.

The head and neck model was subjected to only frontal impacts, as no frontal oblique runs were made with that model. The resulting angular accelerations were significant, although the exact applied torque could not be computed. For pure rotation of the head (with no neck), high angular accelerations (20,000 to 30,000 rad/s^2) were attained, but the range of linear acceleration was the same as that for linear motion (150 to 300 G). The effect of adding a neck was a tendency to produce both lower angular and translational accelerations.

In most cases of pure rotation, there were no high shear strains at the top of the brain. These were encountered on each side of regions of high normal stress. The high strain areas were, in order of significance, the base of the corpus callosum, the forehead, the occiput, and the cerebellum. The same areas were involved in frontal, frontal oblique,

and occipital impacts. It should be noted that, in occipital impact, the location for maximum stress was in the cerebellum.

The top of the brain was one of the most protected areas, having low stresses and strains. This is due to the fact that the lowest peak linear and angular accelerations were found in this area. This is true even in the head/neck model in which the crown angular accelerations were still low relative to other areas of the brain in the same run.

In the absence of a tentorium, there were no local motions and no local areas of high stresses or strains near the region of the tentorium. The brain behaved as a homogeneous material. With a tentorium, there were local motions near the base of the occiput and in the cerebellum where there were high stresses and strains. This was especially true for frontal impact due to high peak angular accelerations in comparison with other areas of the brain. The tentorium also caused higher stresses and strains in the brain stem.

The acceleration response and the resulting stresses and strains due to frontal impact and those due to the application of a pure torque were quite different. The pure torque runs fell into a distinct group, while the frontal impact runs were concentrated in two groups. The pure torque runs exhibited high angular accelerations and low translational accelerations, while one group of frontal impacts exhibited low angular and translational accelerations and the other group had higher translational accelerations. The frontal oblique impacts exhibited high angular and translational accelerations. For linear acceleration, the regions of high strain were found in the inferior portion of the corpus callosum, along the anterior fossa, and on the postero-superior surface of the cerebrum. Those due to angular acceleration were found in the forehead and the occiput.

For validation, the results of the model were compared with experimental data, and the input pulse to the model was modified until a good correlation in head kinematics was observed. That is, the linear and angular accelerations of the head were to be made close to those measured experimentally. Data reported by Nahum et al. (1981), Nusholtz et al. (1984), and Prasad and Daniel (1984) were used as a basis for the selection of input conditions. The simplicity of the model, the inaccuracies in the geometry and in the thickness of the skull, and the lack of information on material properties all contributed to errors in prediction. Validation is therefore restricted to a comparison of trends in strains and stresses. The model is also incapable of simulating skull fracture, although it can predict large deformations. In this section, comparisons will be made with acceleration data, measured pressures, and experimentally observed AIS values.

The validation of acceleration results was based on a comparison of model results with experimental data extracted from Nusholtz et al. (1984). Eight runs were conducted with $5 < dT < 15$ ms. Six of the eight runs were paired with an equivalent run using the model. The criteria for pairing were angular and linear acceleration as well as applied load. A regression analysis was performed to correlate model and experimental data—namely, linear acceleration, angular acceleration, and angular velocity. The correlation for all three variables was good, and it can be concluded that the model was capable of reproducing the desired experimental runs, which cover a variety of impact conditions.

The validation of normal stresses was based on the comparison of results from model runs, with experimental data taken from Nahum et al. (1981). The procedure did not involve a direct comparison of paired runs. Nahum et al. found regression lines between intracranial pressure and the input force for frontal impact at five locations in the brain. At four of the five locations, a comparison with results could be made. They are at the frontal region, the equivalent parietal region (top of the head), the occiput, and the

posterior fossa. A set of similar regression lines from model results was determined for three areas of the brain. Because of the large scatter in the results for the parietal region, a regression line was not drawn for this set of model results. The regression lines were compared, and there was excellent correlation between experimental and model results for pressures in the frontal region. For the other regions, the match was not as good.

For a validation of injury predictive capability, frontal impact injury data were plotted on the same graph with model results. There is a monotonic increase in stresses in the occipital area that correlates qualitatively with experimental data. These stresses represent an injury criterion in the form of the sum of the absolute values of the maximum normal stresses in the forehead and the occiput. No rotational impact results were included in this figure. Due to the scarcity of experimental data, no quantitative analyses could be carried out.

Further investigation of the injury predictive capability of this model was done using the series of eight long-duration runs. Of these eight runs, six simulated frontal impact, one frontal oblique impact, and one purely rotational impact. There were three frontal impact runs in which a neck was included in the simulation.

High shear strains were found to occur at the top of the brain and on the orbital floor for frontal impact with or without a neck. For pure rotation, high shear strains were found in the forehead, the occiput, the medulla, and the corpus callosum. The strain was positive in the midbrain and negative at the top, resulting in a possible tearing of the brain tissue in the corpus callosum. The shear strains in these areas were almost zero due to frontal impact of a free head. For the head/neck model, the strains were zero during the first peak and, except for the forehead, reached a significant peak value during the second peak due to the effect of the neck.

An analysis of the injury potential of stress or strain in different parts of the brain can be made by plotting these values on an (a,α) influence plot. For the orbital floor, the top of the brain, the cerebellum, and the midbrain, lines of constant shear strain were drawn. Lines of constant stress could also be drawn for the forehead and for the occiput, and orthogonal lines of constant stress and strain could be drawn. Since no experimental data are available, it is not clear which of these areas contribute heavily to brain injury. However, it can be said that the occiput and the forehead are the only areas where stress can be an injury criterion. For the other areas, strain is a more likely candidate for injury assessment.

In conclusion, the model yielded realistic results in terms of head kinematics and intracranial pressures, but only short duration runs ($dT < 15$ ms) could be compared with experimental data. The neck is an important part of the model, because it controls the kinematics of the head, and the tentorium is required to demonstrate independent motion of the cerebrum and cerebellum. Skull deformation is an important element of the model. It not only affects the computed angular acceleration but also is a source of brain deformations and stresses at the impact site.

The top of the brain experiences low stresses and strains in comparison with other areas of the brain. For long duration impacts, stress is a function of linear acceleration in the forehead and the occiput because the lines of constant stress are almost horizontal. Shear strains are functions of both linear and angular acceleration at the top of the brain, the orbital floor, the cerebellum, and midbrain.

Influence-Plot Analysis of Head Impact Kinematics. Three-dimensional cadaver head-impact-motion data from both direct impact to the head and from indirect impact during whole-body restraint systems tests were analyzed and displayed in (a,α) influence plots. The data sources were a series of direct impacts to the top of the head, conducted

for NIOSH (Alem et al. 1984) to study neck injury, and a series of three-point harness sled tests conducted for General Motors (Alem et al. 1978). In both series, the head was instrumented with a nine-accelerometer array.

Programs were developed for using test data in the NHTSA format to analyze the nine-accelerometer data and provide transformed head center-of-gravity three-dimensional rigid-body motion information. A total of twelve direct head impacts and five indirect impact head motions were successfully analyzed. The test numbers and their associated test conditions are given in Table 24.

TABLE 24

HEAD MOTION INFLUENCE PLOT DATA BASE

Test No.	Test Severity
Indirect, Three-Point Belt	
A-925	25 km/h, 10 G
A-926	25 km/h, 10 G
A-938	32 km/h, 10 G
76B003	32 km/h, 10 G
76B006	50 km/h, 20 G
Direct, Top of Head	
81H411	7.2 m/s, 5.1 cm padding
81H412	7.1 m/s, 5.1 cm padding
79H201	8.0 m/s, 5.1 cm padding
79H202	8.0 m/s, 5.1 cm padding
79H203	8.0 m/s, 5.1 cm padding
79H204	8.0 m/s, 5.1 cm padding
79H205	8.0 m/s, 5.1 cm padding
79H206	8.0 m/s, 5.1 cm padding
81H410	9.0 m/s, 5.1 cm padding
81H408	9.7 m/s, 5.1 cm padding
81H402	10.9 m/s, 5.1 cm padding
81H403	10.9 m/s, 5.1 cm padding

The results of the (a,α) influence plot analysis provide insight into the general form of such plots for varying levels of impact severity. Figure 40 shows the results of the five indirect-impact three-point-harness restraint tests with severities ranging from 25 km/h, 10 G to 50 km/h, 20 G. The (a,α) plots for these runs are bounded by angular accelerations of 3500 rad/s^2 and translational accelerations of 80 G. The arrows drawn on the curves are to aid in visualizing the development of the curve with time. Brain injuries were not assessed in those tests, but their severity levels would not be expected to produce brain damage in the human.

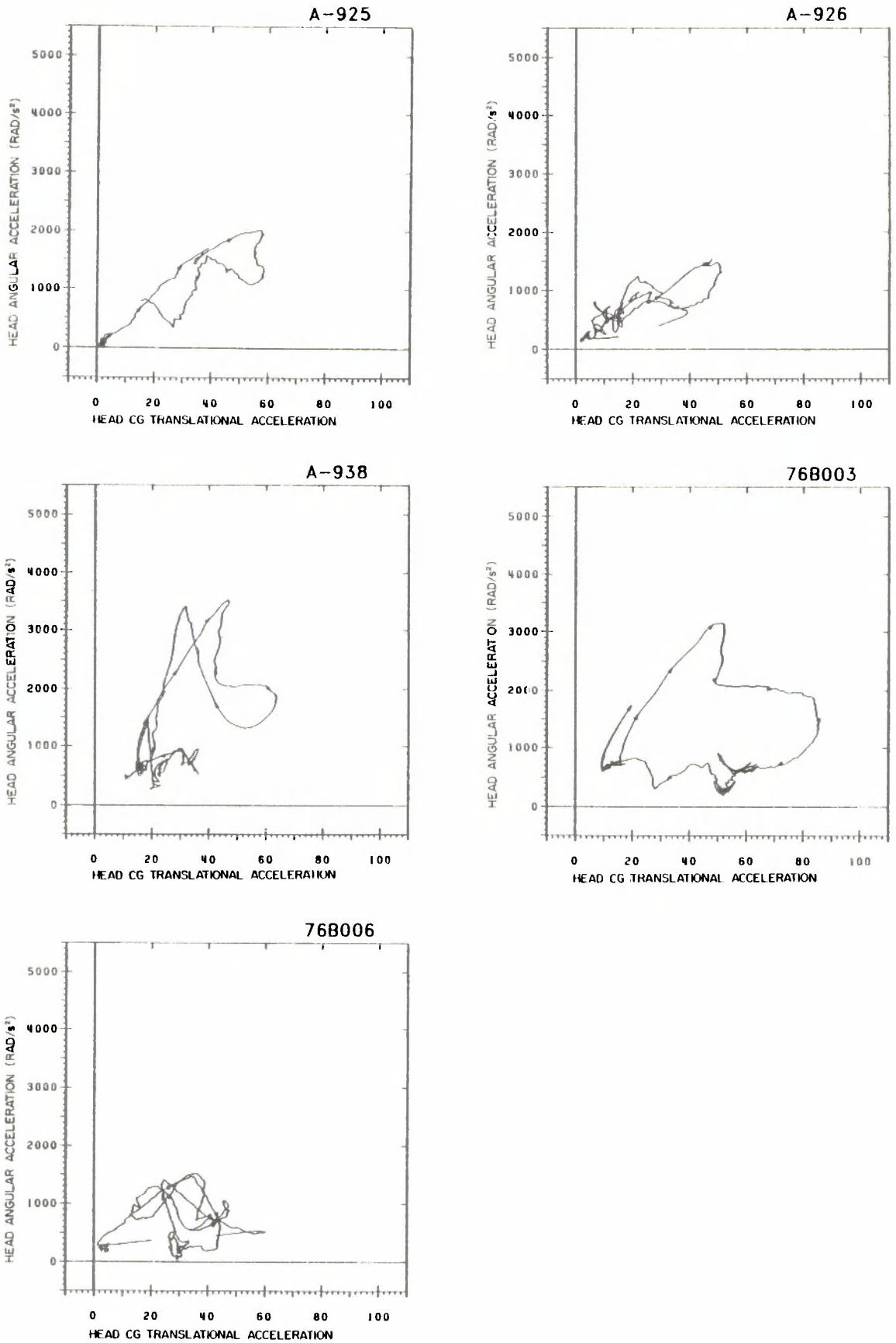

FIGURE 40. (a,α) influence plots for three-point-belt sled tests.

The direct head-impact influence plots produced results that overlap those of the indirect impact tests. Figure 41 shows the two lowest velocity (7.1 and 7.2 m/s) tests, which are bounded by $\alpha = 2000$ rad/s^2 and a = 40 G. Figure 42 shows the results of six 8.0-m/s impacts, which are bounded by $\alpha = 4000$ rad/s^2 and a = 80 G. Finally, Figure 43 shows the results of four high-velocity (9.0 to 10.9 m/s) impacts which are bounded by $\alpha = 8000$ rad/s^2 and a = 200 G.

All of the above results were filtered at 200 Hz in order to eliminate transducer vibration effects, which tend to produce very complicated patterns, such as shown in Test No. 81H410. Of all the direct impacts shown, Test No. 81H403 had the highest HIC value of 1031 while none of the others had HIC values greater than 503. The general trend throughout all these tests was for the angular accelerations and the translational accelerations to both grow with increasing impact severity. Test No. 81H408 is an exception while the translational acceleration remained similar to that of the lower (8.0 m/s) velocity tests. Because the direct impacts were to the top of the head for the purpose of studying neck injury, the brains of the test subjects were not pressurized and therefore no injury assessment was performed.

Conclusions. The development of improved head injury criteria, which include the effects of angular as well as translational acceleration, will require continued experimental and analytical effort. The translational-acceleration/angular-acceleration influence plot has shown promise in displaying the combined effects of the two kinematic parameters. Much more experimental data are needed, however, to define boundaries between injury levels on the plots. In addition, the method of plotting the acceleration parameters eliminates time from the display. Methods need to be developed to include time-duration effects for use with influence plots. One such method might be the determination of the duration of time the plot exceeds a predetermined injury threshold boundary.

Human experimental injury data is almost nonexistent, and much more data from animal and human cadaver experiments are needed, where the measurement of both impact kinematic parameters and injury assessments are made. The finite element modeling of the head is a valuable tool for interpreting experimental data and will play an increasingly important role in injury assessment research.

Finally, most real-world head impact situations include significant components of both translational and rotational accelerations, and the combined effect of these parameters on the production of brain injuries must be included in any improved head injury assessment technique.

Thoracic Injury Criteria. This analysis was aimed at determining a universal thoracic injury criterion for frontal impact that is independent of the impacting surface. Data from cadaver thoracic impact tests performed under a variety of impact conditions over the last 15 years were reduced to a common format for analysis, and the 1980 Abbreviated Injury Scale (AIS) was used as a basis for injury assessment.

Impact tests included in this analysis were conducted at the University of California at San Diego (UCSD), the University of Michigan (UM), Calspan Corporation, and Wayne State University (WSU). The data set was compiled and analyzed using a microcomputer.[3] Table 25 identifies the test series and associated symbols used in some of the graphs in this report.

---

[3]The assistance of R.H. Eppinger of NHTSA and D.C. Viano and I.V. Lau of GM in assembling these data is gratefully acknowledged.

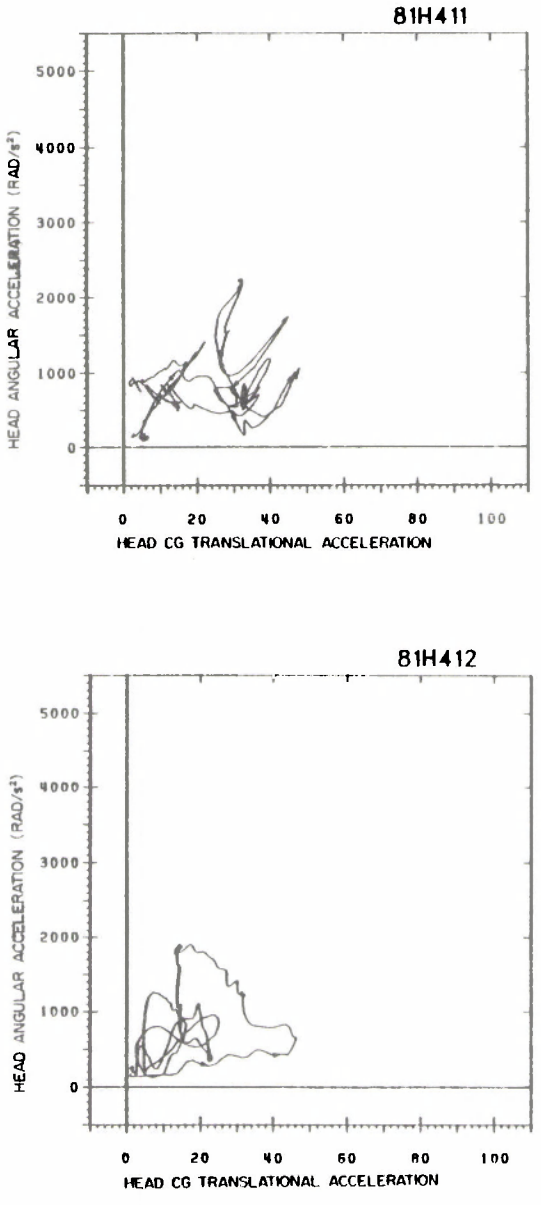

FIGURE 41. (a,α) influence plots for direct top-of-head impacts at 7.1 to 7.2 m/s.

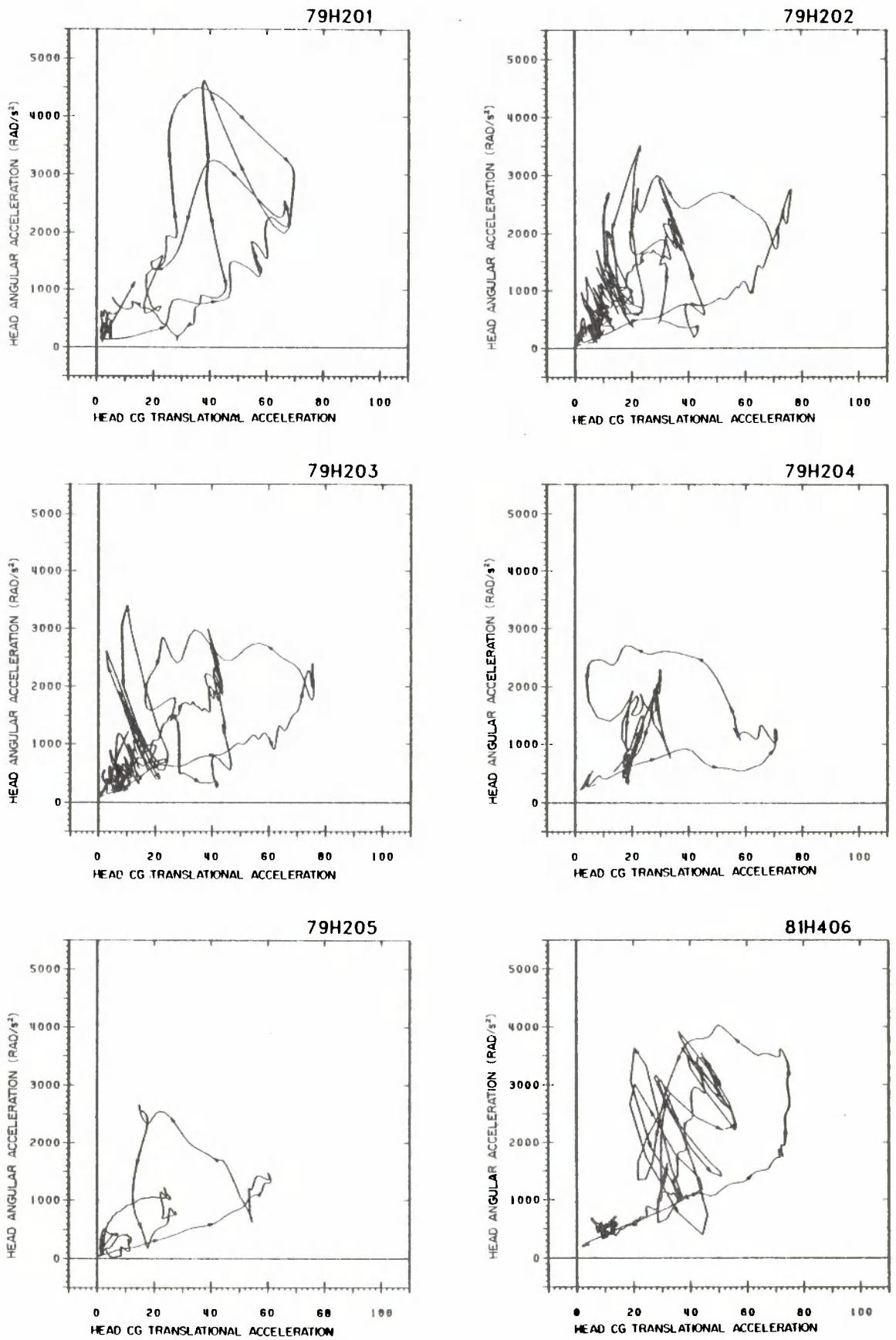

FIGURE 42. (a,α) influence plots for direct top–of–head impacts at 8.0 m/s.

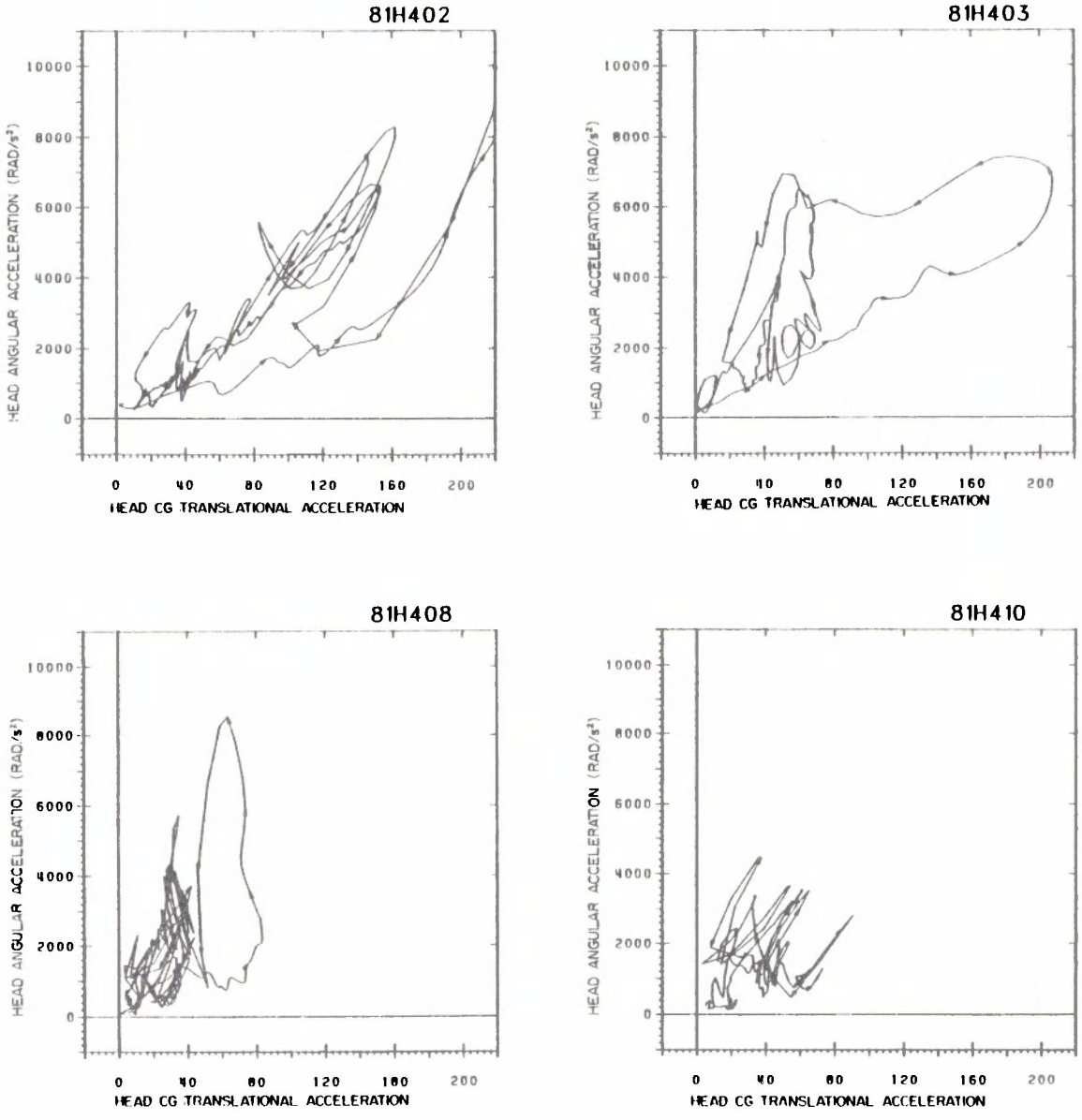

FIGURE 43. (a,α) influence plots for direct top-of-head impacts at 9.0–10.9 m/s.

TABLE 25

IMPACT MODE AND IDENTIFYING SYMBOLS
FOR VARIOUS THORACIC IMPACT SERIES

Symbol	Run Description
*	UCSD pendulum impacts, sponsor GM
#	UM pendulum impacts, sponsor NHTSA
^	WSU low-level pendulum impacts to volunteers
$	Calspan pendulum impacts, sponsor NHTSA
&	UCSD (Schneider) belt impacts
@	WSU airbag sled runs, sponsor NHTSA
?	SRL run 29
%	WSU knee-bolster/belt sled runs, sponsor NHTSA
+	WSU unrestrained driver impacts with steering wheel, sponsor GM
A, etc.	GM pig pendulum impacts

There was some difficulty assigning a consistent set of AIS values to the various cadavers. The data set contains both the thoracic AIS and the maximum AIS, which may be related to injury to a different body region. In this analysis, the thoracic AIS or the abdominal AIS was used if the latter was attributable to frontal chest impact. The AIS values for the UCSD data, however, had first to be converted from the 1976 version to the 1980 version. An additional problem, applicable to all data, related to the occurrence of flail chest. Initially, AIS-4 was assigned to multiple rib fractures in excess of 12 (including the sternum), but this number was later decreased to 8 based on Viano et al. (1978b), which indicates that thoracic injuries are independent of the number of ribs fractured after 8 or more occur. In this report, graphs using these revised AIS values show "revised thoracic AIS" on the axis label.

A variety of injury parameters and combinations thereof were available as possible candidates for a thoracic injury criterion. These included kinematic quantities such as rib or sternal acceleration, spinal acceleration, chest or sternal compression (C) as a percentage of the total chest depth, chest velocity (V) relative to the spine, and the VC_{max} parameter proposed by Viano and Lau (1985). Kinetic variables included the peak impact force, the energy absorbed by the chest, the energy delivered by the striker to the chest, and various normalized versions of these quantities.

The concept of "absorbed energy" is described by Eppinger and Marcus (1985) and originated from a desire to find a parameter that was applicable to all forms of impact, such as impacts with a pendulum, steering wheel and column, an airbag, or a shoulder belt. It uses conservation laws to compute the net energy absorbed by the thorax. "Delivered energy" is an earlier version of the same concept. It is, however, only applicable to pendulum impacts. The VC_{max} parameter was proposed as a viscous component of resistance by the thorax and is considered to be a prime indicator of thoracic injury if chest compression is not excessive.

Most of the effort in this study was directed toward a search for the parameter that is the best predictor of thoracic injury for all forms of impact to the chest. Table 26 lists

all of the parameters that were tested for this predictive capability. In this table, the term "normalization" has a special meaning. The process involves dividing a particular variable by its average so that its magnitude is close to unity. The reported results are in chronological order. In the beginning, the only available injury and physical data were from tests performed at UCSD, in which unembalmed cadavers were impacted by a pendulum. More data were included in the analysis as they became available. The final list of runs contains data from four modes of impact: pendulum, air bag, shoulder belt, and steering system.

The criterion for a good predictive parameter was the correlation coefficient for least squares fit of the parameter when plotted against thoracic AIS. As indicated in Table 26, a large number of plots were made to determine if a selected parameter looked promising as an injury predictor. If the parameter was not capable of separating the low AIS injuries from the higher ones, using visual inspection, it was discarded. If it showed some promise of being a predictor, a linear regression analysis was performed to determine the correlation coefficient and the equation of the least-squares line.

Among the more promising candidates were VC_{max}, absorbed energy, and peak impact force. Both the energy and force parameters were modified by being divided by the product of the mass of the subject, the area of impact, and duration to reach its peak value. The viscous parameter (VC_{max}) performed well only for pendulum impacts, as shown in Figures 44 and 45. The addition of pig data acquired under General Motors sponsorship to the cadaveric data set, however, lowered the correlation coefficient from 0.806 to 0.710 (Figure 45). The peak-force parameter (Figure 46) had a reasonable correlation coefficient only if three of the low-mass, high-velocity UCSD impacts were not considered in the regression analysis. These were runs 27, 28, and 29. The absorbed-energy parameter is also a good predictor, if the unrestrained steering wheel impacts are not considered, as shown in Figure 47. The chest compression in those nine runs was very high (>70%), and the method of computing absorbed energy may not be applicable.

For the analyses listed in Table 27, the AIS values were revised as described above. The more promising parameters were replotted against this revised AIS for the thorax. The correlation coefficient for the peak-force parameter dropped from 0.563 to 0.515 (Figure 48). All four runs involving low mass and high velocity were excluded from the regression analysis. If they were included in the analysis, the coefficient was 0.230. The absorbed-energy parameter was also slightly less well correlated with AIS using the revised values. The correlation coefficient fell to 0.414 for thoracic impacts with the pendulum, air bag, and shoulder belt, as shown in Figure 49. It was even more poorly correlated with the revised AIS if the unrestrained steering-wheel impacts were included in the data set.

TABLE 26

LIST OF VARIABLES INVESTIGATED AS THORACIC INJURY PREDICTORS

Variable Name	Description/Remarks	Cor Coeff (r)
	Cadaver Pendulum Impacts	
VC/(1-C)	Viscous parameter (See Figure 44)	0.806
VC/(1-C)	Normalized by average value	0.806
VC/M	Normalized value/normal body mass	0.787
VCAGE/M	All values normalized	0.790
VC/M+AGE	All values normalized	
VC+AGE+M	All values normalized	
CNM	Normalized % chest compression	
DNM	Normalized chest compression	
VNM	Normalized chest velocity	
VCNM	Normalized V * Normalized C	
VNM+CNM	Normalized V + Normalized C	
CNM+VNM/10		
CNM+VNM/20		
E.D./M	Energy delivered/mass	
E.D./M+0.03*AGE		
	Pig Pendulum Impacts	
VC	Viscous parameter	0.931
C	% chest compression	0.709
F	Peak impact force	
VNM+CNM	Normalized V + Normalized C	0.780
VNM ^ 2+CNM	Normalized V ^ 2 + Normalized C	
VNM/2+CNM	Normalized V/2 + Normalized C	
0.4VNM ^ 2+CNM		
0.6VNM ^ 2+CNM		
VNM ^ 2*CNM		
REL.ACC.	(Sternal-spinal) acceleration	
STN.ACC.	Sternal acceleration	
SPL.ACC.	Spinal acceleration	
VNM ^ 2		
	Pig and Cadaver Pendulum Impacts	
VC	(See Figure 45)	0.710
CNM		
VNM		
VNM+CNM		
VNM ^ 2+CNM		
9.5VNM+CNM		
0.4VNM ^ 2+CNM		
0.6VNM ^ 2+CNM		
VNM ^ 2CNM		

TABLE 26 (Continued)

Variable Name	Description/Remarks	Cor Coeff (r)
Pig and Cadaver Pendulum Impacts		
D.E./M	Delivered energy/mass	
F * DEFL/M	Force change deflection/mass	
REL. VEL.	(Sternal-spinal) velocity	
VNM ^ 2		
V+C+AGE+M	All normalized values	
Cadaver and Volunteer: Pendulum, Airbag, Shoulder Belt, Steering Wheel		
F	Peak force	
F/M	Peak force/mass	
F/A	Peak force/area	
F/M*	Peak force/mass*area	
F/M*A*dT	Peak force/mass*area* (see Figure 46)	0.563[1]
F/MAdTVEL		
EA/MAdT	Absorbed energy/mass*area*dT (see Figure 47)	0.535[2]
EA/MAdT	Absorbed energy/mass*area*dT	

[1]Excludes three cadaveric pendulum impact runs 27, 28, and 29.
[2]Excludes unrestrained "driver" impacts with steering wheel.

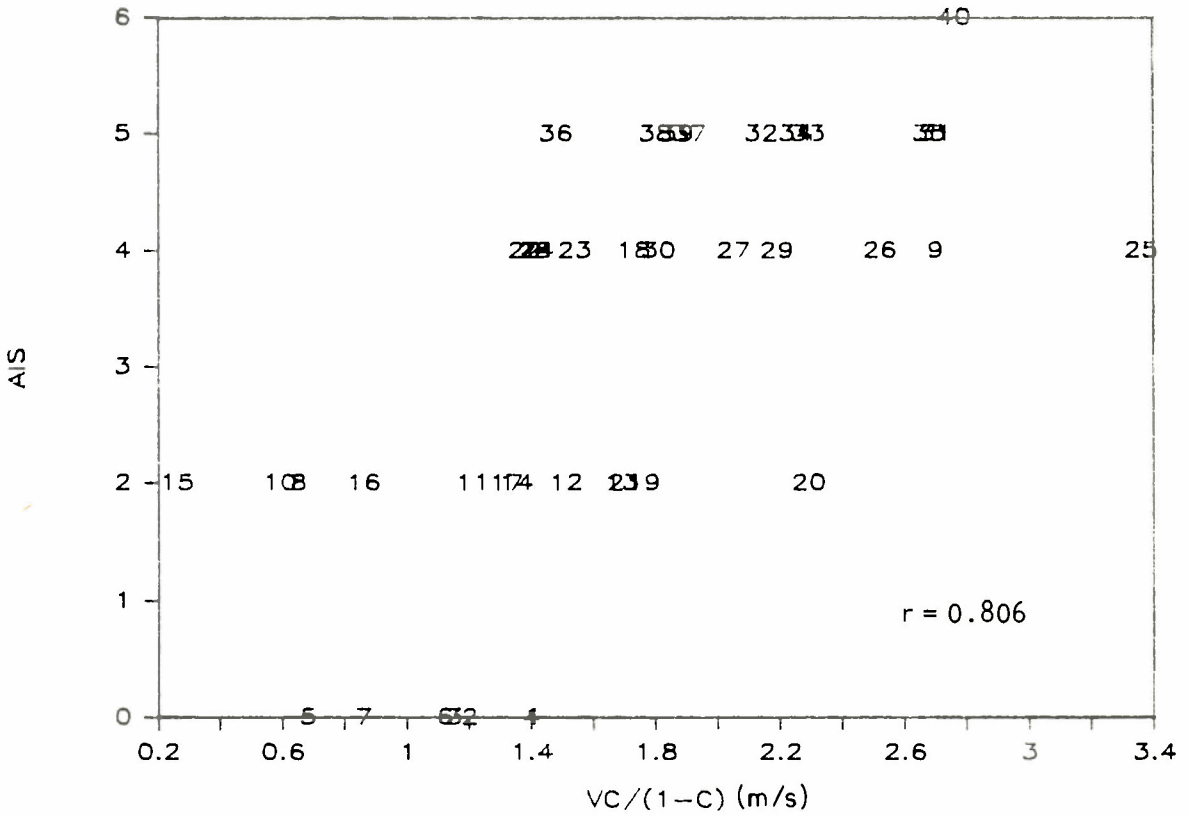

FIGURE 44. UCSD cadaver/pendulum impacts using the viscous parameter as an injury predictor.

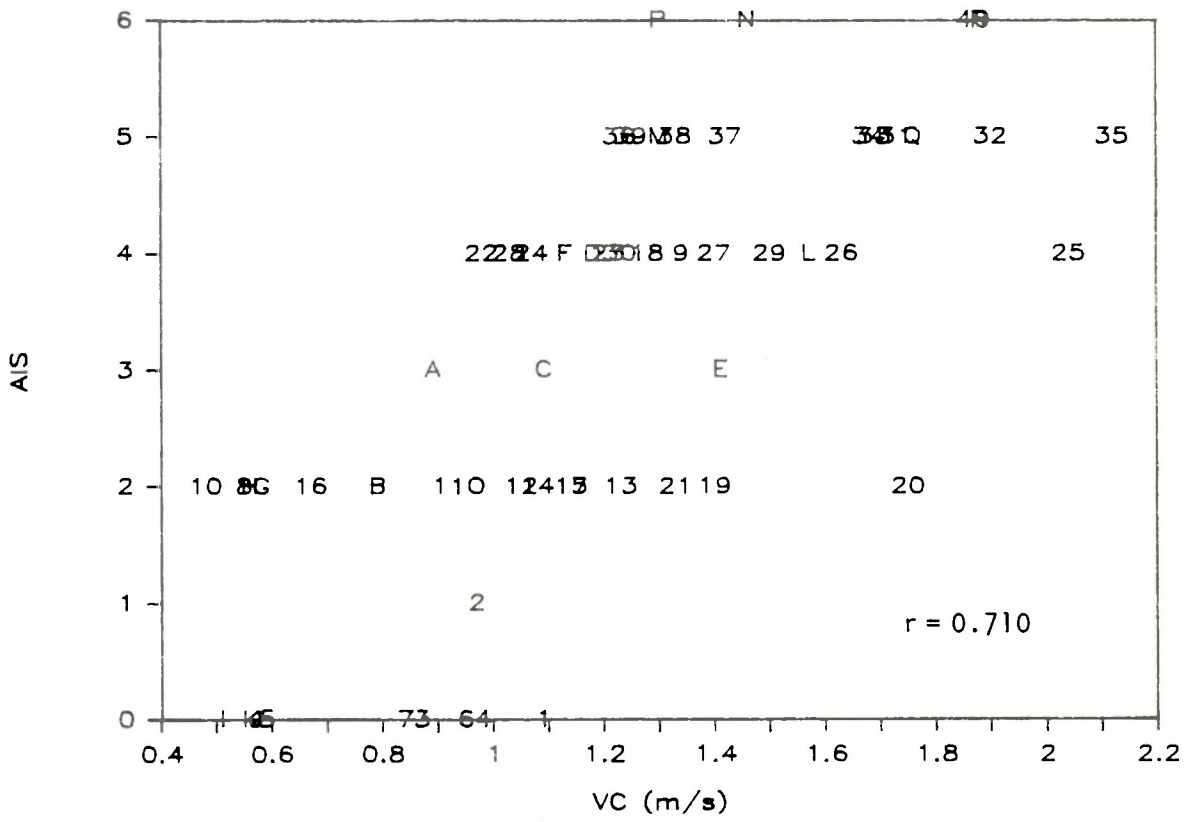

FIGURE 45. UCSD cadaver/pendulum and GM pig/pendulum impacts using the viscous parameter as an injury predictor.

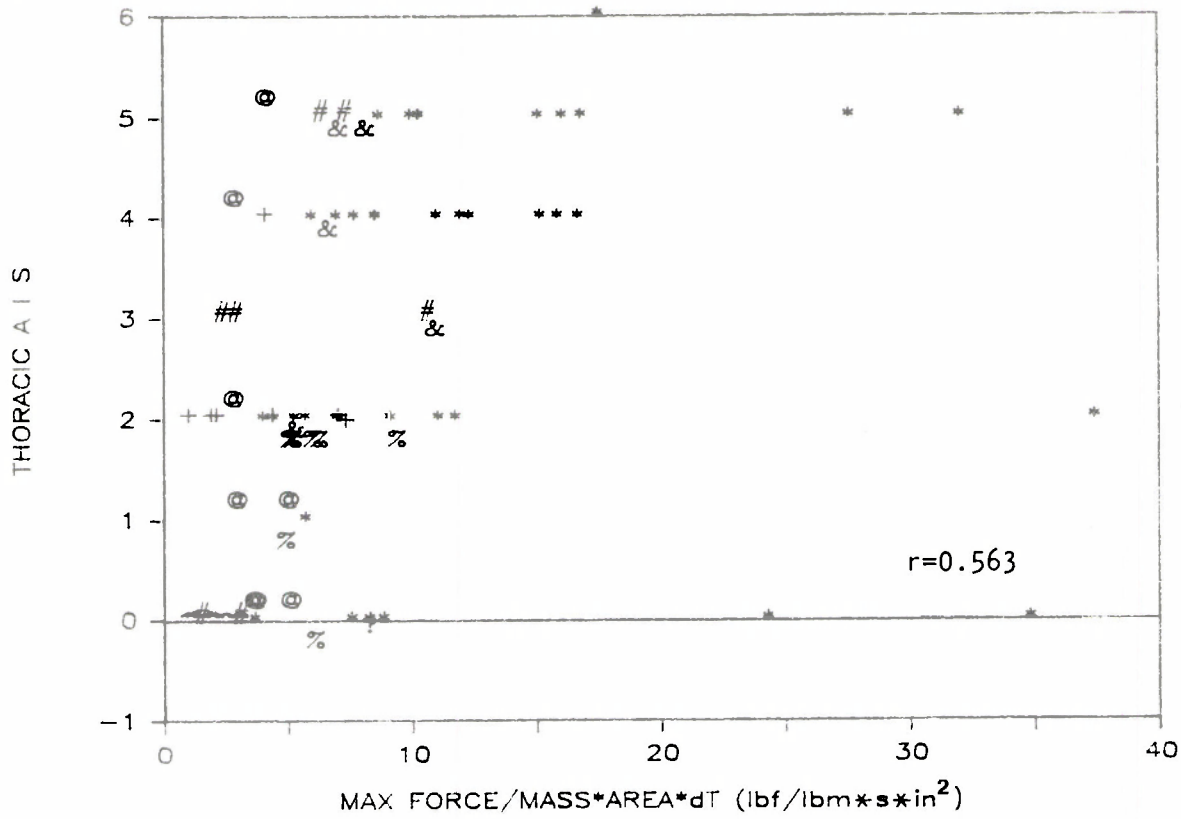

FIGURE 46. Various cadaver and volunteer impacts using peak force as an injury predictor.

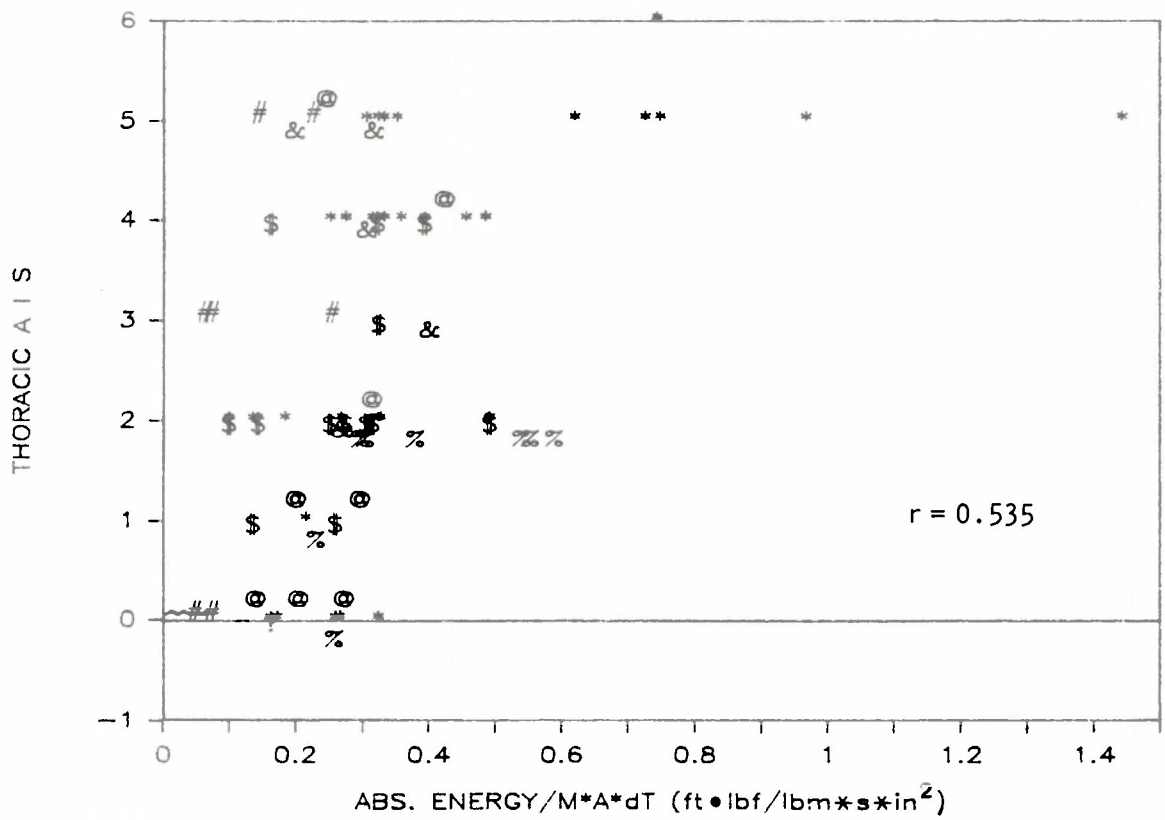

FIGURE 47. Various cadaver and volunteer impacts using absorbed energy as an injury predictor (unrestrained steering-wheel impacts excluded).

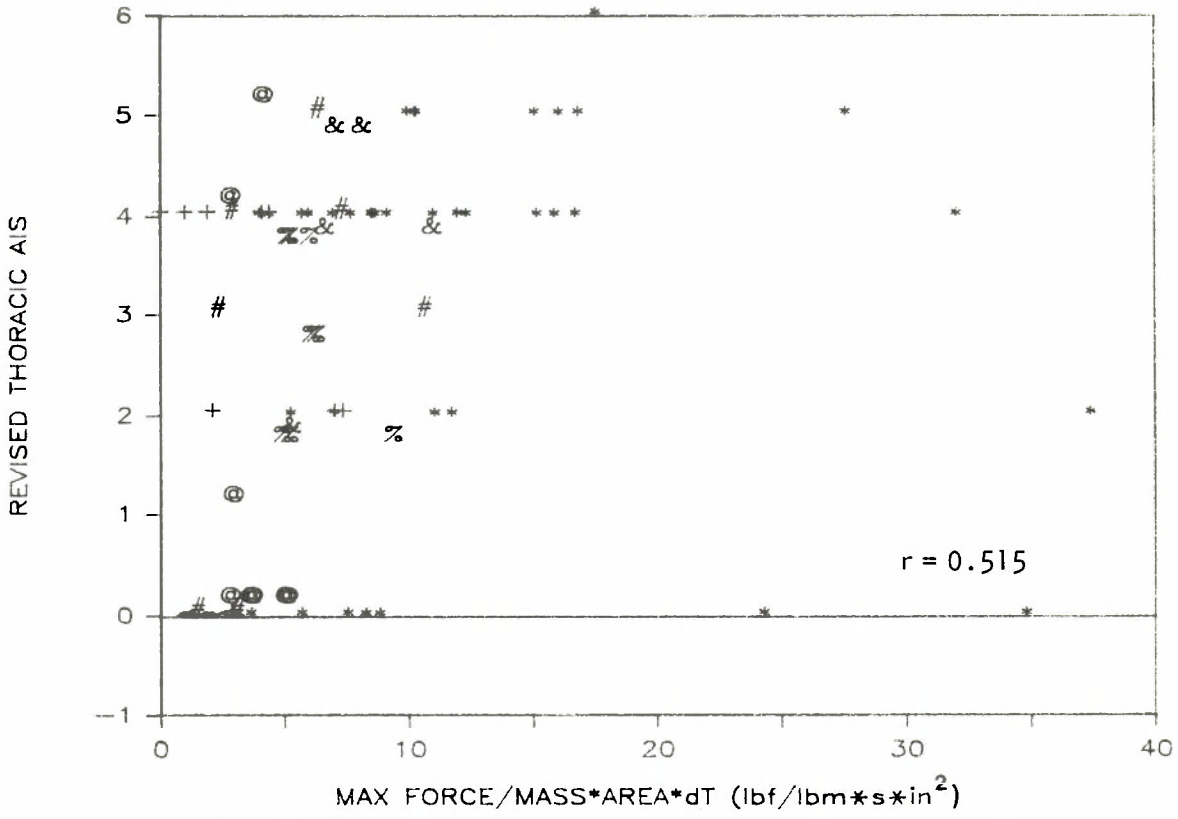

FIGURE 48. Various cadaver and volunteer impacts with revised AIS values using peak force as an injury predictor.

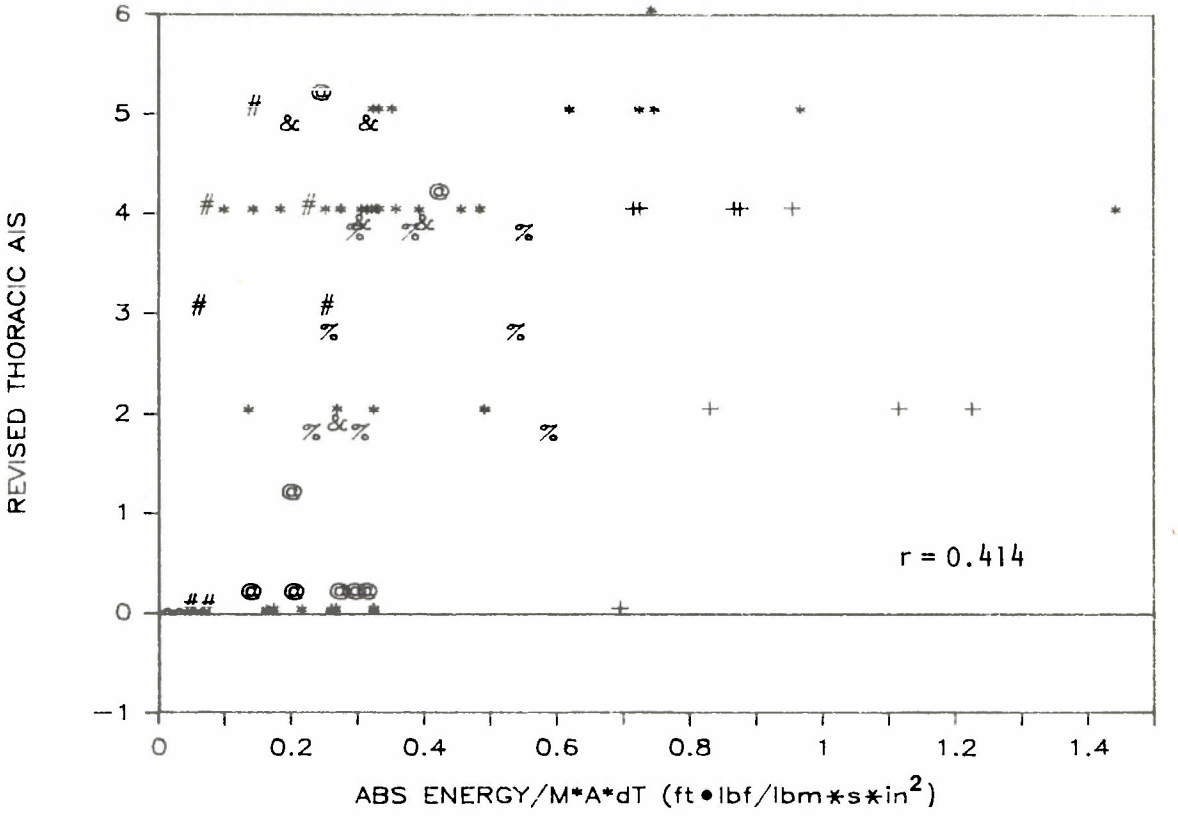

FIGURE 49. Various cadaver and volunteer impacts, with revised AIS values, using absorbed energy as an injury predictor (unrestrained steering-wheel impacts excluded).

TABLE 27

LIST OF VARIABLES PLOTTED AGAINST THE REVISED AIS

Variable Name	Description/Remarks	Cor Coeff (r)
Cadaver Runs: Pendulum, Airbag, and Steering Wheel		
VC	Viscous parameter	
Cadaver and Volunteer: Pendulum, Airbag, Shoulder Belt, Steering Wheel		
V	Peak sternal velocity	
F	Peak force	
F/M	Peak force/mass	
F/A	Peak force/area	
F/MA	Peak force/mass*area	
F/MAdT	Peak force/mass*area*dT (see Figure 48)	0.515[1]
F/M*A*dT	peak force/mass*area*dT	0.230[2]
F/MAdTVEL		
EA/MAdT	Absorbed energy/mass*area*dT (see Figure 49)	0.414[3]
EA/MAdT	Absorbed energy/mass*area*dT	

[1]Excludes four cadaver pendulum runs 26, 27, 28, and 29.
[2]Includes all 82 runs.
[3]Excludes unrestrained "driver" impacts with steering wheel.

In conclusion, a universal thoracic injury criterion was not found in this analysis. The results obtained so far indicate that more than one parameter is probably necessary for predicting thoracic injury due to frontal impact. The inertial, elastic, and viscous injury mechanisms are particularly likely to require a multi-parameter predictor. Candidates include VC_{max} and the absorbed-energy parameters. If a single parameter is to be selected, however, the peak-force parameter is the best overall predictor of thoracic injury.

Further work is needed to include the pig data in the last analysis (Figure 49) using the revised AIS, with the aim of eventually generating a multi-parameter predictor using cadaveric, volunteer, and animal data. In addition, a Weibull analysis should be performed on the data to determine the values of the various parameters for a given level of injury.

APPENDIX

A FINITE ELEMENT MODEL OF THE HEAD

Remi Pluche and Albert I. King
Wayne State University
Detroit, Michigan

For a better simulation of the dynamic behavior of the skull, it was considered to be a linearly elastic and anisotropic material (Element ELMTO2 in the FEAP code). The CSF was assumed to be a linear isotropic and incompressible material, in order for it to be able to resist shear. ELMTO2 was found to be a more realistic element to use than ELMTO1, if the shear modulus of ELMTO2 was assumed to be low. The brain could be considered as a nonlinear anisotropic viscoelastic continuum, but it was assumed initially to be an elastic linear isotropic material (ELMTO1) with a low modulus of elasticity. The material constants used are given in Table A-1.

TABLE A-1

MATERIAL PROPERTIES CONSTANTS FOR USE WITH ELMTO1

Tissue	Modulus of Elasticity (Pa)	Poisson's Ratio	Density (kg/m^3)
Skull	4.46×10^9	0.22	2.00×10^3
Brain	6.90×10^5	0.49	1.04×10^3
CSF	1.00×10^{2}(shear)	0.5	1.03×10^3

The initial FE mesh used in the model had 136 nodes and 122 quadrilateral elements to represent the skull (33), CSF (26), and the brain (63). At the base of the skull, both skull and brain elements were superimposed in an attempt to simulate the foramen magnum. This was not successful and was abandoned in subsequent simulations. In order to simulate various combinations of linear and angular acceleration, A-P (frontal) as well as S-I loads were applied. The latter were always in pairs of equal and opposite forces to generate a pure torque. The magnitude of the applied load was scaled down for impact to a midsagittal slice of the head 1.0 mm thick. For impacts lasting 10 ms or less, the head could be considered as a freely moving mass. However, for longer duration impacts, head motion needed to be constrained by a neck.

A total of eight preliminary runs were made to study the response of the model. They represented impacts that resulted in linear accelerations between 144 and 560 G and angular accelerations between 6,200 and 40,000 rad/s^2. A qualitative summary of the results is given below.

1. When a pure torque was applied for each run, a high linear acceleration value was often associated with a low angular acceleration value at the forehead and at the occiput. A low linear acceleration was associated with a high angular acceleration at the top and base of the skull. This result was due primarily to the manner in which the torque was applied.

2. When a frontal impact was simulated, a low linear acceleration value was associated with a low angular acceleration value at the top of the head and with a high angular acceleration value at the same location, when the neck was added. Angular acceleration was always high at the impact location and at the opposite side, due to local deformations.

3. Locations of high normal stress in the brain ($0.1\ \text{MPa} < \sigma < 0.5\ \text{MPa}$) were associated with areas of high acceleration (300 G or 30,000 rad/s^2), especially for the area of impact and at its contrecoup location on the skull.

4. High normal stresses were located at the forehead and occiput for a frontal impact and at the cerebellum when a torque was applied. The model predicted compression in the forehead (anterior fossa) and tension on the opposite side (occiput) for a frontal impact.

5. For a free model (no neck), high shear strains were located on the border of the high stress areas. The shear strains were the highest strains in every run. Contours of constant shear strain indicated that the brain did not rotate as one mass but had a complex motion due to the tentorium and the geometry of the skull.

Based on the results of this initial model, changes were made to the skull geometry to eliminate high stresses at the corners within the skull, and the base of the skull was enlarged. This resulted in a model, shown in Figure A-1, with 156 nodes and 137 elements, including 36 skull elements, 34 CSF elements, and 67 brain elements, which could be used to identify regions of high stress and strain in the brain (shear and normal) due to an impact. The material behavior of the head tissues was modeled using ELMTO2. The effective constant matrices for this anisotropic, nonlinear representation is given in Table A-2.

TABLE A-2

ANISOTROPIC MATERIAL PROPERTIES MATRICES
FOR USE WITH ELMTO2 (All units in kPa)

Tissue	C_{j1}	C_{j2}	C_{j3}
Skull	1.4×10^9 5.0×10^8 0	5.0×10^8 1.3×10^{10} 0	0 0 $5.0\times^9$
Brain	1.0×10^7 1.0×10^7 0	1.0×10^7 1.0×10^7 0	0 0 2.0×10^3
CSF	5.0×10^6 5.0×10^6 0	5.0×10^6 5.0×10^6 0	0 0 2.0×10^2

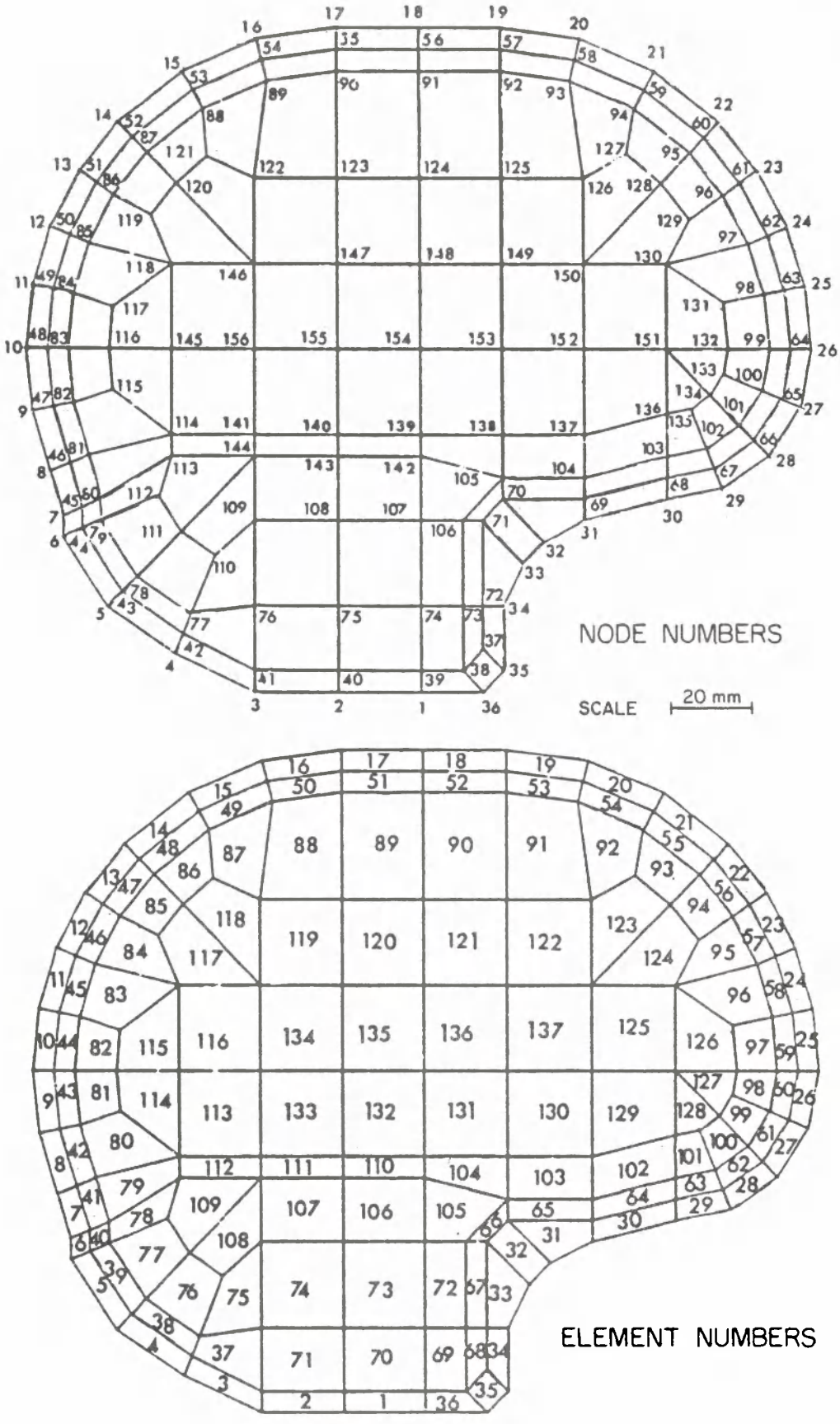

FIGURE A–1. Finite element mesh used in final model.

APPENDIX

The FEAP code required the application of forces to nodes of the skull as input conditions to generate combinations of angular acceleration (α), linear acceleration (a), and angular velocity (ω), which form a three-dimensional surface in the a–α–ω space. For each point on this surface, the model calculated the maximum strain and stress values and determined if the top of the surface corresponded to a high value of stress or strain. If it did, that region was also identified in the mesh. The tentorium was included in the model as a discontinuity in the brain structure filled with CSF, and the neck and its muscles were simulated by adding new elements to the model. Since ω was found to vary linearly in the model α, it did not constitute an independent parameter. Thus, the three-dimensional space was reduced to a two-dimensional space of a and α. In terms of input conditions, it was necessary to cover an acceleration range of 120 to 560 G and an angular acceleration range of 4,000 to 40,000 rad/s^2. The magnitudes and regions of high stress in the brain were recorded in each case, and shear strain contours were drawn. Time histories of stress and strain were also recorded.

For each input condition at least two runs were performed. Changes to the input data file did not involve the material constants. The changes included element types to determine the sign of normal stresses, the addition of a tentorium to look for differences in brain motion, and the distribution of the impact forces on more nodes to alter slightly the resulting skull accelerations. The last change was necessary to obtain runs closer to the desired values of a and α.

Data analysis consisted of four distinct tasks: plotting of mesh kinematics, computation of angular acceleration, computation of angular velocity, and graphical display of stresses and strains.

To provide information on gross head kinematics, the mesh geometry for each time step was plotted to show the velocity and acceleration vectors of each element. Angular acceleration was then computed, but, because there are no known definitions of the angular acceleration of a deformable skull, two methods were used to estimate this value. The first used the generally accepted rigid body assumption, while the second was based on local accelerations.

The first method considered the skull as a rigid body and utilized the computational procedure described by Mital (1978). The effects of local kinematics were minimized by this method by calculating the angular acceleration using linear acceleration values from several pairs of nodes located on opposite sides of the skull. The reported results are the average of two pairs of nodes: 4/18 and 5/19.

The second method accounted for the deformability of the skull and was very sensitive to local deformation. It calculated the location of the instantaneous center of rotation of an element from which the angular acceleration was estimated. This was done for two neighboring elements to obtain an "average local value."

There was a large difference between the results of the two methods. Those from the second method were not used in this study when they compared with results reported in the literature. However, they were meaningful in that they presented the peak angular accelerations that would have been measured by accelerometers placed on the skull.

The original plan called for the plotting of model results in the a–α–ω space. Thus, it was necessary to compute the peak angular velocity for each run. This occurred at the end of the run for the freely moving head, at which time the linear velocity was a constant and the angular and linear accelerations were zero. The maximum angular velocity was

taken as the integral of the average angular acceleration of two nodes located on opposite sides of the head, with one node at the top of the head.

A computer program was written to plot the computed stresses as a function of time for selected elements of the model. It also created an output file for the graphics program MOVIE-BYU to draw shear strain contours on the brain. MOVIE-BYU required nodal data as input, whereas FEAP provided the data at the Gaussian nodes for each element. An interpolation program was needed to compute the shear strain at each node.

The modified model was used to make a total of 35 short time-duration runs. The tentorium was first introduced in Run No. 15 and the bar element neck in Run No. 19. The neck was changed to quadrilateral elements in Run No. 30. The linear and angular acceleration covered by these runs are listed in Table A-3. The linear acceleration range was 100 to 325 G and that for angular acceleration was 4,000 to 30,000 rad/s^2. These resultant acceleration values were computed for the crown (top of the head), so that they could be compared with experimental data taken from the same area.

Normal stresses and shear strains were computed for each brain element of the model. Peak values were identified as well as their locations. For this phase, they were found to occur primarily in seven regions of the brain listed in Table A-4. The unit for stresses used in the table is MPa.

In the final activity of this study, a series of eight runs were made with an impact duration of 30 ms. Five were made with the neck represented by two-bar elements and muscles, and three were run with seven quadrilateral elements without muscles. The typical force pulse was a half-sine wave of the same magnitude as that used in the shorter duration runs. The duration of the runs were 40 ms to ensure that all peak responses had occurred before the run was terminated. The output file time step was at 4-ms intervals. A more accurate determination of the peak angular velocity would require a much finer time increment for those runs. Similar analysis techniques were used for these runs to summarize the data.

The peak linear and angular acceleration values for the long duration runs are listed in Table A-5. The runs were numbered from 301 to 308. Run numbers 316 to 318 do not represent additional runs; they refer to a second peak in the data for runs 306 to 308. Because the same peak forces were used with three times the duration, the impacts could not be compared with available data.

The following discussion of the results of this study addresses (1) the effect of the neck on head motion, (2) the effect of the tentorium on brain response, and (3) the different effects of translational and rotational impacts on brain response.

The head and neck model was subjected to only frontal impacts, as no frontal oblique runs were made with that model. The resulting angular accelerations were significant, although the exact applied torque could not be computed. For pure rotation of the head (with no neck), high angular accelerations (20,000 to 30,000 rad/s^2) were attained, but the range of linear acceleration was the same as that for linear motion (150 to 300 G). The effect of adding a neck was a tendency to produce both lower angular and translational accelerations.

In most cases of pure rotation, there were no high shear strains at the top of the brain. These were encountered on each side of regions of high normal stress (Run Nos. 10 to 13). The high strain areas were, in order of significance, the base of the corpus callosum, the forehead, the occiput, and the cerebellum. The same areas were

TABLE A-3

LIST OF THE VALUES FOR THE MAXIMUM LINEAR AND ANGULAR ACCELERATION AND ANGULAR VELOCITY AT THE TOP OF THE SKULL

Run Number	Force (N)	Torque (Nm)	Max. Lin. Accel. (rad/sec/sec)	Max. Ang. Accel. (rad/sec)	Max. Ang. Vel. (rad/sec)
5	70.7	4.7	530	40000	—
6	80	4.5	560	32000	—
7	0	2.85	210	30000	157
8	0	2.85	220	25000	150
9	0	2.00	144	19600	132
12	40	0.0	155	6200	39
13	40	0.0	160	11000	50
14	50	0.0	240	12000	80
15	40	0.0	290	10000	54
16	40	0.0	165	7000	32
17	0	1.9	120	19500	130
18	0	1.9	130	22000	138
19	40	0.0	170	6200	40
20	40	0.0	189	4000	35
21	40	0.0	190	10000	61
22	40	0.0	167	4500	34
23	40	0.0	135	7000	44
24	40	0.0	132	10000	90
25	50	0.0	275	12000	93
26	50	0.0	290	13000	73
27	52	0.0	210	11000	130
28	42.4	2.0	295	24000	30
29	-32		147	5000	—
30	70		300	8100	—
31	70		323	11000	—
32	-32		175	7300	—
33	44		206	10500	—
34	70		320	19000	—
35	30		205	9400	—

involved in frontal, frontal oblique, and occipital impacts. It should be noted that, in occipital impact, the location for maximum stress was in the cerebellum (Run No. 32).

The top of the brain was one of the most protected areas, having lower stresses and strains than other areas. This is due to the fact that the lowest peak linear and angular accelerations were found in this area, as shown in Table A-4. This is not true in the head-neck model even though the crown angular accelerations were still low relative to other areas of the brain in the same run.

In the absence of a tentorium, there were no local motions and no local areas of high stresses or strains near the region of the tentorium. The brain behaved as a homogeneous material. With a tentorium, there were local motions near the base of the occiput and in the cerebellum where there were high stresses and strains. This is especially true for

TABLE A-4

MAGNITUDE AND LOCATION OF PEAK STRESS (MPa) AND STRAIN FOR SHORT DURATION RUNS WITH FINAL MODEL

BRAIN AREA RUN NO.	ORIBTAL FLOOR		FOREHEAD		TOP		OCCIPUT		CEREBELLUM		MEDULLA		CORPUS CALLOSUM	
	Stress	Strain	Stress	Strain	Stress	Strain	Stress	Strain	Stress	Strain	Stress	Strain	Stress	Strain
5	-0.260		-0.150		0.023		0.270		0.200					
6			-0.300				0.240							
7	-0.110		0.000				-0.170		0.140				0.160	
8	-0.075		0.050				-0.080		0.070		0.030		0.080	
9			0.140				0.120				0.100			
12			-0.180			-0.100	0.165		0.155		0.110			
14			-0.280			-0.100	0.260		0.200		0.100		0.150	
15	-0.100	0.600	-0.273	0.000	0.000	-0.327	0.300	0.141	0.127	0.251	0.123	0.000	0.106	0.100
16	0.100			-0.010	-0.170	-0.127		-0.100		0.100	0.200	0.090	0.210	0.348
17	0.145	0.090	0.135	0.117	-0.080	0.094	0.070	0.090	0.040		-0.090	-0.050		
18	-0.165		-0.100	0.149	0.031	-0.133	0.060	0.133	-0.099	0.000	0.082	-0.050	0.101	-0.240
19	-0.222	-0.133	-0.191	-0.320	0.143	-0.225		0.357		0.323		0.287	0.190	0.150
21		0.349	0.210	0.420	-0.146	-0.240	0.251	-0.270	0.225	0.430	0.000		0.402	0.332
22		0.140	-0.177	0.415	-0.128	0.200	0.155	0.295	0.090	0.358		0.263	0.241	0.237
23		0.120	-0.160	0.360	-0.140	-0.200	0.160	-0.310	0.090	0.380			0.293	0.260
24		-0.120	-0.162	0.367	-0.141	-0.195	0.168	-0.300	0.099	0.380			0.254	0.293
25			-0.241	0.540	-0.254	-0.523	0.277	0.432	0.164	0.684		0.510	0.100	0.430
27	0.230		0.520	-0.231	-0.400	-0.158	0.343	0.217	0.491	0.125	0.362		0.350	0.326
28	0.103	0.150	0.173	-0.301	-0.149	-0.288		-0.040		-0.070				0.250
31		0.300	-0.270	0.000	0.000	-0.400	0.250	0.000	0.360	0.300	0.000		-0.155	0.780
32		-0.100	0.127	0.000	0.000	0.209	-0.113	-0.020	-0.162	-0.130	0.000			-0.325
33			-0.142	0.130	0.030	-0.250	0.113	0.070	0.115	0.050	0.000			0.220
35			-0.226	0.240	0.067	-0.400	0.180	0.100	0.184	0.154			0.060	0.351

TABLE A-5

TABLE OF ACCELERATION FOR LONG DURATION RUNS, LINEAR AND ANGULAR
(G, rad/s^2 for dT = 30 ms)

Brain Area Run No.	Forehead		Top		Occiput		Base/Cerebellum	
	Linear	Angular	Linear	Angular	Linear	Angular	Linear	Angular
301	245	20000	303	8000	263	5000	262	5000
302	105	2500	110	2500	115	6000	130	2000
303	127	12000	110	13000	142	17000	138	14000
304	250	16000	325	24000	270	20000	165	22000
305	168	14000	182	2000	180	3000	170	2000
306	96	4500	104	4500	60	5000	35	90
316	215	8000	264	14000	160	8000	90	8000
307	150	8000	167	8000	100	6000	50	7000
317	350	10500	423	15000	250	17000	130	10000
308	85	5000	97	5000	50	5000	30	5000
318	200	6500	230	12000	130	8000	70	8000

frontal impact due to high peak angular accelerations in comparison with other areas of the brain. This result was based on data from Run Nos. 20 through 27. The tentorium also caused higher stresses and strains in the brain stem.

The acceleration response and the resulting stresses and strains due to frontal impact and those due to the application of a pure torque are quite different. The pure torque runs fell into a distinct group, while the frontal impact runs are concentrated in two groups. The pure torque runs exhibited high angular accelerations and low translational accelerations, while one group of frontal impacts exhibited low angular and translational accelerations and the other group had higher translational accelerations. The frontal oblique impacts exhibited high angular and translational accelerations. For linear acceleration, the regions of high strain were found in the inferior portion of the corpus callosum, along the anterior fossa, and on the postero-superior surface of the cerebrum. Those due to angular acceleration were found in the forehead and the occiput.

The areas of compressive and tensile stress are shown in Figure A-2 for the four modes of impact in which the plus sign designates a tensile stress. The configuration is reversed from frontal to occipital impact, as shown in Figure A-2(a) and (b). There were alternate regions of tension and compression due to a pure torque (Figure A-2b). For a frontal oblique impact, there was a rotation of the demarcation line between the tensile and compressive regions (Figure A-2d).

Brain motion can be deduced from model results by two methods. The first is based on shear strain data from successive time steps. The direction of the motion can be established for all four modes of impact, as shown in Figure A-3. The sign convention is shown in the figure. The deformation is always relative to an element closer to the dura to which the brain is attached. The second method utilizes mesh deformation to determine the motion of the brain. Node locations from successive time steps were compared to establish the direction of flow. In Figure A-4(a) and (b), the directions are shown along

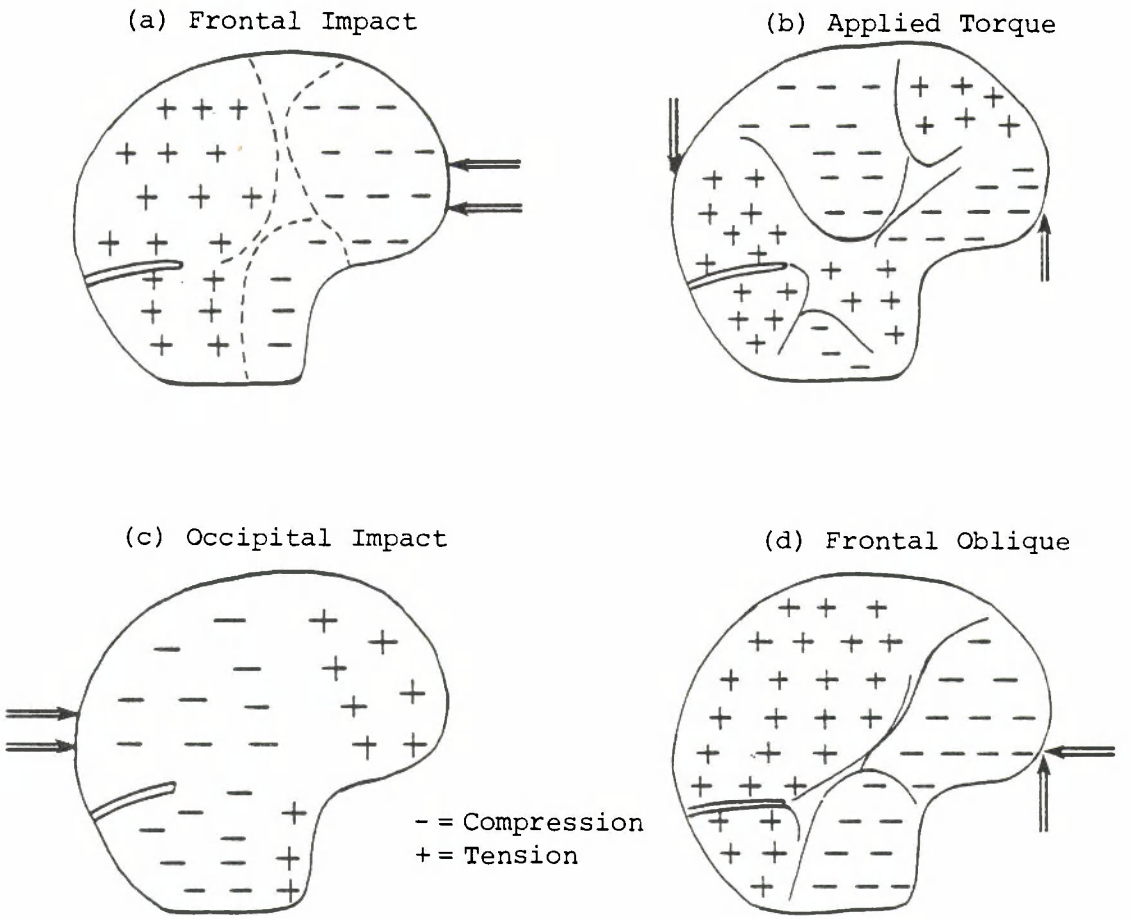

FIGURE A-2. Areas of tension and compression for four modes of impact.

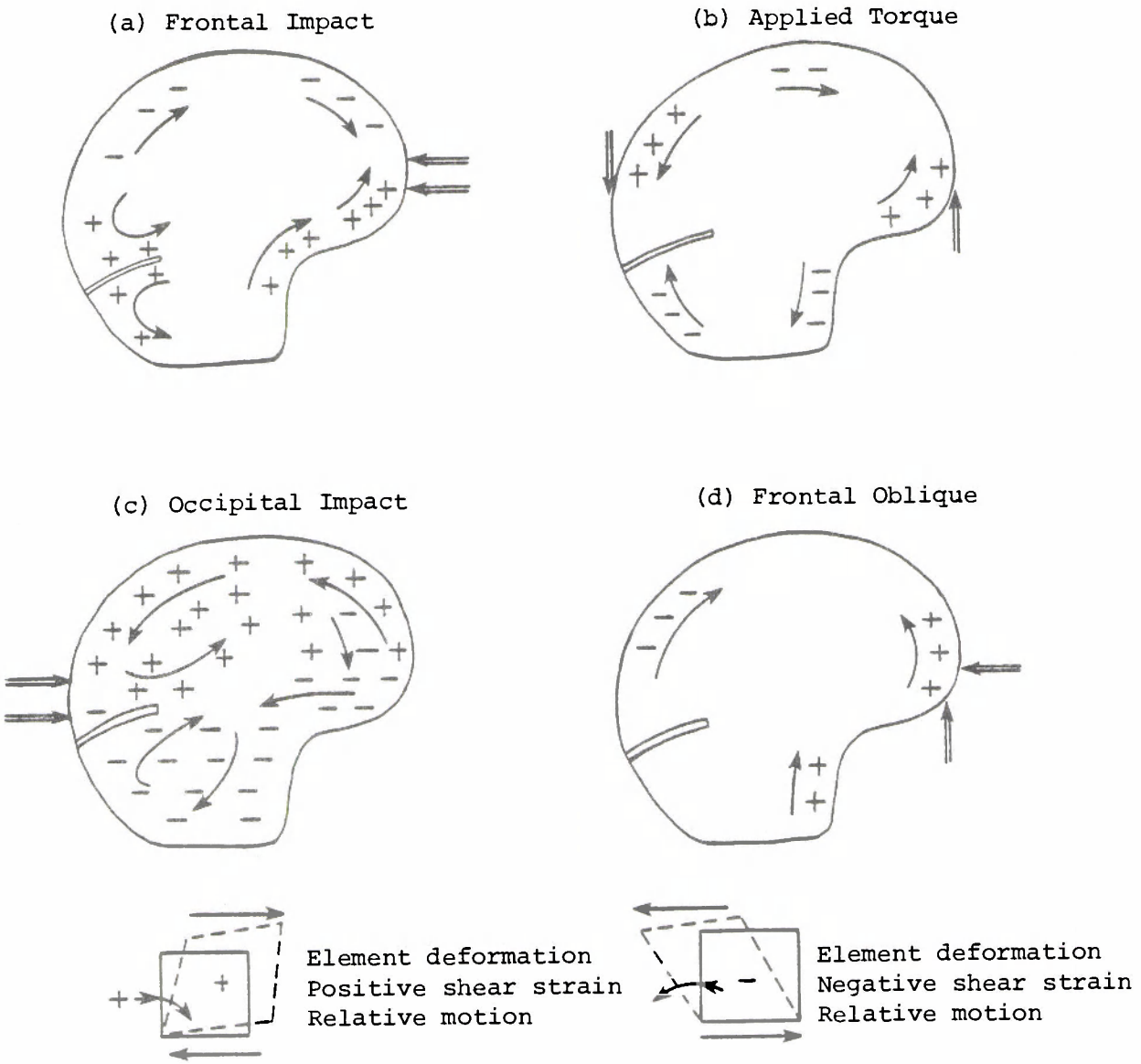

FIGURE A–3. Direction of brain motion deduced from shear strains.

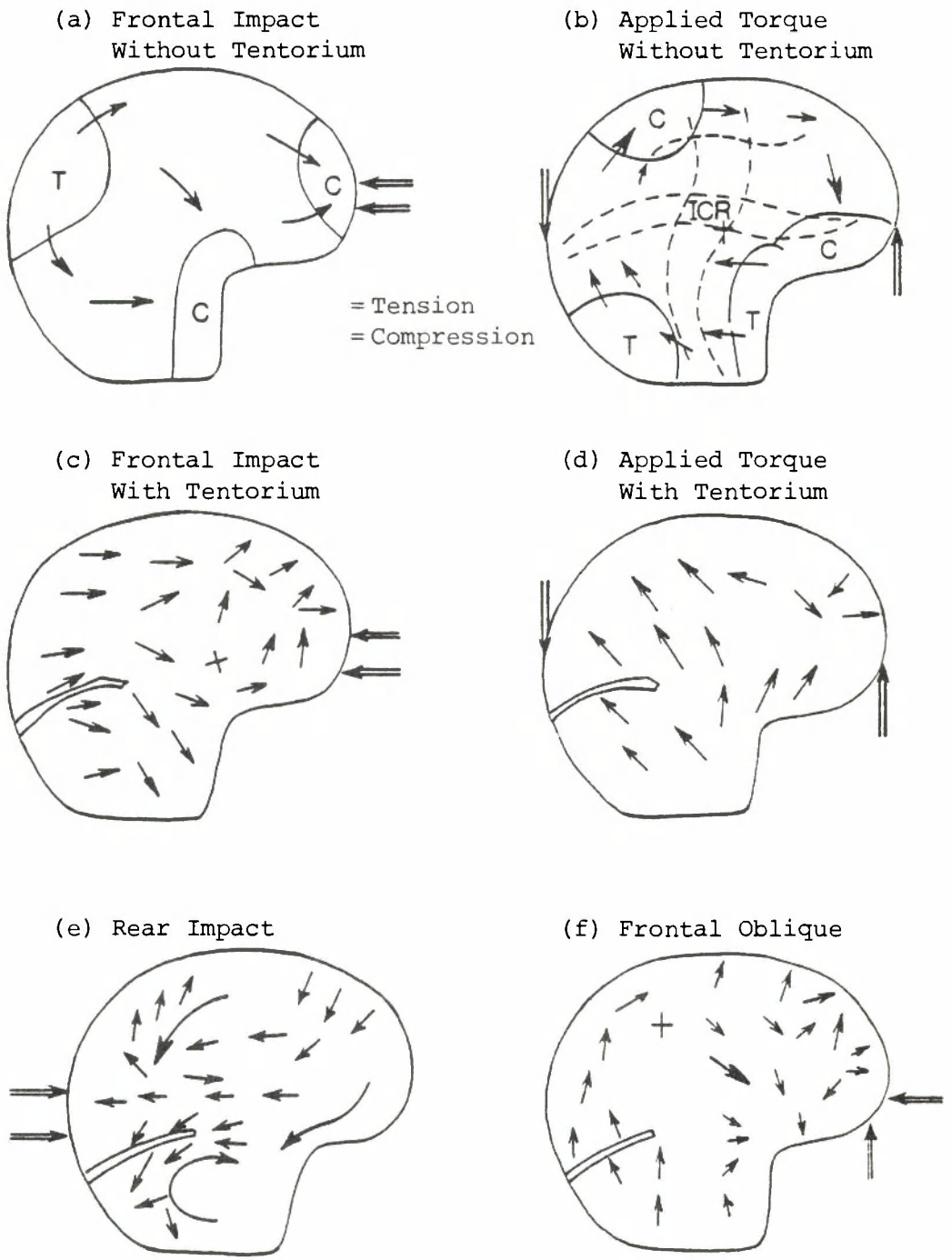

FIGURE A-4. Comparison of brain motion with and without a tentorium.

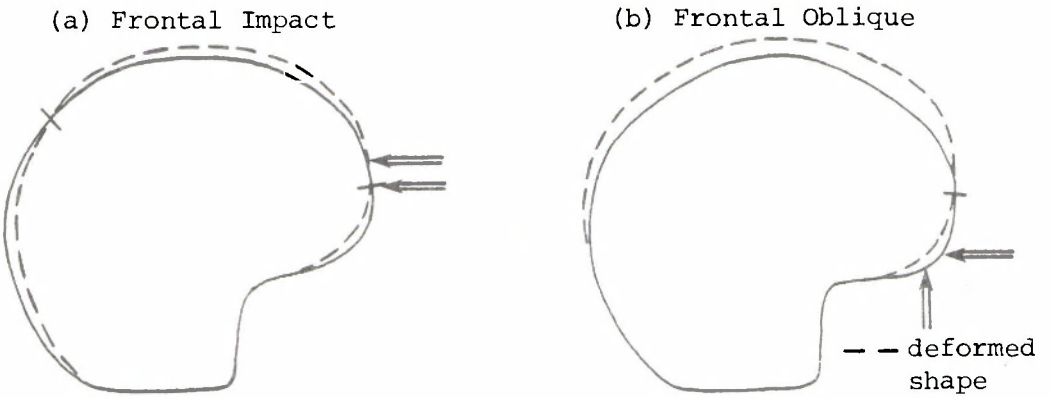

FIGURE A-5. Deformation of the skull due to frontal and frontal oblique impact.

with the regions of high normal stress (compression and tension) for frontal impact and rotational impact. The motion is consistent with the stresses predicted by the model and is also consistent with the results shown in Figure A-3. With the addition of a tentorium, the cerebellum moved as a separate entity, but the stresses were not changed significantly. Figure A-4(c), (d), (e), and (f) shows brain motion for all four modes of impact with a tentorium. The shape of the deformed skull is shown in Figure A-5 for two modes of impact. The nodes of zero displacement and the approximate magnitudes of the deformation are similar to previously published results (see, for example, Nusholtz et al. 1984).

For validation, the results of the model were compared with experimental data, and the input pulse to the model was modified until a good correlation in head kinematics was observed. That is, the linear and angular accelerations of the head were to be made close to those measured experimentally. Data reported by Nahum et al. (1981), Nusholtz et al. (1984), and Prasad and Daniel (1984) were used as a basis for the selection of input conditions. The simplicity of the model, the inaccuracies in the geometry and in the thickness of the skull, and the lack of information on material properties all contributed to errors in prediction. Validation is therefore restricted to a comparison of trends in strains and stresses. The model is also incapable of simulating skull fracture, although it can predict large deformations. In this section, comparisons will be made with acceleration data, measured pressures, and experimentally observed AIS values.

The validation of acceleration results was based on a comparison of model results with experimental data extracted from Nusholtz et al. (1984). Eight runs were conducted with $5 < dT < 15$ ms. The peak accelerations and OAIS values are shown in Table A-6. Six of the eight runs were paired with an equivalent run using the model. The criteria for pairing were angular and linear acceleration as well as applied load. The paired results are shown in Table A-7. A regression analysis was performed to correlate model and experimental data—namely, linear acceleration, angular acceleration, and angular velocity. The slopes, intercepts, and correlation coefficients are shown in Table A-8. The correlation for all three variables is good, and it can be concluded that the model was capable of reproducing the desired experimental runs, which cover a variety of impact conditions.

TABLE A-6

SUMMARY OF ACCELERATION AND OAIS
(Nusholtz et al. 1984)

Test Number	Lin. Acc. (G)	Ang. Acc. (rad/s/s)	dT (ms)	OAIS	Parietal Press. Left/Right
82E001	450	42000	10	4	75/36
82E022	190	7250	10	3	180/47
82E042	180	8000	12	3	58/53
82E062	160	7500	12	1	55/31
83E082	100	7000	8	0	46/13
84E141D	120	16000	8	3	46/62
84E151B	220	25000	10	3	41/30
84E161B	84	3750	15	0	19/32

TABLE A-7

MODEL RUNS PAIRED WITH EXPERIMENTS
PERFORMED BY NUSHOLTZ ET AL. (1984)

Run No./ Test No.	X/Y Pair	Lin. Acc. (G)	Ang. Acc. (rad/s/s)	Ang. Vel. (rad/s)	Force (N)	dT (ms)
5/6 average	X1	530	40000	200		
82E001	Y1	450	42000	52	9100	10
7/8 average	X2	215	27500	153		
84E151B	Y2	220	25000	44	8000	10
18	X3	130	22000	138		
84E141C	Y3	57	20000	45	7500	10
17	X4	120	619500	130		
84E141D	Y4	120	16000	45	7500	8
23	X5	135	7000	44		
83E081	Y5	135	7500	22	9600	12
19	X6	170	6200	40		
82E061	Y6	170	6000	25	9000	10

TABLE A-8

REGRESSION ANALYSIS RESULTS FOR LINEAR AND ANGULAR ACCELERATION AND ANGULAR VELOCITY FROM TABLE A-7

Variable	Slope	Intercept	Correlation Factor
Linear Acceleration	0.849	8.120	0.972
Angular Acceleration	1.022	1.381	0.988
Angular Velocity	0.189	16.670	0.975

Note: There is a linear relationship between angular acceleration and angular velocity.

The validation of normal stresses was based on the comparison of results from model runs, with experimental data summarized in Table A-9 taken from Nahum et al. (1981). The procedure did not involve a direct comparison of paired runs. Nahum et al. found regression lines between intracranial pressure and the input force for frontal impact, at five locations in the brain. At four of the five locations, a comparison with results could be made. They are at the frontal region, the equivalent parietal region (top of the head), the occiput, and the posterior fossa. A set of similar regression lines from model results was determined for three areas of the brain. Because of the large scatter in the results for the parietal region, a regression line was not drawn for this set of model results. The results of the regression analysis are summarized in Table A-10. The regression lines were compared, and there was excellent correlation between experimental and model results for pressures in the frontal region. For the other regions, the match was not as good.

For a validation of injury predictive capability, frontal impact injury data were plotted on the same graph with model results (Figure A-6). It can be seen that there is a monotonic increase in stresses in the occipital area that correlates qualitatively with experimental data. These stresses represent an injury criterion in the form of the sum of the absolute values of the maximum normal stresses in the forehead and the occiput. No rotational impact results were included in this figure. Due to the scarcity of experimental data, no quantitative analyses could be carried out.

Data from a test performed by Nusholtz et al. (1984) were compared directly with model results in detail. The parameters are listed in Table A-11. The kinematics were comparable as was the peak impact force. The pressures were different, however, by an order of magnitude. This can be explained by the fact that the transducers were epidural. It should be noted that the predicted intracranial pressures were comparable to those reported by Nahum et al. (1981).

Further investigation of the injury predictive capability of this model was done using the series of eight long-duration runs. Of these eight runs, six simulated frontal impact, one frontal oblique impact, and one purely rotational impact. There were three frontal impact runs in which a neck was included in the simulation. The existence of two peaks in linear and angular acceleration data as well as in the stresses and strains needs to be discussed. Whenever the neck was simulated, there were two peaks. They are shown in Figure A-7 for linear acceleration (Run 306), Figure A-8 for angular acceleration

TABLE A-9

SUMMARY OF INTRACRANIAL PRESSURE DATA
(Nahum et al. 1981)

Run No.	Force (kN)	Lin. Acc. (G)	Intracranial Pressures (MPa)					AIS
			Frontal	Parietal	Occipital (Avg)	Post. Fossa	Carotid Siphon	
36	7.28	230	0.130	0.078	−0.027	−0.063		1
37	7.90	200	0.140	0.078	−0.045	−0.059		0
38	10.80	242	0.137	0.065	−0.027	−0.064		2
41	14.84	390	0.422	0.186	0.133	−0.056	0.047	2
42	5.20	159				−0.043	0.072	0
43	10.59	223	0.267	0.219	0.063	−0.118	0.107	0
44	6.53	152	0.100	0.020	0.014	−0.002	0.113	2
45	10.84	234	0.271	0.178	0.033	−0.063	0.047	0
46	1.50	31	0.023	0.017	0.003	−0.006	0.021	NA
47	1.22	29	0.025	0.016	0.005	−0.003	0.019	NA
48	4.27	128	0.122	0.052	0.008	−0.035	0.047	NA
49	9.35	342	0.259	0.166	0.041	−0.055	0.068	NA
50	6.28	149	0.154	0.083	0.016	−0.031	0.177	NA
51	16.60		0.498	0.312	0.131	−0.081	0.366	NA
52	13.34	429	0.461	0.248	0.070	−0.087	0.292	NA

TABLE A-10

REGRESSION ANALYSIS OF PRESSURE-ACCELERATION
RESULTS (FROM TABLE A-9 AND TABLE A-4)

Pressure	Slope	Intercept	Corr. Factor	No. of Samples
Forehead	0.00103	−0.0260	0.920	13
Parietal	0.00057	−0.0182	0.819	14
Occipital	0.00023	−0.0124	0.796	13
Posterior Fossa	0.00017	0.0133	0.643	14
Forehead	0.00148	0.0740	0.703	14
Top	0.00079	−0.0160	0.369	14
Occiput	0.00039	0.1248	0.400	13
Cerebellum	0.00047	0.0847	0.312	13

Note: The data for the first part of this table is extracted from Table A-9 frontal impact exclusively.

TABLE A-11

COMPARISON OF TEST DATA WITH MODEL RESULTS

Variable Units	Run No. 84E41	Model Run No. 11
Linear Acceleration (m/s^2)	1800	1650
Angular Acceleration (rad/s^2)	7000	11000
Angular Velocity (rad/s)	15	73
Linear Velocity (m/s)	6.4	10
Force (N)	9600	10000
dT (ms)	12	10
Pressure Epid. Forehead (kPa)	22.2	−220
Epidural Parietal (kPa)	−20.11	−238
Epidural Top (kPa)	−55.28	−400
Epidural Occipital (kPa)	39/31	343

Brain Injuries: Subarachnoid hematoma, frontal lobes (cerebrum), subarachnoid hemorrhage, parietal lobe (cerebrum).

(Run 306), and for stresses in Figure A-9, where there is a change in sign from compression to tension in the forehead in Run 306. The first peak was due to the head alone, before any interaction with the neck. The forehead stress was compressive. At about 15 ms, the effect of the neck was felt by the head, and the skull was slowed down momentarily while the brain continued to accelerate rearward. In addition, the skull acquired a high angular acceleration due to the restraining influence of the neck. The combined effect of relative brain motion and angular acceleration resulted in a tensile stress in the forehead. For pure rotation, there was only one peak in linear and angular acceleration, as shown in Figures A-7 and A-8 for Run No. 303. The stress near the top of the brain was initially tensile and became compressive at the end of the run. This is shown in Figure A-9 for Run No. 303. There was only one significant peak for frontal impact for a free head for linear and angular acceleration and for stress as shown in Figures A-7, A-8, and A-9 for Run No. 301. These peaks occurred at about the same time as the peak of the input pulse.

High shear strains were found to occur at the top of the brain and on the orbital floor for frontal impact with or without a neck. For pure rotation, high shear strains were found in the forehead, the occiput, the medulla, and the corpus callosum. The strain was positive in the midbrain and negative at the top, resulting in a possible tearing of the brain tissue in the corpus callosum. The shear strains in these areas were almost zero due to frontal impact of a free head. For the head-neck model, the strains were zero during the first peak and, except for the forehead, reached a significant peak value during the second peak due to the effect of the neck.

An analysis of the injury potential of stress or strain in different parts of the brain can be made by plotting these values on an (a,α) influence plot. For the top of the brain, the cerebellum, and the midbrain, lines of constant shear strain are shown in Figures A-10 through A-12, respectively. Lines of constant stress can be drawn for the forehead, as shown in Figure A-13. For the occiput, orthogonal lines of constant stress and strain can

be drawn, as shown in Figure A-14.[4] The plot for the orbital floor (Figure A-15) produced varied results, and thus no contours could be drawn. Since no experimental data are available, it is not clear which of these areas contribute heavily to brain injury. However, it can be said that the occiput and the forehead are the only areas where stress can be an injury criterion. For the other areas, strain is a more likely candidate for injury assessment.

In conclusion, the model yielded realistic results in terms of head kinematics and intracranial pressures, but only short duration runs ($dT < 15$ ms) could be compared with experimental data. The neck is an important part of the model, because it controls the kinematics of the head, and the tentorium is required to demonstrate independent motion of the cerebrum and cerebellum. Skull deformation is an important element of the model. It not only affects the computed angular acceleration but also is a source of brain deformations and stresses in the brain at the impact site.

In short duration impacts, the top of the brain experiences low stresses and strains in comparison with other areas of the brain. For long duration impacts, stress is a function of linear acceleration in the forehead and the occiput because the lines of constant stress are almost horizontal. Shear strains are functions of both linear and angular acceleration at the top of the brain, the orbital floor, the cerebellum, and midbrain.

---

[4]Each cluster of numbers and symbols around a data point includes the stress value above, the strain value below, the run number to the left, and the impact type to the right. The impact types are indicated as follows.

WITHOUT neck: + frontal, 30 N; = frontal, 40 N; @ frontal, 50 N; & frontal, 70 N; * pure torque, 1.9 Nm; 0 frontal oblique. WITH neck: # frontal oblique; +' frontal, 30 N; =' frontal, 40 N; &' frontal, 70 N.

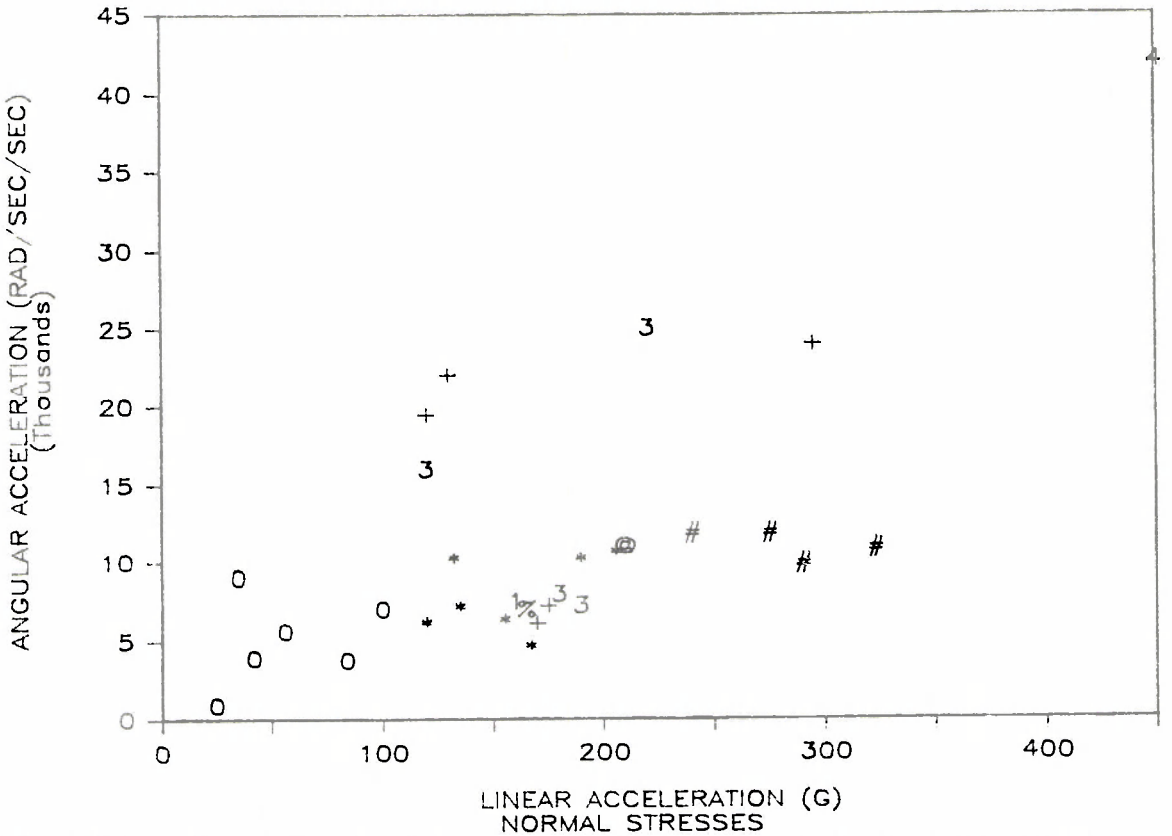

FIGURE A-6. Correlation of AIS with sum of normal stresses in the forehead and occiput.

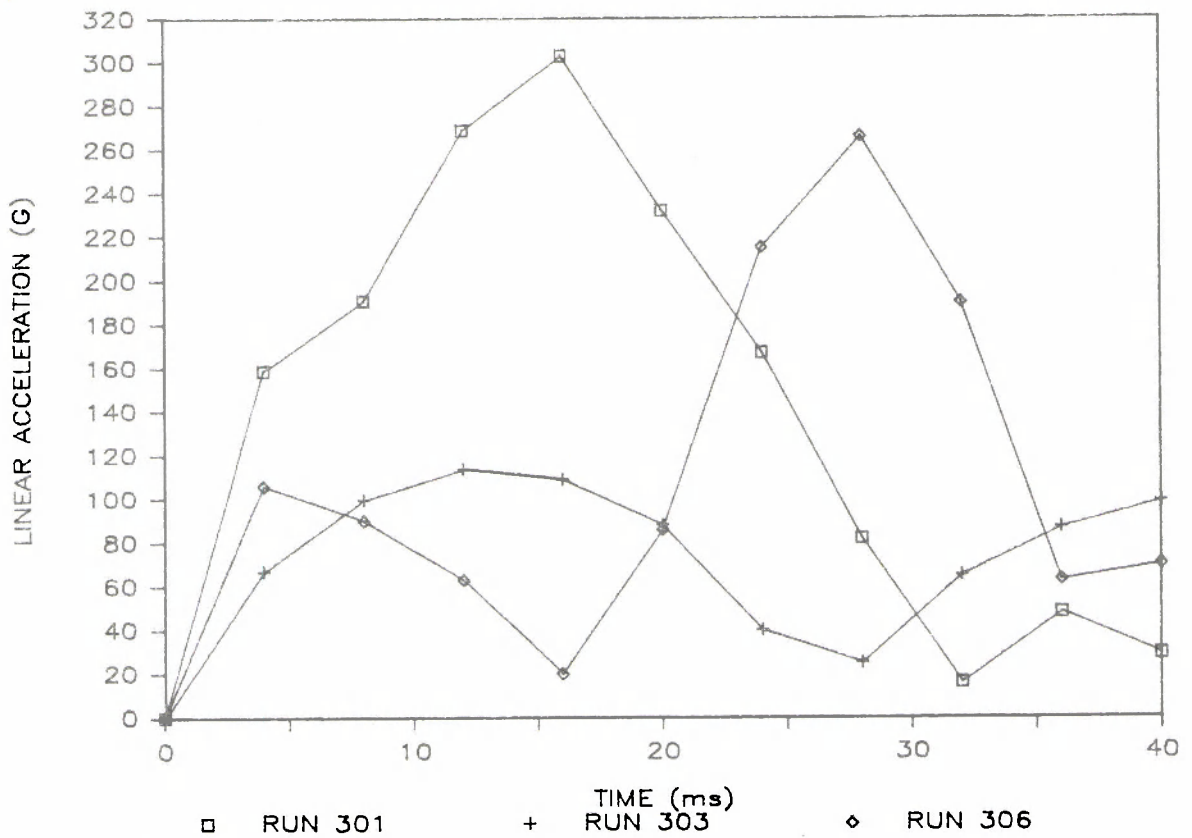

FIGURE A-7. Linear acceleration time histories of long duration runs.

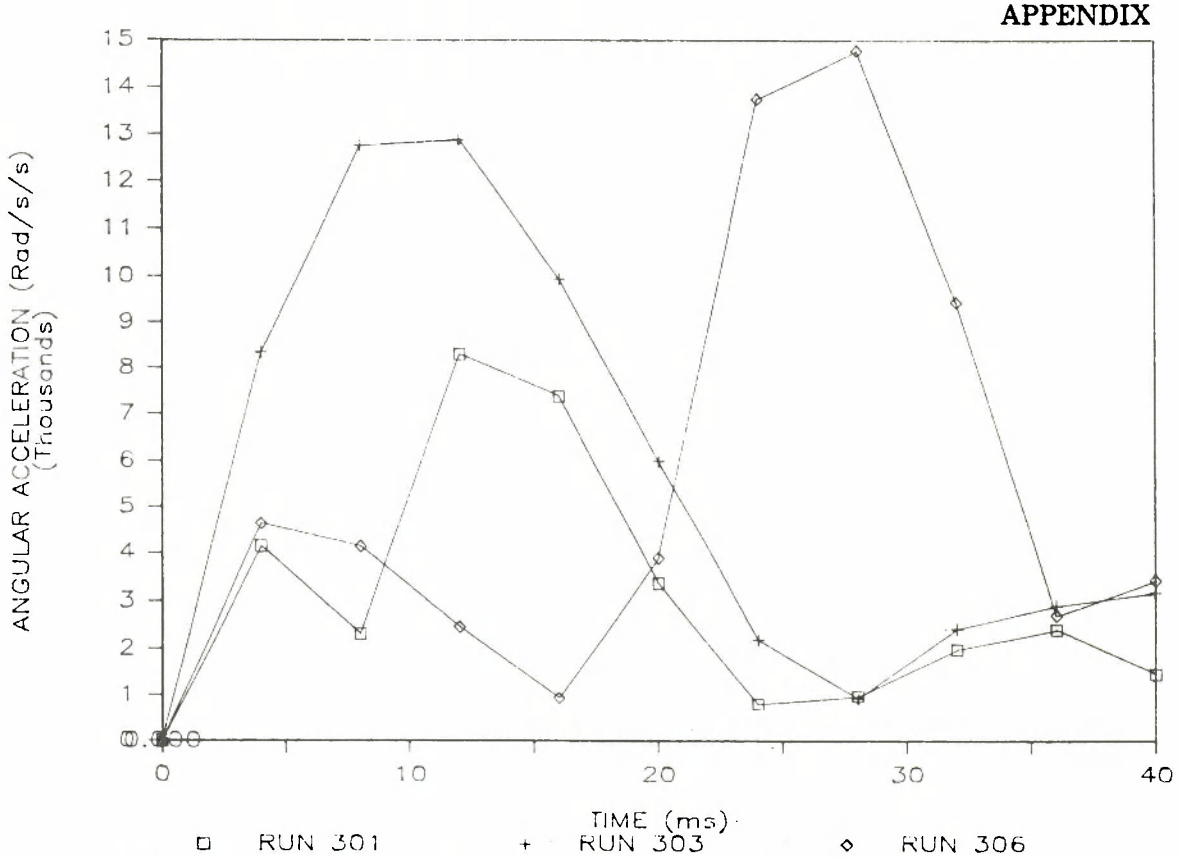

FIGURE A-8. Angular acceleration time histories for long duration runs.

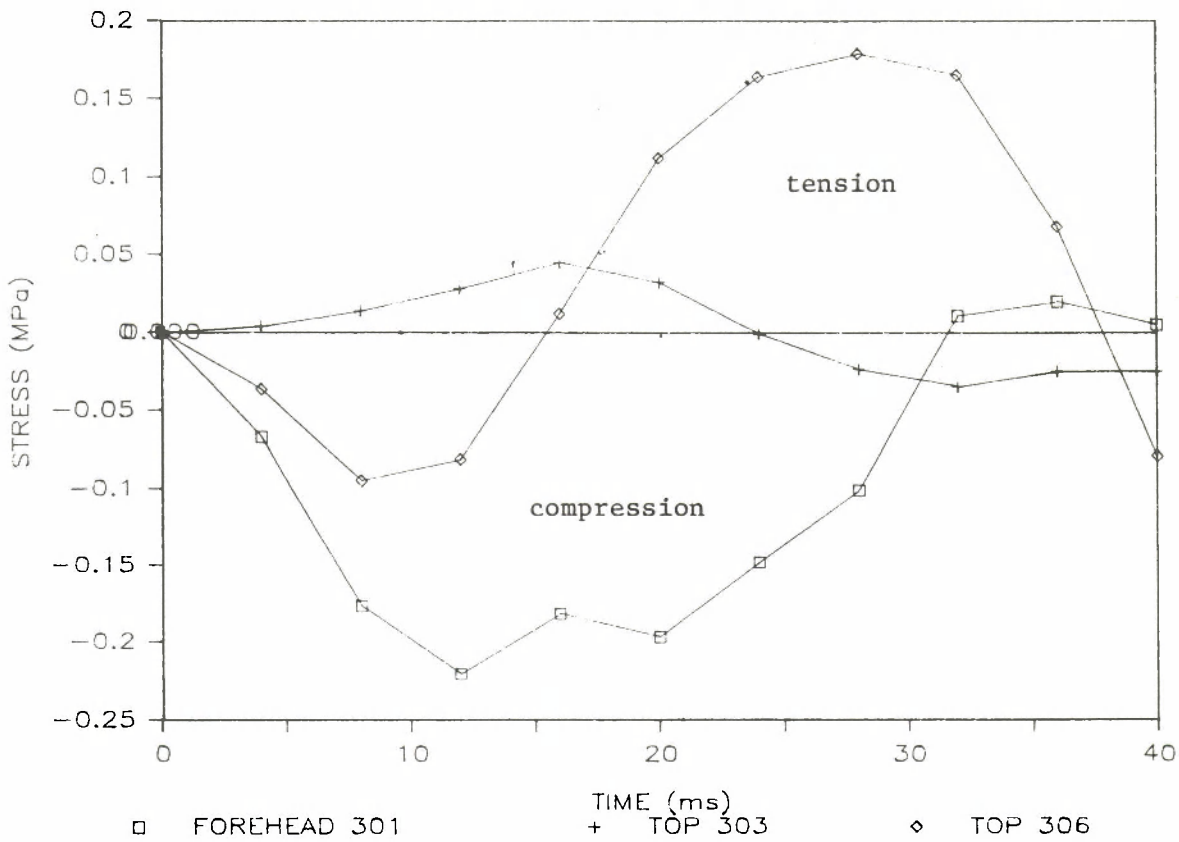

FIGURE A-9. Stress time-histories for long duration runs.

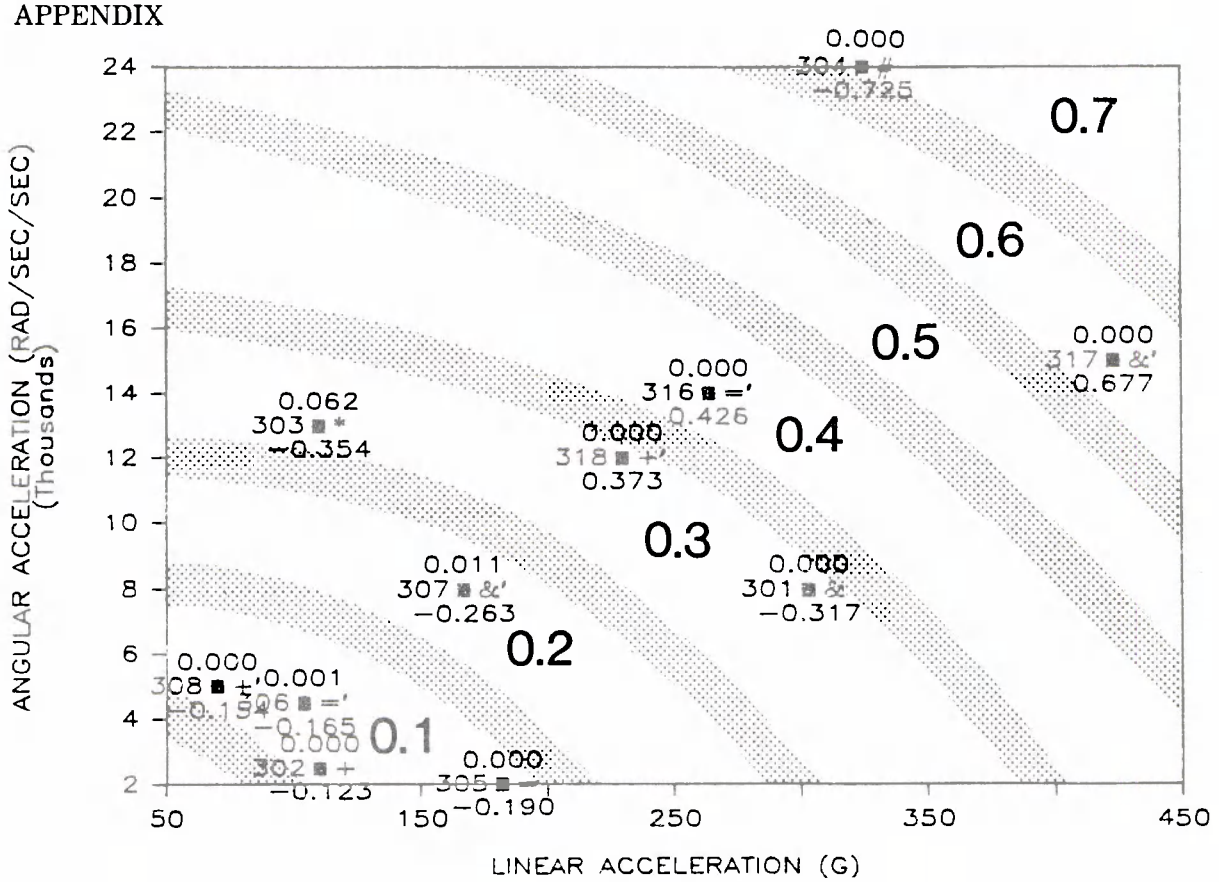

Figure A-10. Constant strain lines for top of the brain (long duration runs).

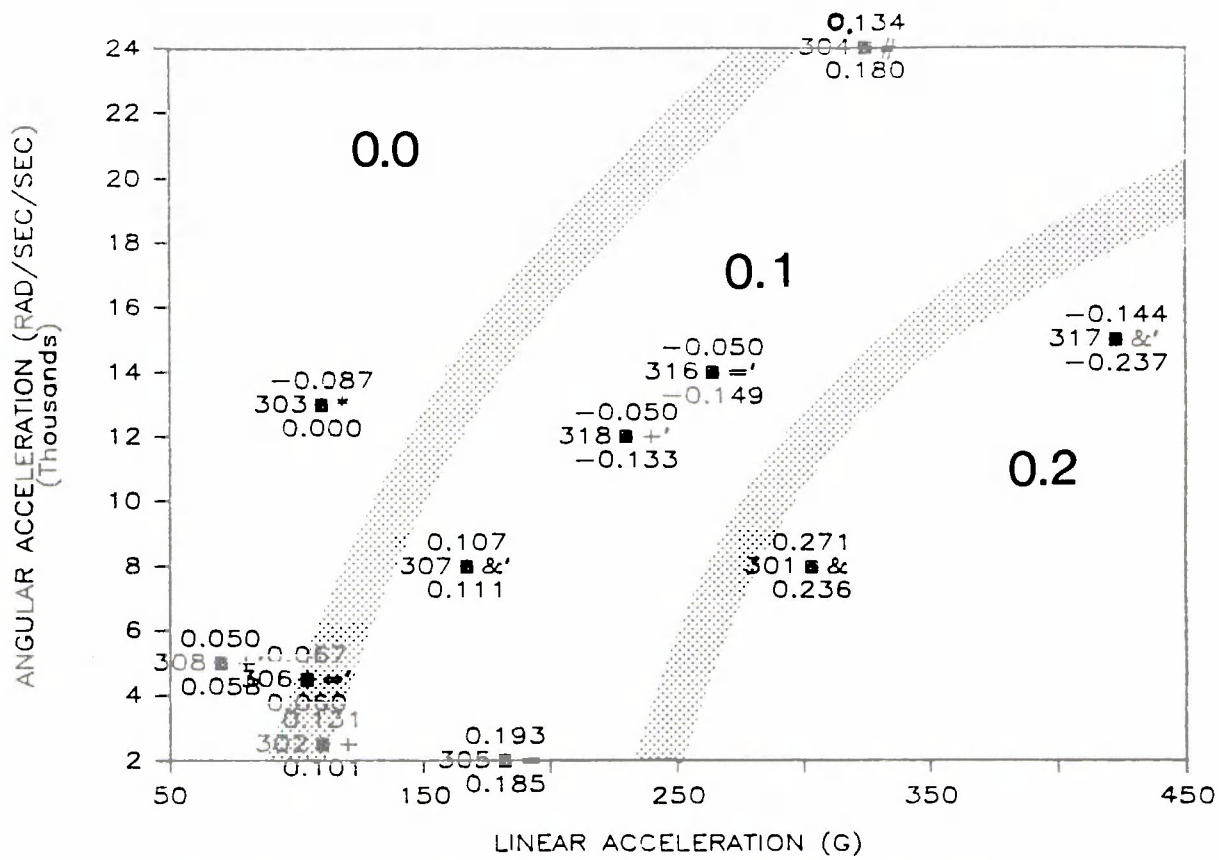

FIGURE A-11. Constant strain lines for the cerebellum (long duration runs).

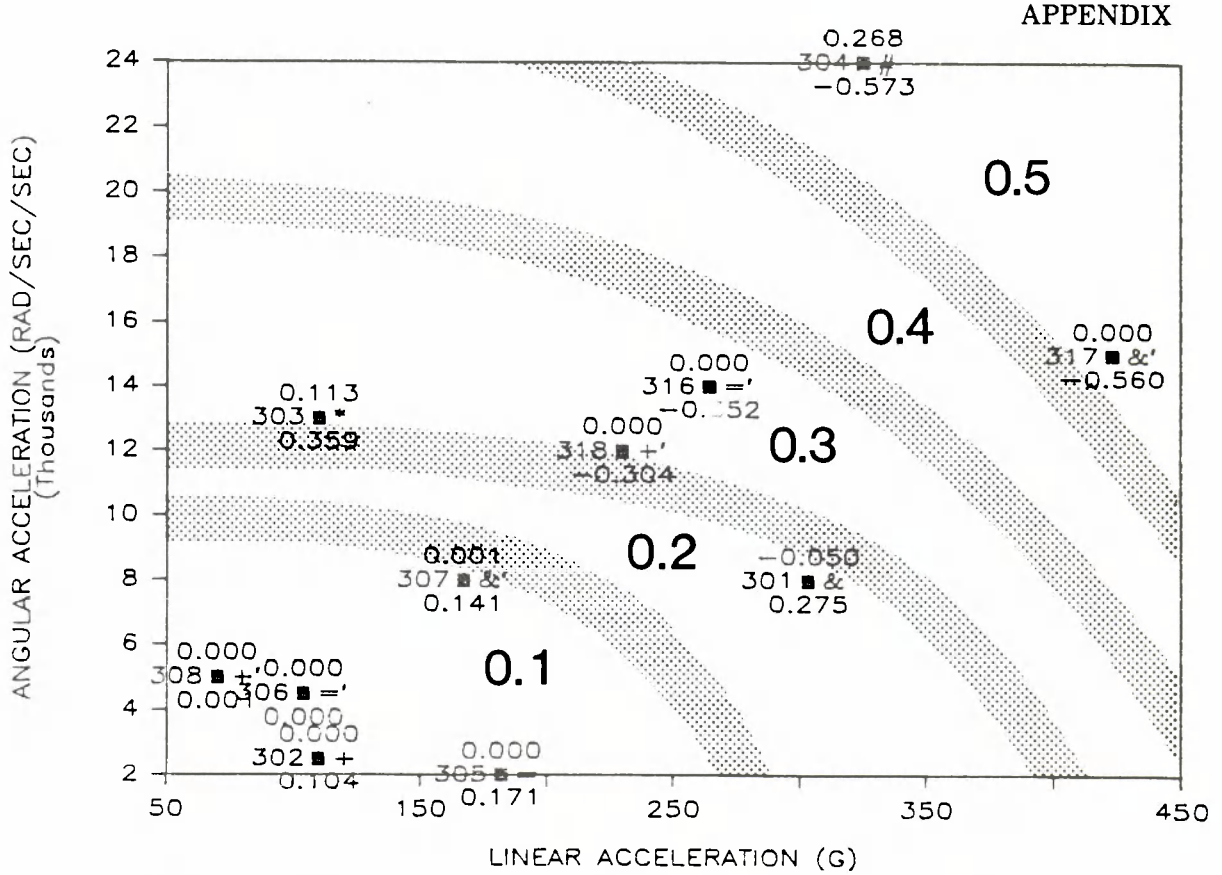

FIGURE A-12. Constant strain lines for the midbrain (long duration runs).

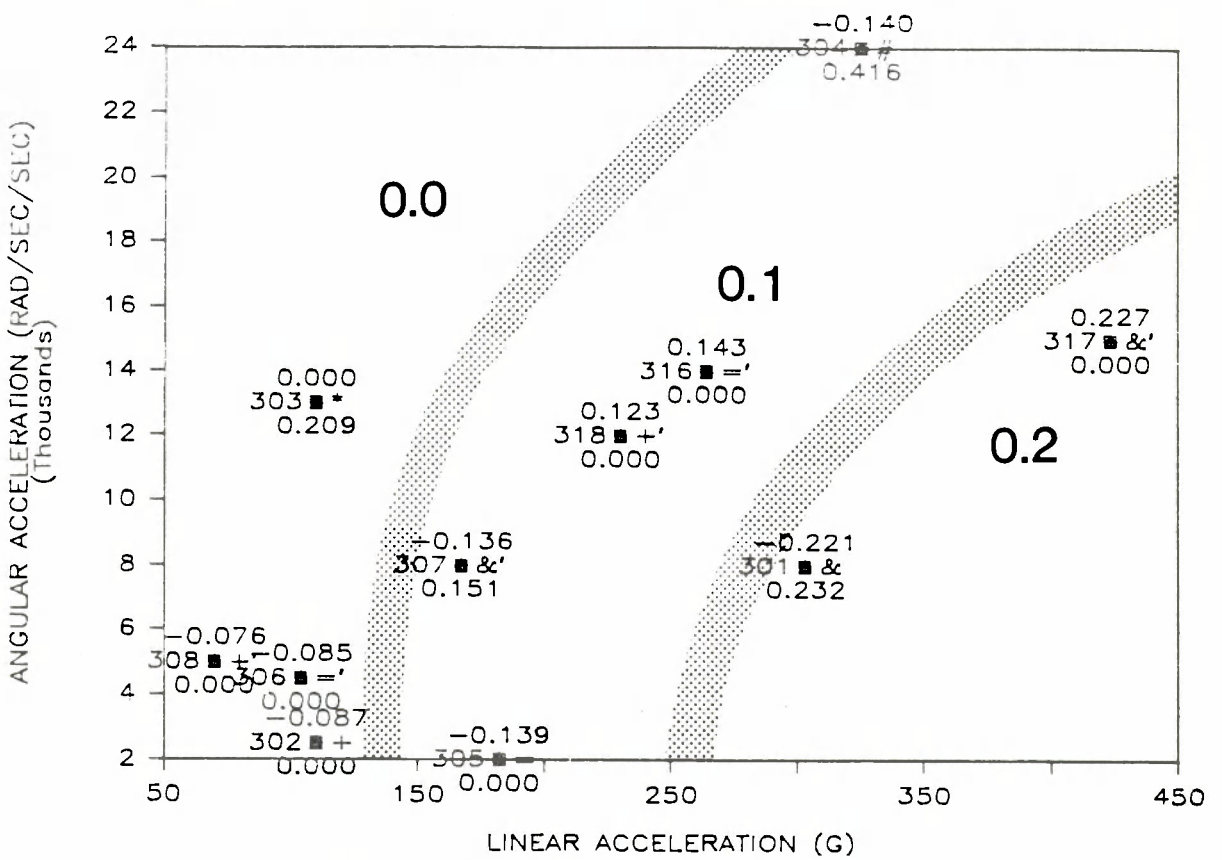

FIGURE A-13. Stress lines of the forehead (long duration runs).

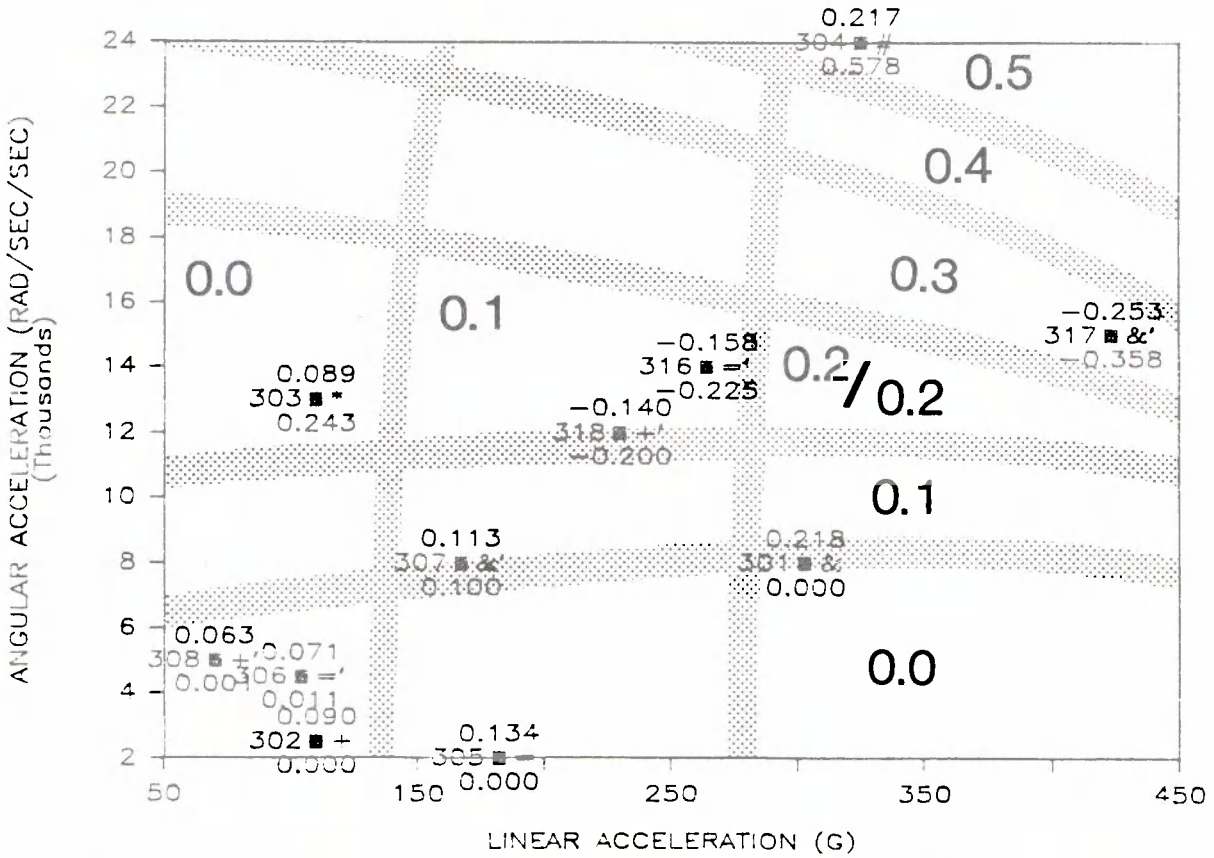

FIGURE A-14. Constant stress and strain lines for the occiput (long duration runs).

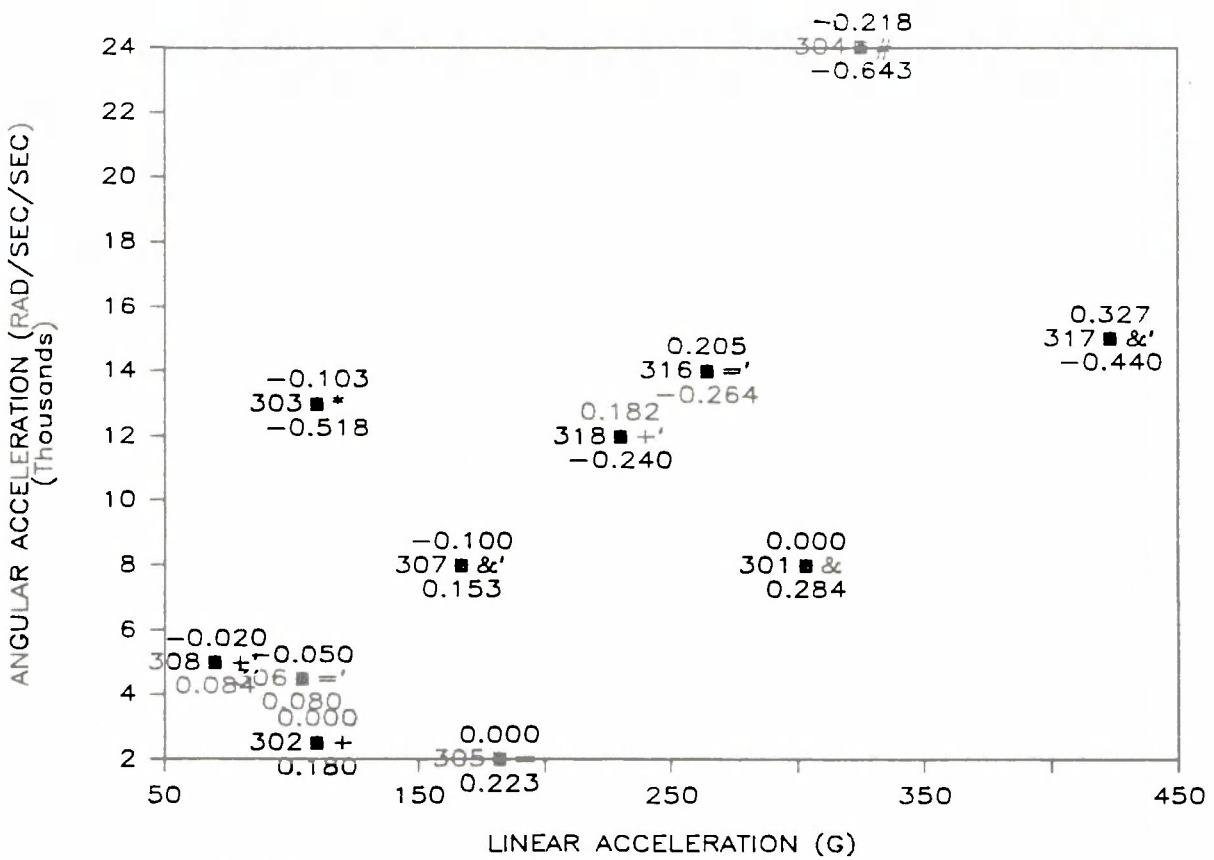

FIGURE A-15. Strain at the orbital floor (long duration runs).

REFERENCES

Abraham, S.; Johnson, C.L.; and Najjar, M.F. (1979) Weight and height of adults 18-74 years of age: United States, 1971-74. *Vital and Health Statistics*, Series 11, No. 211. U.S. Public Health Service, Hyattsville, Md.

Alem, N.M.; and Nakhla, S. (1986) *Characterization of the thorax via mechanical impedance.* Technical Supplemental Report. UMTRI-86-53. University of Michigan Transportation Research Institute, Ann Arbor.

Alem, N.M.; Bowman, B.M.; Melvin, J.W.; and Benson, J.B. (1978) Whole-body human surrogate response to three-point harness restraint. *Proc. 22nd Stapp Car Crash Conference*, pp. 359-399. Society of Automotive Engineers, Warrendale, Pa.

Alem, N.M.; Nusholtz, G.S.; and Melvin, J.W. (1984) Head and neck response to axial impacts. *Proc. 28th Stapp Car Crash Conference*, pp. 275-281. Society of Automotive Engineers, Warrendale, Pa.

Arendt, R.H.; Segal, D.J.; and Cheng, R. (1984) *Review of anthropomorphic test device instrumentation, data processing, and certification test procedures.* AATD Task C Final Report. UMTRI 84-41. University of Michigan Transportation Research Institute, Ann Arbor.

Bowman, B.M.; Schneider, L.W.; Lustick, L.S.; Anderson, W.R.; and Thomas, D.J. (1984) Simulation analysis of head and neck dynamic response. *Proc. 28th Stapp Car Crash Conference*, pp. 173-194. Society of Automotive Engineers, Warrendale, Pa.

Carsten, O.; and O'Day, J. (1984) *Injury priority analysis.* AATD Task A Final Report. UMTRI-84-24. University of Michigan Transportation Research Institute, Ann Arbor.

Cesari, D.; Bouquet, R.; and Zac, R. (1984) A new pelvis design for the European side impact dummy. *Proc. 28th Stapp Car Crash Conference*, pp. 1-11. Society of Automotive Engineers, Warrendale, Pa.

Cheng, R.; Mital, N.K.; Levine, R.S.; and King, A.I. (1979) Biodynamics of the living human spine during $-G_x$ impact acceleration. *Proc. 23rd Stapp Car Crash Conference*, pp. 721-763. Society of Automotive Engineers, Warrendale, Pa.

Clauser, C.E.; McConville, J.T.; and Young, J.W. (1969) *Weight, volume, and center of mass segment of the human body.* AMRL-TR-69-70. Aerospace Medical Research Laboratory, Wright-Patterson AFB, Ohio.

Culver, C.C.; Neathery, R.F.; and Mertz, H.J. (1972) Mechanical necks with humanlike responses. *Proc. 16th Stapp Car Crash Conference*, pp. 61-75. Society of Automotive Engineers, New York.

Dempster, W.T. (1955) *Space requirements of the seated operator.* WADC-TR-55-159 (AD87802). Wright Air Development Center, Wright-Patterson AFB, Ohio.

REFERENCES

Eppinger, R.H.; and Marcus, J.H. (1985) Production of Injury in blunt frontal impact. *Proc. 10th International Technical Conference on Experimental Safety Vehicles.* National Highway Traffic Safety Administration, Washington, D.C. (in press).

Eppinger, R.H; Marcus, J.H.; and Morgan, R.M. (1984) *Development of dummy and injury index for NHTSA's thoracic side impact protection research program.* SAE 840885. Society of Automotive Engineers, Warrendale, Pa.

Haffner, M. (1985) Synthesis of pelvic fracture criteria for lateral impact loading. *Proc. 10th International Technical Conference on Experimental Safety Vehicles.* National Highway Traffic Safety Administration, Washington, D.C. (in press).

Horsch, J.D.; and Patrick, L.M. (1976) *Cadaver and dummy knee impact response.* SAE 760799. Society of Automotive Engineers, Warrendale, Pa.

Hodgson, V.R.; and Thomas, L.M. (1975) *Head impact response.* Vehicle Research Institute, Society of Automotive Engineers, Warrendale, Pa.

Hubbard, R.P.; and McLeod, D.G. (1974) Definition and development of a crash dummy head. *Proc. 18th Stapp Car Crash Conference*, pp. 599–628. Society of Automotive Engineers, Warrendale, Pa.

ISO 6487. (1980) *Road vehicles—Techniques of measurement in impact tests—Instrumentation.* International Organization for Standardization, Geneva.

Khalil, T.B.; and Hubbard, R.P. (1977) Parametric study of head response by finite element modeling. *Journal of Biomechanics*, 10:119–132.

Khalil, T.B.; and Viano, D.C. (1977) *Impact response of a viscoelastic head model.* GMR-2380. General Motors Research Laboratories, Biomedical Science Department, Warren, Michigan.

Khalil, T.B.; and Viano, D.C. (1982) Critical issues in finite element modeling of head impact. *Proc. 26th Stapp Car Crash Conference*, pp. 87–102. Society of Automotive Engineers, Warrendale, Pa.

King, A.I.; and Cheng, R. (1984) *Kinesiology of the human shoulder and spine.* Final Report, DOT Contract No. DOT-HS-5-01232. Wayne State University, Detroit.

Kroell, C.K.; Schneider, D.C.; and Nahum, A.M. (1971) Impact tolerance of the human thorax. *Proc. 15th Stapp Car Crash Conference*, pp. 84–134. Society of Automotive Engineers, New York.

Kroell, C.K.; Schneider, D.C.; and Nahum, A.M. (1974) Impact tolerance of the human thorax II. *Proc. 18th Stapp Car Crash Conference*, pp. 383–457. Society of Automotive Engineers, Warrendale, Pa.

L'Abbé, R.J.; Dainty, D.A.; and Newman, J.A. (1982) An experimental analysis of thoracic deflection response to belt loading. *Proc. 7th International Conference on the Biomechanics of Impacts*, pp. 184–194. IRCOBI, Bron, France.

Lau, V.K.; and Viano, D.C. (1981) An experimental study of hepatic injury from belt-restraining loading. *Aviation, Space, and Environmental Medicine*, 52:611–617.

Mallikarjunarao, C.; Padgaonkar, A.J.; Levine, R.S.; Gurdjian, E.S.; and King, A.I. (1977) Kinesiology of the human spine under static loading. *1977 Biomechanics Symposium*, pp. 99–102. American Society of Mechanical Engineers, New York.

Maltha, J.; and Janssen, E.G. (1984) EEC comparison testing of four side impact dummies. *Biomechanics of Impacts in Road Accidents, Proceedings of a Seminar, 21–23 March 1983*, pp. 391–409. Commission of the European Communities, Luxembourg.

Marcus, J.H.; Morgan, R.M.; Eppinger, R.H.; Kallieris, D.; Mattern, R.; and Schmidt, G. (1983) Human response to and injury from lateral impact. *Proc. 27th Stapp Car Crash Conference*, pp. 419–432. Society of Automotive Engineers, Warrendale, Pa.

Melvin, J.W.; McElhaney, J.H.; and Roberts, V.L. (1972) Improved neck simulation for anthropometric dummies. *Proc. 16th Stapp Car Crash Conference*, pp. 45–60. Society of Automotive Engineers, New York.

Melvin, J.W.; Stalnaker, R.L.; Roberts, V.L.; and Trollope, M.L. (1973) Impact injury mechanisms in abdominal organs. *Proc. 17th Stapp Car Crash Conference*, pp. 115–126. Society of Automotive Engineers, Warrendale, Pa.

Melvin, J.W.; and Weber, K. eds. (1985) *Review of biomechanical impact response and injury in the automotive environment.* AATD Task B Final Report. UMTRI-85-3. The University of Michigan Transportation Research Institute, Ann Arbor.

Melvin, J.W.; Hess, R.L.; and Weber, K. (1985) Thorax. *Review of Biomechanical Impact Response and Injury in the Automotive Environment*, pp. 93–124. Task B Final Report. UMTRI-85-3. University of Michigan Transportation Research Institute, Ann Arbor.

Mertz, H.J. (1984) *A procedure for normalizing impact response data.* SAE 840884. Society of Automotive Engineers, Warrendale, Pa.

Mertz, H.J. (1985) *Biofidelity of the Hybrid III head.* SAE 851245. Society of Automotive Engineers, Warrendale, Pa.

Mertz, H.J.; and Patrick L.M. (1967) Investigation of the kinematics and kinetics of whiplash. *Proc. 11th Stapp Car Crash Conference*, pp. 267–317. Society of Automotive Engineers, New York.

Mertz, H.J.; and Patrick, L.M. (1971) Strength and response of the human neck. *Proc. 15th Stapp Car Crash Conference*, pp. 207–255. Society of Automotive Engineers, New York.

Mertz, H.J.; Neathery, R.F.; and Culver, C.C. (1973) Performance requirements and characteristics of mechanical necks. *Human Impact Response: Measurement and Simulation*, pp. 263–288. Edited by W.F. King and H.J. Mertz. Plenum Press, New York.

Mertz, J.H.; Hodgson, V.R.; Thomas, L.M.; and Nyquist, G.W. (1978) An assessment of compressive neck loads under injury-producing conditions. *The Physician and Sports Medicine*, 6:95–106.

REFERENCES

Messerer, O. (1880) *Uber Elasticitat and Festigkeit der Menschlichen Knochen.* J.G. Cotta, Stuttgart.

MIL-C-45662A. (1962) *Calibration system requirements.* U.S. Defense Department, Washington, D.C.

MIL-STD-810D. (1983) *Environmental test methods and engineering guidelines.* U.S. Department of Defense, Washington, D.C.

Mital, N.K. (1978) *Measurement of angular acceleration.* Ph.D. dissertation. Wayne State University, Detroit.

Mital, N.K.; Cheng, R.; King, A.I.; and Eppinger, R.H. (1978a) A new design for a surrogate spine. *Proc. 7th Experimental Safety Vehicle Conference*, pp. 427-438. U.S. Government Printing Office, Washington, D.C.

Mital, N.K.; Cheng, R.; Levine, R.S.; and King, A.I. (1978b) Dynamic characteristics of the human spine during $-G_x$ acceleration. *Proc. 22nd Stapp Car Crash Conference*, pp. 139-165. Society of Automotive Engineers, Warrendale, Pa.

Nahum, A.M.; Raasch, F.; and Ward, C. (1981) Impact response of the protected and unprotected head. *Head and Neck Injury Criteria: A Consensus Workshop*, pp. 31-39. Edited by A.K. Ommaya. U.S. Department of Transportation, National Highway Traffic Safety Administration, Washington, D.C.

Neathery, R.F. (1974) An analysis of chest impact response data and scaled performance recommendations. *Proc. 18th Stapp Car Crash Conference*, pp. 459-493. Society of Automotive Engineers, Warrendale, Pa.

Neilson, I.; Lowne, R.; Tarriére, C.; Bendjellal, F.; Gillet, D.; Maltha, J.; Cesari, D.; and Bouquet, R. (1985) The Eurosid side impact dummy. *Proc. 10th International Technical Conference on Experimental Safety Vehicles.* National Highway Traffic Safety Administration, Washington, D.C. (in press).

Newman, J.A. (1985) A generalized acceleration model for brain injury threshold (GAMBIT). Presented at the *Winterlude Head Injury Workshop.* Biokinetics, Ottawa.

Nusholtz, G.; Alem, N.M.; and Melvin, J.W. (1982) Impact response and injury to the pelvis. *Proc. 26th Stapp Car Crash Conference*, pp. 103-144. Society of Automotive Engineers, Warrendale, Pa.

Nusholtz, G.S.; Huelke, D.F.; Lux, P.; Alem, N.M.; and Montalvo, F. (1983a) Cervical spine injury mechanism. *Proc. 27th Stapp Car Crash Conference*, pp. 179-197. Society of Automotive Engineers, Warrendale, Pa.

Nusholtz, G.S.; Melvin, J.W.; and Lux, P. (1983b) The influence of impact energy and direction on thoracic response. *Proc. 27th Stapp Car Crash Conference*, pp. 69-94. Society of Automotive Engineers, Warrendale, Pa.

Nusholtz, G.S.; Lux, P.; Kaiker, P.; and Janicki, M. (1984) Head impact response: Skull deformation and angular acceleration. *Proc. 28th Stapp Car Crash Conference*, pp. 41-74. Society of Automotive Engineers, Warrendale, Pa.

Nyquist, G.W.; and King, A.I. (1985) Spine. *Review of Biomechanical Impact Response and Injury in the Automotive Environment*, pp. 45–87. Edited by J.W. Melvin and K. Weber. Task B Final Report. UMTRI–85–3. University of Michigan Transportation Research Institute, Ann Arbor.

Nyquist, G.W.; and Murton, C.J. (1975) Static bending response of the human lower torso. *Proc. 19th Stapp Car Crash Conference*, pp. 513–541. Society of Automotive Engineers, Warrendale, Pa.

Nyquist, G.W.; Begeman, P.C.; King, A.K.; and Mertz, H.J. (1980) Correlation of field injuries and GM Hybrid III responses for lap–shoulder belt restraint. *Journal of Biomechanical Engineering*, 102:103–109.

Patrick, L.M.; and Chou, C. (1976) *Response of the human neck in flexion, extension, and lateral flexion.* VRI–7–3. Vehicle Research Institute, Society of Automotive Engineers, Warrendale, Pa.

Patrick, L.M.; Lissner, H.R.; and Gurdjian, E.S. (1965) Survival by design: Head protection. *Proc. 7th Stapp Car Crash Conference*, pp. 483–499. Charles C. Thomas, Springfield, Ill.

Prasad, P.; and Daniel, R. (1984) A biomechanical analysis of head, neck, and torso injuries to child surrogates due to sudden torso acceleration. *Proc. 28th Stapp Car Crash Conference*, pp. 25–40. Society of Automotive Engineers, Warrendale, Pa.

Prasad, P.; and Mertz, H.J. (1985) *The position of the United States Delegation to the ISO Working Group 6 on the use of HIC in the automotive environment.* SAE 851246. Society of Automotive Engineers, Warrendale, Pa.

Prasad, P.; Melvin, J.W.; Huelke, D.F.; King, A.I.; and Nyquist, G.W. (1985) Head. *Review of Biomechanical Impact Response and Injury in the Automotive Environment*, pp. 1–43. Edited by J.W. Melvin and K. Weber. Task B Final Report. UMTRI–85–3. University of Michigan Transportation Research Institute, Ann Arbor.

Robbins, D.H. (1983) *Development of anthropometrically based design specifications for an advanced adult anthropomorphic dummy family. Volume 2: Anthropometric specifications for mid–sized male dummy.* UMTRI 83–53–2. University of Michigan Transportation Research Institute, Ann Arbor.

Robbins, D.H.; Melvin, J.W.; and Stalnaker, R.L. (1976) The prediction of thoracic impact injuries. *Proc. 20th Stapp Car Crash Conference*, pp. 697–729. Society of Automotive Engineers, Warrendale, Pa.

Rouhana, S.W.; Lau, I.V.; and Ridella, S.A. (1985) Influence of velocity and forced compression on the severity of abdominal injury in blunt, nonpenetrating lateral impact. *Journal of Trauma*, 25:490–500.

Schneider, L.W.; and Nahum, A.M. (1972) Impact studies of facial bones and skull. *Proc. 16th Stapp Car Crash Conference*, pp. 186–203. Society of Automotive Engineers, New York.

REFERENCES

Schneider, L.W.; Robbins, D.H.; Pflug, M.A.; and Snyder, R.G. (1983) *Development of anthropometrically based design specifications for an advanced adult anthropomorphic dummy family.* 3v. UMTRI-83-53. The University of Michigan Transportation Research Institute, Ann Arbor.

Shugar, T.A. (1977) *A finite element head injury model.* Final report on DOT-HS-289-3-500-IA. Naval Civil Engineering Laboratory, Point Hueneme, California.

Society of Automotive Engineers, Human Mechanical Response Task Force. (1985) *Human mechanical response characteristics.* SAE J1460. Society of Automotive Engineers, Warrendale, Pa.

Stalnaker, R.L.; and McElhaney, J.H. (1970) *Head injury tolerance for linear impacts by mechanical impedance methods.* ASME 70-WA/BHF-4. American Society of Mechanical Engineers, New York.

Stalnaker, R.L.; and Ulman, M.S. (1985) Abdominal trauma—Review, response, and a new criteria. *Proc. 29th Stapp Car Crash Conference.* Society of Automotive Engineers, Warrendale, Pa. (in press).

Stalnaker, R.L.; Roberts, V.L.; and McElhaney, J.H. (1973) Side impact tolerance to blunt trauma. *Proc. 17th Stapp Car Crash Conference*, pp. 377-408. Society of Automotive Engineers, New York.

Tarriére, C.; Fayon, A.; and Hartemann, F. (1980) *Contribution for a new regulation insuring an upgraded protection for side impact.* Presentation to NHTSA Hearing on Side Impact Protection Upgrading, January 31 and February 1, 1980. Association Peugeot-Renault, Paris.

Tarriére, C.; Leung, Y.C.; Fayon, A.; Got, C.; Patel, A.; and Banzet, P. (1981) Field facial injuries and study of their simulation with dummy. *Proc. 25th Stapp Car Crash Conference*, pp. 435-468. Society of Automotive Engineers, Warrendale, Pa.

Viano, D.C.; and Lau, I.V. (1985) Thoracic impact: A viscous tolerance criterion. *Proc. 10th International Technical Conference on Experimental Safety Vehicles.* National Highway Traffic Safety Administration, Washington, D.C. (in press).

Viano, D.C.; Culver, C.C.; Haut, R.C.; Melvin, J.W.; Bender, M.; Culver, R.H.; and Levine, R.S. (1978a) Bolster impacts to the knee and tibia of human cadavers and an anthropomorphic dummy. *Proc. 22nd Stapp Car Crash Conference*, pp. 403-428. Society of Automotive Engineers, Warrendale, Pa.

Viano, D.C.; Haut, R.C.; Golocovsky, M.; Absolon, K. (1978b) Factors influencing biomechanical response and closed chest trauma in experimental thoracic impacts. *Proc. 22nd American Association for Automotive Medicine Conference and 7th International Association for Accident and Traffic Medicine Conference*, Vol. 1, pp. 67-83. AAAM, Morton Grove, Illinois.

Viano, D.C.; Lau, I.V. (1985) Thoracic impact: A viscous tolerance criterion. *Proc. 10th International Technical Conference on Experimental Safety Vehicles.* National Highway Traffic Safety Administration, Washington, D.C. (in press).

Walfisch, G.; Fayon, A.; Tarriére, C.; Rosey, J.P.; Guillon, F.; Got, C.; Patel, A.; and Stalnaker, R.L. (1980) Designing of a dummy abdomen for detecting injuries in side impact collisions. *Proc. 5th International Conference on the Biomechanics of Impacts*, pp. 149-164. IRCOBI, Bron, France.

Walker, L.B., Jr.; Harris, E.H.; and Pontius, U.R. (1973) Mass, volume, center of mass, and mass moment of inertia of head and head and neck of human body. *Proc. 17th Stapp Car Crash Conference*, pp. 525-537. Society of Automotive Engineers, New York.

Ward, C.C. (1981) Status of head injury modeling. *Head and Neck Injury Criteria: A Consensus Workshop*, pp. 157-162. Edited by A.K. Ommaya. U.S. Department of Transportation, National Highway Traffic Safety Administration, Washington, D.C.

Ward, C.C. (1982) Finite element models of the head and their use in brain injury research. *Proc. 26th Stapp Car Crash Conference*, pp. 71-85. Society of Automotive Engineers, Warrendale, Pa.

Wismans, J.; and Spenny, D.H. (1983) Performance requirements for mechanical necks in lateral flexion. *Proc. 27th Stapp Car Crash Conference*, pp. 137-148. Society of Automotive Engineers, Warrendale, Pa.

Wismans, J.; and Spenny, D.H. (1984) Head-neck response in frontal flexion. *Proc. 28th Stapp Car Crash Conference*, pp. 161-171. Society of Automotive Engineers, Warrendale, Pa.

Yamada, H. (1970) *Strength of biological materials*, pp. 75-80. Edited by F.G. Evans. Williams and Wilkins, Baltimore.